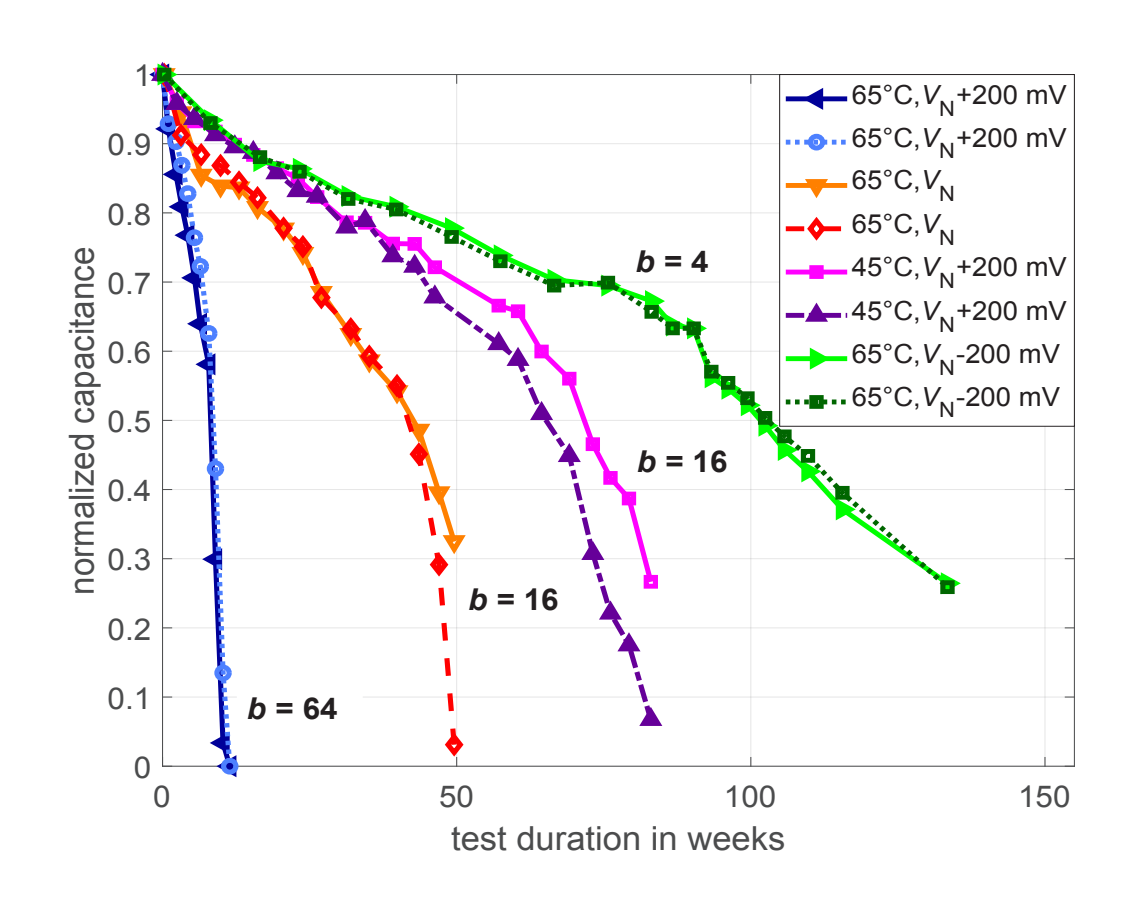




# Julia Drillkens

# Aging in Electrochemical Double Layer Capacitors

- An Experimental and Modeling Approach -



# Aging in Electrochemical Double Layer Capacitors

- An Experimental and Modeling Approach -

Von der Fakultät für Elektrotechnik und Informationstechnik der Rheinisch-Westfälischen Technischen Hochschule Aachen zur Erlangung des akademischen Grades eines Doktors der Ingenieurwissenschaften genehmigte Dissertation

vorgelegt von

Diplom-Ingenieurin
Julia Drillkens
aus Tönisvorst

Berichter:

Universitätsprofessor Dr. rer. nat. Dirk Uwe Sauer Universitätsprofessor Dr.-Ing. Ulrike Krewer

Tag der mündlichen Prüfung: 22. Februar 2017

Diese Dissertation ist auf den Internetseiten der Hochschulbibliothek online verfügbar.

# **Julia Drillkens**

# Aging in Electrochemical Double Layer Capacitors

- An Experimental and Modeling Approach -

### **Bibliographic information published by the Deutsche Nationalbibliothek**

The Deutsche Nationalbibliothek lists this publication in the Deutsche Nationalbibliographie; detailed bibliographic data are available in the Internet at: <a href="http://dnb.d-nb.de">http://dnb.d-nb.de</a>.

#### **Electronic version**

The electronic version is available online on the institutional repository of RWTH Aachen University (<a href="https://publications.rwth-aachen.de">https://publications.rwth-aachen.de</a>).

D82 (Diss. RWTH Aachen University, 2017)

### **AACHENER BEITRÄGE DES ISEA**

Vol. 93

Editor:

Univ.-Prof. Dr. ir. Rik W. De Doncker Director of the Institute for Power Electronics and Electrical Drives (ISEA), RWTH Aachen University

Copyright ISEA and Julia Drillkens 2017

All rights reserved. No part of this publication may be reproduced, stored in a retrieval system, or transmitted in any form or by any means, electronic, mechanical, photocopying, recording, or otherwise, without prior permission of the publisher.

ISSN 1437-675X

Institut für Stromrichtertechnik und Elektrische Antriebe (ISEA)

Jägerstr. 17/19 • 52066 Aachen • Germany

Tel: +49 (0)241 80-96920 Fax: +49 (0)241 80-92203 post@isea.rwth-aachen.de

#### Vorwort

Die hier vorliegende Dissertation entstand während meiner Zeit als wissenschaftliche Mitarbeiterin von Prof. Dirk Uwe Sauer am Institut für Stromrichtertechnik und elektrische Antriebe (ISEA) der RWTH Aachen.

Schon während meiner Studien- und Diplomarbeit habe ich mich in der Arbeitsgruppe Elektrochemische Energiewandlung und Speichersystemtechnik mit verschiedenen Batterietechnologien beschäftigt. Zunächst habe ich äußere thermische Einflüsse bei Tests an Lithium-Ionen-Batterien simuliert, um dann vorrangig bunte Redox-Flow-Batterien im Labormaßstab zu untersuchen und zu optimieren. Während meiner Zeit als wissenschaftliche Mitarbeiterin habe ich mich dann den Doppelschicht-Kondensatoren und speziell deren Alterung zugewendet.

Ich möchte mich ganz herzlich bei Professor Sauer für die Chance als wissenschaftliche Mitarbeiterin am ISEA zu arbeiten und für die hervorragende Betreuung dieser Arbeit bedanken. Außerdem gilt mein Dank Professor Krewer für die Übernahme des Koreferats.

Das ISEA hat sich immer durch eine besondere Atmosphäre ausgezeichnet. Während der Arbeit wurde neben der Diskussion von inhaltlichen Fragestellungen auch immer viel gelacht und es gab einen tollen Zusammenhalt unter den Kollegen. Die lustigen Abende bei diversen Sportturnieren, Grillfesten und ganz besonders bei den Exkursionen werde ich immer in sehr guter Erinnerung behalten. Da gilt mein Dank an alle Kollegen für die schöne Zeit.

Ganz besonders möchte ich mich noch bei denen bedanken, die mich bei der Erstellung dieser Arbeit unterstützt haben. Mein Dank gilt Julia Kowal, die mir das Thema Doppelschichtkondensatoren nähergebracht hat, und Moritz Teuber, der mich von meiner Funktion als Teamleiter und Team Supercaps in Personalunion erlöst hat und das Thema auch weiter verfolgen wird. Außerdem danke ich den Kollegen im Labor, die teils über Jahre meine Alterungstests betreut haben, wie auch allen Studenten, deren Experimente und Simulationen zu dieser Arbeit beigetragen haben. Weiterhin möchte ich den Ballsaal-Kollegen für Anregungen und Unterstützung bei meiner Arbeit danken.

Zuletzt möchte ich noch meiner Familie danken. Mein Vater hat schon, als ich noch ein Kind war, gesagt, dass Ingenieurin eine gute Berufswahl für mich wäre. Auch wenn ich damals anderer Meinung war, hat er letztendlich doch recht gehabt. So habe ich studiert und dann auch noch promoviert, auch wenn mein Bruder sich immer nur gewundert hat, warum ich denn immer noch zur Schule gehe. Meine Mutter hat mich bei diesem Werdegang immer unterstützt. Diese Arbeit möchte ich daher meinen Eltern und meinem Bruder widmen.

Bamberg im Dezember 2017, Julia Drillkens

Introduction 1

## Content

1.		Introduction				
2.		Fundamentals				
	2.	1	Sup	ercapacitors	9	
	2.	2.2 Stor		age Principle of Electrochemical Double Layer Capacitors	11	
		2.2.	1	The Electrochemical Double Layer	12	
		2.2.	2	Pseudocapacitance	15	
	2.	3	Elec	trochemical Double Layer Capacitor Structure	16	
		2.3.1		Electrodes	16	
		2.3.	2	Electrolyte	18	
		2.3.	3	Separator	21	
		2.3.	4	Cell Geometry	22	
3.		Elec	trica	l Characterization	25	
	3.	1	Cha	racterization Methods	25	
		3.1.1		DC Characterization Methods	25	
		3.1.	2	AC Characterization Methods	27	
	3.	2	Ехр	erimental Results of EDLC's Electrical Performance	32	
		3.2.	1	Comparison of EDLCs with different solvents	34	
	3.	3	Con	nparison of EDLC and Commercial Li-Ion Capacitor	35	
		3.3.	1	Temperature Dependency	36	
4.		Pore	e Stri	ucture of Activated Carbons	39	
	4.	4.1 E		trolyte-Electrode Interface	40	
	4.	2	Ion	Redistribution Processes and Self-Discharge	41	
		4.2.	1	Results of Self-Discharge Measurement on AN-based EDLCs	44	
		4.2.	2	Long-Time Experiment	46	
5.	Modeling of Porous Carbon Electrodes			49		
	5.	1	Mod	del Representation Assuming Uniform Cylindrical Pores	49	
		5.1.	1	Generalized Pore Impedance Model	53	
	5.	2	Mod	deling Approach Considering Different Pore Sizes	54	
		5.2.	1	${\bf Modeling\ Approach\ Considering\ Dynamic\ Behavior\ and\ Diffusion\ Processes \dots}$	56	
6.		Elec	tro-1	Thermal Modeling	59	
	6.	1	Elec	trical Model	59	
	6.	2	The	rmal Model	60	

	6.2.1		Thermodynamic Principles	60	
	6.	2.2	Separation in Volume Elements	65	
	6.	2.3	Simulation of Thermal Transients	67	
	6.	2.4	Single Cell Model Validation	69	
(	6.3	Мо	dule Model	70	
7.	Αį	ging Be	ehavior	73	
	7.1	Agi	ng Phenomena	73	
	7.2	Acc	elerated Aging Tests	75	
	7.	2.1	Calendric Aging Tests	75	
	7.	2.2	Cyclic Aging Test	98	
•	7.3	Pos	t Mortem Analysis	107	
	7.	3.1	EDLCs with Cellulose-Based Separator	108	
	7.	3.2	Porosimetry	111	
	7.	.3.3	EDLCs with Polypropylene Membrane Separator	112	
	7.	3.4	Coin Cells	121	
	7.	3.5	Conclusions from Post Mortem Analysis	132	
	7.4	Cor	nclusions from Experimental Aging Investigations	134	
8.	Αį	ging M	lodel	137	
;	8.1	Cal	endric Aging Model	138	
;	8.2	Val	dation of Calendric Aging Model	139	
;	8.3 Mo		deling of Cyclic Aging	142	
;	8.4	App	olication of Aging Models on EDLC Modules	143	
9.	Co	onclus	ion and Outlook	149	
	9.1	Cor	nclusion	149	
	9.2	Out	:look	152	
10	•	Refer	ences	155	
A.	ΑĮ	ppend	ix	165	
В.	. Deutsche Zusammenfassung 1				

Introduction 3

#### 1. Introduction

Electrochemical double layer capacitors (EDLC), also known under the brand names supercapacitors or ultracapacitors, are energy storage devices that offer high power density, very high cycling capability and mechanical robustness. In contrast to batteries, EDLCs do theoretically not undergo chemical reactions while storing energy. EDLCs are an interesting option for applications with the need of high charging or discharging current rates for a short time since their energy density is much lower compared to batteries. Thus, they are discussed especially for trains or automotive applications [1,2], but also for stationary applications, e.g. for frequency and voltage stabilization or power quality applications. Due to their high cycle life, EDLCs are also used in applications where numerous cycles of the storage devices are required, e.g. container cranes or excavators [2,3].

The working principle is based on an electrostatic effect that is purely physical and therefore highly reversible. However, parasitic chemical reactions might occur during the storage process of EDLCs. Predominantly voltage and temperature driven reactions can lead to capacity fade and resistance increase. Due to the operation conditions, such as elevated ambient temperatures and high current rates, a temperature increase of the EDLC itself is often unavoidable. Furthermore, EDLCs, e.g. in uninterruptable power supply (UPS) systems, have always to be fully charged so that they are able to deliver maximum power immediately. The impact of temperature and voltage in EDLC's capacitance and resistance characteristics is exemplarily shown for one EDLC type in Figure 1.1. The device was stored at constant temperature and constant voltage conditions.

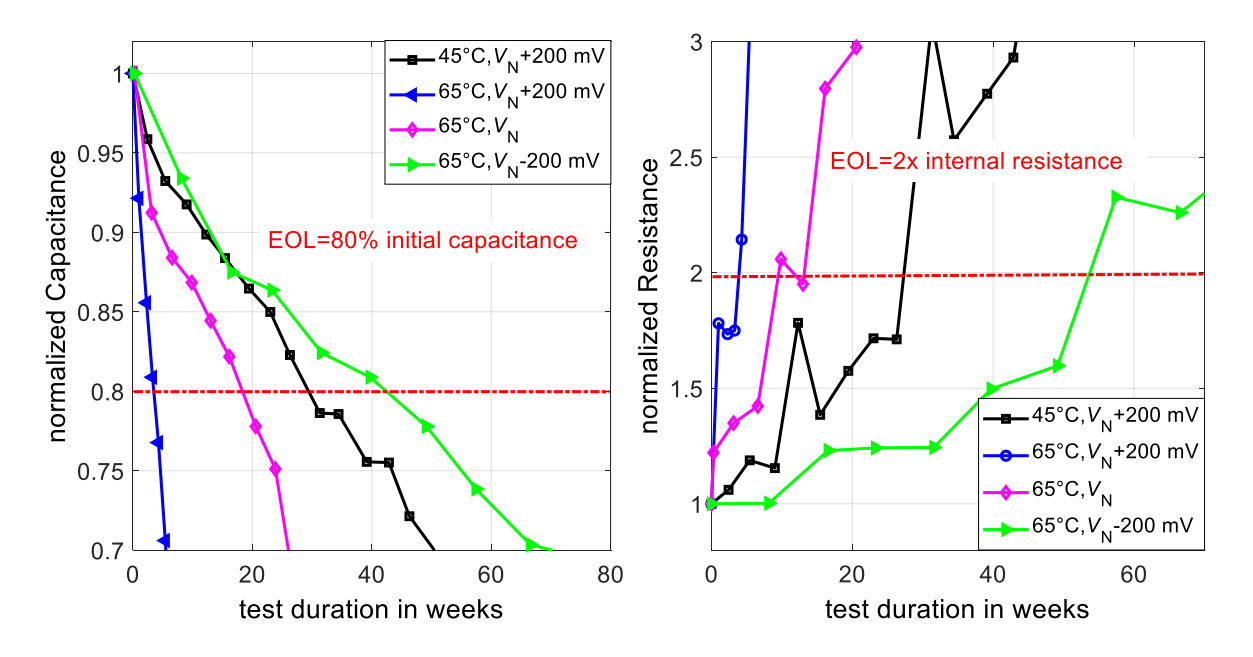


Figure 1.1: Capacitance decrease (left) and resistance increase (right) of one EDLC type under storage conditions at different temperatures and voltages;  $V_N$  means rated working voltage

The results indicate that high temperatures and/or high voltages shorten EDLC's lifetime significantly. To analyze the voltage and temperature impact on the aging behavior, highly accelerated aging test are usually performed at voltage and temperature conditions far beyond the typical operation conditions. The question is then how accurate are conclusions from these aging tests to real life conditions.

To minimize EDLC's aging, optimized operating strategies are required to enlarge the EDLC's lifetime and therefore save costs. This also needs to be considered for the designing of EDLC modules and packs. Hot spots can occur due to bad heat transfer. It is essential to avoid these hot spots because they lead to accelerated aging of the affected cells. The resulting resistance increase leads then to a higher temperature increase and further aging. The weakest cell of an EDLC module, where all cells are connected in series, limits its performance, uneven aging must be prevented. That's why high temperatures and large temperature differences need to be avoided by applying cooling strategies.

For optimal system design, e.g. operating and cooling strategies, an electro-thermal model that is able to predict the EDLC performance and temperature development is a useful tool. By adding an aging model, lifetime prediction under the considered operation conditions can be carried out. However, for a good lifetime prediction a good understanding of the aging processes and their impact factors is essential otherwise the model cannot be parameterized properly.

Thus, the causes for the observed aging processes in EDLCs, such as capacitance loss or resistance increase, have to be analyzed. A deeper understanding of aging processes of EDLCs helps to improve the EDLC materials as well as the manufacturing process and therefore prolong their lifetime. However, aging processes in EDLCs are very complex. They predominantly result from decomposition reactions of the organic electrolyte, depending on the chemical composition of the EDLC materials. Moreover, different reactions on the positive and the negative electrode lead to different aging behavior of both electrodes.

Differences can already be observed by optical inspection, as can be seen from Figure 1.2. It shows the wound off electrodes of an aged cylindrical EDLC. The stiff positive electrode sticks slightly to the polymeric separator and must be pulled off. The separator side facing the positive electrode got brownish, whereas the other side stayed white.

By answering the question, which chemical reactions occur and how they affect the capacitance and resistance behavior of EDLCs, as well as if one electrode dominates the aging behavior, the material design can be improved.

Introduction 5

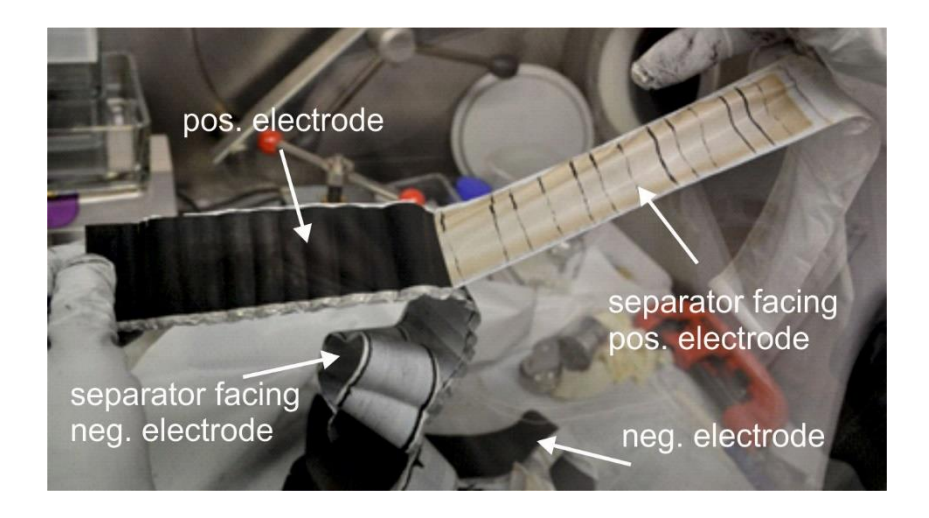


Figure 1.2: Unwound aged EDLC electrodes: the positive electrode is very stiff and the facing separator side got a brownish color whereas the separator side facing the negative electrode stayed white

This thesis focusses on the aging behavior of commercially available EDLCs with acetonitrile-based electrolyte and carbon-based electrodes. By means of extensive calendric and cyclic aging tests the impact of temperature, voltage and current rate on the EDLC's lifetime and the applicability of accelerated aging tests are discussed. Furthermore, post mortem analyses of selected cells from the accelerated aging tests were carried out to achieve first indications of the processes occurred inside the cells during the accelerated aging tests. Subsequently, a modular electro-thermal aging model was developed which is a useful tool for lifetime prediction.

Initially, chapter 2 presents the fundamentals of the so-called supercapacitors. First, different types of capacitors belonging to this family such as EDLCs, pseudocapacitors and hybrid capacitors are presented. In chapter 2.1, the theory of the electrochemical double layer and its contribution to the EDLC capacitance are explained. Chapter 2.2 gives an overview of different cell geometries and multiple materials used in EDLCs and their impact on the performance.

Afterwards, chapter 3 shows the electrical behavior of different supercapacitors. In chapter 3.1 several electrical characterization methods that are used in this thesis are explained. Experimental results of EDLCs with different solvents are shown, and the solvent-impact on electrical performance, especially on the deep temperature performance, is analyzed. Then, in chapter 3.3, the electrical performance of an EDLC with acetonitrile-based electrolyte is compared to a Lithium hybrid capacitor.

In chapter 4, the complex pore structure of activated carbon is discussed, the commonly used electrode material in commercial EDLCs on which this work focusses. Chapter 4.1 introduces the concept of macro, meso and micropores and explains their different influences

on the characteristics of the capacitor. Furthermore, ion transport processes in porous carbon electrodes filled with organic solvents are described. Then, chapter 4.2 highlights the electrolyte-carbon-interface, the accessibility of small micropores and the resulting available capacity, followed by the discussion of ion redistribution processes and self-discharge in chapter 4.3.

Subsequently, modeling approaches for porous carbon electrodes are presented in chapter 5. The porous structure of EDLC's electrodes leads to electrical effects that cannot be described with only the standard capacitive elements. The introduced approaches are weighted for several current profiles followed by a discussion of advantages and disadvantages.

Based on the electrical modeling approach of chapter 6, an electro-thermal model is developed in chapter 6.1. Chapter 6.2 introduces a thermal modeling approach considering different types of heat generation and heat transfer. Finally, the developed electro-thermal single cell model was enlarged to a module model.

Chapter 7 deals with the aging behavior of EDLCs. Initially, various aging mechanisms are discussed in chapter 7.1. Afterwards, the results of accelerated aging tests are presented in chapter 7.2. The calendric aging of different EDLC types and its dependency on voltage and temperature was analyzed. Additionally, a superimposed aging impact of cyclic aging is discussed. Experimental results with more than 1,000,000 full equivalent cycles will be presented and analyzed. Subsequently, the results of post mortem analyses of selected cells are presented and some first conclusions regarding the causes of capacity fade and resistance increase are drawn.

Finally, the electro-thermal model of chapter 6 was enlarged to an aging model, considering calendric aging which is presented in chapter 8. Additionally, this model has the option to add the influence of cyclic aging. This allows the use of the model for lifetime prediction. A proper model parameterization is challenging. Thus, the model developed in this thesis should be seen as a first step and basic model for lifetime simulations. With a deeper understanding of the aging processes and therefore a more appropriate parameterization this model can be adopted and further developed. In this thesis lifetime predictions for different cooling strategies are discussed by using the electro-thermal aging model for an example configuration and parameterization.

Until today lifetime tests on EDLCs are mostly done by means of calendric aging tests at elevated temperatures and voltages. Such operating conditions are chosen because they allow tests within a period of time from 6 weeks to 6 months. However, various results presented in this thesis show that the extrapolation from these accelerated tests to operation within normal voltage and temperature ranges does not work.

Introduction 7

This thesis will show that calendric aging tests hardly give meaningful results regarding the way of performance change during aging, the aging processes and the achievable lifetimes in cyclic operation. The thesis was started to show how cycle lifetimes could be calculated from calendric life tests, but the main result is, that this simply not working. Therefore, the standard methods of lifetime prediction for EDLCs are in question now.

#### 2. Fundamentals

Supercapacitors are nowadays widely used in various applications because of their high power capability and long cycle life. Commercially available products, on which this thesis focusses, usually store energy by means of the electrochemical double layer. They are often sold under the brand names "supercap" or "supercapacitor". However, in this thesis the term supercapacitor is used in a wider range, namely for the entire capacitor family including pseudocapacitors and hybrid capacitors, whereas capacitors storing their energy in an electrochemical double layer are named electrochemical double layer capacitors, or in short EDLCs. This chapter gives an overview of different capacitor types and their characteristics. Afterwards the storage principle of EDLCs by means of the electrochemical double layer and other contributions to the overall capacity such as pseudocapacitance are discussed. Finally, the materials that can be used in EDLCs for electrodes, separators and electrolytes and their properties are discussed as well as different cell geometries.

### 2.1 Supercapacitors

Supercapacitors are capacitors that can achieve capacitance values up to several thousand Farads. Regarding energy density, they are in a mid-position between conventional capacitors and batteries. But they are able to offer very high power densities at high charge/discharge current rates for a short time. Therefore, they are widely used in applications requiring for short higher power pulses ranging from seconds to some ten seconds and a huge number of cycles [2–8]. This thesis focuses on electrochemical double layer capacitors (EDLCs) with carbon-based electrodes and organic electrolyte which are mainly used in commercial applications. They are sold under brand names such as "Supercaps", "Ultracaps" or "Goldcaps" by manufacturers like Maxwell, Nesscap, LS Mtron, Batscap and others. The storage principle of this kind of capacitors is purely electrostatic. Energy is stored due to the accumulation of charge carriers at the oppositely charged electrode. Since in theory no chemical reactions occur during charging EDLCs are able to undergo more than 500,000 cycles and have therefore a significant longer cycle life than batteries [6]. The storage principle of EDLCs is described in detail in chapter 2.2.

The energy *E* that can be stored in a capacitor can be determined by means of the following formula:

$$E = \frac{1}{2}C V^2 {(2.1)}$$

*C* is the capacitance and *V* the rated voltage of the capacitor. Hence, energy depends on the squared cell voltage. However, beside EDLCs other types of capacitors with different designs and materials belong to the group of supercapacitors as can be seen from Figure 2.1.

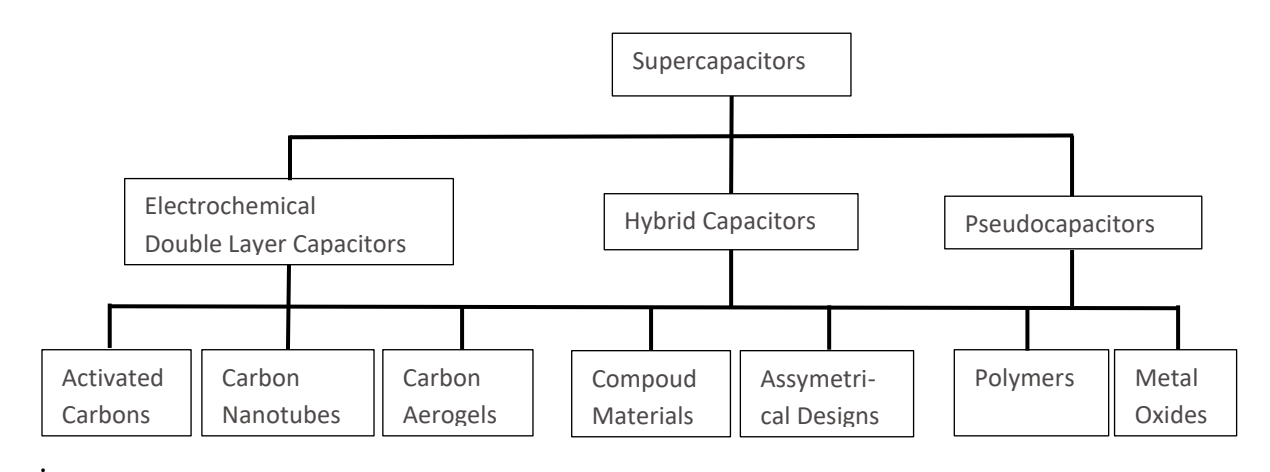


Figure 2.1: Overview on different types of supercapacitors

Hybrid capacitors, also known as "asymmetric capacitors", are a mixture of an EDLC and a battery. They are usually based on one capacitor electrode and one battery electrode. Special types of these hybrid capacitors are "lithium-ion capacitors" or abbreviated "lithium capacitors" (LIC). They use one activated carbon based positive electrode like an EDLC, one graphite negative intercalation electrode like a Li-ion battery (LIB) and Li<sup>+</sup> containing organic electrolyte [9]. Thus, this capacitor type is a series hybrid connection. It can reach higher voltages (> 4 V) than a conventional EDLC (< 3 V) and possesses therefore higher energy density. However, due to the intercalation process hybrid capacitors suffer like batteries from aging processes during charging/discharging and can therefore not achieve a cycle life as long as EDLCs [10]. But first manufacturers like Taiyo Yuden or JSR Micro offer nowadays commercial hybrid capacitors. The internal serial connection of these hybrid capacitors usually results in a device with doubled capacitance compared to EDLCs with activated carbon electrode on both sides. Moreover, since the battery electrode is cycled in a very narrow state-of-charge range, the cycle life of the hybrid capacitor is higher than cycle life of batteries [9].

Another approach in combining EDLC and battery electrodes is the internal parallel connection. Therefore, EDLC and battery material are combined at every electrode to so-called bimaterial electrodes. Cericola et al. showed in simulations of external parallel connection of an EDLC and a battery that parallel connections are more promising than a series one [11]. Therefore, there is some research effort on internally parallel hybrid capacitors using bimaterial electrodes. These electrodes consist of purely capacitive material, such as activated carbon, and faradic insertion material as it is used e.g. in Li-ion batteries. Cericola et al. investigated e.g. capacitors with bi-materials based on activated carbon and LiMn<sub>2</sub>O<sub>4</sub> for hybrid capacitors [12].

However, Li-ion batteries show severe safety problems under abusive conditions like "thermal runaway" [13] and since lithium capacitors uses in "one-half" the same materials they could therefore carry the same risks. Smith et al. showed that at temperatures > 90 °C the lithiated carbon electrode of LIC undergoes the same type of exothermic reactions as Li-ion batteries. But since the hybrid capacitor does not contain a highly energetic, faradaic electrode, the carbon electrode does not contribute to self-heating [14]. Thus, one may conclude

that LICs are more abuse tolerant than Li-ion batteries but there is still some research effort needed. Some electrical characteristics of LICs compared to EDLCs are shown in chapter 3.3.

Pseudocapacitors are the third group of supercapacitors. They store energy not purely electrostatically like EDLCs but predominantly by faradaic processes. Chemical reactions occur, in a certain measure also on EDLCs, always due to material impurities during the production process. Pseudocapacitors even force the contribution of chemical reactions to the energy storage process by introducing redox-active material into the electrodes. Therefore, a faradaic component is added to the energy storage process and thus the working point of the EDLC is shifted from high power density to higher energy density.

The electrode surfaces of pseudocapacitors undergo adsorption processes or redox-reactions of metal oxides during charging/discharging which causes the pseudocapacitive effect [15]. In this case faradic currents occur due to chemical reactions on the electrodes surface. This "pseudo"-capacitance has no electrostatic origin and occurs when an electro-chemical charge transfer process takes place limited by a finite amount of active material or available surface [3].

This effect also occurs in EDLC due to impurities of the used materials. Because this is inevitable there are intentions to further increase the pseudocapacitance of EDLC by using certain electrode materials. In this way, EDLC's capacitance can be increased by a factor of more than 10 at the expense of speed and power performance. Typical pseudocapacitive materials are transition metal oxides, especially ruthenium oxide and conducting polymers like polyaniline (PANI), polypyrrole (PPy), or derivates of polythiophene (PTh) [16–19].

Another approach of achieving a pseudocapacitive energy storage is doping of the carbon materials with pseudocapacitive molecules [20,21]. However, the high prices of the electrode materials hinder a commercial use of pseudocapacitors.

Highly porous carbons which are usually used in EDLCs possess a significant amount of heteroatoms like nitrogen or oxygen and/or functional groups at the carbon surface. They can also add a certain pseudocapacitive component to their overall capacity. The storage principle is described in detail in chapter 2.2.2.

## 2.2 Storage Principle of Electrochemical Double Layer Capacitors

This thesis focusses on capacitors whose storage principle is based on the formation of an electrochemical double layer at the electrode/electrolyte interface. The energy of an EDLC is stored purely electrostatically in the double layer at the electrode/electrolyte interface. Figure 2.2 shows the schematics of the functional principle of an EDLC. Basically, an EDLC consists of two solid electrodes, typically activated carbon containing a large surface, and separated by an ion-permeable separator which is soaked in electrolyte. This electrolyte contains positively and negatively charged ions that accumulate at the carbon surface and form the

so-called double layer in case a potential is applied to the electrode. Simply spoken, a plate capacitor arises at each electrode, consisting of one solid carbon electrode and one electrode of accumulated ions. The overall capacitance results then from the series connection of both double layer capacitances. If both capacitances are equal the overall capacitance results in half of the capacitance of a single electrode.

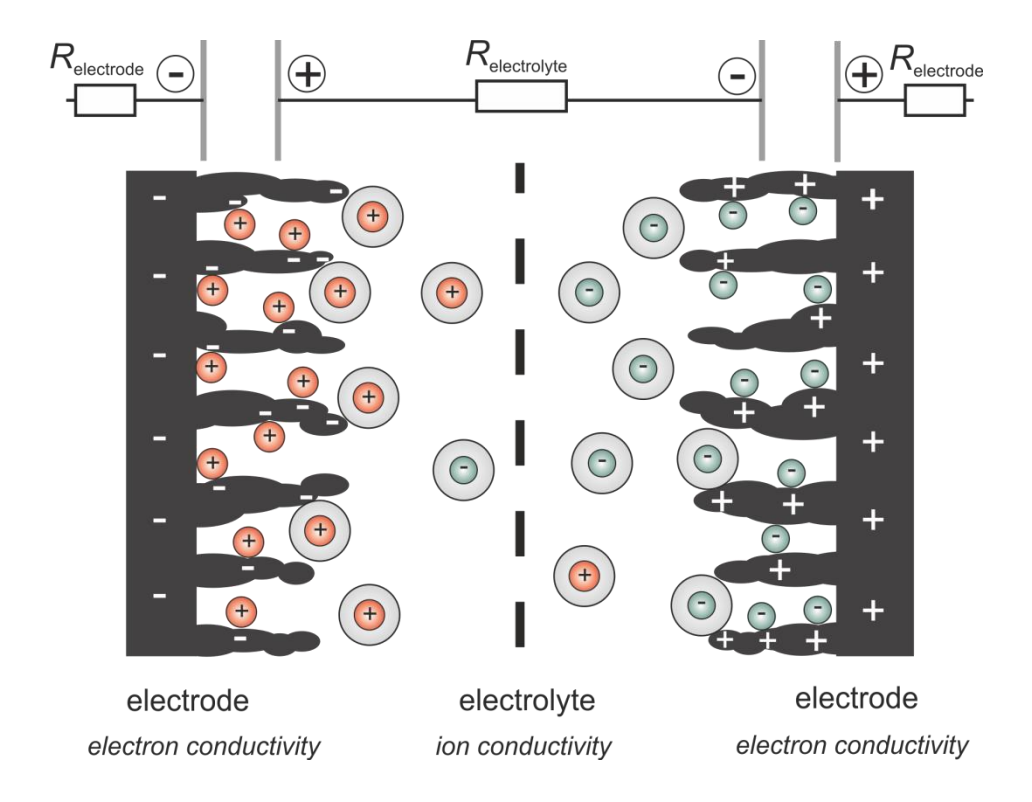


Figure 2.2: Principle of an electrochemical double layer capacitor

From Figure 2.2 it can also be seen that solvent molecules build a solvation shell around the ion which influences the double layer and the electrode's pore accessibility. This effect is discussed in detail in chapter 4.1.

In the following the phenomenon of the electrochemical double layer is discussed.

#### 2.2.1 The Electrochemical Double Layer

The phenomenon of an electrochemical double layer was first observed by Helmholtz in 1879 [22]. Hence, this double layer at the solid/liquid interface is also called Helmholtz-layer.

The basic principle of an electrochemical double layer capacitor is the interaction of a solid electrode and charged ions in the electrolyte. By applying a voltage to a solid electrode, oppositely charged ions of the liquid electrolyte are attracted. Thus, the electrode and the ion layer form a capacitor with a linear voltage curve as shown in Figure 2.3.

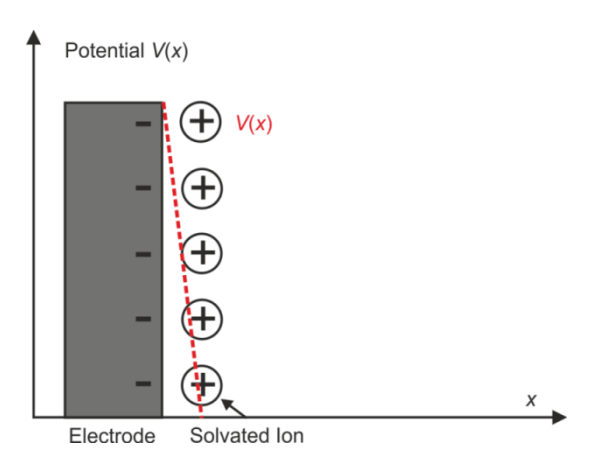


Figure 2.3: Helmholtz double layer

However, this model is quite simple and Helmholtz' assumption that surface charges on the electrode side are compensated by oppositely charged ions in case of an applied electric potential was further developed by Gouy and Chapman in 1913 [23,24]. They regarded the thermal diffusion of the ions. The rigid ion layer described by Helmholtz was then being seen as diffuse and wider-stretched. Due to the temperature-dependent statistic ion distribution, the electric field decreases exponentially and the capacitance is voltage dependent, see Figure 2.4.

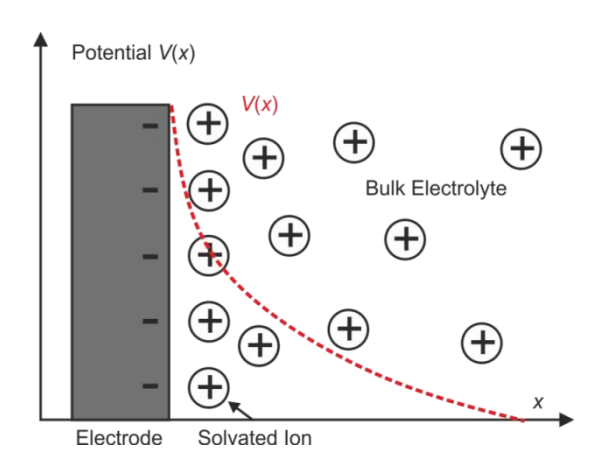


Figure 2.4: Gouy-Chapman double layer

Stern combined in 1924 both double layer models [25]. The Stern model consists of a Helmholtz-layer close to the solid electrode and a diffuse double according to Gouy-Chapman, see Figure 2.5. As the later assumed ions in the electrolyte to be point charges, the predicted capacitance was too high. Stern was the first who regarded electrolyte ions not as point charges but as a charged ion core with solvation respectively hydration shells around it as shown in Figure 2.5. Thus, the ions have a certain dimension and therefore the capacitance can be predicted more accurately by using the Stern model.

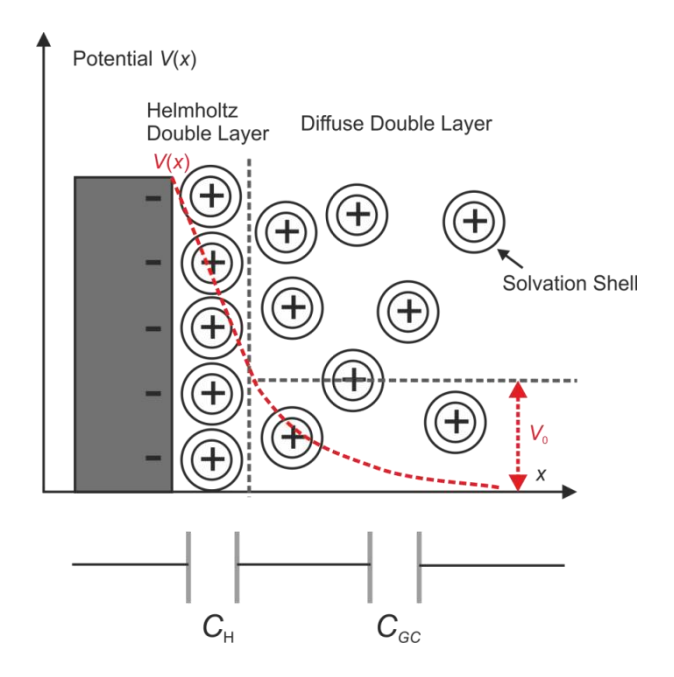


Figure 2.5: Double layer according to Stern

The electrochemical double layer contributes significantly to the high capacitance of EDLCs because the distance between the electrode and the charged ions is very small, only a few Ångström. This becomes clear according to the capacity formula of a plate capacitor:

$$C_H = \varepsilon \cdot \frac{A}{d} \tag{2.2}$$

According to formula (2.2) the capacitance  $C_H$  can be determined from the quotient of the electrode's surface A and the distance between the electrodes d, multiplied with the dielectric constant  $\varepsilon$  of the material in-between. In case of an EDLC electrode d means the distance from ions to the carbon electrode and the dielectric constant results from the chosen electrolyte. The influence of the Gouy-Chapman double layer can be determined according to equation (2.3) [23]:

$$C_{GC} = A \cdot z \cdot F \cdot \sqrt{\frac{2 \cdot \varepsilon \cdot c}{R \cdot T}} \cdot \cosh\left(\frac{z \cdot F}{2 \cdot R \cdot T} \cdot U_{DL}\right)$$
 (2.3)

Where A is the surface, z the number of ions, F the Faraday constant,  $\varepsilon$  the dielectric constant, c the ion density directly at the electrode, R the gas constant, T the absolute temperature and  $U_{DS}$  the voltage over the entire double layer. Since the double layer according to Stern is composed of the Helmholtz and the Gouy-Chapman double layer in series, as can be seen from Figure 2.5, the overall capacitance results to:

$$C_{DL} = \frac{C_H \cdot C_{GC}}{C_H + C_{GC}} \tag{2.4}$$

Equation (2.4) implies that the smaller of both capacitances determines the double layer capacitance. This must be considered for the properties of the double layer. Its capacitance depends on the electrode potential as well as on the ionic concentration of the solution.

#### 2.2.2 Pseudocapacitance

Double layer capacitors as well as conventional capacitors form an electric field between the capacitor plates if a potential is applied to the electrodes. The major charging energy is then stored in the electric field. Beside this electrostatic behavior several chemical reactions might occur at the electrode/electrolyte interface and contribute to the storage process. These reactions can be concluded generally as faradic behavior according to Faradays laws.

The contribution of these processes to the charge storage leads to a capacity increase that is called pseudocapacitance because it is not based on the electrostatic storage principle of the double layer but on reversible redox reactions between electrode and electrolyte at the electrode's surface. Cations at the negative electrode pass away one electron to the electrode during charging and these electrons goes to the positive electrode via the external current circuit. At the same time, many anions go through the electrolyte from the negative to the positive electrode. There, these ions do not absorb the electrons again, but in charged state highly ionized transition metal oxide ions do so instead.

Hence, also in case of carbon-based EDLCs pseudocapacitive contributions to the over-all capacity exist. The contribution of the pseudocapacitance to the overall capacitance of a carbon-based EDLC is in a ratio of 1-5% [26]. Functional groups at the electrodes surfaces undergo redox reactions and contribute to the charging and discharging accumulation. If these redox processes are reversible, the pseudocapacitive storage process is fast since no transport or diffusion processes occur [27]. Functional groups at the carbon surface containing nitrogen [28] or oxygen [15,29] lead to pseudo-capacitive behavior. However, it is very hard to distinguish between contribution of the double layer capacitance and of the pseudocapacitance to the overall capacitance since they depend on each other [18,30].

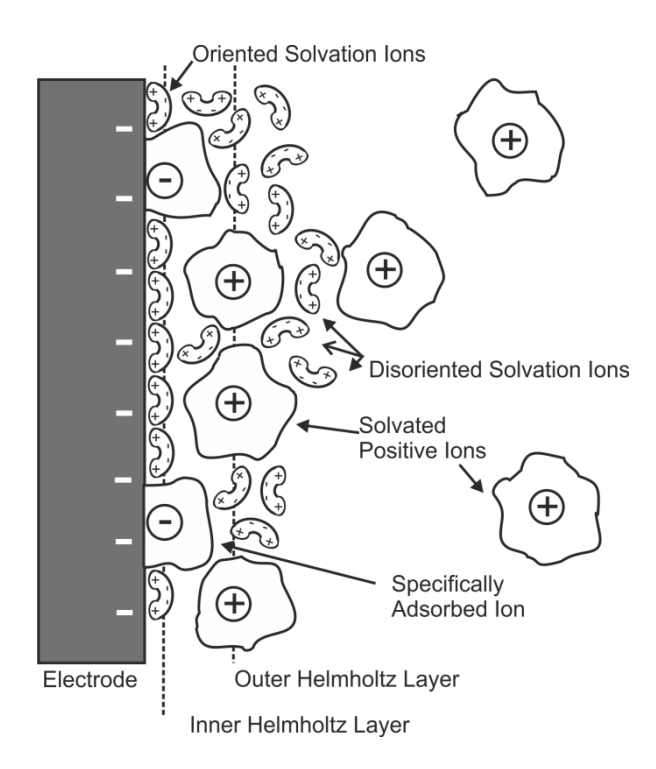


Figure 2.6: Schematic of a complex electrochemical double layer with pseudocapacitive effects based on [26]

Figure 2.6 shows the schematic of the double layer at the negative electrode's surface. Some ions are specifically adsorbed at the electrode's surface and contribute to pseudocapacitance. They lost partly their solvation shell<sup>1</sup> and are then bonded via Van-der-Waals-forces to the electrode's surface. Especially anions tend to specific adsorption and can be adsorpted at the electrode's surface although this has negative access charge. The double layer has to be divided therefore into an inner Helmholtz-layer containing the specifically adsorpted ions and into an outer Helmholtz-layer as shown in Figure 2.6. More information can be found in [26,31,32].

## 2.3 Electrochemical Double Layer Capacitor Structure

This chapter gives a brief overview on materials used in EDLCs as electrodes, separators and electrolytes and their properties. Furthermore, different cell geometries are considered.

#### 2.3.1 Electrodes

The electrical performance of an EDLC depends strongly on the selected electrode material because the surface characteristics of the electrode influence the capacitance of the EDLC. The required characteristics that must be fulfilled to make the electrode material suitable for EDLCs are:

<sup>&</sup>lt;sup>1</sup> Solvation shells are explained in detail in chapter 4.1.

- High conductivity
- High surface area (up to 2500 m²/g are reported [33])
- Good corrosion resistance against the electrolyte
- High temperature stability
- Controlled pore structure
- Easily to manufacture and low costs

#### 2.3.1.1 Activated Carbon

A typically used electrode material for EDLCs is activated carbon. It is a carbon material with very high surface area und high porosity. The basic raw material can be derived from natural precursors [34], such as coconut [35] or extraordinary materials like cow dung [36]. Activated carbons are then produced from so-called "graphene sheets". Due to thermal or chemical activation processes, the surface of carbon is significantly enlarged, whereas surface conditions and porosity of the resulting activated carbons highly depend on the manufacturing conditions [37]. During the activation process the links between adjacent graphene sheets can be broken. Thus, some sheets are able to rotate into parallel orientation. Thus, an activated carbon can be seen as a combination of numerous small domains consisting of a few graphene sheets in parallel. In order to explain the complex structure of activated carbons Dahn and co-workers proposed the model of "falling cards" [38].

By means of thermal activation, carbon is modified by controlled gasification of carbon chars also called "burn-off". This process is usually carried out in a temperature range between 700 °C and 1100 °C [39]. In contrast, chemical activation is carried out at slightly lower temperatures, 400 °C to 700 °C, and involves dehydration processes due to the presence of certain agents such as phosphoric acids, zinc chloride and potassium hydroxide [39].

Temperature and involved reactants influence pore size and structure. The resulting porosity is in the range of 65% to 75% [40]. More information on carbon activation processes can be found in [39].

The electrode material must be matched to the ions of the electrolyte, which means that the pores must be accessible for the ions. Otherwise the smallest pores will not contribute to the capacitance, see chapter 4.1. Although surface areas of more than 2000 m²/g are reported [32,[41]], Barbieri et al. found that the gravimetric capacitance does not increase linearly with the surface area. They observed a maximum gravimetric capacity at 1200 m²/g. They concluded that this phenomenon is not due to poor ion accessibility of very small micropores but due to the thickness of the pore wall which is close to the screening length of the electric field. Therefore, the pore cannot accommodate sufficient charge at high potentials and is saturated [42].

Beside activated carbon which is used in most commercial EDLCs, there are some promising research activities using carbon nanotubes [43–46], carbon aerogels [47,48] or graphene [49,50] or mixtures of these as electrode material for EDLCs.

Further improvements of the electrode characteristics can be achieved by adding certain conducting additives like carbon black [51]. This gives better electron conductivity to all parts of the electrode material.

#### 2.3.1.2 Current Collectors

In commercial electrode technology, the current collector is the main physical link between the electrode and the EDLC external junction. Deposition of active material on current collectors is the most popular solution for electrode preparation because of its low ESR impact. Therefore, carbon material with additives and binders like polytetrafluoroethylene (PTFE) [41] are applied to the current collector. The material used as current collector needs to satisfy not only the electrical properties, especially high conductivity, but it also needs to be stable in the used electrolyte. An overview of possible EDLC electrolytes is given in chapter 2.3.2.

In commercial EDLCs, commonly using organic electrolyte, aluminum foils are usually used as current collectors [7]. Due to the high corrosion potential of aluminum in aqueous electrolytes, this type of EDLC uses conducting plastic sheets or nickel foils as current collectors [52].

#### 2.3.2 Electrolyte

The types of electrolytes that are suitable for EDLC can be generally divided into three groups: (I) aqueous electrolytes, (II) organic solvents with dissolved salts and (III) ionic liquids.

The required properties for a good electrolyte-solution system of an EDLC are a good ion conductivity which results in a low equivalent series resistance (ESR) and high power capability. Furthermore, high voltage and temperature stability is needed, and finally the electrolyte, especially the electrolyte ions, must be suitable for the porous carbon electrodes.

#### 2.3.2.1 Aqueous Electrolytes

Early EDLCs have been constructed with aqueous electrolytes. The most common aqueous electrolytes are sulfuric acid or potassium hydroxide (KOH). Due to these alkali or acidic solvents, current collectors and casings have to be selected carefully to avoid metal corrosion. Advantageously, aqueous electrolyte offers high conductivity (up to  $^{-1}$  S cm $^{-1}$  [41]) and therefore low ESR which leads to high power capability and low costs. Moreover, the specific capacitance (F g $^{-1}$ ) of carbons in aqueous electrolytes is higher than in non-aqueous electrolytes [41]. This effect is due to the higher dielectric constant of aqueous systems [51] and

due to the higher surface accessibility of smaller aqueous ions compared to organic ions [53,54].

However, the decomposition voltage limit is in theory the redox potential of water at 1.23 V, practically, in kinetic terms, in a range of 1.3 V to 1.4 V. Since energy of an EDLC depends on the squared value of voltage according to equation (2.1), EDLCs with aqueous electrolytes are not able to offer high energy densities. Thus, EDLCs with aqueous electrolytes are seldom used in commercial applications with the need of high energy and are therefore not regarded in this thesis. However, there is still a lot of research effort on aqueous electrolytes [54,55] because they are environmentally friendly and offer low costs.

#### 2.3.2.2 Organic Electrolytes

Commercial EDLCs usually use organic electrolytes instead of aqueous electrolytes because they are able to withstand much higher voltages (up to 3 V cell voltage with organic electrolyte compared to 1.2-1.5 V with aqueous electrolyte [6]). Organic electrolytes are composed of a salt solved in an organic solvent. The salt mostly utilized is tetraethyl ammonium tetrafluroroborate (TEA $^+$  TFB $^-$ ) and the most common organic solvents are acetonitrile (AN) and propylene carbonate (PC). Table 2.1 shows their physical characteristics.

Acetonitrile is commonly used as solvent in commercial EDLCs due to its high voltage stability and good conductivity even at low temperatures [56]. However, acetonitrile is highly flammable and toxic. In contrast, propylene carbonate is non-toxic but offers a significantly lower performance at low temperatures as can be seen in chapter 3.2.

Solvent	Freezing point	<b>Boiling point</b>	Dielectric constant	Viscosity	Electrolyte conductivi- ty <sup>2</sup>
acetonitrile H3C- C ≡ N	-45.7 °C	81.60 °C	37.5	0.345 cP (25 °C)	60 mS cm <sup>-1</sup>
propylene carbonate	-49 °C	242 °C	65	2.5 cP (25 °C)	11 mS cm <sup>-1</sup>

Table 2.1: Characteristics of acetonitrile [41] and propylene carbonate [57]

\_

<sup>&</sup>lt;sup>2</sup> Conductivity of electrolyte consisting of 1 M solution of tetra-ethylammonium tetrafluoroborate (TEABF<sub>4</sub>) in acetonitrile respectively propylene carbonate

Beside the general questions of voltage stability, conductivity and viscosity, the utilized electrolyte must be suitable to the carbon electrode. A carbon active material with a very microporous structure possesses a very high surface area but this fact does not automatically lead to a very high capacitance. The key point in electrode/electrolyte design is the pore accessibility of the ions of the electrolyte. If a pore is too narrow and can therefore not be accessed by the ions, the effective surface area is reduced. Kim et al. found out that a pore around two to three times larger than the ion diameter should be the most suitable pore size for high capacitance [58].

An overview of the characteristics of the most common salt tetraethylammonium tetrafluoroborate containing the ions TEA<sup>+</sup> and TFB<sup>-</sup> is given in Table 2.2. In solution the ions are surrounded by a solvation shell and therefore the radius is larger. The radius depends on the solvent. To enter small micropores ions can completely or partly lose their solvation shell [59] as discussed in chapter 4.1.

Beside solvent characteristics such as conductivity and dielectric constant the ion salt concentration influences also the electrolyte's chemical stability and the energy limitations of organic electrolytes [60].

	TEA <sup>+</sup>	TFB-
Structure	N <sup>+</sup>	Н — В — н Н — н
molecular diameter [61]	0.74 nm	0.49 nm
molecule size solvated in acetonitrile [62]	1.30 nm	1.16 nm
molecule size solvated in propylene carbonate [62]	1.35 nm	1.40 nm

Table 2.2: Diameters of salt molecules with and without solvation shell

#### 2.3.2.3 Ionic Liquids

In recent years, much research effort has been done to overcome the thermal and voltage stability limits of common organic electrolytes to achieve higher energy densities. Ionic liquids (IL) seem to satisfy the basic characteristics and are able to withstand higher potentials at the same time. ILs are at room temperature molten salts, offer good conductivity and negligible vapor pressure. They can withstand voltages up to 4 V and the boiling point is higher than 400 °C. Moreover, they are neither flammable nor toxic [41]. But the temperature dependency of cells with IL is much higher than the temperature dependency of cells with organic electrolyte. Due to the high viscosity of ILs at low temperatures their deep temperature performance is very poor [63]. Hence, EDLCs with IL electrolyte were investigated with an operating temperature of >60 °C [64].

However, the prices for ILs are still very high and therefore they are not used in EDLCs that can be purchased on the market now. More information on ionic liquids can be found in literature [65–67].

#### 2.3.3 Separator

A separator of an EDLC has to be electrochemically stable and must possess high purity, high porosity and must be chemically inert against the utilized electrolyte and electrode. Of course, the thickness of a separator should be as thin as possible to achieve low internal resistance and to reduce the separator's costs. The limiting factors for minimum thickness are the risk of electrical shortening due to free carbon particles and the mechanical strength in order to allow the winding process during manufacturing [41].

The porosity of EDLC separators is very high (up to 80%) compared to approximately 30 to 50% of a battery separator [41]. The rate of porosity in commercial cells is limited because the higher the porosity is the greater is the amount of required electrolyte and therefore the higher are the costs.

An often-used separator type in EDLC is a paper separator mostly based on cellulose fibers. It offers low prize and a low resistance. However, it requires an intensive drying process in order to remove water traces because any humidity in the cell would shorten its lifetime [68]. But the maximum drying temperature of a cellulose-based separator is limited. Furthermore, paper separators are not suitable for voltages higher than 2.5-2.7 V because at voltages of about 3 V oxidative deterioration occurs [41].

To overcome these problems several types of polymeric separators have been developed. However, separator materials and their thicknesses must be chosen carefully especially for high power applications since polymeric separators have higher resistance than cellulose-based separators of the same thicknesses and lead therefore to lower power. Tõnurist et al. have investigated several separator types and their properties in EDLCs [69].

#### 2.3.4 Cell Geometry

Beside different materials, geometries of commercial EDLCs differ depending on manufacturer and application. They are usually available in two different geometries: cylindrical and prismatic shape. Both types consist of one or several windings of aluminum current collector double-side coated with activated carbon, separator soaked with electrolyte, and then again coated current collector and separator. Most manufacturers offer both types in varied sizes. Cylindrical EDLCs are easier to manufacture since there is only one winding and prismatic EDLCs are easier to stack. Figure 2.7 shows the simplified winding schematics of these two cell geometries.

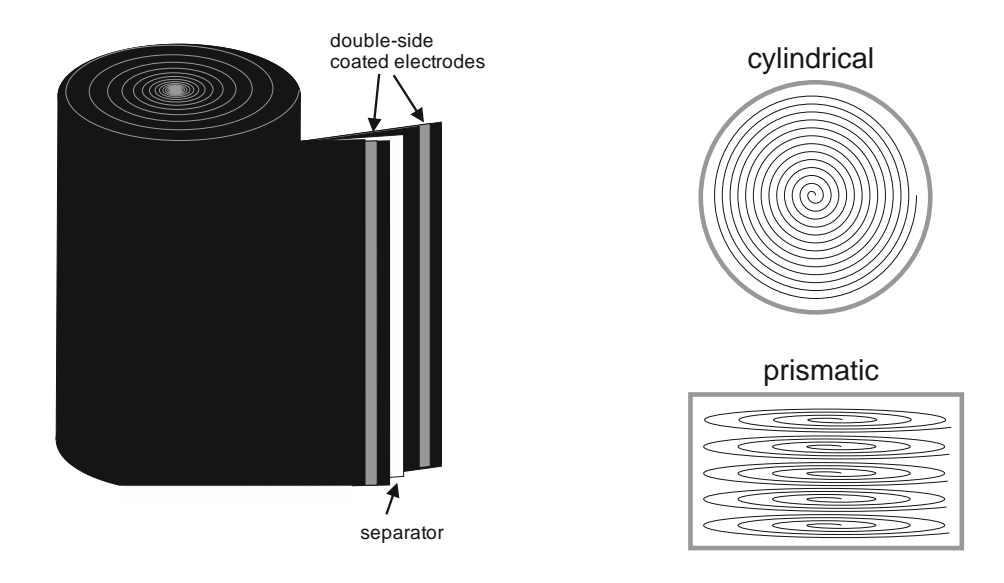


Figure 2.7: Simplified winding schematics of EDLCs

In case of a cylindrical EDLC there is only one winding consisting of one negative electrode layer, one separator layer, one positive electrode layer, and another separator layer. Both separator layers are soaked in electrolyte. On the other hand, in case of a prismatic EDLC multiple flat windings are stacked in a prismatic case.



Figure 2.8: Commercial EDLCs of different sizes and geometries

Figure 2.8 gives an overview of different commercial EDLCs as they are investigated in this thesis. Their geometrical shape is especially important for thermal considerations. Since cylindrical EDLCs have in many cases one pole on top and one on bottom they have a more homogeneous heat generation and distribution than prismatic EDLCs that have commonly both poles on top. These thermal aspects are essential for thermal modeling as it is done in chapter 6.2.

Electrical Characterization 25

#### 3. Electrical Characterization

Depending on the different materials such as electrodes or electrolyte's solvent EDLCs respectively LICs vary especially in their performance and temperature depending behavior. This chapter initially presents several characterization methods for capacitance and resistance determination, DC measurements as well as AC measurements. Then the results of EDLCs with different organic solvents are compared in their electrical and thermal behavior as well as an EDLC is compared to a commercial LIC.

#### 3.1 Characterization Methods

Several characterization methods for capacitance and resistance determination are presented in the following. Generally, it is distinguished between DC and AC characterization methods.

#### 3.1.1 DC Characterization Methods

In the following different DC characterization methods for the determination of capacitance and resistance are presented.

#### 3.1.1.1 Capacitance Determination

The DC capacitance is measured according to Figure 3.1 by means of the voltage slope at constant current discharge. As can be seen the voltage decay is nearly linear. For the capacitance determination, the EDLC devices were discharged first to 0 V, and afterwards the voltage was hold for 15 min (V-phase) at 0 V. Then the EDLC was charged to rated working voltage followed by another V-phase of 15 min. Finally, the EDLC was discharged with a current rate of 10 mA/F.

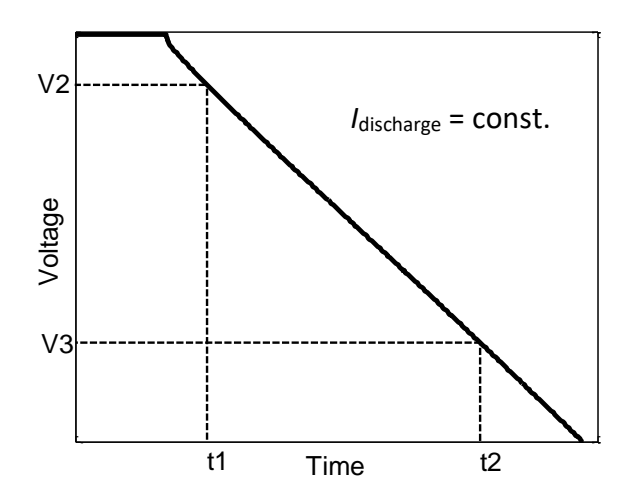


Figure 3.1: Determination of the DC capacitance from the voltage slope at discharge

The capacitance can be then determined by using the following formula:

$$C = \frac{I \cdot (t_2 - t_1)}{V_2 - V_1} \tag{3.1}$$

Alternatively, the capacitance can be determined by the discharged charge Q which means the integration of the discharge current. The capacitance is then calculated from:

$$C = \frac{Q}{V} = \frac{\int I_{\text{discharge}} \, dt}{V}$$
 (3.2)

During the accelerated aging tests presented in chapter 7.2 EDLCs were charged with constant current till nominal voltage followed by a constant voltage phase for 15 min and a constant current discharge. The second method is applied for capacitance determination.

#### 3.1.1.2 Resistance Determination

Several resistance components contribute to the internal resistance *R*i of an EDLC that can be associated with charge-transfer processes, electrolyte and ion transport [6,80]. Due to the intrinsic charge accumulation in the double layer, the contribution of charge transfer processes can be usually neglected. The contribution of the electrode resistance is also very small since electrodes of conventional EDLCs are made of highly porous carbon possessing a very high electric conductivity due to added conducting agents like carbon blacks or graphite. Thus, the electrolyte resistance is believed to be the major contributor to the total internal resistance of an EDLC. It can be divided into the bulk electrolyte resistance and the electrolyte resistance in the pores as described in detail in [70].

According to [70] the DC resistance can be determined by measuring the voltage drop at the beginning of discharge.

Electrical Characterization 27

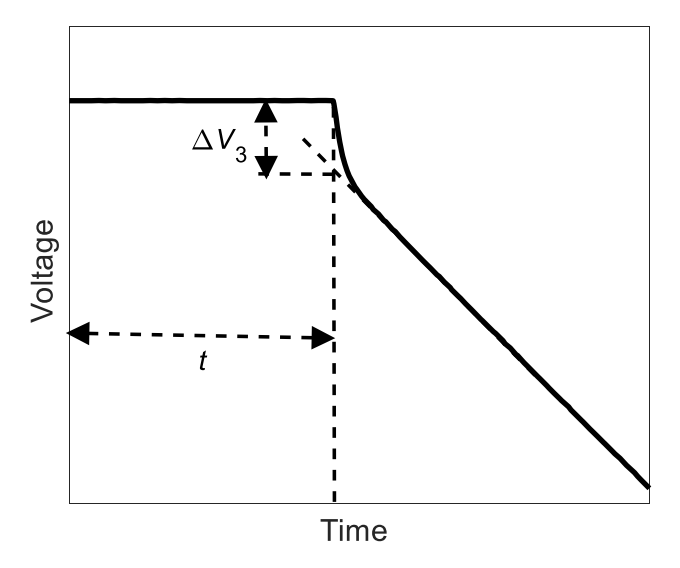


Figure 3.2: Determination of the DC internal resistance by measuring the voltage decay at the beginning of discharge

The DC resistance  $R_{\rm DC}$  calculates then to:

$$R_{\rm DC} = \frac{\Delta V_3}{I} \tag{3.3}$$

Since the voltage does not decrease linearly immediately after the beginning of discharge because the current distribution in the electrodes is not fully established, EDLC resistance varies with time. Therefore, voltage is extrapolated linearly till the beginning of discharge to receive the steady state resistance.

Another method to measure the DC resistance of an EDLC is to determine it from the voltage recovery after the discharge current pulse [71]. In this case no current is applied but this method depends on the complex ion redistribution processes [72] and the resistance value depends on the time period after the current cut-off when the voltage is read [41].

#### 3.1.2 AC Characterization Methods

In the following different AC characterization methods for the determination of capacitance and resistance are presented.

#### 3.1.2.1 Electrochemical Impedance Spectroscopy

Electrochemical impedance spectroscopy (EIS) is a widely used non-invasive method that allows analyzing the dynamic behavior of electrochemical systems, e.g. electrochemical storage devices such as batteries or supercapacitors by a stationary measuring procedure. In

electrochemistry EIS can be used to identify electrochemical processes and to characterize materials or devices [73].

The measuring principle is as follows: Small sinusoidal current or voltage signals are applied to the device over a wide frequency range. Then the resulting complex impedance of the device is calculated from the measured current or voltage response for each frequency.

Generally, it has to be distinguished between two measurement methods:

- Galvanostatic: A sinusoidal current signal with a defined frequency is used as excitation and the voltage response is measured.
- Potentiostatic: A sinusoidal voltage signal is used as excitation and the current response is measured.

In order to achieve comparable results by using impedance spectroscopy the following conditions have to be fulfilled: linearity, time invariance and causality [73].

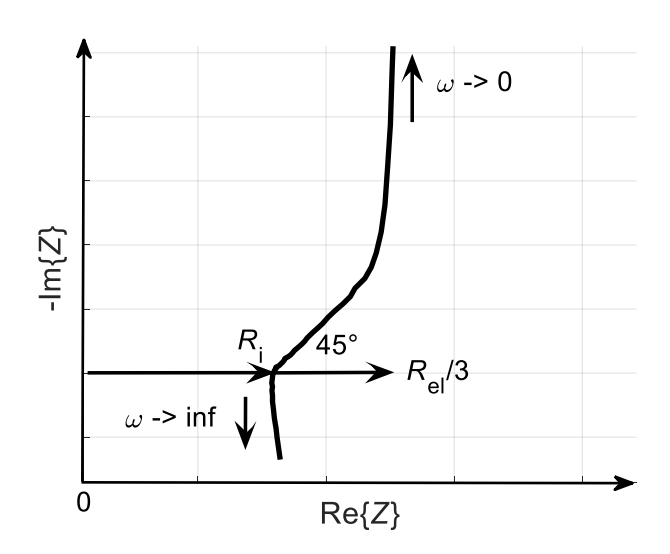


Figure 3.3: Schematic of a typical Nyquist chart of an EDLC

The typical Nyquist plot of an EDLC is shown in Figure 3.3, where the negative imaginary part of the impedance is plotted over the real part. It can be divided into three main sections: At low frequencies ( $f \le 0.1$  Hz) and therefore high AC penetrability a large amount of the pore volume contributes to the responding signal. In this region of Nyquist plot the EDLC behaves nearly purely capacitive and the phase-angle approaches asymptotically to -80 to  $-90^{\circ 3}$ . The second section is in the frequency region of 10 Hz < f < 0.1 Hz, where the AC signal stems from less porous material. The curve slope in this region is approximately 45°. In the high-frequency region of AC the porous electrode behaves like a flat. The resistance observed at

<sup>&</sup>lt;sup>3</sup> An ideal capacitor would have a phase angle of 90° but due to the porous carbon structure and/or possible leakage currents the phase angle is in reality a little bit less than 90°.

Electrical Characterization 29

Im{Z=0} represents all ohmic resistance components of the EDLC. Due to the complex pore structure of EDLCs, which is explained in detail in [81] and [73], there are different time constants for the accessibility of different pore sizes. Small micropores are accessed by ions after a certain time that is longer than a short current pulse. In case of very short current pulses respectively high frequencies small pores cannot be accessed and therefore the measured resistance is smaller at high frequencies. Ion redistribution processes can also affect the measured resistance [51]. Therefore, knowing the testing procedure and the charge/discharge history is essential because different methods lead to different results as discussed by Burke et al. in [74]. In practice, the internal or ohmic resistance is determined by measuring the resistance at f=1000 Hz or f=100 Hz. The Nyquist plot shows additionally a small high frequency part with positive imaginary part of the impedance. This inductive behavior is caused by connectors, cables and cell geometry.

Nevertheless, the Nyquist plot shown in Figure 3.3 represents the impedance behavior of an ideal capacitor with an ideally homogeneous cylindrical pore structure. Especially in case of aged EDLCs and possible pore blocking due to decomposition products of the electrolyte as analyzed by Bittner et al. [61] this ideal pore structure is no longer existent. Keiser et al. simulated the Nyquist plots for different pore shapes as shown in Figure 3.4. Case 1 represents the ideal cylindrical pore considered in Figure 3.3. Cases 2 to 4 shows different pore shapes with narrowed pore opening which results in an angle less than 45° of the diffusion arc. If the pore shape is like a ball as in case 4 the Nyquist plot shows a semi-circle arising. In case of a narrowing pore like a horn (case 5), the diffusion arc results in an angle higher than 45°.

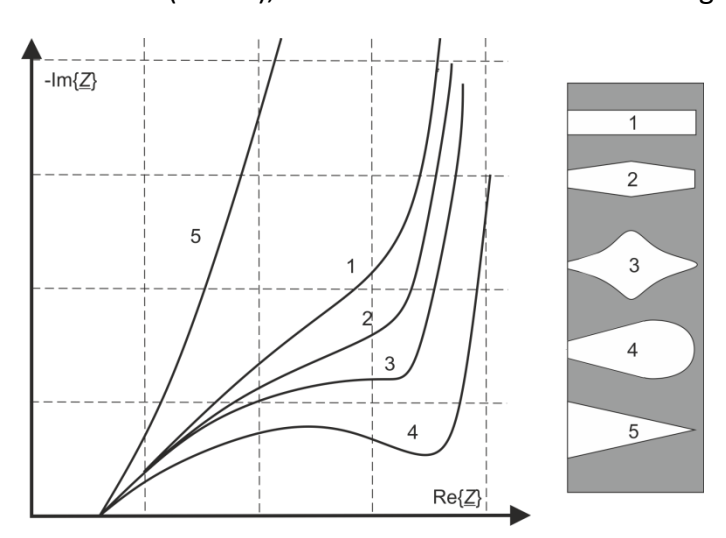


Figure 3.4: Nyquist plots of different pore shapes, based on [75]

#### 3.1.2.2 Characterization by Using Imaginary Capacitance

An ideal capacitor can be represented by a capacitor in series with a resistance. The capacitance of an ideal capacitor is independent of the frequency. However, this ideal behavior does not match the behavior of a real EDLC. The capacitance is represented as nearly vertical line in the Nyquist chart. But since it does not incline with an exact angle of 90° but less, it is

not independent on frequency. The resistance is frequency-dependent as well. Therefore, the impedance of an EDLC can be written in complex form as follows:

$$Z = R(\omega) + \frac{1}{j\omega \cdot C(\omega)}$$
(3.4)

Taberna et al. used a method to model impedance data by using a so-called supercapacitance K [76]. By taking this method into account the total impedance of the EDLC can be expressed as:

$$Z = R(\omega) + \frac{1}{j\omega \cdot C(\omega)} = \frac{1}{j\omega \cdot K}$$
(3.5)

leading to

$$K = \frac{C(\omega)}{1 + jR(\omega) \cdot C(\omega) \cdot \omega}$$

$$= \frac{C(\omega)}{1 + R^{2}(\omega) \cdot C^{2}(\omega) \cdot \omega^{2}} - \frac{jR(\omega) \cdot C^{2}(\omega) \cdot \omega}{1 + R^{2}(\omega) \cdot C^{2}(\omega) \cdot \omega^{2}}$$
(3.6)

or

$$K = C' - jC'' \tag{3.7}$$

where C' and C" are the real and imaginary components of supercapacitance, respectively:

$$C' = \frac{C(\omega)}{1 + R^2(\omega) \cdot C^2(\omega) \cdot \omega^2}; \quad C'' = \frac{R(\omega) \cdot C^2(\omega) \cdot \omega}{1 + R^2(\omega) \cdot C^2(\omega) \cdot \omega^2}$$
(3.8)

By considering the EDLC impedance in a complex form as

$$Z(\omega) = Z'(\omega) + jZ''(\omega)$$
(3.9)

It is alternatively possible to derive the real and imaginary parts of supercapacitance directly from the impedance data by using equation (3.5) and equation (3.7):

$$C'(\omega) = \frac{-Z''(\omega)}{\omega |Z(\omega)|^2}; \quad C''(\omega) = \frac{Z'(\omega)}{\omega |Z(\omega)|^2}$$
(3.10)

The real part  $C(\omega)$  corresponds to the DC or low frequency AC conditions of the considered EDLC whereas the imaginary part  $C'(\omega)$  is directly proportional to resistance and corresponds to losses in form of energy dispersion [77].

A typical plot of the imaginary capacitance of an EDLC is shown in Figure 3.5.

Electrical Characterization 31

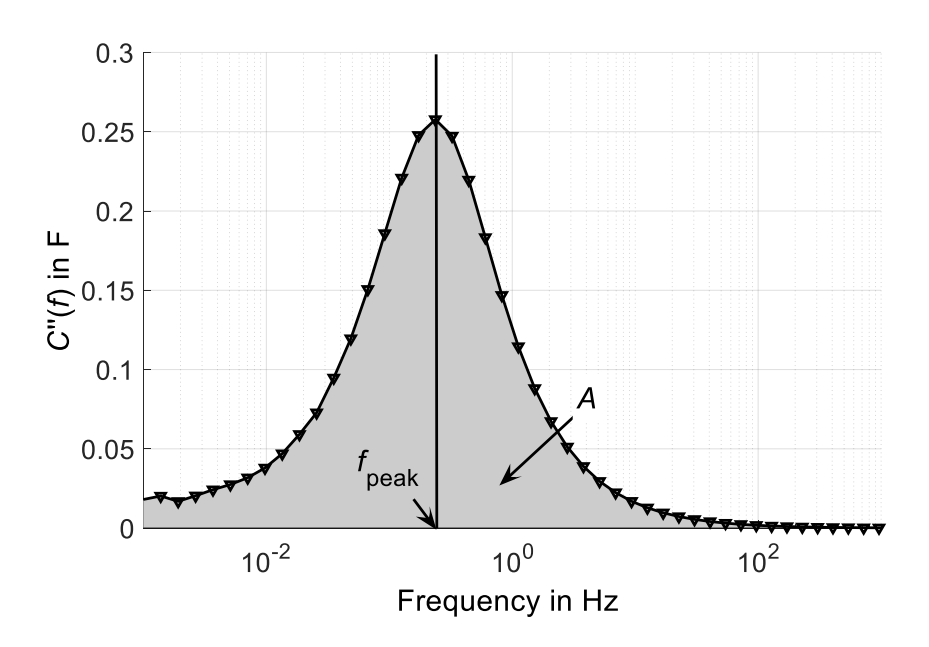


Figure 3.5: Imaginary Capacitance plot over frequency

Capacitance and impedance of the characterized EDLC are related by

$$C = \frac{1}{j\omega Z} \tag{3.11}$$

The capacitance  $\mathcal{C}$  of one electrode can be determined from the area A under the imaginary part of the capacity, according to formula (3.12) from [78].

$$C = \frac{2 \cdot \ln 10}{\pi} \left| \int_{-\infty}^{\infty} C''(f) d[\log f] \right| = 1.446 A$$
 (3.12)

The factor 2 ln 10)/ $\pi$  = 1.446 results from the Kramers-Kronig transformation, see appendix A.4.

Since impedance measurements to very low frequencies are quite time consuming, Yoo et al. have shown in [78] that for symmetrical peaks it is also possible to determine the capacity from the peak frequency  $f_{\text{peak}}$ .

$$C = 2C'(f_{\text{peak}}) = 2.932 \left| \int_{\log f_{\text{peak}}}^{\infty} C''(f) d[\log f] \right|$$
(3.13)

The time constant  $\tau$  can be obtained from the peak frequency  $f_{\text{peak}}$  [79].

$$\tau = R \cdot C = \frac{0.404}{f_{\text{peak}}} \tag{3.14}$$

This procedure is applied in this thesis to determine changes in time constants of EDLC that can be caused by different solvents or by changes in pore structure due to aging processes, see chapter 7.3.4.4.

# 3.2 Experimental Results of EDLC's Electrical Performance

As described in the previous chapters, capacitance and resistance values of an EDLC depends strongly on the applied measured method but are also influenced by other parameters, especially temperature. This chapter gives some experimental results of characteristic data of various EDLC types at different ambient conditions.

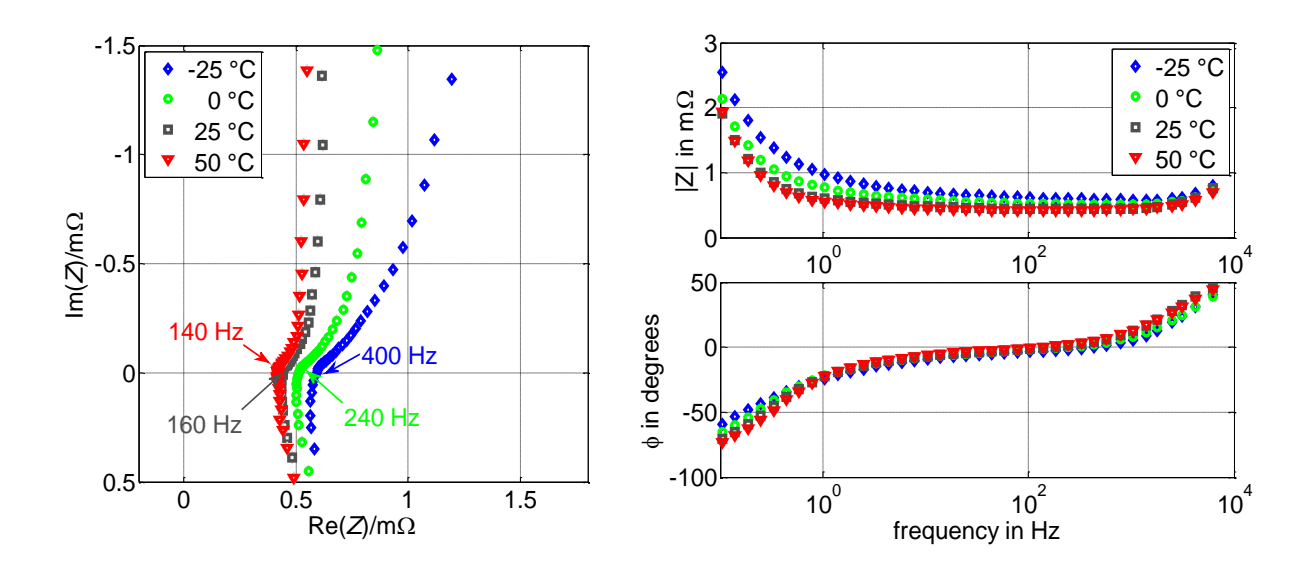


Figure 3.6: EIS measurements of an EDLC at rated working voltage in a range of 6 kHz to 0.15 Hz, measured at -25, 0, 25 and 50 °C shown as Nyquist plot (left) and Bode plot (right)

Also, the resistance of an EDLC depends strongly on temperature. Figure 3.6 shows exemplarily Nyquist and Bode plots of one new 1000 F EDLC from which the AC-resistance can be deduced. Galvanostatic impedance measurements were carried out at nominal voltage by using an impedance spectrometer called EISmeter developed by ISEA, RWTH Aachen University [80]. The pure ohmic resistance is represented as the intersection of the spectra with the x-axis. It can be seen from Figure 3.6 that the resistance increases significantly at lower EDLC temperatures. Furthermore, the frequency, where the imaginary part of the impedance is zero, is not constant but increases strongly with temperature. These effects can be explained by the high viscosity of the electrolyte at low temperatures. Therefore, the ion mobility is limited which leads to higher electrolyte resistance values [81,82].

Electrical Characterization 33

In contrast to the temperature dependency, the dependency of the internal resistance on the state of charge (SOC) is not very distinctive as shown in (Figure 3.7). Only a slight difference between the impedance spectra of different SOCs can be observed.

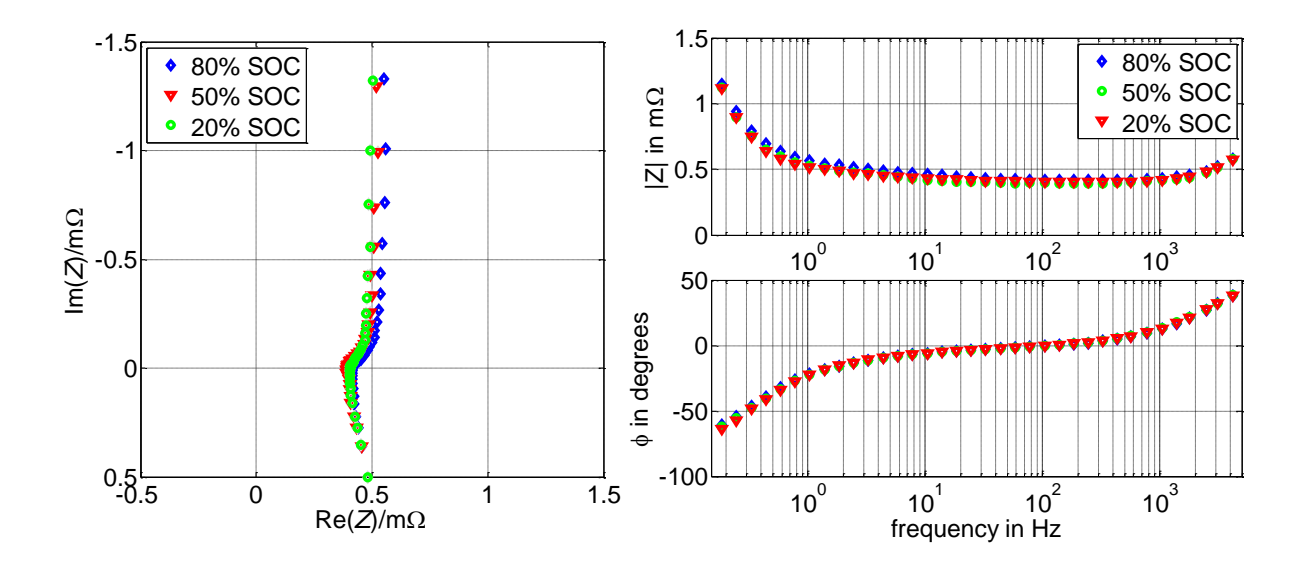


Figure 3.7: EIS measurements of an EDLC at 25°C in a range of 6 kHz to 0.15 Hz

Many manufacturers of EDLCs provide in the data sheets the AC resistance of the device as the value measured at 1 kHz and room temperature. Some of them also give the value at 100 Hz. The difference between both values is negligible at temperatures higher than room temperature as can be seen in Table 3.1. The larger deviations at lower temperatures are due to the reduced ion mobility as describes above.

Temperature	-25 °C	0°C	25 °C	50 °C
Re(Z)@100 Hz	0.61 mΩ	$0.52~\text{m}\Omega$	0.44 mΩ	0.42 mΩ
Re(Z)@1000 Hz	0.58 mΩ	$0.50~\text{m}\Omega$	0.43 mΩ	0.43 mΩ
Relative deviation	6.5%	3.4%	1.3%	1.9%

Table 3.1. Comparison of AC resistances at 100 Hz and 1 kHz

The presented results show that the values obtained from resistance measurements depend strongly on the measurement conditions. Temperature influences the ion mobility and therefore the resistance. Another important impact factor is the complex pore structure. The measured DC resistance is typically higher than the AC resistance. Thus, the measure procedure must be clearly specified to make values comparable.

## 3.2.1 Comparison of EDLCs with different solvents

The experimental results presented in the previous chapter were taken from a 1000 F EDLC with acetonitrile-based electrolyte. Since the solvent influences the performance this chapter shows the differences in electrical behavior between commercial EDLCs with acetonitrile-based (AN) and propylene-carbonate-based (PC) electrolytes. Two different capacitor sizes were investigated for every electrolyte type. For simplification, those cells with acetonitrile-based electrolyte are named AN and those with polypropylene-carbonate-based electrolyte are named PC.

#### 3.2.1.1 Impedance Spectra

Figure 3.8 shows the Nyquist charts of different commercial EDLCs with different electrolytes. Since the investigated EDLCs were of different sizes (1000 F and 3000 F for AN; 350 F and 1400 F for PC) results are not directly comparable, but, however, some general conclusion can be done.

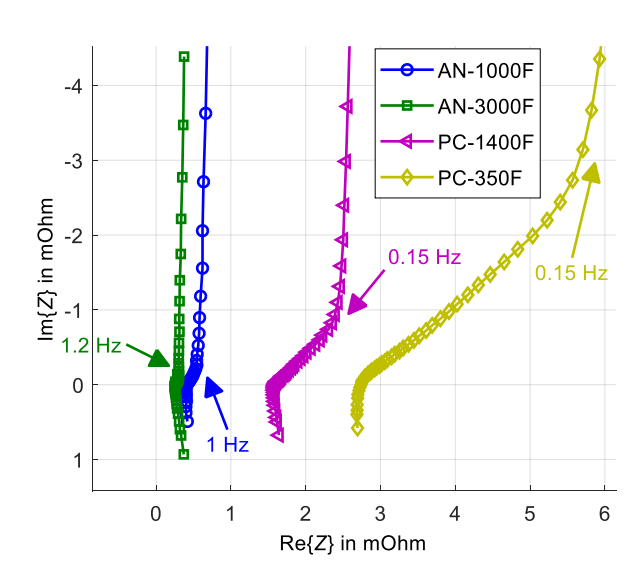


Figure 3.8: Nyquist charts of EDLCs with AN and PC based electrolytes at 100% SOC and 25 °C

The internal resistance of the AN-devices is much lower than the  $R_i$  of the PC-devices. This effect is due to the lower conductivity of a PC-based electrolyte, compare Table 2.1. Furthermore, the 45°-arc of the Nyquist plot is much more pronounced and the frequency from which on the impedance behavior of EDLC is nearly purely capacitive is much lower for PC-based electrolyte compared to AN-based electrolyte. Since the viscosity of PC is higher than the viscosity of AN the pore accessibility at higher frequencies is lower which leads to higher internal resistance values and poorer pore accessibility especially at high frequencies [56].

Electrical Characterization 35

### 3.2.1.2 Energy Efficiency

For the analysis of the temperature depending electrical performance of EDLCs with different solvents performance tests have been carried out. Therefore, cells were put in a temperature chamber (Binder) and kept at constant ambient temperature while they were cycled with several constant current rates without constant voltage phase (V-phase). 3 charge/discharge cycles between 0 V and nominal voltage were performed at every current rate, and the energy efficiency was calculated from the third cycle. It is the ratio of the energy needed for charging and the energy delivered during discharge of the EDLCs and is calculated as follows:

$$\eta = \frac{Wh_{discharge}}{Wh_{charge}} \cdot 100\%$$
 (3.15)

In Figure 3.9 the energy efficiency of an AN-based EDLC type compared to a PC-based EDLC type is shown as a function of current at different temperatures. Both cells show performance losses due to lower temperatures, but in case of the PC-based EDLC these losses are significantly higher. Only at very small current rates results of both cells were approximately comparable, but with increasing current rates, the performance of the PN-based cell deteriorated faster. At current rates above 100 mA/F, the performance test could not even have been carried out because the ohmic resistance was too high. Furthermore, at -25 °C the electrical performance even at low current rates is very poor.

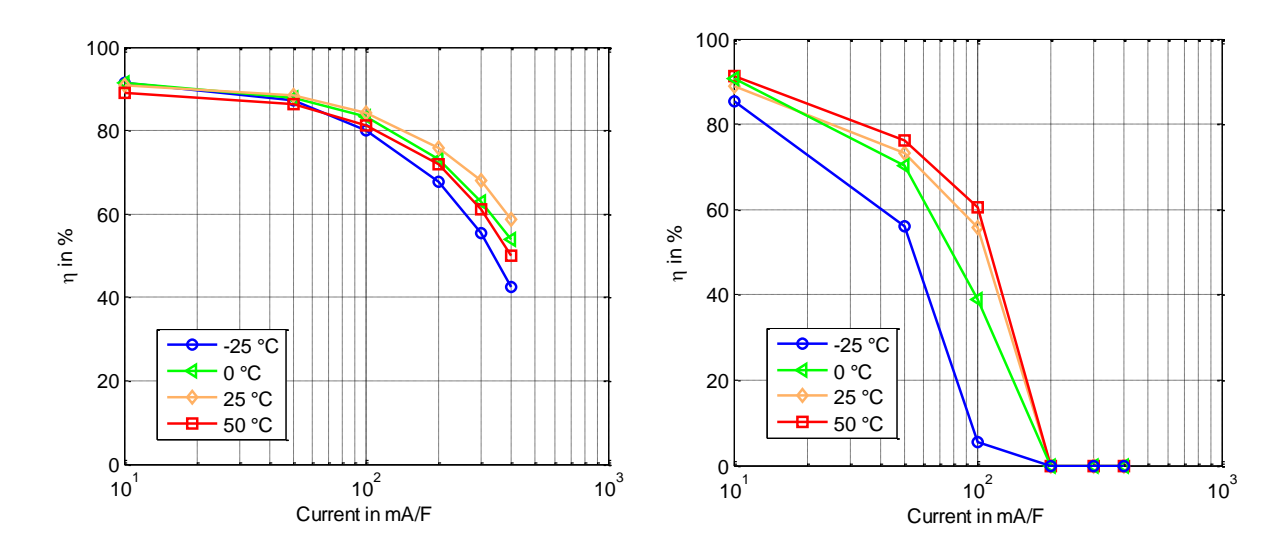


Figure 3.9: Temperature dependent efficiency of a 1000 F EDLC with AN-based electrolyte (left) and of a 1400 F EDLC with PC-based electrolyte (right)

# 3.3 Comparison of EDLC and Commercial Lithium-Ion Capacitor

Lithium-ion capacitors (LIC) promise to close the gap between batteries and EDLCs by offering higher energy density due to higher rated voltages and longer cycle life compared to Li-

ion batteries. However, deep temperature behavior is also an important aspect for many applications. AN-based EDLCs overcome the battery performance at low temperatures because of the higher electrolyte's viscosity at lower temperatures and because no chemical reactions occur that can be decelerated. Therefore, in this chapter one EDLC device and one LIC device, both with a rated capacity of 3000 F, were characterized. The rated voltage of the EDLC was 2.8 V and the rated voltage of the LIC 4.2 V due to the different electrolytes.

#### 3.3.1 Temperature Dependency

Unlike acetonitrile-based EDLCs who show satisfactory performance even at low temperatures, the performance of Li-ion capacitors degrades significantly at low temperatures. It shows at low temperature conditions characteristics of a typical Li-ion battery. As shown in Figure 3.10 the impedance behavior of LICs change significantly if the cell temperature is varied. At room temperature, about 25 °C, the LIC shows a Nyquist chart similar to the Nyquist chart of an EDLC, no semi-circle but a vertical line at low frequencies. This behavior changes drastically down to lower temperatures. Then a significant semi-circle develops, and the Nyquist charts resemble more a Li-ion battery spectrum than an EDLC spectrum. From the Bode plot it can also be observed that the impedance' absolute value at low frequencies increases drastically at low temperatures and the capacitive behavior of LIC starts at much lower frequencies.

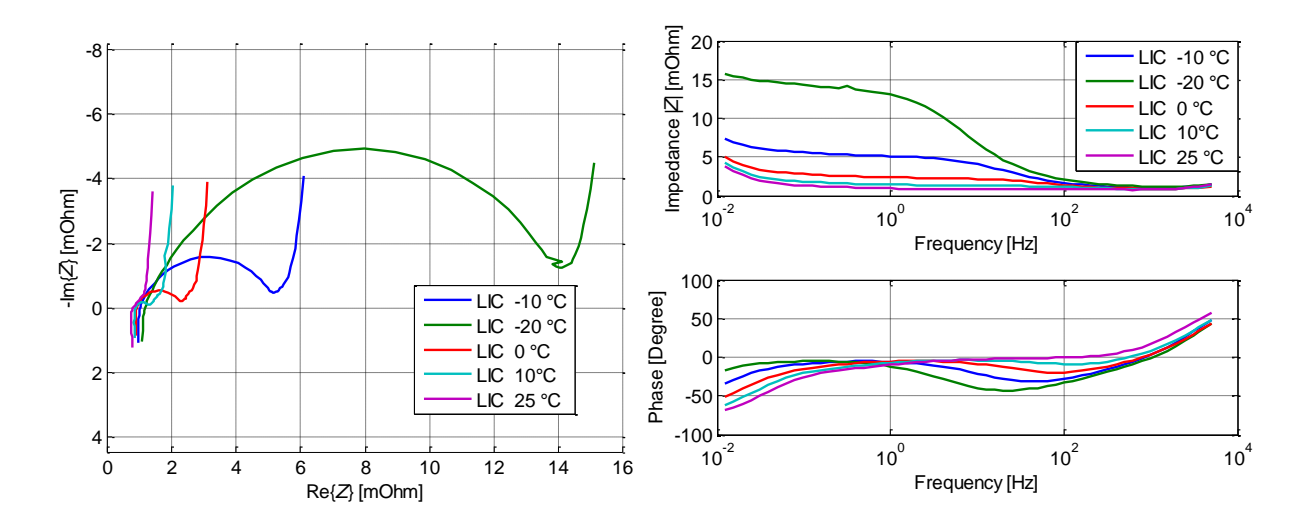


Figure 3.10: Nyquist charts and Bode plots of a 3000 F LIC at different temperatures

For comparison, Figure 3.11 shows the results of electrochemical impedance spectroscopy of the EDLC device. The 3000 F EDLC showed only a minor temperature dependency. All spectra approximately overlay.

Electrical Characterization 37

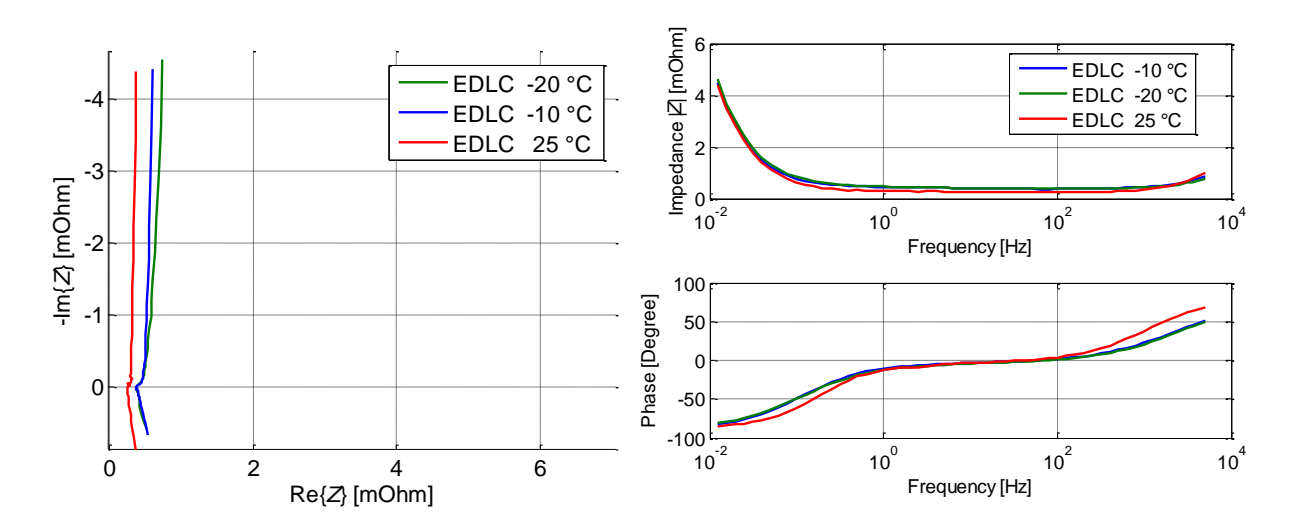


Figure 3.11: Nyquist charts and Bode plots of a 3000 F EDLC at different temperatures

The results from impedance spectroscopy show that the EDLC resistance increases slightly at deep temperatures, too. But the deep temperature behavior of EDLCs is significantly better than that of LICs.

### 4. Pore Structure of Activated Carbon

Activated carbon material used in EDLCs is highly porous to achieve high capacitance values. Their porosity influences strongly their capacitive behavior, as was shown by de Levie [83–85]. He showed that the electrode system does not react uniformly on charge or discharge processes. This is caused by the finite conductivity of the electrolyte and the porous electrode material. According to [86] porous solids can be divided into three categories referring to their pore structure. The criterion for the classification is their pore diameter  $\emptyset$ :

Macropores: Ø > 50 nm

• Mesopores: 2 nm < Ø < 50 nm

Micropores: Ø < 2 nm</li>

Figure 4.1 shows exemplarily the pore size distribution of a commercial EDLC electrode material. Since two determination methods for the different pore sizes were used, the incremental pore volume over pore width is presented by means of two plots<sup>4</sup>.

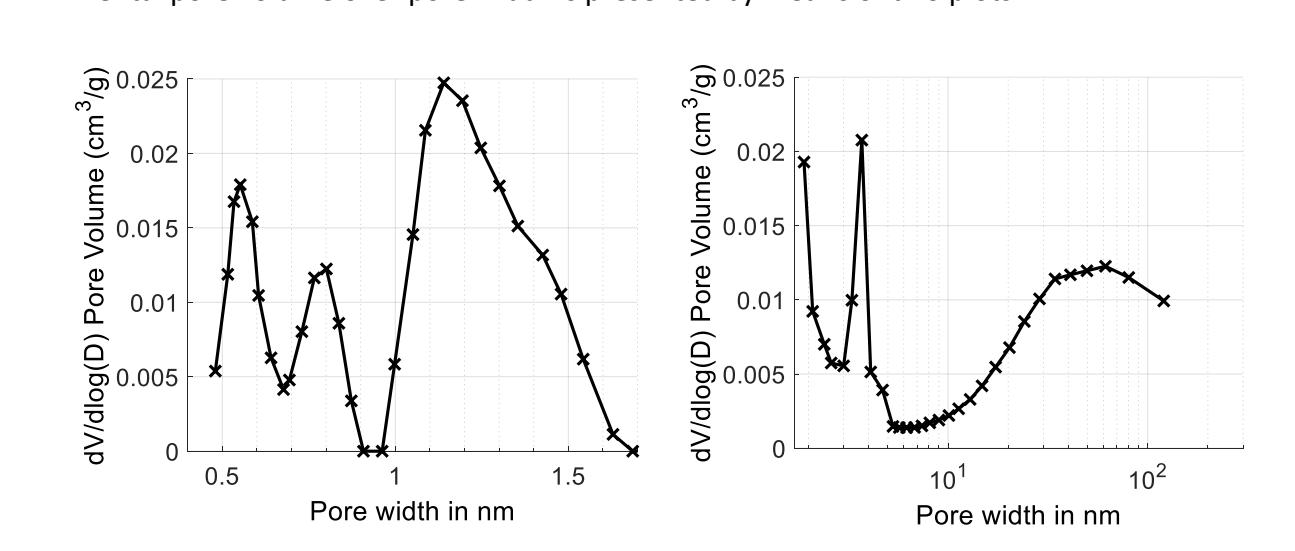


Figure 4.1: Exemplarily pore size distribution of activated carbon used in commercial EDLCs<sup>5</sup> (left: pore volume distribution of micropores up to 1.7 nm, right: pore volume distribution meso- and macropores (logarithmic scale))

The left plot shows the distribution of micropores in linear scale whereas the right plot shows the distribution of larger pore sizes in logarithmic scale. The major contribution to the overall pore volume comes from the micropores. Macro pores are not represented in Figure 4.1, but they are not that important for the energy storage of EDLCs.

<sup>4</sup> The measurement and calculation techniques for pore size distribution are described in chapter 7.3.2.

<sup>&</sup>lt;sup>5</sup> The investigated material was taken from a new commercial 600 F EDLC and the pore structure was analyzed by means of nitrogen adsorption using a 3Flex Version 3.00 by Micromeritics.

The peak distribution of pore volume, as exemplarily shown in Figure 4.1, varies for different electrode materials. They all have a unique pore size distribution as presented by Qu et al. in [86]. The pore size distribution results from the involved precursors and activation processes.

The micro-porous structure of EDLC electrodes provides high surface area and is the major contributor to the double layer capacitance. Nevertheless, this structure leads to higher complexity of the carbon, not only due to the kinetics of electrochemical accessibility to the micropores [86], which are discussed in chapter 4.1, but it results also in the presence of various functional groups on the electrodes' surface. Due to redox reactions of these functional groups on the carbon surface, pseudocapacitance arises besides the predominant double layer capacitance. Furthermore, some functional groups are electrochemically inert within the potential range of operation and improve the wettability of the carbon material whereas others undergo irreversible reactions and decrease the capacitance [37].

# 4.1 Electrolyte-Electrode Interface

The available capacitance of an EDLC depends on the surface area of the activated carbon material used in the electrodes. Since the capacitance is proportional to the electrodes surface area, according to equation (2.2), it could be concluded that the higher the surface area the higher is the capacitance. However, the relationship between surface area and capacitance is not linear, because experiments show that some activated carbon materials with very high surface do not show the expected high capacitance values. Carbon materials with a high amount of micropores which have very small diameters are not useful for EDLCs, because these very small pores might not be accessible to electrolyte solution. These ions, especially those with solvation shells, are too big to enter the pores [86].

As shown before, pores can be divided into three types of pores: macropores, mesopores (between 20 and 500 Å) and micropores (less than 20 Å). In case of activated carbons, the contribution of macropores to the capacitance is negligible (in a range of 2 m²/g) compared to the contribution of meso- and micropores [87]. In addition, the total surface area of activated carbon can be divided into two parts: The internal surface or microporous area and the external surface area which is in most cases equivalent to the mesoporous area [87]. The external surface includes all the outer surface of secondary particles and all those cracks that are wider than deep. The internal surfaces includes the walls of all those cracks, pores and cavities that are deeper than they are wide [86]. Carbon electrode materials that have pores with different pore sizes do also have different time constants. Larger pores can be reached much faster than smaller pores.

In various experiments, it was shown that ions of the electrolyte carry a shell of solvent molecules with them. This effect enlarges the charged molecule significantly, as shown in Table 2.2. The diameters of the salt/solvent molecules are, depending on solvent, much larger

than 1 nm. Thus, entering sub-nanometer pores should be impossible for the electrolyte ions. However, Chmiola et al. showed that EDLC capacity increases significantly for pores smaller than the ion/solvent-molecule diameter [59]. Since these molecules cannot enter the narrow pores with intact solvation shell, they must be at least partly desolvated or even be bare while entering these pores.

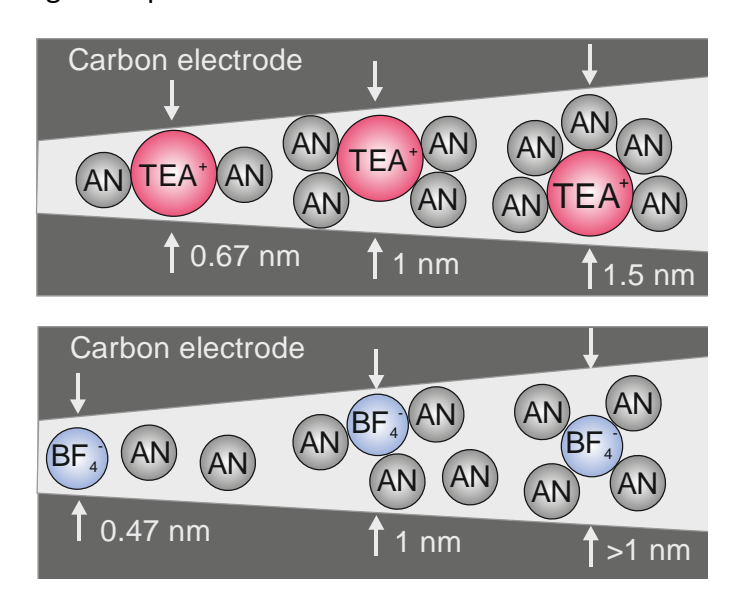


Figure 4.2: Pore entering of positive and negative ions in sub-nanometer pores

# 4.2 Ion Redistribution Processes and Self-Discharge

Self-discharge of EDLCs is an important factor when considering the suitability of EDLCs for several applications. It is not that important for applications with a highly dynamic load profile but therefore very important for applications with long rest times such as uninterruptable power supply systems (UPS). Some studies have already investigated self-discharge of EDLCs [72,88,89]. These studies show that self-discharge of EDLCs depends strongly on temperature and short-time history.

In experimental studies undertaken by Kowal et al., a voltage decrease after charging, as shown in Figure 4.3, was observed [72]. As can be seen, Kowal et al. divided the voltage decrease of an EDLC during self-discharge into three phases. Firstly, a strong exponential decrease occurs, followed by a second slower exponential phase till finally the voltage decreases linearly. Kowal et al. introduced the following formula for the description of voltage decay during self-discharge [72]. It consists of two exponential terms and one linear term.

$$U(t) = a_1 \cdot \exp\left(-\frac{t}{\tau_1}\right) + a_2 \cdot \exp\left(-\frac{t}{\tau_1}\right) + a_4 - a_5 \cdot t \tag{4.1}$$

How pronounced this different phases are, depends strongly on the charge history and the ambient temperature [72,90].

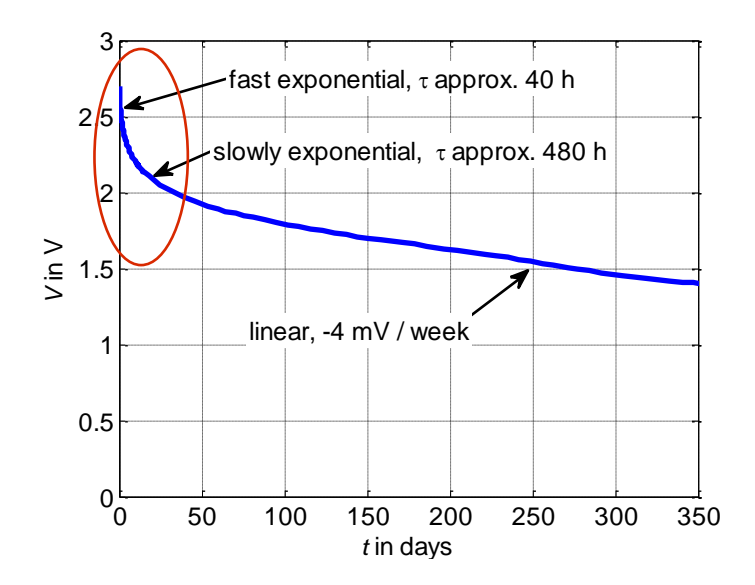


Figure 4.3: Self-discharge of an EDLC according to [72]

The strong voltage decrease at the beginning of self-discharge, during the fast and slowly exponential phase, can be explained by ion redistribution processes within the pores, i.e. no charge is lost but it is redistributed. In contrast, the linear voltage decrease is real self-discharge, in which charge is lost due to leakage currents.

To explain the ion redistribution processes, a negative pore is exemplarily regarded, as shown in Figure 4.4. Initially, the pore is completely discharged (case a) and positive and negative charge carriers are equally distributed. With the beginning of charging (case b) electrons move to the electrodes' surface, and the positive ions in the electrolyte are attracted. Negative ions, still present in the pore, are rejected and move to the pore opening. With ongoing charging (case c), also positive ions from the bulk electrolyte are attracted, while negative ions move away from the pore opening to the bulk electrolyte. The attracted positive ions accumulate first in the pore opening (case d). When charging is stopped, no further ions will accumulate at the pore opening, and the present positive ions will move deeper in the pore, till all ions in the pore are equally distributed. This ion redistribution process leads to the voltage drop observed in Figure 4.2. How pronounced this voltage drop is depends on the charging/discharging history.

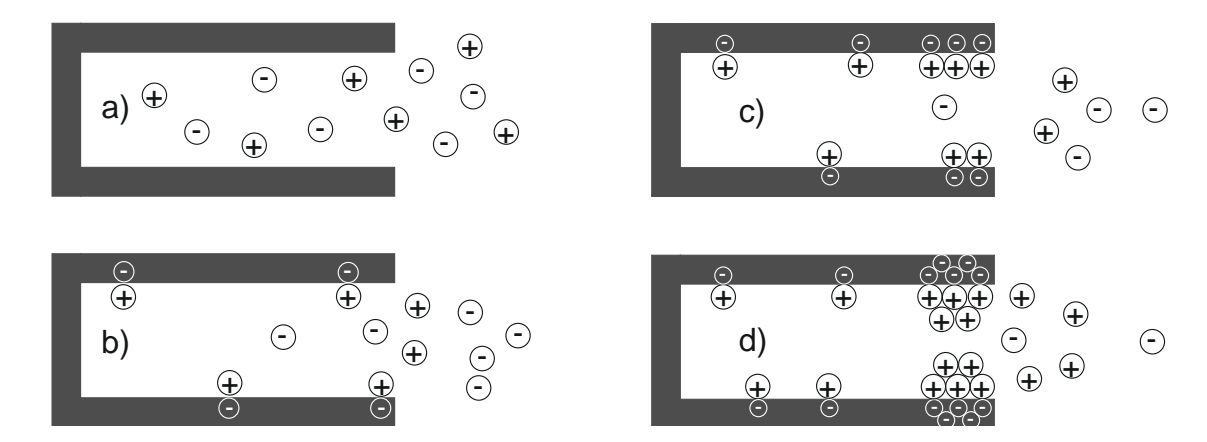


Figure 4.4: Ion redistribution processes during charging

- a) discharged: positive and negative ions are equally distributed
- b) positive ions are attracted; negative ions are rejected
- c) more positive ions move to the pore
- d) ions accumulate in the pore opening

In case (e) charging is stopped after a short time, ions will also distribute equally with time, but this redistribution leads to a voltage decrease as shown in Figure 4.3. After a longer charging period (case e in Figure 4.5), e.g. several days, such a voltage decrease cannot be observed, because the ions are already equally distributed due to the long charging time, and therefore no redistribution processes occur anymore.

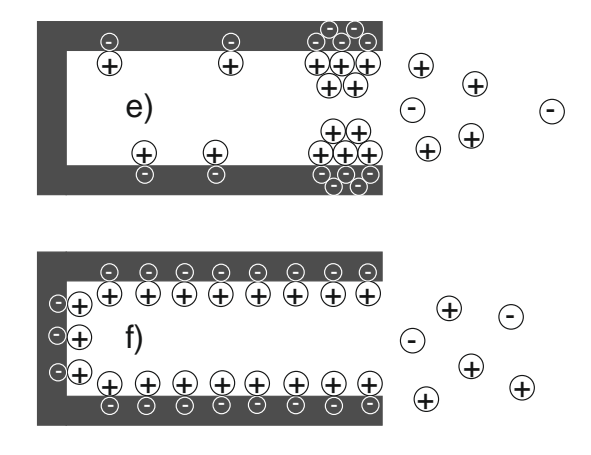


Figure 4.5: schematic ion distribution after e) short charge phase f) long charge phase

To analyze the impact of charging history and temperature on the open circuit voltage characteristics of an EDLC, various self-discharge measurements were carried out. The results are presented in the following chapter.

## 4.2.1 Results of Self-Discharge Measurement on AN-based EDLCs

In this thesis, self-discharge measurements were carried out for one carbon-based EDLC type with acetonitrile as solvent and a rated capacitance of 600 F. The dependency of self-discharge behavior on temperature and charge history respectively charge duration was investigated.

Initially, all cells were completely discharged and afterwards short-circuited for 24 hours to keep them completely discharged and to avoid redistribution processes before the open circuit measurements started. Afterwards, cells were charged until testing voltage followed by a constant voltage phase of different periods by using a Hameg HM 8413 voltage/current source. Then, EDLCs were disconnected from the power supply and the open circuit voltage was measured for a period of 72 hours by using a data logger ICP 100 by Gartner Instruments. All tests were performed in a temperature chamber by Binder, regulated to the appropriate testing temperature.

Figure 4.6 shows the impact of charge duration on the self-discharge at 25 °C ambient temperature and 2.25 V charging voltage.

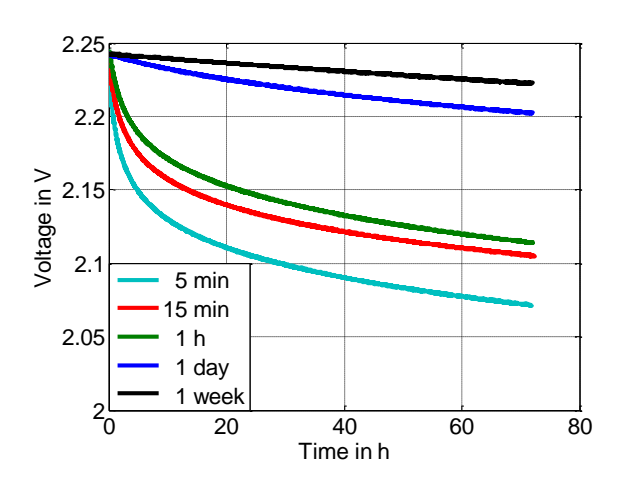


Figure 4.6: Ion redistribution and self-discharge at 25 °C and 2.25 V charging voltage depending on the charge duration

It can be seen that there is a strong exponential voltage decrease in case of only 5 min constant voltage charging. Within the first 5 hours, the voltage drops by approximately 100 mV before it decreases slower exponentially. After 72 hours, voltage has been dropped by approx. 180 mV. This behavior can be explained by ion redistribution processes. In case of charging with a very short constant voltage phase, ions accumulate solely next to the pore opening and do not move into deeper pores. After disconnecting the power supply, the charge distributes over the entire pore depth which results in a remarkable voltage drop. The longer the constant voltage phase, the weaker is the voltage drop, because more charge carriers have moved into the deeper pores. In case of constant voltage phase of 1 day, the

exponential voltage drop is much smaller. It is approx. 50 mV after 3 days which can be seen from Figure 4.7.

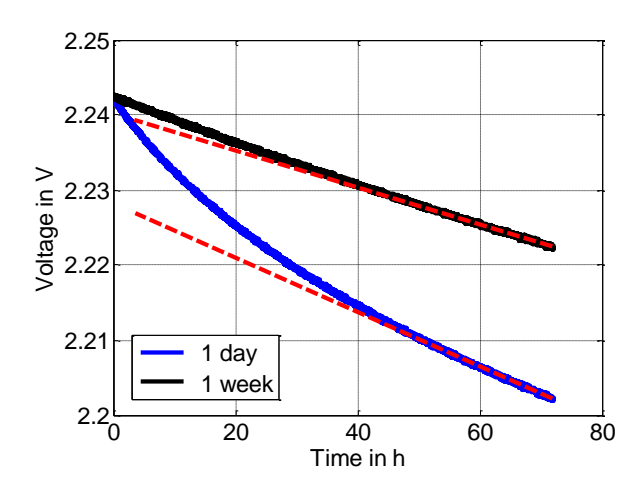


Figure 4.7: Ion redistribution and self-discharge after long constant voltage phases with marked tangents

At charging with a constant voltage phase of one week, the voltage characteristics seem to be linear at first sight. But Figure 4.7 shows, that even after one week charging, the voltage decreases exponentially at the beginning of the open circuit period. That means, still not all accessible pores are filled, and redistribution processes still take place. Furthermore, 72 hours measurements are not sufficient to reach the linear voltage decrease.

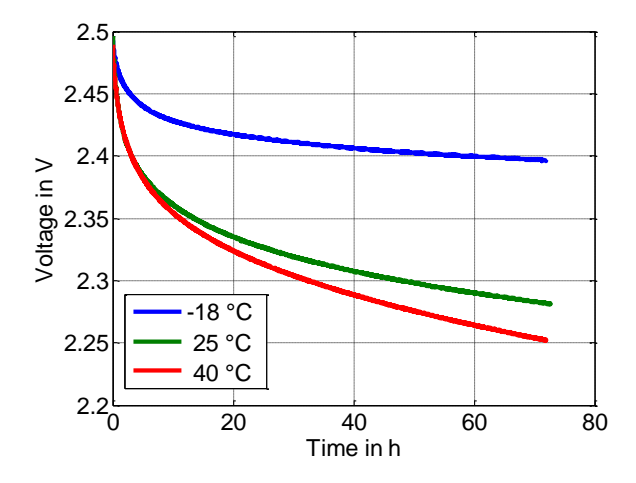


Figure 4.8: Ion redistribution and self-discharge at 2.5 V charging voltage and 15 min U-phase depending on temperature

Beside charge duration, also the impact of temperature on ion redistribution and self-discharge characteristics was analyzed. As can be seen from Figure 4.8, the voltage decrease of an EDLC in open circuit mode is strongly temperature dependent. At 40 °C the voltage decrease is the most pronounced, at 25 °C it is a little bit less, but it is much smaller at very low ambient temperatures such as -18 °C. This behavior can be explained by the viscosity of the electrolyte and the mobility of the ions. At low temperatures, the EDLCs electrolyte is

much more viscous than at room temperature, and therefore the ion mobility is limited which leads to a lower voltage drop.

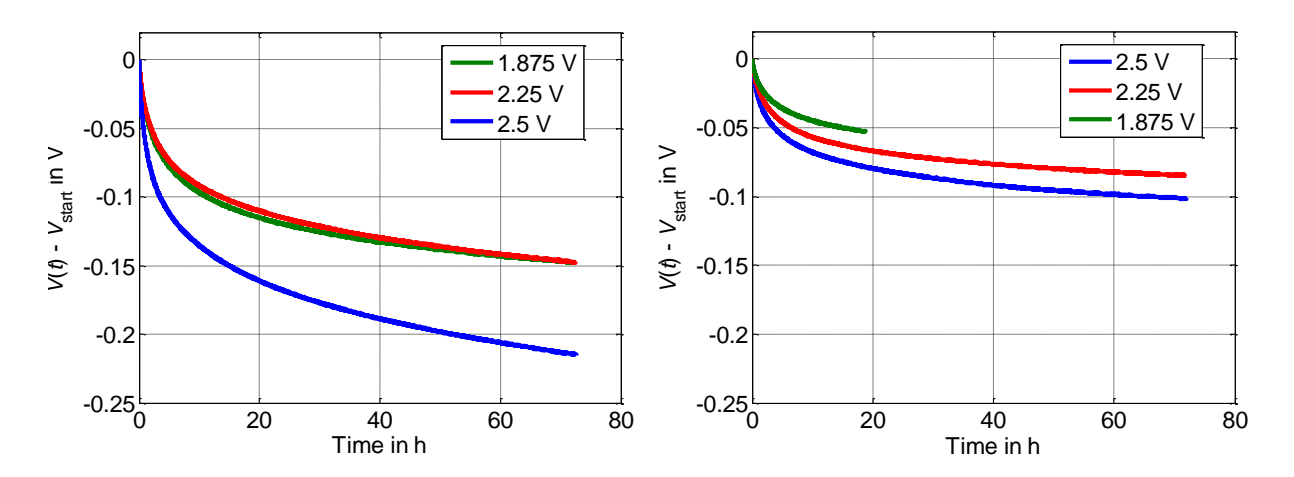


Figure 4.9: Relative ion redistribution and self-discharge after 15 min U-phase at 25 °C (left) and -18 °C (right)

As shown in Figure 4.9 (left), voltage drops exponentially much faster at 25 °C in case of the cell charged to 2.5 V, then the cells charged to 2.25 V or 1.875 V. The results of these last voltages do not differ significantly. In contrast to these results, open circuit measurements at -18 °C show significant differences between investigated charge voltages, see Figure 4.9 (right). The voltage drops after about 19 hours amount to 75 mV at 2.5 V and to 53 mV at 1.875 V. Generally, voltage drops per time are higher at room temperature. They result to about 158 mV after 19 hours at 2.5 V and to approx. 107 mV at 1.875 V. Due to a failure in data logging open circuit voltage at 1.875 V and -18 °C was only logged for 19 hours instead of 72 hours. Therefore, voltage values after 19 h are considered for all measurements, to make the results comparable.

The observed effect, that the voltage drop is higher the higher the initial charge voltage was, can be explained by the porous carbon structure. If the charging voltage is higher, more ions accumulate at the pore opening and diffuse into deeper pores after current cut off. Therefore, the voltage drop is higher. At room temperature, this effect is very pronounced for a fully-charged EDLC, whereas the voltage characteristics at 75% SOC and 90% SOC and 15 min U-phase hardly differ. At deep temperatures, the voltage drop is generally much less pronounced within the same time span compared to room temperature, due to the high electrolyte viscosity. Therefore, the diffusion processes in the pore are slower, and the voltage drop depends strongly on the charge voltage, which means on the amount of charge carriers accumulated at the pore opening.

### 4.2.2 Long-Time Experiment

The long-time experiment of Kowal et al. presented in Figure 4.3 was continued. The cell was stored under more or less constant ambient temperature conditions of about 20 °C, and the

open circuit voltage was measured in defined time steps. The voltage decay of almost six years is presented in Figure 4.10.

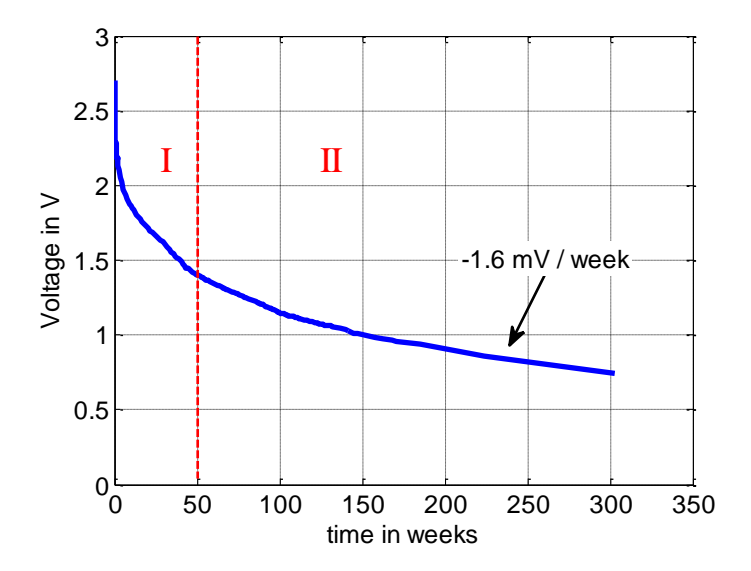


Figure 4.10: Exemplarily voltage characteristics of an EDLC in case of self-discharge

Kowal et al. concluded from their experiment shown in Figure 4.3 that under their test conditions the linear voltage decay of the considered EDLC device starts after about 100 days. But the further open circuit voltage development shown in Figure 4.10 indicates clearly, that the further voltage decay is not linear.

Phase I of Figure 4.10, lasting till approximately 50 weeks, represents the voltage decay measured by Kowal, and phase II the ongoing experiment in this thesis. Even after 100 weeks of test duration, the voltage drops still exponentially. After 100 weeks, the voltage drop is nearly. However, the voltage drop is much less than 4 mV per week determined by Kowal but only approximately 1.6 mV per week.

The EDLC potential most likely influences the voltage decay. When the experiment started the EDLC had a potential of 2.5 V and showed a significant voltage decrease. But after more than three years of testing the cell potential dropped to less than 1 V. As it was shown in Figure 4.9, the cell potential has a significant impact on the voltage decay. The less pronounced voltage decrease after about three years of testing is therefore influenced by the low cell potential.

# 5. Modeling of Porous Carbon Electrodes

Many different approaches for EDLC modeling have been investigated in recent years. These models differ significantly in accuracy and complexity. However, what kind of model is used depends strongly on the application. Models developed for the representation of the dynamic electrical behavior of modules consisting of a large number of cells cannot be as complex as a model representing the processes in single pores.

Impedance-based models using an equivalent circuit diagram consisting of passive elements for the modeled device are an appropriate tool to describe the dynamic electrical behavior of EDLCs. The simplest approach is a basic model consisting of an ideal capacitor in series with an internal resistance. This model can be enlarged by a series inductance which is predominantly influenced by cables and connectors, or a leakage resistance in parallel with the capacitor that should represent the self-discharge. Such a model might be sufficient for many applications but fails to describe the electric behavior of an EDLC caused by the porous electrode structure such as redistribution processes.

This chapter presents several approaches on modeling of porous carbon electrodes from the assumption of uniform cylindrical pores up to models considering the complex pore structure of EDLC electrodes.

# 5.1 Model Representation Assuming Uniform Cylindrical Pores

As described in chapter 2.3.1, the electrodes of EDLCs are made from highly porous activated carbons and the behavior of porous electrodes deviates remarkably from the behavior of flat electrodes. To represent this porous structure in an equivalent circuit diagram de Levie proposed in the 1960s an approach for modeling porous electrodes [83,84]. He regarded only one single pore and assumed it to be an ideal cylindrical pore, see Figure 5.1.

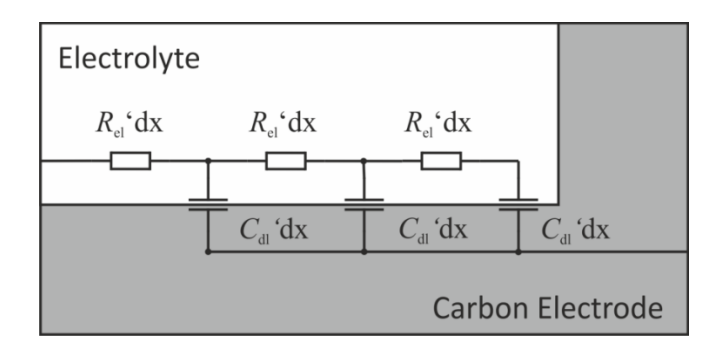


Figure 5.1: Modeling approach of porous electrodes at electrode/electrolyte interface by means of an *RC* ladder network<sup>6</sup>

<sup>&</sup>lt;sup>6</sup> The resistance of the carbon electrode is neglected here since it is assumed that  $R_{\text{carbon}} << R_{\text{electrolyte}}$ .

The impedance of one single pore was calculated by de Levie with the following assumptions:

- (i) The pore is cylindrical which means that the cross section  $A_{pore}$  and the circumference  $u_{pore}$  are uniform along the pore length.
- (ii) All conditions such as reactant concentrations, electrode kinetics and electrolyte conductivity are homogeneous within the pore.
- (iii) The resistance of the electrode material is negligible.
- (iv) The actual potentials in the pores are replaced by their average values in planes perpendicular to the pore axis which is justified for "thin" pores (length *l* >> radius *r*).

In Figure 5.2 a segment with the length dx of such a pore is shown.

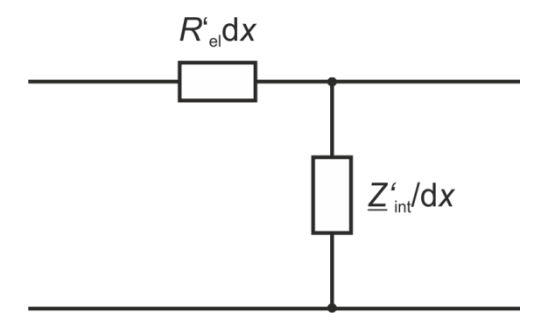


Figure 5.2: Equivalent circuit diagram of a pore segment

The quantities  $R'_{el} dx$  and  $\underline{Z'}_{int}/dx$  represent the electrolyte resistance and the impedance of the pore wall of a pore section of length dx.

The impedance of the pore results then to:

$$\underline{Z}_{p} = \sqrt{R'_{\text{el}} \cdot \underline{Z}_{\text{int}}} \cdot \coth\left(\sqrt{\frac{R'_{\text{el}}}{\underline{Z'_{\text{int}}}}} \cdot l\right)$$
 (5.1)

 $R_{\rm el}$  and  $Z_{\rm int}$  can be calculated from the electrolyte conductivity  $\kappa_{\rm el}$  and the interfacial impedance per unit electrode/electrolyte interface, where  $A_{\rm pore}$  is the cross-section area of the pore,  $r_{\rm pore}$  the pore radius, and  $u_{\rm pore}$  the pore circumference.

$$R'_{\rm el} = \frac{1}{\kappa_{\rm el} \cdot A_{\rm pore}} = \frac{1}{\kappa_{\rm el} \cdot \pi r_{\rm pore}^2}$$
 (5.2)

$$\underline{Z'}_{\text{int}} = \frac{\underline{z}_{\text{int}}}{u_{\text{pore}}} = \frac{\underline{z}_{\text{int}}}{2\pi r_{\text{pore}}}$$
(5.3)

Since in EDLCs no charge transfer takes place at the electrodes (so called blocking or ideally polarizable electrodes)  $Z'_{int}$  corresponds to the double-layer capacitance of the pore wall per unit cell length  $C'_{dl}$  or per unit interface area  $c_{dl}$ .

$$\underline{Z'}_{\text{int}} = \frac{1}{j\omega C'_{\text{dl}}} = \frac{1}{j\omega \cdot c_{\text{dl}} \cdot 2\pi r}$$
(5.4)

This leads to the electrical equivalent circuit of the porous electrode of an EDLC shown in Figure 5.3.

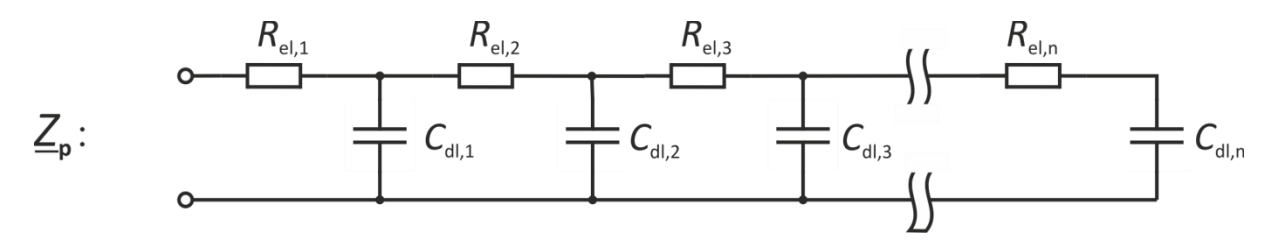


Figure 5.3: Electrical equivalent circuit of the porous electrode of an EDLC

With

$$R_{\rm el} = R'_{\rm el} \cdot l \tag{5.5}$$

$$C_{\rm dl} = C'_{\rm dl} \cdot l \tag{5.6}$$

The complex pore impedance of EDLCs can be written as:

$$\underline{Z}_{p} = \sqrt{\frac{R_{\text{el}}}{j\omega C_{\text{dl}}}} \cdot \coth(\sqrt{j\omega C_{\text{dl}} R_{\text{el}}})$$
 (5.7)

Equation (5.7) can be approximated for high and low frequencies as follows:

$$\underline{Z}_{p}(\omega \to \infty) \approx \sqrt{\frac{R_{el}}{j\omega C_{dl}}} = \sqrt{\frac{R_{el}}{\omega C_{dl}}} \cdot e^{-j\pi/4}$$
 (5.8)

$$\underline{Z}_{p}(\omega \to 0) \approx \frac{1}{j\omega C_{dl}} + \frac{R_{el}}{3}$$
 (5.9)

In the high frequency region described by equation (5.8), the pore impedance behaves like a so-called constant-phase element (CPE) with a 45° angle in the complex plane. The pore impedance at low frequencies is equal to that of an ideal capacitor in series with a resistor. This is due to the fact, that after a potential was applied for a sufficiently long time, the current is distributed equally on all capacitors  $dC_{dl}$  and the corresponding resistors  $dR_{el}$ .

An impedance model that describes the behavior of an EDLC over a wide frequency range can be achieved by a series connection of the pore impedance with an ohmic resistance representing the ohmic parts of conductors and bulk electrolyte, an inductance representing the stray inductance of the EDLC and the inductance of the connectors as shown in Figure 5.4.

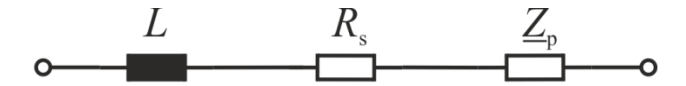


Figure 5.4: Equivalent electrical circuit of an EDLC

This standard model can be expressed by

$$\underline{Z_{ELDC,std.}} = R_{s} + j\omega L + \sqrt{\frac{R_{el}}{j\omega C_{dl}}} \cdot \coth(\sqrt{j\omega C_{dl}R_{el}})$$
 (5.10)

whereas L represents the inductive behavior of the connectors, Rs represents the ohmic parts of connectors, electrodes and electrolyte, and the pore impedance  $\underline{Z}$ p that represents the electrical behavior caused by the electrode's porosity. This pore impedance is represented in the model by a lattice network consisting of RC-elements where Rp is the electrolyte resistance inside the pore and  $C_{\text{dl}}$  is the double layer capacitance.

The representation of these parameters in the Nyquist plot can be taken from Figure 5.5. L is represented by the positive imaginary part,  $R_i$  is the intersection with the x-axis, and the pore impedance  $\underline{Z}p$  is represented by the 45°-arc and the low frequency part with nearly pure capacitive behavior.

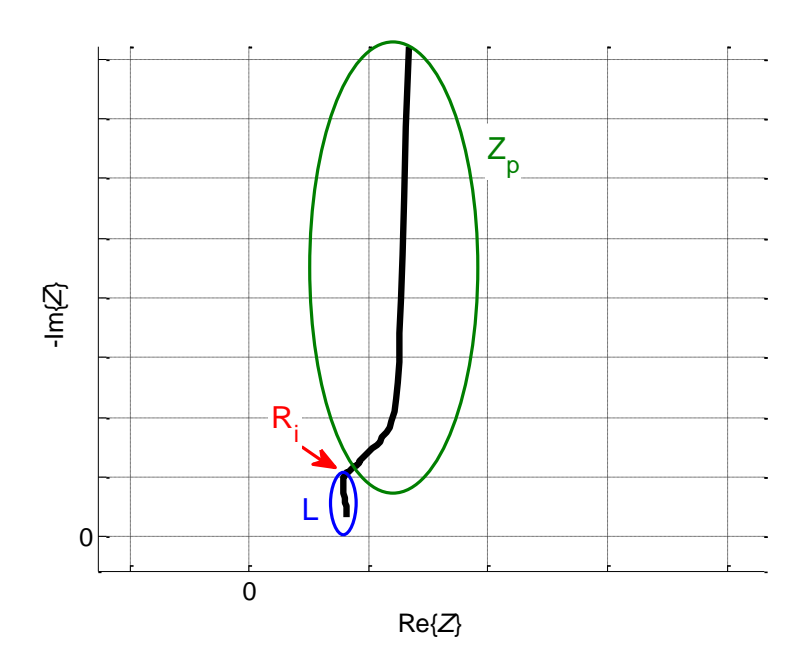


Figure 5.5: Frequency dependency of the impedance behavior of an EDLC

## 5.1.1 Generalized Pore Impedance Model

However, the presented standard impedance model of an EDLC does not match perfectly the low frequency behavior of a commercial EDLC. The standard model predicts the behavior of an ideal capacitor which means the low frequency part of the Nyquist spectrum would be a straight line with an angle of 90°. But Figure 5.6 shows, that the measured low frequency branch is not equal to 90°. This so-called constant-phase behavior can be observed at EDLCs or other electrochemical systems with porous electrodes and might be caused by a non-ideal pore structure, surface roughness or adsorption processes [73].

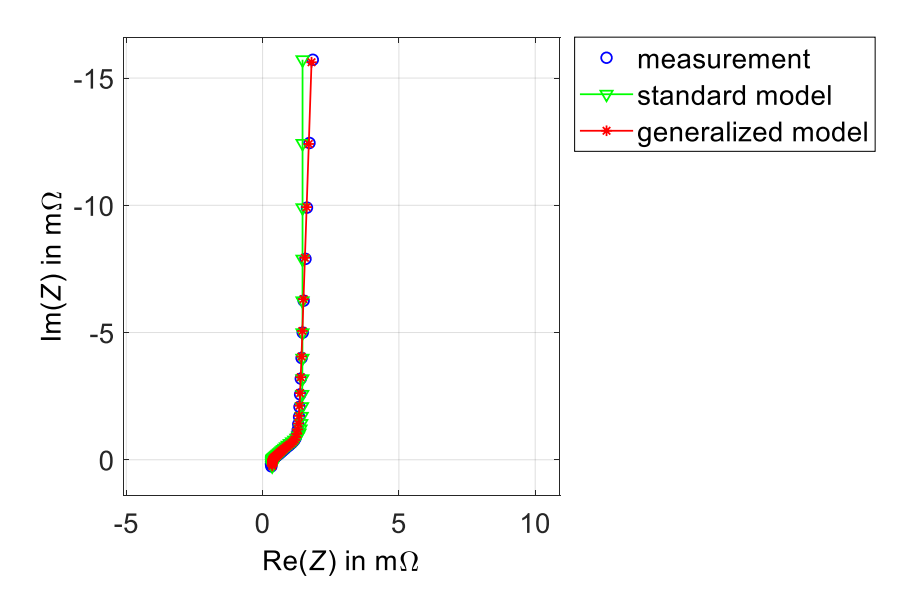


Figure 5.6: Comparison of the standard and the generalized EDLC model

To overcome this problem, Kötz et al. proposed to replace the frequency dependent terms  $(j\omega)$  in the expression for the pore impedance (equation (5.7)) by a constant phase term with the form  $(j\omega)^{\gamma}$  with  $0<\gamma\le 1$  [6]. Thus, the expression for the impedance of the generalized model results to [91]:

$$\underline{Z_{ELDC,gen.}} = R_{s} + (j\omega)^{\gamma}L + \sqrt{\frac{R_{el}}{(j\omega)^{\gamma}A_{dl}}} \cdot \coth\left(\sqrt{(j\omega)^{\gamma}A_{dl}R_{el}}\right)$$
 (5.11)

Formally,  $\mathcal{C}_{dl}$  is replaced by  $A_{dl}$ , the magnitude of the constant phase element. The term  $(j\omega)^{\gamma}A_{dl}$  consists of a real part  $\cos(\gamma\pi/2)\omega^{\gamma}A_{dl}$  and an imaginary part  $\sin(\gamma\pi/2)\omega^{\gamma}A_{dl}$ . In case of  $\gamma=1$  the device behaves purely capacitive, in case of  $\gamma=0.5$  a -45°-branch arises in the Nyquist chart and  $\gamma=0$  results in a purely resistive behavior. Since  $\gamma$  is usually close to one the values of  $\mathcal{C}_{dl}$  and  $\mathcal{C}_{dl}$  are nearly identical.

Buller developed a transmission line model to represent the dynamic behavior of EDLCs considering the generalized impedance given in equation (5.11) [92,93]. He used this model explicitly to represent the dynamic behavior of EDLCs and not for the representation of self-discharge processes.

# 5.2 Modeling Approach Considering Different Pore Sizes

The EDLC model proposed by de Levie in [83] that was presented in previous chapter is based on the assumption that all pores are ideally cylindrical and have uniform length. Regarding a carbon particle within the porous structure of an EDLC electrode this assumption is too simplistic, since pores are not uniform but of different size. Figure 5.7 shows the interface of the porous carbon with the electrolyte.

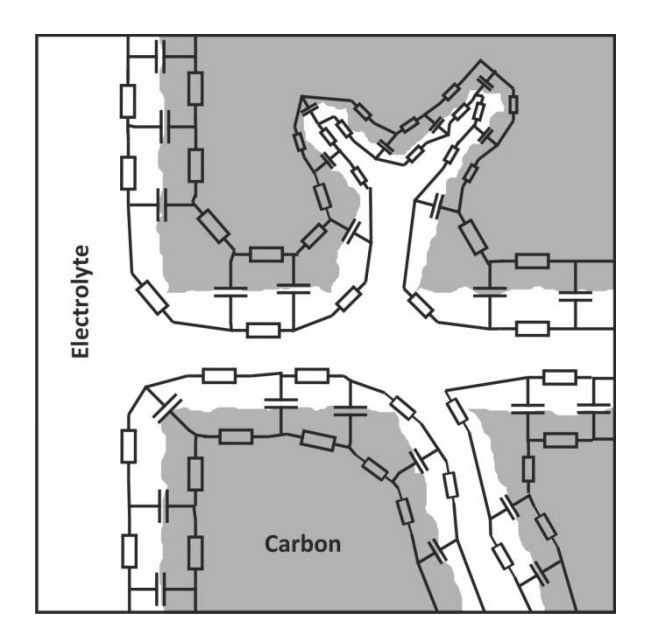


Figure 5.7: Carbon-electrolyte-interface of porous carbon with different pore sizes

Starting from the macropores, meso- and finally micropores can be reached via a branching system that gets finer. Thus, ions in the finest pores had to pass a longer way and therefore a higher electrolyte and carbon resistance. Depending on carbon pore size distribution, different pore sizes differ in their contribution to the overall capacity.

Since the transmission line model proposed by de Levie does not represent long-time ion distribution processes properly, other models with different time constants were developed. Zubieta et al. based their model on a transmission line consisting of three branches but unlike to de Levie and Buller the *R* and *C* parameters are not equal but represent processes with different time constants [94]. Kang et al. considered in their transmission line based model also the bulk electrolyte [95]. Belhachemi et al. developed a transmission-line model consisting of one part with low time constants based on the Zubieta model and two additional branches with large time constants, parameterized by the voltage response of short current pulses [96,97].

In the following a modeling approach considering different pore sizes is presented.

The equivalent circuit diagram that can be deducted from the macro, meso and micro porous structure is presented in Figure 5.8.  $C_{\rm macro}$ ,  $C_{\rm meso}$  and  $C_{\rm micro}$  represent the capacitances for every pore size.  $R_{\rm Carbon}$  and  $R_{\rm Electrolyte}$  represent the resistances of the carbon electrode and the electrolyte whereas the parallel  $R_{\rm Leakage}$  resistance represents leakage reactions that lead to self-discharge.

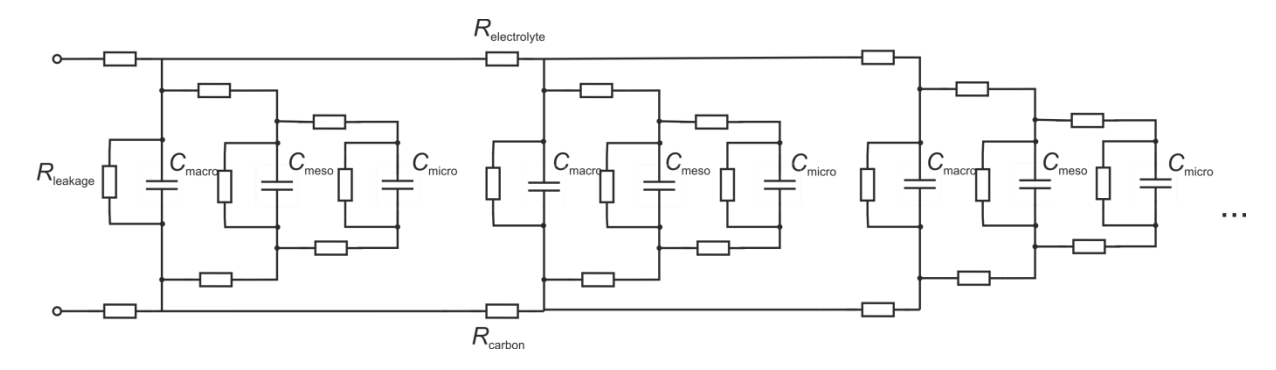


Figure 5.8: Deducted equivalent circuit diagram regarding different pore sizes

Since the equivalent circuit diagram presented above is very complex by having numerous parameters, Kaus et al. simplified this equivalent circuit diagram to a model only considering three pore types [90], see Figure 5.9.

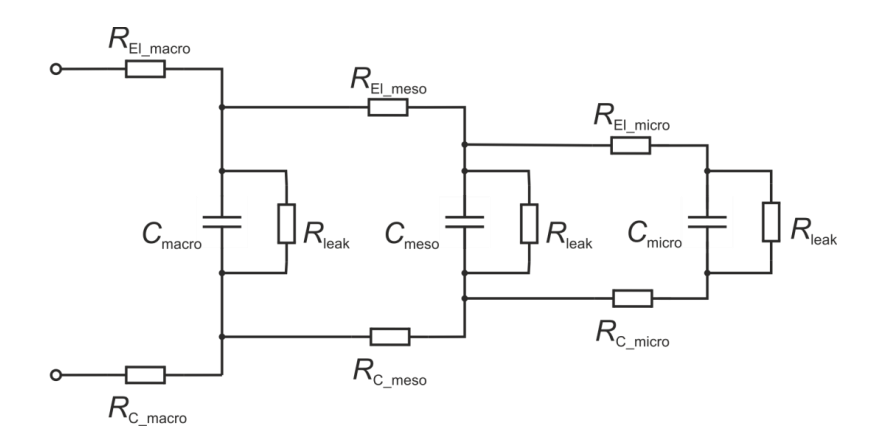


Figure 5.9: Equivalent circuit diagram of an EDLC regarding different pore sizes according to Kaus [90]

While using the equivalent circuit diagram of Figure 5.9 for simulations, the carbon resistance was neglected since  $R_c \ll R_{El}$ .

Kaus parameterized his model by means of self-discharge measurements and achieved quite good correlation between self-discharge measurements and simulation [90]. However, this parameterization with  $R_{\rm macro} < R_{\rm meso} < R_{\rm micro}$  and  $C_{\rm macro} >> C_{\rm meso} > C_{\rm micro}$  is plausible regarding the resistance values because ions have to pass a longer path with narrowing pore diameter to reach micropores. But regarding capacitance, these parameters are in contradiction to the pore size distribution shown in Figure 4.1. The micro pore capacitance should have the major contribution to the over-all capacitance.

### 5.2.1 Modeling Approach Considering Dynamic Behavior and Diffusion Processes

As shown in the previous chapter, on the one hand the model approach considering different pore sizes is able to simulate self-discharge processes, on which it was parameterized,

very well but fails in simulation of highly dynamic processes such as impedance simulation. On the other hand, models solely parameterized by impedance spectroscopy, like the Buller model, are not able to represent processes with large time constants such as ion redistribution processes. Therefore, a new model approach was developed that is able to simulate sufficiently the voltage response of very dynamic current profiles as well as the voltage decay during self-discharge.

Therefore, the transmission line model was enlarged to a five-branch model as shown in Figure 5.10. All *RC*-branches have different time constants. The first three branches were parameterized by using impedance spectroscopy. The parameters were fitted to impedance measurements of the considered EDLC. The last two branches with the largest time constants were fitted to self-discharge measurements according to Kaus.

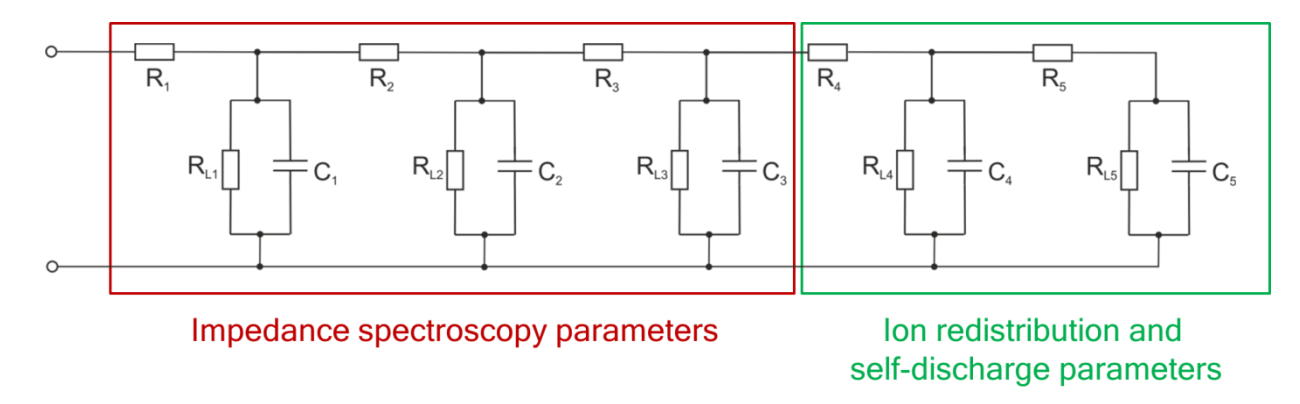


Figure 5.10: Equivalent circuit diagram of the considered modeling approach

To show the applicability of the model the first three branches were parameterized by impedance spectroscopy of a 1000 F AN-based EDLC. The last two branches were parameterized by ion-redistribution and self-discharge measurements of the same cell type. By means of this parameterization two different simulations of the electrical behavior at 25 °C were carried out, namely one impedance simulation over a frequency range between 5 kHz and 10 mHz and one self-discharge simulation of the same cell. The simulation results compared to measurement are shown in Figure 5.11.

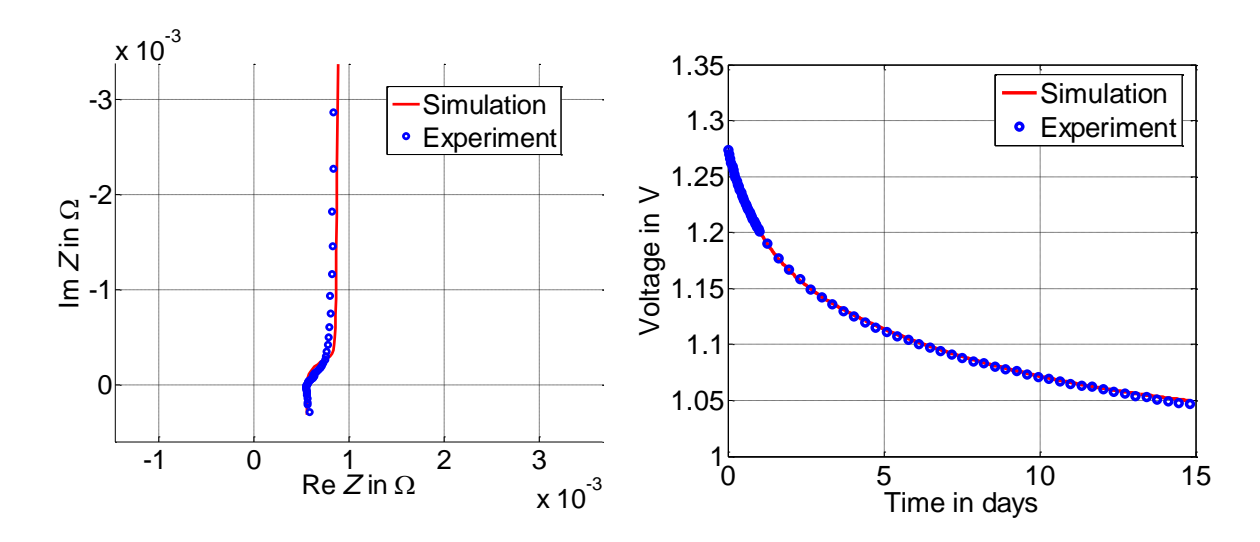


Figure 5.11: Simulation results of a 1000 F AN-based EDLC, impedance spectroscopy (left) and self-discharge (right)

The left graph shows the measured and simulated Nyquist plot. Multiple sinusoidal currents with different frequencies, in this case from 7 kHz to 10 mHz, were applied to the model and from each single simulation one point of the Nyquist chart was calculated. As can be observed from the presented results, simulation and experimental data match quite well. The model is able to represent the significant 45° arc and the low frequency behavior.

The right graph shows simulation and experimental data of a long-time self-discharge measurement. After a short-circuited period of 24 hours the EDLC was charged with 2 A up to 1.275 V followed by a U-phase of 15 min and then the open circuit voltage was measured for 15 days.

The ion redistribution processes and the resulting voltage decay over this long testing period of 15 days can be represented by the new model approach, as can be observed from the right graph of Figure 5.11. Hence, in a first approach the model is able to combine the ability to represent highly dynamic processes as well as ion redistribution processes that last over several weeks. Further work must be done to validate the model under further conditions.

However, it was shown that additional *RC*-branches are needed to represent the long-term ion-redistribution processes as well, 3 branches are not sufficient. Since the larger the number of *RC*-branches is the longer is the model's calculation time, a good balance has to be found between needed accuracy and simulation speed, especially regarding simulations of modules with numerous cells.

# 6. Electro-Thermal Modeling

Besides purely electrical modeling of EDLCs, as presented in the previous chapter, the knowledge of thermal behavior of considered cells or modules is essential for good system design. Cooling strategies can be developed to avoid high cell temperatures that would lead to accelerated aging, as discussed later in chapter 8. Therefore, an electro-thermal model was developed that allows simulating temperature development of different cell geometries, single cells as well as modules.

The electro-thermal model is developed in a modular way to keep it flexible. Thus, the model can be internally divided into two sub-models: an electrical and a thermal model. These models depend on each other as can be seen in Figure 6.1.

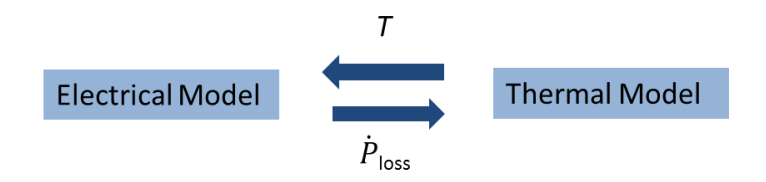


Figure 6.1: Schematics of the electro-thermal model

The electrical model calculates the current and voltage characteristics of each single cell and based on current rate and internal resistance the heat generation inside the cells whereas the thermal model calculates the temperatures of all cell and module parts as well as the heat transfer between neighbored cells and the heat transfer between cells and the module casing as well as from module casing to environment.

The physical principles, on which the thermal calculations for heat generation and heat transfer of the single volume elements within the model are based, are presented below.

### 6.1 Electrical Model

Due to the modular structure of the electro-thermal model, it is possible to use various electrical models as they are discussed in chapter 5. The model requires an equivalent circuit consisting of distinct elements like R and C and can be parameterized in several ways. For highly dynamic profiles a purely impedance-based model can be sufficient but for the representation of long-term ion redistribution processes a more complex model is needed.

The inductance is neglected in the model because of its minor impact on the impedance. As the *RC*-parameters depend on temperature and state of charge, they are re-calculated in each time step.

### 6.2 Thermal Model

For module design the knowledge of thermal behavior of the entire module and of each single cell under operation is essential. Hot spots lead to accelerated aging of the considered cells and results in higher resistance and lower capacitance. A higher resistance leads then to higher heat generation and further aging.

Several thermal models for EDLCs are reported in literature [98,99]. D'Entremont et al. [100] and Gualous et al. [101] developed a model for the simulation of the reversible heat effect.

Thermal processes typically involve heat or mass transfer. Thus, calculation of thermal processes is very complex and presents a huge conflict between computing time and accuracy. For calculation and for simplification a discretization is necessary. This can be done by means of the finite difference method (FDM). FDM separates the body into uniform volume elements and calculates then the heat transfer between these elements.

First, detailed knowledge on generated heat and heat transfer of the system that should be simulated is necessary. Furthermore, thermal parameters, such as heat capacity and heat conductivity, must be known for simulation of heat transfer processes. They must be determined experimentally or by calculation. The following sections give an overview on the considered heat generation and heat transfer mechanisms considered in the thermal model.

### 6.2.1 Thermodynamic Principles

Energy balance for each volume element of the thermal model is calculated by considering different heat generation and heat transfer mechanisms. The following section gives an overview on these mechanisms and describes how the heat transfer from volume element to volume element is calculated.

#### 6.2.1.1 Heat Generation

Due to a current flow through an EDLC, heat losses occur depending on current rate and conductivity respectively resistance of the EDLC. The dominant part of the internal resistance of an EDLC is caused by the electrolyte where most losses occur. These losses are transferred into heat according to the following formula:

$$P = R_i \cdot I^2 \tag{6.1}$$

Where P is the generated heat,  $R_i$  the internal resistance of the EDLC and I the current rate.

Due to the high porosity of the electrodes, equalizing currents flow within the pores depending on frequency and amplitude of the applied current. Thus, the resulting heat has to be calculated using the pore impedance.

#### 6.2.1.2 Reversible Heat

Furthermore, a superimposed alternating component of the temperature has been observed during cycling of an EDLC [102]. For the measurement shown in Figure 6.2 an 3000 F EDLC was put into a foamed polystyrene box as described in [102] and cycled with a constant current rate of 100 A while the temperature on the cell's surface was measured. The measurement shows a temperature ripple which is caused by the so-called reversible heat. Additional to Joule heat, endothermic and exothermic heat processes occur during charging or discharging the EDLC. In case of carbon electrodes on both sides, the process is exothermic during charging and endothermic during discharging. Whereas in case of a hybrid capacitor with faradic reactions, it is the other way around as shown by Dandeville et. al. for a C-MnO<sub>2</sub> capacitor [103].

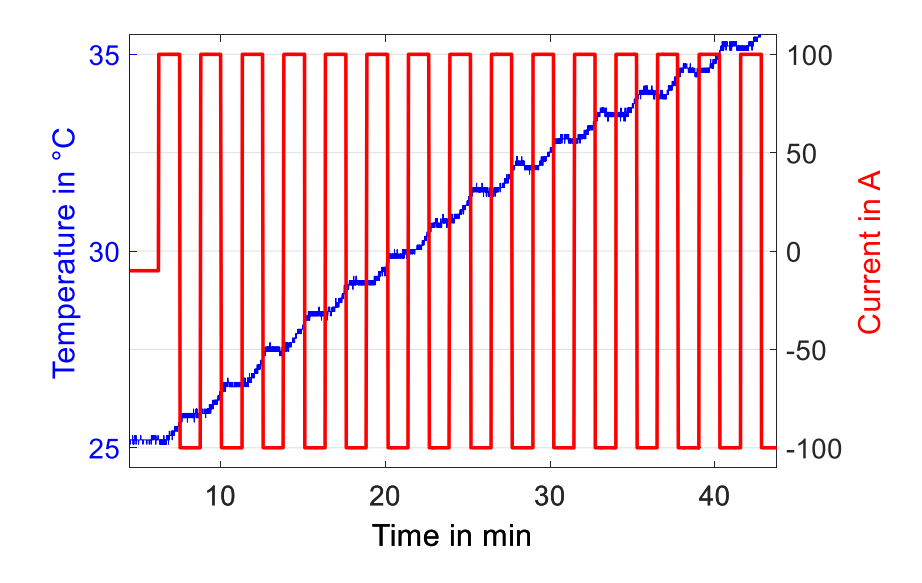


Figure 6.2: Current dependent alternating part of cell heating during constant current cycling of a 3000 F EDLC

These temperature ripples can be explained by entropy changes of the EDLC.

For the entropy calculation, the increasing and decreasing number of ions in the volume of the Helmholtz double layer  $V_H$  is regarded. Figure 6.3 shows the ion distribution in charged and discharged state under the simplified assumption of a Helmholtz layer with constant capacitance and dimensions (plate capacitor). In case of the ideally charged capacitor (left), all the ions are in the Helmholtz layer and thus in the state of maximum order respectively minimum entropy. In contrast, in case of a discharged condenser ions are distributed over

the whole electrolyte volume  $V_e$  which results in the state of maximum disorder and therefore maximum entropy.

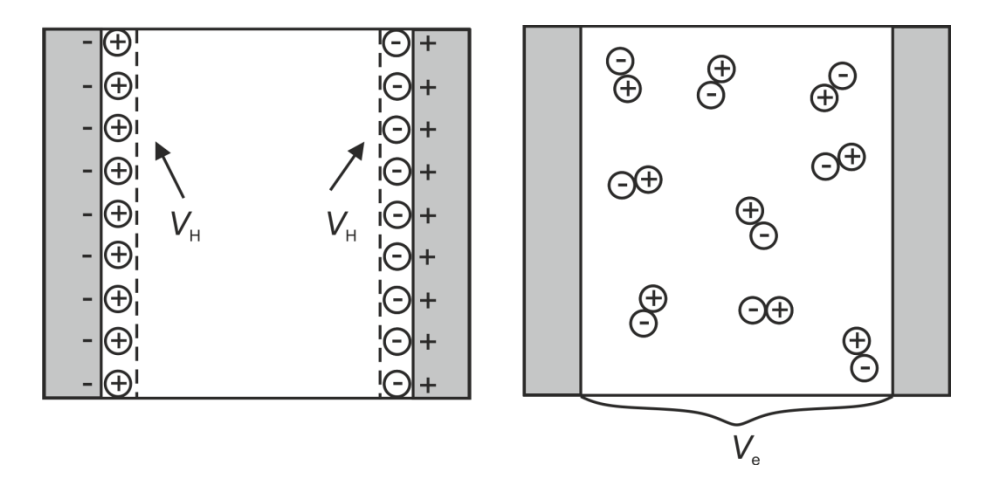


Figure 6.3: Ordered and disordered ions in charged mode (left) and discharged mode (right) according to [102]

The entropy changes  $\Delta S$  of the EDLC depending on the voltage difference  $\Delta U$  can be calculated according to [102] as follows:

$$\Delta S = -\frac{2 \cdot k_B}{e} \cdot C \cdot \Delta U \cdot \ln \left( \frac{V_H}{V_e} \right) \tag{6.2}$$

C represents the capacitance,  $k_B$  the Boltzmann constant and e the electron charge.

With

$$\frac{\mathrm{d}Q_{\text{reversible}}}{\mathrm{d}t} = -T\frac{\mathrm{d}S}{\mathrm{d}t} \tag{6.3}$$

and

$$\frac{\mathrm{d}V}{\mathrm{d}t} = \frac{i(t)}{C} \tag{6.4}$$

The reversible heat effect can be described by equation (6.5), whereas the factor  $a = -\ln(V_{\rm H}/V_{\rm e})$  represents the relation of double layer volume and electrolyte volume and depends on the double layer capacitor's inner geometry.

$$\dot{Q}_{\text{reversible}} = -\frac{2 \cdot T \cdot k_{\text{B}} \cdot a}{e} \cdot i(t)$$
(6.5)

The calculated reversible heat of a 5000 F EDLC with T = 298K and  $\alpha$  = 1.957<sup>7</sup> is exemplarily shown in Table 6.1. The heat capacity of this EDLC was measured by Schiffer et al. in [102] to 1118 J/K.

Current	$\dot{Q}_{ m reversible}$
50 A	5.03 W
100 A	10.05 W
200 A	20.10 W
400 A	40.20 W

Table 6.1:  $\dot{Q}_{\rm reversible}$  of a 5000 F EDLC depending on current

#### 6.2.1.3 Heat Transfer

In case of non-uniformly distributed heat within a closed system, a heat transfer will always occur until the entire system has reached the same temperature level. This heat transfer is caused by direct heat conduction, heat radiation or is related to a mass transport, as in case of convection.

#### Heat Conduction

Generally, heat conduction is described by the heat conduction equation (equation (6.6)) whereas T is the temperature,  $\lambda_{th}$  the specific thermal conductivity and  $c_{th}$  the specific thermal capacity of the considered body.

$$\frac{\partial}{\partial t}T(\vec{r},t) = \frac{\lambda_{th}}{c_{th}} \cdot \Delta T(\vec{r},t) \tag{6.6}$$

The heat flow between two points based on heat conduction depends on the temperature difference and thermal conductivity of the body. It can be described via a thermal equivalent circuit diagram in an analog way to electrical equivalent circuit diagrams.

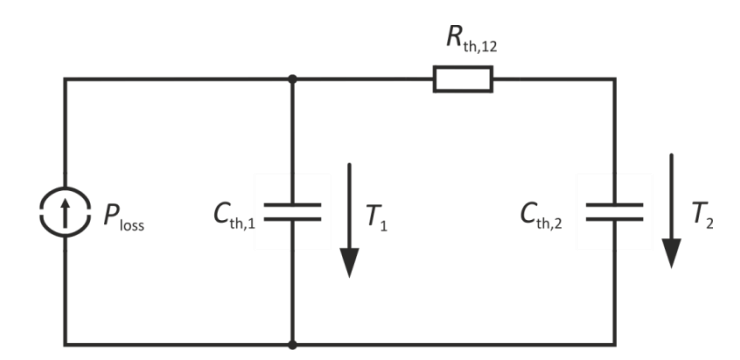


Figure 6.4: Thermal equivalent circuit for heat generation and heat transport between two points

<sup>&</sup>lt;sup>7</sup> Value for a was taken from the measurements by Schiffer et al. for a 5000 F [102].

In the thermal equivalent circuit diagram presented in Figure 6.4, the current source  $P_{loss}$  represents the heat generation at point 1. The heat flow over the thermal resistance  $R_{th,12}$  according to the Fourier heat transfer law depends on the temperature difference between point 1 and point 2. The thermal resistance is calculated depending on heat conductivity  $\lambda$ , the distance between point 1 and point 2, I and the lateral cut A where the heat flows through, compare equation (6.7).

$$R_{\rm th} = \frac{1}{\lambda} \cdot \frac{l}{A} \tag{6.7}$$

The resulting heat flow between point 1 and 2 depends on the temperature difference between these points and the thermal resistance, compare equation (6.8).

$$\dot{Q}_{\rm cond} = \Delta T \cdot \frac{1}{R_{\rm th}} \tag{6.8}$$

#### Heat Radiation

Beside heat conduction, heat transfer due to radiation and absorption on the surface of the compound is considered in the model. The resulting heat flow depends on temperature T, the compounds surface A, emissivity  $\varepsilon$  of the compound and on the Stefan-Boltzmann-constant  $\sigma$ , compare equation (6.9).

$$\dot{Q}_{\rm rad} = \varepsilon \cdot \sigma \cdot A \cdot T^4 \tag{6.9}$$

In case two compounds are face to face, a heat transfer due to radiation occurs. Thereby, their position to each other and their emissivities are summarized in one radiation coefficient (equation (6.10)).

$$\alpha_{12} = \varphi_{12} \cdot \varepsilon_{12} \cdot \sigma \tag{6.10}$$

The dissipated heat via heat radiation from one compound to its neighbor results to:

$$\dot{Q}_{rad,1} = \alpha_{12} \cdot A_1 \cdot (T_1^4 - T_2^4) \tag{6.11}$$

The radiation coefficient depends on the geometry, e.g. a cylindrical or prismatic cell is considered. Equations for the heat flow calculation of different configurations and geometries can be found in literature [104–106].

#### Convection

Finally, heat transfer can also be caused by movements of particles. This phenomenon is called convection, whereas the causes of particle movements can be different. One distinguishes between free and forced convection. While in case of free convection particle movements are caused by thermal induced density differences of a medium, in case of forced convection particle movements are forced by supplied mechanical work like a fan. Generally, heat transfer by means of convection depends of the difference between solid temperature  $T_s$  and fluid temperature  $T_r$ , the area  $A_r$ , and the heat transfer coefficient for convection  $\alpha$ .

$$\dot{Q}_{convec} = \alpha \cdot A \cdot (T_{S} - T_{F}) \tag{6.12}$$

For the calculation of  $\alpha$ , typically approximation equations based on empirical investigations are used for calculation of cooling of boundary surfaces caused by convection. Empirical formulas for these calculations for different configurations and geometries can be found in literature [104–106].

### 6.2.2 Separation in Volume Elements

The simulation of thermal processes is complex and forms an enormous conflict between accuracy and speed. Therefore, thermal calculations in this thesis are based on the finite difference method (FDM).

FDM divides the simulated compound into several volume elements. Then heat conduction is calculated between these volume elements. The model presented in this thesis exists in two different variations, for cylindrical and for prismatic cells. The cylindrical model divides the cells into arc elements and the prismatic model divides the cells into cuboid elements.

The thermal model calculates the heat transfer between neighbored cells and the heat transfer between cells and module casing. The considered heat transfer mechanisms are heat conduction, heat radiation and additionally convection from module casing to ambiance. Furthermore, the generated heat in cells and cell connectors due to current flow determined in the electrical model is considered. Within the thermal model every cell and the module casing parts are divided into several volume elements. For each volume element, the generated heat and the applied and dissipated heat and the resulting temperature are calculated. Thus, during simulation an energy balance is performed for each volume element. To achieve a preferably high spatial resolution, a large number of volume elements are needed. But more volume elements lead to longer simulation times. Therefore, a compromise between accuracy and simulation time has to be found. Figure 6.5 shows a possible cell partition of cylindrical and a prismatic EDLC with a high number of volume elements.

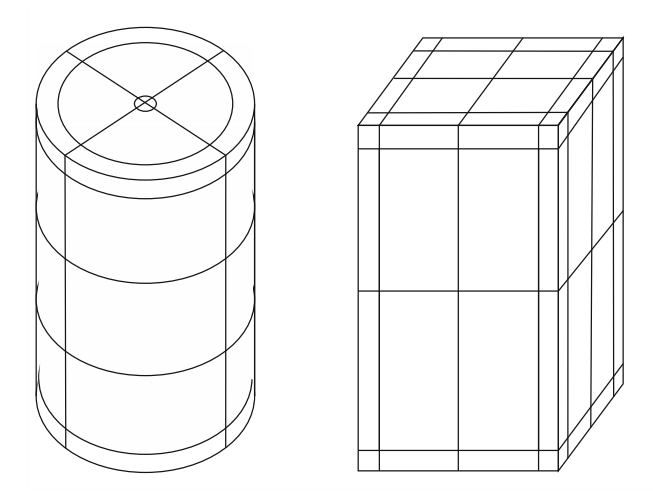


Figure 6.5: Partition of cylindrical and prismatic cell into volume elements

Since module models consisting of more than 100 cells were developed, the number of volume elements in this thesis was limited to seven in this case, as shown in Figure 6.6, to minimize calculation time. The resulting heat flow rate between two volume elements depends on the temperature difference and the heat conductivity between their center points.

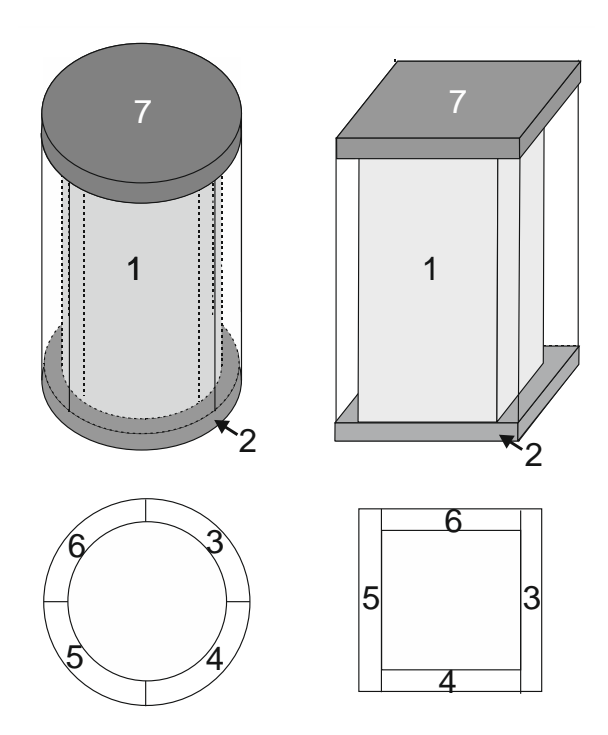


Figure 6.6: Partition of cylindrical and prismatic cell into seven volume elements (core, top, four side walls, bottom)

For electro-thermal simulations, the electrical and the thermal model interact as shown in Figure 6.7. An EDLC is separated into several volume elements. On the one hand the temperature for each volume element is calculated based on its energy balance considering the generated heat  $P_{\rm oss}$  and the heat capacity of each volume element both calculated by the

electrical model. On the other hand, the temperature calculated by the thermal model influences the performance calculated by the electrical model.

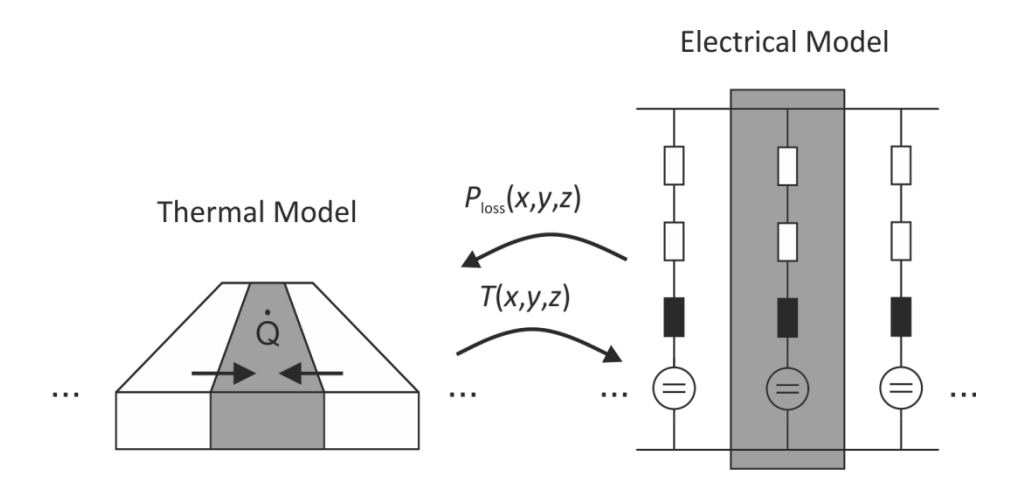


Figure 6.7: Principle of spatially resolved electro-thermal modeling

#### 6.2.3 Simulation of Thermal Transients

To analyze the thermal interaction between multiple volume elements, thermal transients must be calculated.

Generally, the temperature change of a single volume element can be described by the following formula.

$$\dot{T} = \frac{1}{C_{th}} (\dot{Q}_{\text{supplied}} - \dot{Q}_{\text{dissipated}})$$
(6.13)

Supplied and dissipated heat flows depend on the temperature difference between the considered and neighbored volume elements as well as on the heat transfer between these elements, whereas the dissipated heat flow can be calculated as follows:

$$\dot{Q}_{\rm dissipated} = \dot{Q}_{\rm cond} + \dot{Q}_{\rm rad} + \dot{Q}_{\rm convec}$$
 (6.14)

To calculate the energy balances for several volume elements a system of equations due to the interaction of these volume elements is required. The size of this system of equations corresponds to the number of volume elements since the temperature of each volume element must be calculated. Furthermore, heat flows caused by heat generation or heat losses to ambient must be added. Thus, the resulting differential system of equations is:

$$\dot{T} = A \cdot T + B \cdot \dot{Q} \tag{6.15}$$

Equation (6.15) includes the vectorial parameters  $\dot{T}$ , T and  $\dot{Q}$  as well as the coefficient matrices A and B. The coefficient matrices A and B are composed of the thermal parameters of the considered volume elements that are determined via material characteristics and geometry. If one volume element consists of more than one material as it is the case for the EDLC core an equivalent value is assumed. For the thermal capacity averaging is possible without any further considerations since the volume ratios of each material influence directly the specific thermal capacity. Thus, the total heat capacity can be calculated by adding up the thermal capacities of all components within the volume element (6.16).

$$c_{ ext{th,winding}} = n_{ ext{electrodes}} \cdot c_{ ext{electrodes}} + n_{ ext{current collector}} \cdot c_{ ext{current collector}} + n_{ ext{separator}} \cdot c_{ ext{separator}} + n_{ ext{electrolyte}} \cdot c_{ ext{electrolyte}}$$

$$(6.16)$$

 $c_{\text{material}}$  represents the specific thermal capacity and  $n_{\text{material}}$  represents the volume ratio of the considered material. For the determination of all volume ratios, the layer thicknesses of all materials must be known or at least assumed. Since there is no electrolyte layer in the EDLC core, the volume ratio of the electrolyte can be determined by means of the assumption that all pores of electrodes and separator are filled with electrolyte.

Thermal conductivity of an EDLC depends on direction, if the conductivity is regarded through the layers or parallel to the layers of the winding. In the first case, thermal conductivity is a series connection of the thermal conductivities of all components, whereas the overall thermal conductivity in direction along the layers is a series connection. Thermal conductivity values for every material depend on the layer thickness.

In fact, the electrolyte distribution in the carbon pores of the electrode should be considered since the porous structure lead to a higher contact surface between electrode and electrolyte and therefore a higher heat flow compared to two layers. However, this calculation would become very complex, and usually the pore structure of an EDLC is not known in detail. Thus, the electrolyte is simplified to a layer, whose volume results from the porosity estimation of separator and electrodes see Figure 6.8.

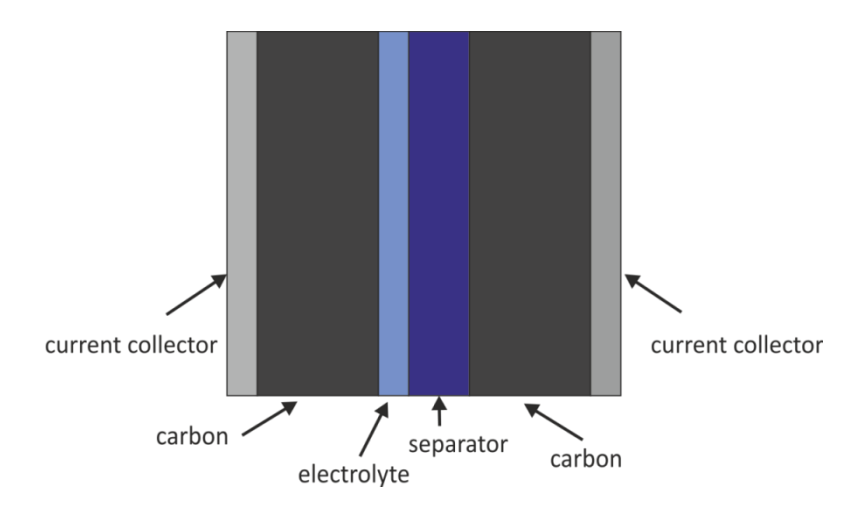


Figure 6.8: Assumed electrode layers for thermal modeling

Initially, the generated heat and the present heat transfer processes must be known. Furthermore, all thermal parameters have to be identified to be able to accurately simulate the heat transfer processes. These parameters can be determined mathematically or experimentally.

#### 6.2.4 Single Cell Model Validation

Cycling experiments on single cells at constant current rates were used to validate the thermal model. Tests were carried out in temperature chambers at constant temperature and free convection. The temperature increase at the cells surface was measured during the test.

The temperature increase of a single 650 F EDLC respectively a 3000 F EDLC during charging/discharging between 0 V and 2.7 V with a constant current rate of 100 A was used for the validation of the thermal model. The resulting temperature increase, measured on the cells surface, is presented in Figure 6.9. The simulated temperature curve for the 650 F EDLC matches the experimental data very well. Very small ripples due to reversible heat can be observed from the simulated data. Since a quite small cell is considered, the charge/discharge times are quite short which lead to less pronounced ripples. In contrast temperature ripples are much more pronounced in case of the larger EDLC, 3000 F, see right plot in Figure 6.9. Again, simulation and measurement match very well.

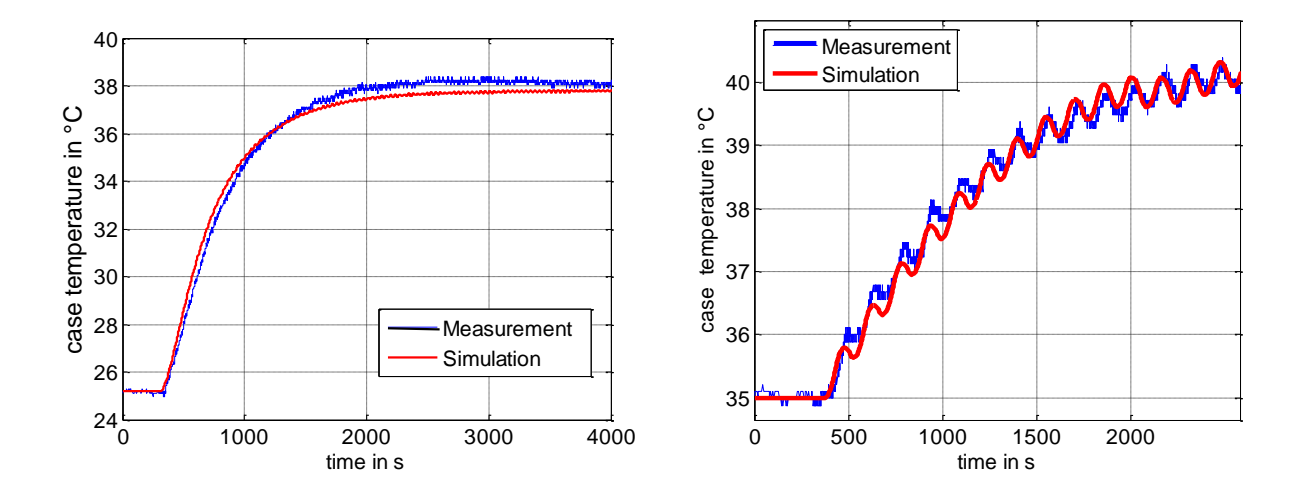


Figure 6.9: Model validation via simulation of the case temperature increase of a 650 F cylindrical EDLC (left) and 3000 F cylindrical EDLC (right) while cycling, both at a current rate of 100 A

#### 6.3 Module Model

Based on the above presented electro-thermal single cell model, a module model was developed. The module model considers the electrical and thermal behavior of each single cell and the cell connectors.

The thermal module model calculates the heat transfer between single cells and the heat transfer between cells and module case. Therefore, the following heat transfer mechanisms are considered: heat conduction, heat radiation and from module case to ambiance additionally convection. Moreover, generated heat caused by current flow through cells and cell connectors is considered. Within the module convection is neglected. This assumes, that in a closed system like a module case, practically no air flow can occur. The thermal model divides each cell and the parts of the module case in multiple volume elements and calculates the energy balance for each volume element.

The module configuration is very flexible. Number of cells, their geometry and their position in the module can be chosen. Within the module model, each cell is just one vector element containing the information on its position. Figure 6.10 shows the schematics of the module with vectorial parameters. The cell positions (x and y value in Cartesian coordinates) and the module dimensions are input for the thermal model.

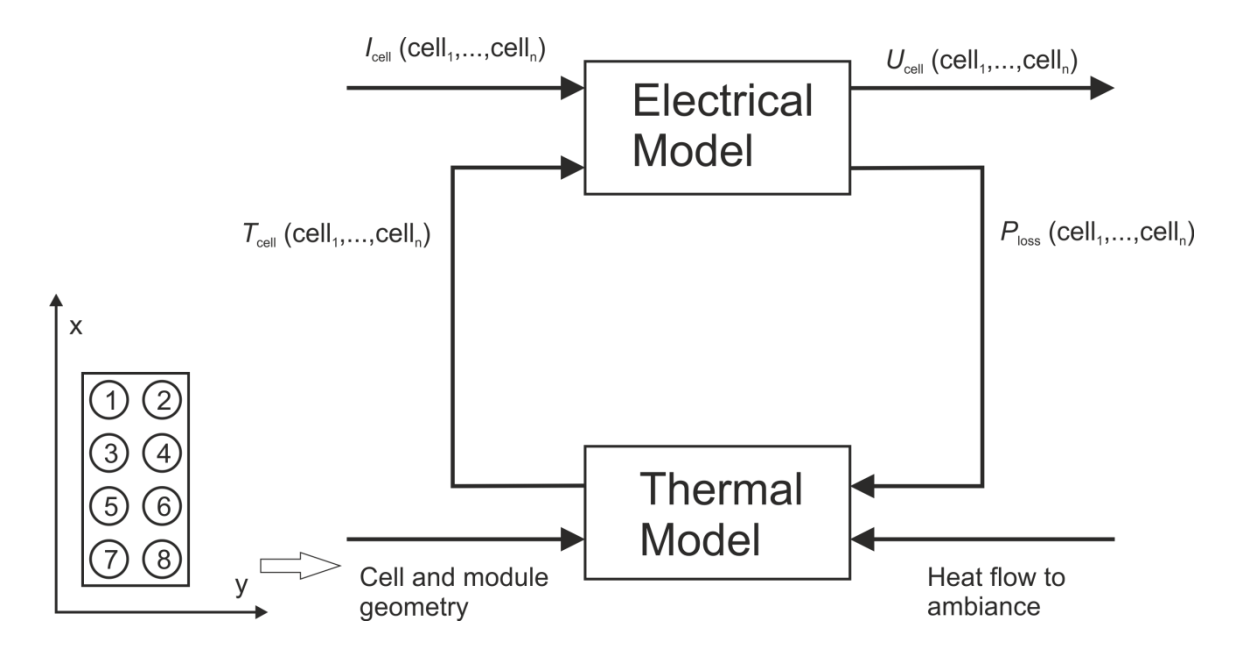


Figure 6.10: Schematics of the module model

During simulation, all module parameters such as current, voltage and temperature or heat flow are vectors. The sizes of these vectors are the number of cells respectively the number of volume elements. A module case can be considered as well. For simplification, it consists only of six volume elements, top, bottom and the four case sides.

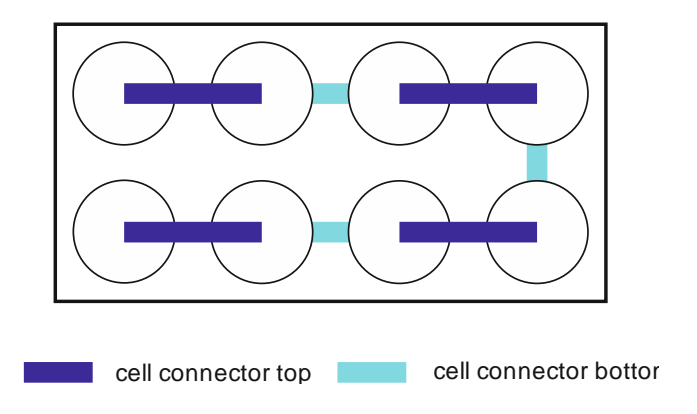


Figure 6.11: Exemplarily module configuration

Cell connectors can be positioned on top as well as under module cells, as shown in Figure 6.11. The generated heat due to current flow through the connectors and the heat flow are considered in the module model, too.

By means of these flexible configuration possibilities, many different modules can be simulated. Furthermore, different cooling strategies like e.g. forced air cooling via cooling fins or water cooling can be simulated.

# 7. Aging Behavior

Since the storage principle of EDLCs is in theory purely electrostatic, no lifetime limiting degradation processes as in batteries should occur. However, although EDLCs possess a very long lifetime, more than 500,000 cycles are reported [6], parasitic chemical reactions forced by high voltage and high temperature occur nevertheless. These aging processes lead to capacity fade and resistance increase and therefore limit the EDLC lifetime [83,107,108]. Thus, understanding the impact of temperature and voltage on the aging processes of EDLCs and being able to predict their effect on performance and lifetime quantitatively is essential for good system design [91,92,109].

In this thesis aging behavior of commercially available carbon-based EDLC types with acetonitrile-based electrolyte is investigated and analyzed quantitatively. Accelerated aging tests were carried out with several samples of this EDLC types, especially differing in geometry, capacity, and separator material.

# 7.1 Aging Phenomena

Aging processes in EDLCs can be caused on the one hand by physical processes e.g. gas evolution and accumulation in a closed system [110] that may lead in worst case to a severe structural damage of the cell casing. On the other hand, chemical processes shorten EDLCs lifetime. These chemical mechanisms are primarily decomposition processes of the electrolyte [60,110,111] and occur predominantly at the carbon surface [61].

Hahn et al. investigated the gas evolution of an EDLC with activated carbon-based electrodes and propylene carbonate based electrolyte. They detected the formation of propene and H<sub>2</sub> as a result of solvent reduction at the negative electrode and CO<sub>2</sub> as a result of solvent oxidation at the positive electrode [112]. Kötz et al. found out that the pressure evolution in EDLCs due to gas formation depend strongly on the used solvents. In their experiments, PC was slightly better at lower voltages but at higher voltages AN showed lower pressure evolution. But both were drastically better than the other tested solvents [113]. Azaïs et al. analyzed the aging processes of EDLCs in organic electrolyte. They showed that the active surface of the carbon electrode is decreased due to decomposition products of the electrolyte that block the pores which results in capacity fade and an increase of the internal resistance. The loss of active surface is significantly stronger at the positive electrode [114].

Generally, carbon is supposed to be chemically and structurally very stable. However, carbon is thermodynamically quite unstable regarding oxidation and reduction. Zhu et al. characterized the behavior of activated carbon with conductive additives in organic electrolyte [115]. They avoided the presence of aluminum in their experimental set-up to avoided side reactions with the aluminum that would have made it even more complex.

New electrodes of EDLCs are characterized by a good adhesion of the aluminum current collector and the carbon/binder composite. It is achieved by a glue present at the aluminum/carbon interface, usually carboxymethylcellulose [61]. Furthermore, aluminum has a thin oxide layer which does not affect the electrical conduction significantly.

Kurzweil et al. studied the abusive aging behavior of different commercial EDLCs with acetonitrile based electrolytes [116]. After aging tests under extreme conditions (up to 90 °C respectively 6 V) they investigated the decompositions products. One reason for undesirable chemical reactions inside the cell are water traces in the electrolyte and the carbon material. Although the electrode material is dried up to 150 °C during the manufacturing process not all water traces can be removed and cause the hydrolysis of acetonitrile. Furthermore, the carbon electrodes catalyze the thermal decomposition of the TEABF4 electrolyte. Kurzweil et al. showed that decomposition reactions in the electrolyte only occur with the presence of carbon material. Another observation was the loss of the oxide layer of the etched aluminum current collector material under the carbon layer. It was destroyed by fluorination and the process acts as a source of oxygen.

Chiba et al. investigated the voltage stability and decomposition products of different electrolytes [117]. They used the common TEABF<sub>4</sub> salt but new solvents like Ethyl isopropyl sulfone (EiPS) and compared it to propylene carbonate (PC). As experimental set-up, they used an H-type cell to analyze electrodes and electrolyte of the positive and the negative compartment separately. Each compartment consists of a separate glass tube with an additional compartment for the gaseous products resulting from the positive and negative electrodes. The set-up is described in detail in [111]. In case of both solvents, EiPS and PC, the amount of water in the positive electrode has increased drastically after a 50 h float test at 4 V. Additionally, they observed that the pH changed from neutral in both compartments to acidic in the positive electrolyte compartment and basic in the negative compartment. The authors have shown in [111] that H<sub>2</sub>O is originally held in clusters by the functional groups on the surface of active carbon electrode. Due to an application of voltage the degradation of these functional groups takes place. The generated H<sub>2</sub>O reacts then with the electrolyte anion BF<sub>4</sub> and produces hydrofluoric acid (HF).

In case of the EiPS system they observed a kind of a slight SEI formation on the positive electrode containing elements of F, Al and S. Furthermore, HF reacts with the aluminum current collector and form  $AlF_3$  and  $H_2$ .

Water traces in electrolyte can also lead to accelerated aging. Water can be located in small micropores and it is very hard to remove it [118] or water might come from parasitic reactions with oxygen containing functional groups on the carbon surface. Cericola et al. investigated the influence on capacity fade of water trace in electrolyte. They observed a significant impact for AN-based electrolyte and even more pronounced for PC-based electrolyte in case of a storage potential of 2.75 V. At higher voltages, other degradation processes are predominant. Cericola et al. observed higher capacitance decrease at the negative electrode

and explained it by the formation of trapped gaseous hydrogen in micropores of activated carbon [68].

# 7.2 Accelerated Aging Tests

Accelerated aging tests are a way to measure the impact of different operating conditions on the lifetime of EDLCs faster than under real-life conditions. These aging tests can be divided in two types: calendar life tests and cycle life tests. The first type of tests is a storage test, where cells are stored at constant voltage and temperature without being in operation, while the second type includes alternating charging and discharging with constant current or constant power at a defined cycle depth, or application-like profiles. In both kinds of tests aging is interrupted after defined intervals to determine the remaining capacity and the internal resistance. So-called check-up tests may include tests at different temperatures and/or different current rates.

Since the lifetime of EDLCs under normal conditions- rated voltage and 25 °C - is in the range of 10-20 years, aging tests under real life conditions can be very time consuming and cost intensive depending on the considered application. Therefore, accelerated aging tests are a fast way to measure the impact of different operating conditions on the lifetime of EDLCs. In this work calendar life behavior of two commercially available carbon-based EDLC types with acetonitrile-based electrolyte is investigated and analyzed quantitatively. Moreover, cyclic aging behavior of one of these EDLC types is investigated.

#### 7.2.1 Calendric Aging Tests

Based on the calendric aging investigations this thesis analyzes the influence of high temperature and high cell voltages on the EDLCs lifetime and compares the aging characteristics of both investigated cell types.

The calendric aging of commercial EDLCs has been widely investigated [82,91,107,108,119–125] but few of these tests lasted longer than a couple of month and no one longer than one year. To achieve results in a comparable short time these cells were stored at high temperatures and at polarized voltage well above the rated voltage. The main problem of all tests is, that lifetime tests are hardly ever done at conditions which are within the typical operational range during real-world operation. In this thesis, tests conditions are kept at least at acceptable acceleration factors, but they are also above normal operation conditions.

Lifetime expectancy of EDLCs is defined for nominal conditions, i.e. rated maximum voltage  $U_N$  and room temperature. Under nominal conditions it is in the order of 10-20 years. Aging can be accelerated by increasing voltage and temperature during the tests.

According to the estimation given in equation (7.1), the aging rate doubles if either the cell

voltage is increased by 100 mV or the temperature is increased by 10 K [82]. This was considered for the test design.

$$t_{\text{lifetime}} = t_0 \cdot 0.5 \left( \frac{V - V_{\text{RWV}}}{100 \text{ mV}} \right) + \left( \frac{T - 298 \text{ K}}{10 \text{ K}} \right)$$
 (7.1)

 $t_{\text{lifetime}}$  is the expected lifetime at the aging conditions,  $t_0$  is the lifetime at nominal voltage  $V_{\text{RWV}}$  and 25 °C, V is the applied voltage, and T the storage temperature.

As discussed later in this chapter, equation (7.1) delivers only a very rough estimation. The factors 100 mV and 10 K leading to halving of lifetime needs to be adapted to experimental results. Therefore, equation (7.1) is written according to [126] in a more generalized way.

$$t_{\text{lifetime}} = t_0 \cdot 0.5 \left( \frac{V - V_{\text{RWV}}}{\Delta V} \right) + \left( \frac{T - 298 \text{ K}}{\Delta T} \right)$$
(7.2)

The factors  $\Delta V$  and  $\Delta T$  have to be evaluated in calendric aging tests.

#### 7.2.1.1 Test Configuration

The calendric aging behavior of two different types of commercially available electrochemical double layer capacitors (EDLC), in the following named Type A and Type B, with carbonbased electrodes and acetonitrile-based electrolyte has been investigated at various aging conditions. They were made by different manufacturers and differ in their capacitance, rated voltage and geometry. Additionally, the calendric aging behavior of a third EDLC type, named Type C, was analyzed. Type B and Type C possess the same geometry and electrode material. The main difference is the utilized separator. Type B is a standard commercial product and uses a cellulose-based separator whereas Type C is a prototype and uses a polymer membrane. The calendric aging behavior of both cell types was investigated to compare the paper separator impact on calendric aging. Unlike to Type B cells, Type C cells have been dried at temperatures by far higher than 100 °C which is impossible with paper separators (Type B). This improved drying procedure is expected to have a beneficial impact on EDLCs' lifetime. There are slight differences in electrolyte composition but both electrolytes are ANbased. The differences are a result of the specific preparation within a research. Some cells of Type C with the standard electrolyte of Type B were prepared and aged for comparison reasons as well. The results showed no significant difference to the aging results of Type B. Therefore, the electrolyte's influence is neglected.

Table 7.1 gives an overview on the investigated cells types and their characteristics.

	Capacity	Rated volt- age	Geometry	Separator	Electrolyte solvent
Туре А	1000 F	2.8 V	prismatic	membrane	AN
Туре В	600 F	2.5 V	cylindrical	cellulose-based	AN
Туре С	600 F	2.7 V	cylindrical	polypropylene membrane	AN

Table 7.1: Cell types investigated in calendric aging tests

All EDLCs that had to be tested were aged at constant load (float conditions) and at increased ambient temperatures. The devices were stored in ovens (Memmert UFE500 30 °C-250 °C) at increased temperatures and were connected to a power supply (HM8143 0-30 V/2 A) to keep the devices at the defined voltage level. For the analysis of temperature and voltage impact on calendric aging of EDLCs an extensive test matrix with many different temperature and voltage levels were carried out. In contrast to previous calendric aging tests, not all cells were stored at nominal voltage or even above but also at lower voltages but higher temperatures. Thus, it was investigated if lowering the voltage has a beneficial influence on the life time of EDLCs. The test conditions for both EDLC types can be seen in Table 7.2 and Table 7.3. The accelerated aging factors given in these tables were calculated by using equation (7.1).

For the aging tests of cell type A two EDLC devices were tested at each aging condition and for the tests of cell type B and C three devices were tested.

Accelerated aging factor		Voltage level			
		<i>V</i> <sub>N</sub> -200mV	<b>V</b> <sub>N</sub>	<i>V</i> <sub>N</sub> +200mV	
	45 °C	-	-	1	
Temperature				Type A	
	CE °C	4	16	64	
65 °C		Type A	Type A	Type A	

Table 7.2: Configuration of the aging tests and acceleration factor according to formula (7.1) of cell type A

Accelerated aging factor / tested cell type		Voltage level					
		<i>V</i> <sub>N</sub> - 200mV	<i>V</i> <sub>N</sub> - 100mV	V <sub>N</sub>	<i>V</i> <sub>N</sub> + 100mV	<i>V</i> <sub>N</sub> + 200mV	<i>V</i> <sub>N</sub> + 300mV
	45°C	-	-	4 Type B,C	-	16 Type B	32 Type B
Temperature	55°C	2 Type B,C	-	8 Type B,C	-	32 Type B,C	64 Type B,C
	65°C	4 Type B	8 Type B	16 Type B,C	32 Type B	64 Type B	-
	75°C	-	-	32 Type B,C	64 Type B	-	-

Table 7.3: Configuration of the aging tests and acceleration factor according to formula (7.1) of Type B and  $C^8$ 

Aging tests and therefore the connection of EDLCs to the power supply were only interrupted for checkups including electrochemical impedance measurements and measuring the remaining capacity of the test devices. For capacitance measurement cells were cooled down to room temperature. Then after discharging to 0 V EDLCs were charged to their maximum rated voltage and this voltage was kept for 15 min. After that EDLCs were completely discharged with 10 mA/F. The capacitance was determined from the discharged Ah. These measurements were performed with a Digatron ECO (200 A, 0-6 V).

Electrochemical impedance measurements were carried out to analyze the dynamic behavior of EDLCs as a function of frequency during the aging process. Measurements were performed by using an EISmeter, a multi-channel galvanostatic impedance spectrometer manufactured by ISEA, RWTH Aachen University [80]. The impedance measurements were conducted at the test voltages for Type A and at nominal voltage for Type B and Type C in open circuit mode, i.e. without bias current, and in a frequency range from 7 kHz to 10 mHz.

The cells were immediately reheated after check-up and after recharging reconnected to the power supply afterwards. The frequency of these investigations depends on the acceleration factor (high acceleration factor  $\rightarrow$  high frequency of interruption for investigation).

All tests were continued until the capacitance of the EDLC under test has decreased at least by 20% of the initial capacitance. In case the cell case opened by high pressure due to internal gas evolution and electrolyte has escaped the test was terminated immediately. Fur-

<sup>&</sup>lt;sup>8</sup> Since a smaller number of cells for Type C was analyzed not all aging conditions could be tested.

thermore, some cells showed a sudden resistance increase and could not be recharged anymore and were therefore removed from the test as well.

Depending on the aging conditions some cells were aged for a test duration of more than three years that is far beyond the typical end of life (EOL) criteria, 80% or 70% of the initial capacitance or doubling of the internal resistance. Thus, the aging behavior of EDLCs far beyond these typical criteria could be observed. The end of test (EOT) criterion was 20% remaining capacitance respectively an increase of the internal resistance by a factor of 5.

#### 7.2.1.2 Capacitance Decrease

The relative capacitance development of cells at different aging configurations over test duration for cells of Type A is shown in Figure 7.1.

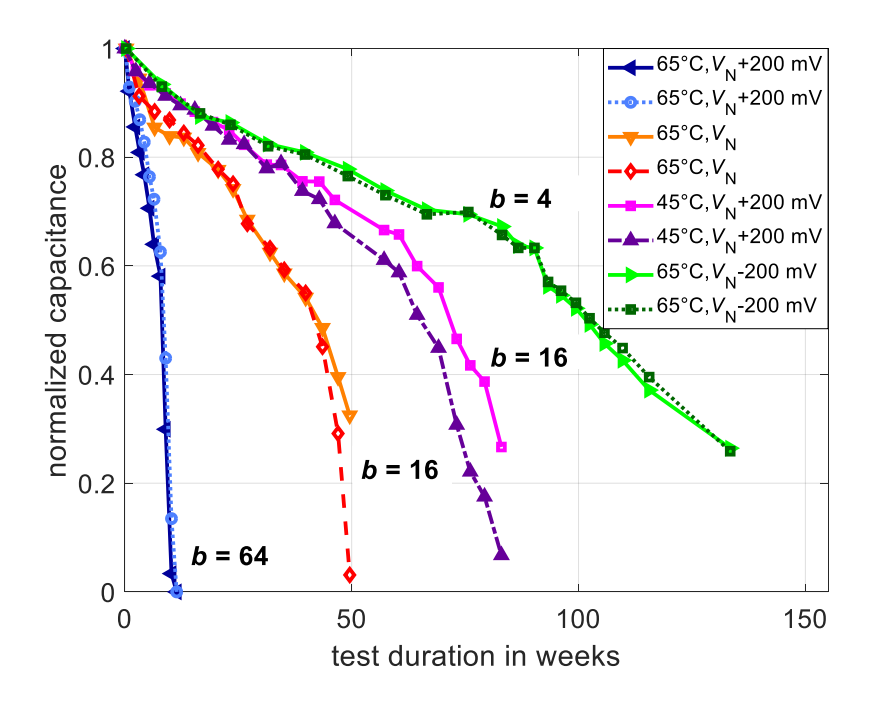


Figure 7.1: Capacitance decrease of Type A EDLCs with acceleration factors *b* calculated from formula (7.2)

It can be seen from Figure 7.1 that the cell capacitance of those cells which are stored at 65 °C and  $V_N$ +200 mV with the aging factor b=64 age very rapidly but almost linearly till approximately 60% capacitance. Below 60%  $C_{\text{initial}}$  the cell capacitance breaks down. This break down point can be also observed at other aging conditions as well. However, regarding the accelerated aging factors, significant differences within the aging behavior occurred. Cells aged with a similar aging factor of b=16 at test temperatures of 65 °C res. at 45 °C obviously age differently. This is a clear indication that formula (7.2) with the factors  $\Delta V$ =100 mV and  $\Delta T$ =10 K on which the calculation of b is based cannot be valid here. The capacitance of those cells stored at the higher temperature decreases much faster than that of cells stored at the lower temperature but higher voltage. Furthermore, the cells stored with b=4 are ex-

pected to have four times higher the lifetime of those cells with b=16. But it is obvious from Figure 7.1 that this not the case, lifetime for test condition b=4 is much shorter than expected. Even lowering the voltage of 200 mA under nominal voltage, while storing the cells at 65 °C, cannot compensate the high temperature impact.

Moreover, it can be seen from Figure 7.1, that there is only a slight deviation between two devices exposed to the same aging conditions. Only in case of advanced aging, when a capacitance break-down can be observed, the deviations become more pronounced. However, the statistic relevance of the data remains low since only two devices have been tests under similar conditions.

From the results shown above it can be concluded that the accelerated aging factors  $\Delta T$ =10 K and  $\Delta V$ =100 mV derived from equation (7.2) do not match the aging behavior of the investigated cells. The impact of temperature on the calendric aging is much higher than expected from this equation.

The results of the capacitance decrease of Type B show again that the assumed accelerated aging factors do not match the aging behavior. The following graphs in Figure 7.2 show the results for the different accelerated aging factors. The mean value of 3 tested cells is plotted over time.

At the beginning of the aging test, the capacitance decreases almost linearly. But once the capacitance is below 80% of the initial value, the capacitance drops significantly faster and the cell resistance increases strongly. The large error bars show at this aging condition indicate a big spread of cells as well.

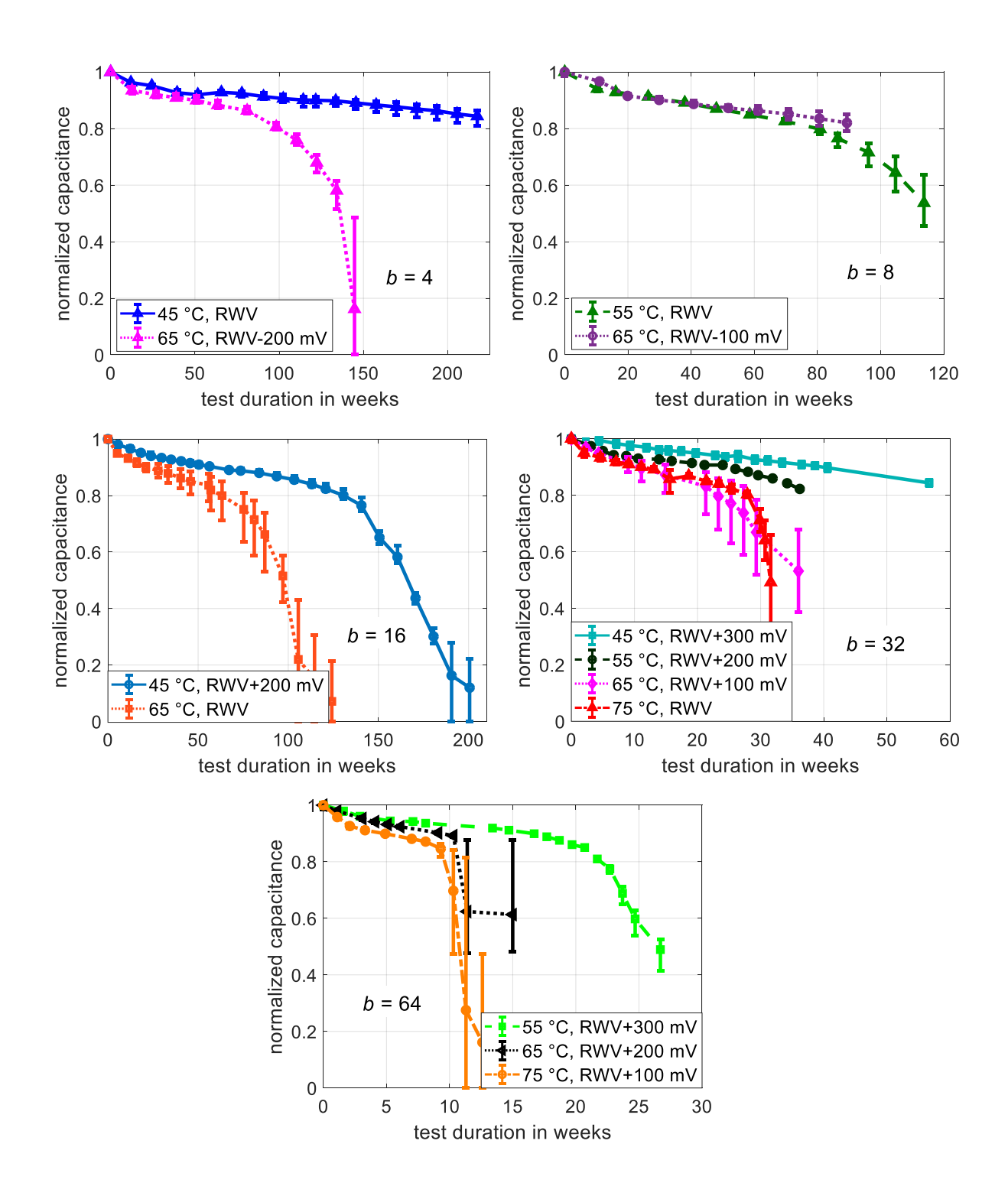


Figure 7.2: Capacitance decrease of Type B EDLCs for different accelerated aging factors

#### 7.2.1.3 Resistance Increase

The strong impact of temperature on calendric aging of Type A cells can be observed as well for the resistive aging, see Figure 7.3. Initially, the cell resistance increases nearly linear but at advanced aging the resistance curve inclines much stronger. As already seen in the capacitive aging behavior, the curves with the assumed aging factor b=16 differ significantly. Those cells which were stored at higher temperature, namely 65 °C, age faster than those stored at 45 °C.

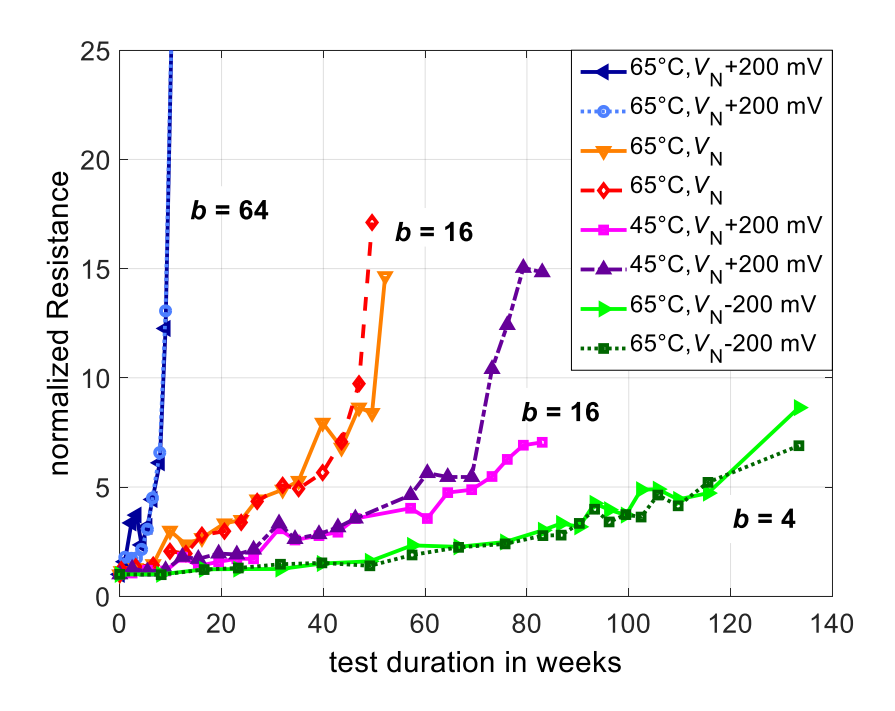


Figure 7.3: Resistance increase of Type A EDLCs

Comparable to Type A the strong temperature impact was also observed in case of Type B. in case of all acceleration factors the cell at the highest temperature shows the fastest resistive aging. Especially those cells aged at high voltages and high temperatures show very soon a strongly exponential aging behavior.

In the following figures every plot shows the normalized resistance increase for one accelerated aging factor. For all factors, the cell stored at the highest temperature shows the strongest resistance increase. Since the resistance increase, especially at high temperatures and high voltages, is very high, the normalized resistance is plotted in logarithmic scale for Type B.

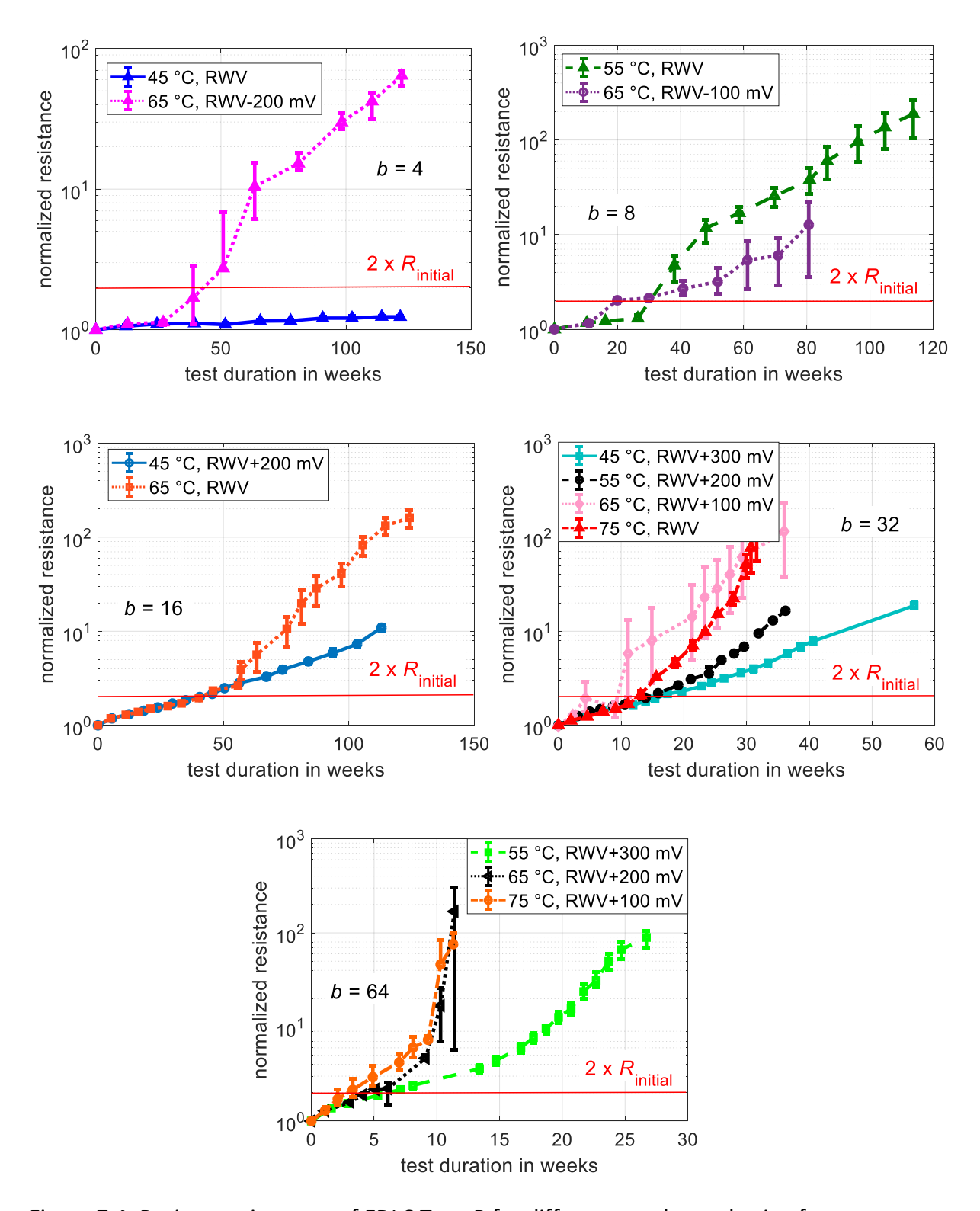


Figure 7.4: Resistance increase of EDLC Type B for different accelerated aging factors

Furthermore, it can be observed from Figure 7.5, that the resistance increase of Type B shows very early exponential behavior. The phase of linear increase is much shorter than in case of cell Type A. While the resistance of cell Type A increases quasi-linear till approximately 5 times  $R_{\text{initial}}$ , the linear increase phase of Type B lasts in many cases not even till the end of life criterion, 2 times the initial resistance, is reached. This behavior is probably

caused by the cell construction. Unlike to cells of Type A, cells of Type B lose weight during calendric aging tests. Thus, these cells must be leaky. Thus, some amount the of electrolyte's solvent can evaporate which results in weight loss. Furthermore, this effect can finally result in drying out of the cell. A nearly dry cell leads then to an extremely high internal resistance.

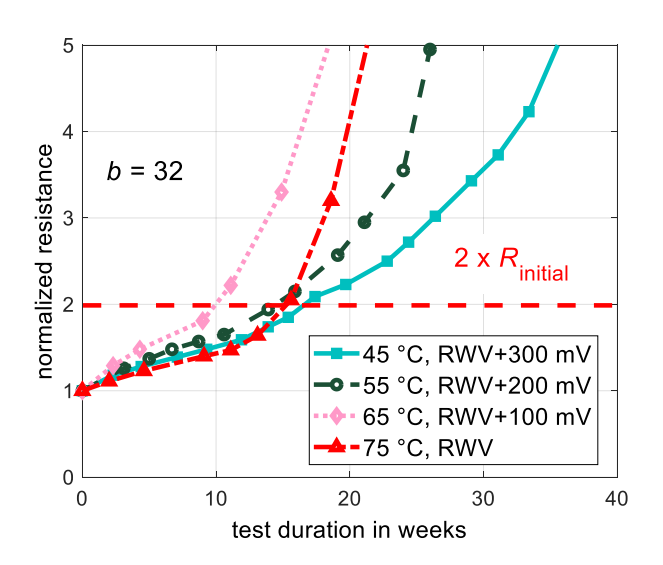


Figure 7.5: Initial resistance increase of Type B on linear scale, b=32

The evaporation process is moreover temperature driven because the resistance of those cells stored at higher temperatures starts earlier with exponential increasing<sup>9</sup>.

#### 7.2.1.4 Analysis of Calendric Aging Tests of Type A and B

From Figure 7.6 it becomes obvious that the development of resistance and capacitance is different for both cell types. The exemplarily presented cells were stored at 65 °C and rated voltage. Although, only one aging condition is presented the general characteristics of the resistance and capacitance development were observed at all aging conditions.

The resistance increases faster than the capacitance decreases for both types and the resistance increase is much stronger in case of Type B. Moreover, the capacitance characteristics are different. In case of Type A, the capacitance decreases initially nearly linear and beyond 60% of the initial capacitance it breaks down. In case of Type B, the capacitance decreases also firstly approximately linear but the capacitance break-down occurs already at about 80% of the initial capacitance. The resistance of Type A has doubled at a capacitance value of about 84%  $C_{\text{initial}}$ . In contrast, the resistance of Type B has already doubled at 87%  $C_{\text{initial}}$ . Regarding the typical end of life criteria for the capacitance the difference is even

 $<sup>^{9}</sup>$  An exception is the cell stored at 65  $^{\circ}$ C and  $U_{N}$ +100 mV but this cell was probably very leaky and aged therefore faster than the other cells.

more drastic. At 80% of the initial capacitance Type A has a resistance of 2.9 times  $R_{\text{inital}}$  but Type B has at that time already a resistance of 9.4 times  $R_{\text{inital}}$ .

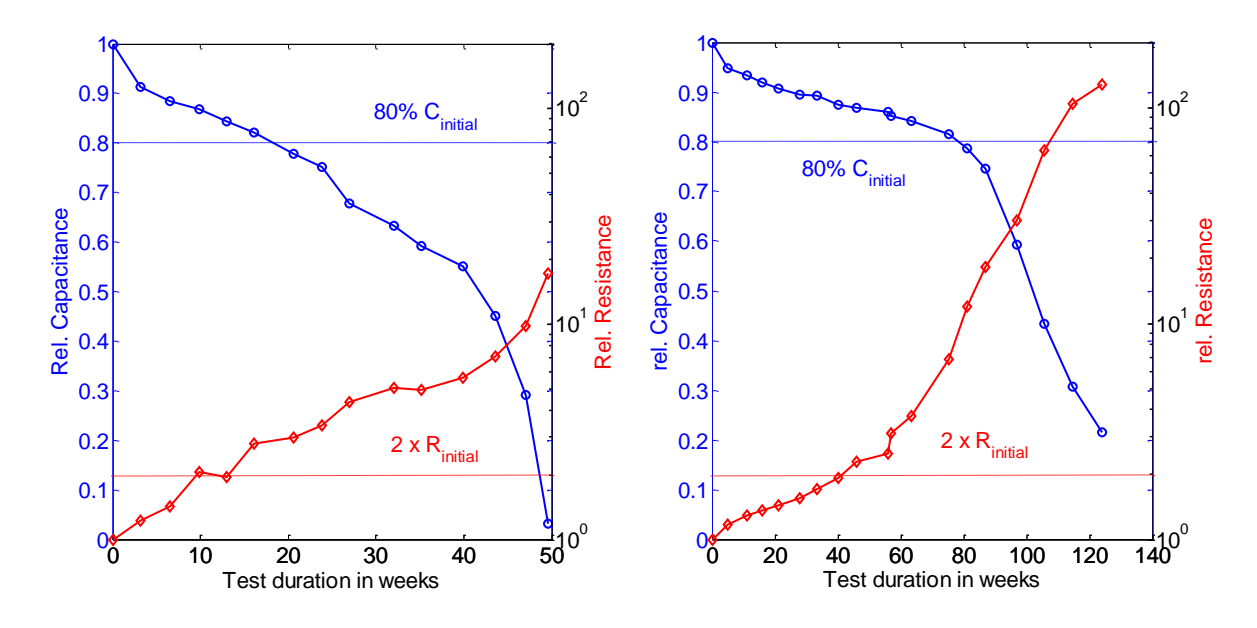


Figure 7.6: Capacitance and resistance characteristics while storing at 65°C and nominal voltage of Type A (left) and Type B (right)

These results show that the aging behavior of different EDLC types can differ significantly and since the capacitance and resistance characteristics might vary and therefore it is not sufficient simply to observe one end of life criterion, doubling of the resistance or a capacitance decrease of 20%.

The different aging behavior of both EDLC types was also analyzed by impedance spectroscopy. Figure 7.7 compares the development of the impedance spectra during the aging tests of Type A and B.

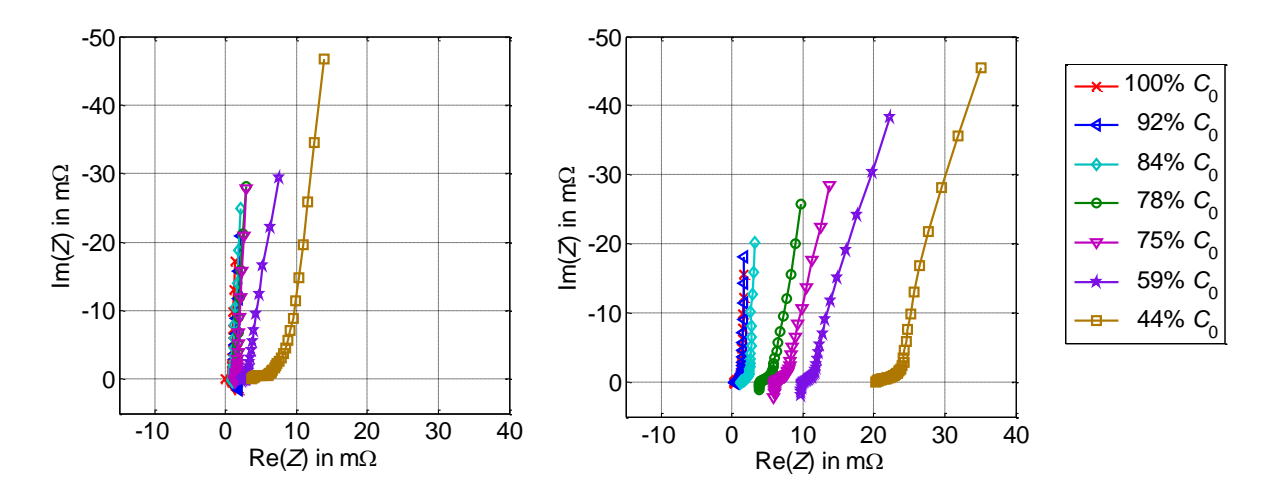


Figure 7.7: Development of impedance spectra during storage test at 65°C and nominal voltage (Type A (left), Type B (right))

It is obvious that cells of Type A and B differ in their aging behavior regarding impedance analysis. The ohmic resistance of Type A represented as the intersection with the x-axis in the Nyquist plot increases moderately with advanced aging. Furthermore, the shape of the spectra, changes with time. At capacitances lower than 50% of the initial capacitance the formation of a semi-circle can be observed which can be caused by the formation of a double layer.

In contrast, the impedance spectra of Type B cells do not change their shape significantly but a remarkable increase of the real part of the impedance can be observed.

The difference in the inductive part at high frequencies that can be observed with the spectra of Type B from 78% C<sub>initial</sub> on is due to a change of the cell connectors and therefore does not refer to cell aging.

Figure 7.8 compares the impedance spectra of the aged cells of both types at approximately 44% *C*<sub>initial</sub>. Beside the significantly higher ohmic resistance of cell Type B the shape of both spectra differs as well. In case of Type A, a clear semi-circle can be seen whereas in case of Type B no obvious semi-circle occurs but only a slightly but continuously increasing region. According to Keiser et al. [75] these different shapes can be explained by different pore shapes respectively different kinds of pore blocking. If the pore narrows, the spectrum lowers from the 45° of an ideal pore and if the pore expands behind a narrow pore opening a semi-circle occurs. To further analyze the pore structure of both aged EDLC types a post mortem analysis must be done.

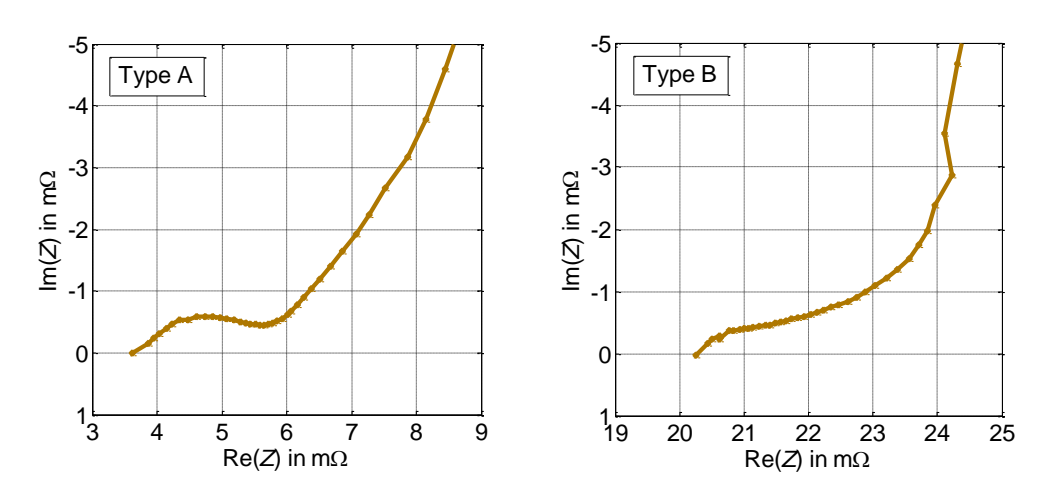


Figure 7.8: Zoom of the impedance spectra shown in Figure 7.7 at 44%  $C_0$ 

Figure 7.9 shows the Bode plots which belong to the same tests for which the Nyquist plots have been shown in Figure 7.7 and Figure 7.8. Regarding the absolute impedance values, cells of Type B shows a general increase of the absolute value over the entire frequency range with aging. Contrary to Type B cells of Type A show only in the low frequency range significant changes in the absolute value.

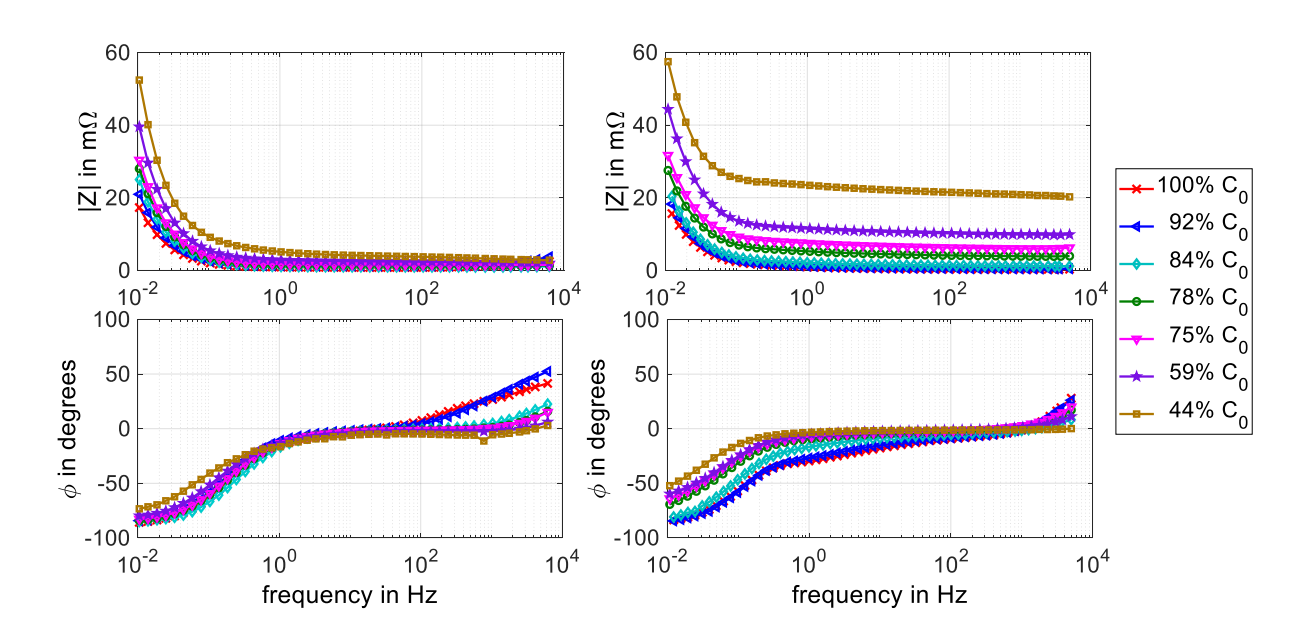


Figure 7.9: Bode Plots of Type A (left) and Type B (right)

While the previously presented cells of Type A showed no weight loss during the entire aging period, the cell of Type B has lost about 9% of its initial weight, the strong increase of the resistance of EDLC Type B is probably caused by a drying-out of the cell. Such a weight loss in correlation with a strong resistance increase was observed with most of the aged cells of Type B.

#### 7.2.1.5 Analysis of Lifetime Dependency on Voltage and Temperature

From the results of the accelerated aging tests the dependency of aging behavior on ambient temperature and cell voltage has been analyzed. The following analysis is based on the end of life criteria of 80% of the initial capacitance respectively doubling of the internal resistance.

Figure 7.10 shows the lifetime results for the cells of Type A. Most cells age faster regarding resistance. In case of the temperature dependency the trend lines through the data points of capacitive and resistive aging are nearly parallel.

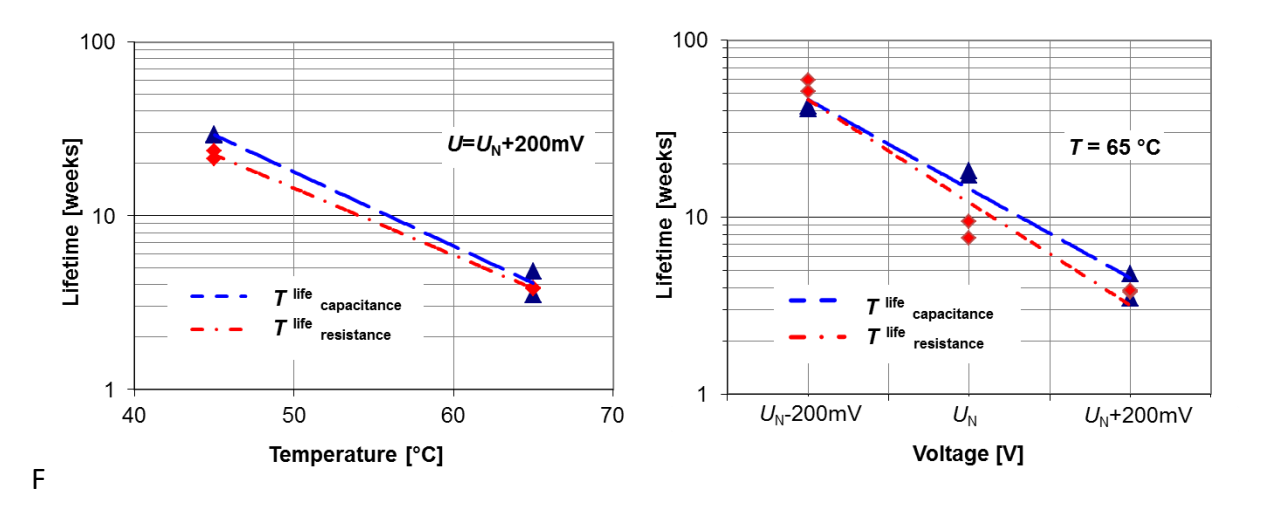


Figure 7.10: Lifetime of Type A depending on temperature (left) and voltage (right)

From the slope, it can be concluded that the temperature increase that halves the cells lifetime is about 7 K. In case of the voltage dependency the slope of both trend lines is slightly different. Regarding capacitive aging the voltage increase that halves lifetime is about 100 mV and regarding resistive aging it is about 120 mV. The exact values for each curve are given in Table 7.4.

Type A		Capacitive	Resistive
ΔV	65 °C	120 mV	104 mV
ΔΤ	<i>U</i> <sub>N</sub> +200 mV	7.1 K	7.7 K

Table 7.4: Lifetime halving factors of Type A taken from results presented in Figure 7.10

For the lifetime analysis of Type B all cells were considered except those that failed during the test due to an internal short circuit or opening of the cell case. All cells have reached the end of life criterion regarding resistance but some e.g. those stored at 45 °C and rated working voltage (RWV) have not lost 20% of their initial capacitance even after more than 4 years of testing but show at least more than 15% capacity loss. Their lifetime was linearly extrapolated.

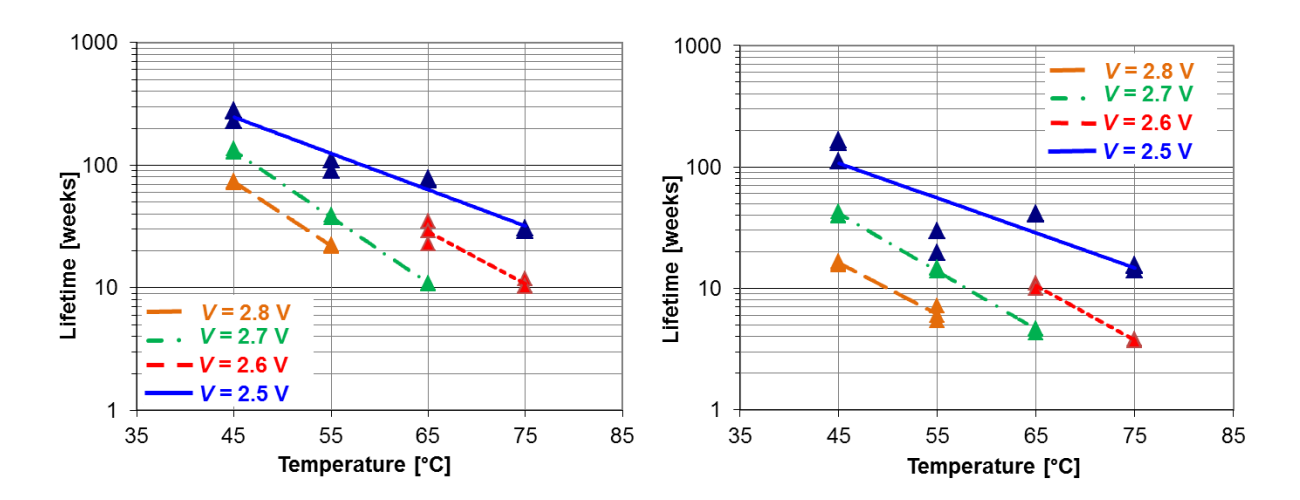


Figure 7.11: Lifetime of Type B depending on temperature, capacitive (left) and resistive (right)

The lifetime plots of Figure 7.11 show no clear temperature dependency of Type B. It is remarkable that the lifetime of those cells stored at RWV and 55 °C, which means aged at quite moderate aging conditions, showed shorter lifetime than expected compared to the other aging conditions, especially regarding resistance. This is even more distinctive for the resistive aging, see left plot in Figure 7.11.

The lifetime of cells, stored at 65°C and RWV-200 mV, RWV-100 mV or RWV, does not differ that much as expected for both, capacitance and resistance, see Figure 7.12. Some cells stored at higher potential show even a longer lifetime. Furthermore, the slop of both curves for 75 °C in the logarithmic plot is much higher than the slope for other temperatures. These results show that there are aging processes taking place which cannot be described by equation (7.2).

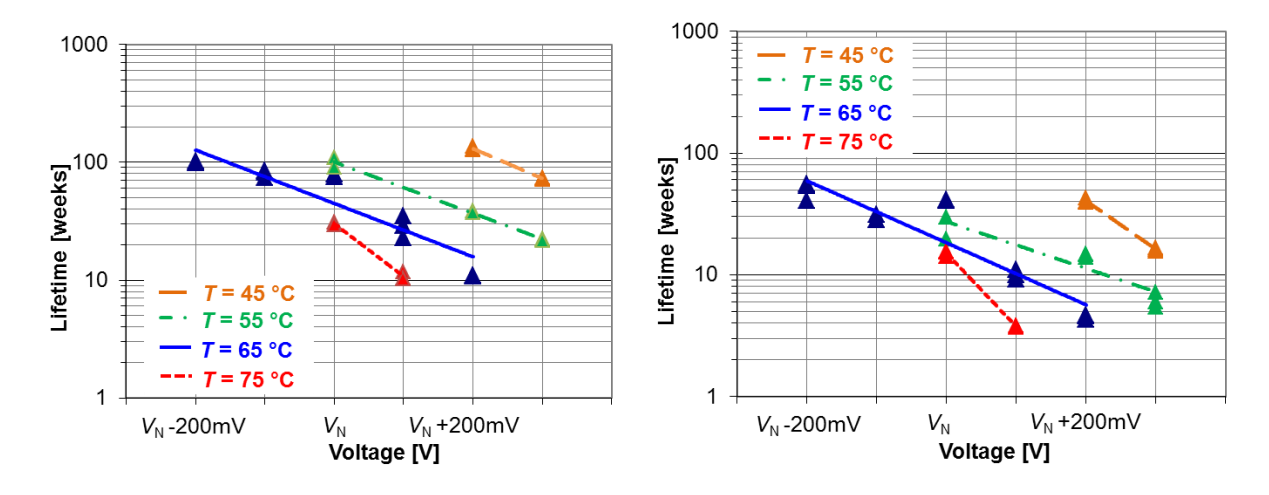


Figure 7.12: Lifetime of Type B depending on voltage at different temperatures (capacitive (left), resistive (right))

The factors  $\Delta V$  and  $\Delta T$  that can be deduced from the curves' slope in Figure 7.11 and Figure 7.12 are summarized in Table 7.5.

Туре В		Capacitive	Resistive
Δ <b>V</b>	45 °C	119 mV	76 mV
	55 °C	138 mV	156 mV
	65 °C	133 mV	118 mV
	75 °C	68 mV	50 mV
∆ <b>T</b>	2.5 V	10.2 K	10.5 K
	2.6 V	7.1 K	6.7 K
	2.7 V	5.6 K	6.3 K
	2.8 V	5.8 K	7.1 K

Table 7.5: Lifetime halving factors of Type B taken from results presented in Figure 7.11 and Figure 7.12

The values for  $\Delta V$  and  $\Delta T$  vary significantly. Both values for  $\Delta V$  at 75 °C are much less compared to  $\Delta V$  at other temperatures. At such a high temperature, slightly under the boiling temperature of acetonitrile, other more accelerated aging processes seem to occur. Furthermore, values for  $\Delta T$  at 2.5 V are significantly higher than the values at higher voltages. As discussed later, most cells of type B lost weight during the storage process. Thus, the cell case seems to be leaky. Therefore, electrolyte can evaporate and the dry out process can falsify the lifetime measurements. Moreover, as can be seen from the curve at 65 °C, there is a significant deviation of the measured lifetime value at 65 °C and nominal voltage to the fitted line. With just two measured points for one aging condition such deviations can of course not be observed and even a small deviation would result in a remarkable difference in aging factor.

Summing up, no average values for  $\Delta V$  and  $\Delta T$  could be deduced from the calendric aging tests of Type B because the deviations are too large. In case of Type A the results of  $\Delta V$  and  $\Delta T$  are derived from a limited number of cells and therefore a limited test matrix. At further test conditions, there might be also a deviation to the aging factor results of Type A presented in this thesis.

#### 7.2.1.6 Comparison of Calendric Aging of Type B and C

Additionally, to the aging tests of Type A and B the calendric aging of a third cell type, in the following named Type C, was investigated. According to Table 7.1 the differences between Type B and Type C are the separator and the electrolyte. Calendric aging tests with cells manufactured like Type C but with the same electrolyte as Type B, that are not presented in this thesis, showed comparable results as Type B. Therefore, the influence of a slightly different electrolyte is neglected here. But the new PP-separator of Type C allowed higher drying temperatures during manufacturing and results in an extended lifetime, as can be seen

from Figure 7.13. In both cases the results of two cells at every test condition is presented and it can be observed that there is only a very slight deviation between these two cells.

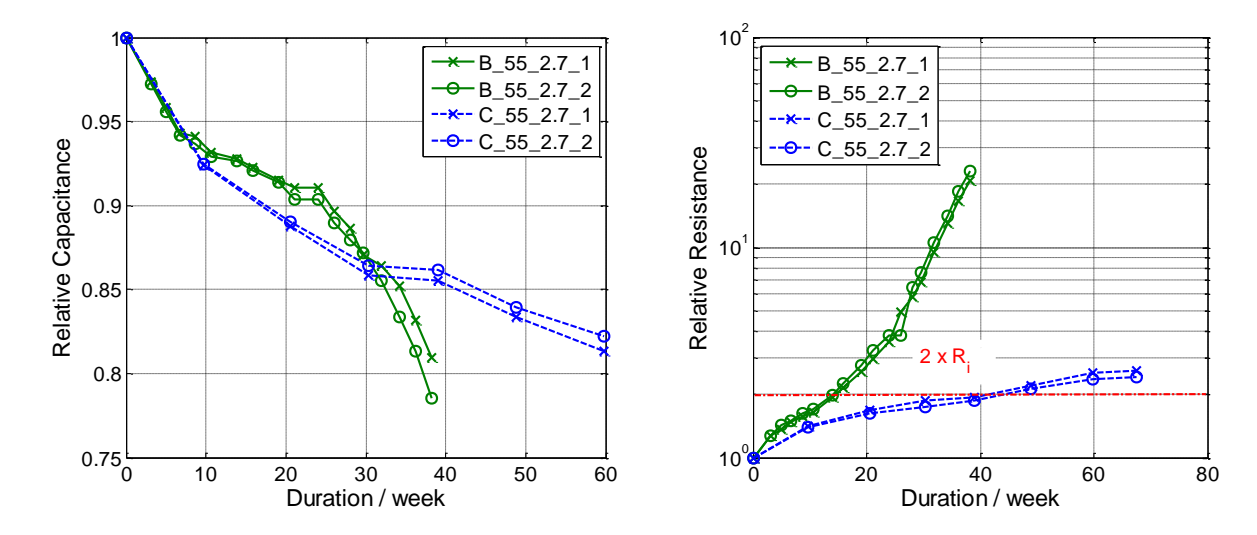


Figure 7.13: Comparison of capacitance (left) and resistance characteristics (right) of Type A and Type B cells stored at 55 °C and 2.7 V

Firstly, the capacitance loss is comparable for both cell types. At some point the capacitance of Type B is even slightly higher but then the capacitance of Type B breaks down whereas the capacitance of Type C continues to decrease nearly linear. The differences in resistance increase are even more obvious. While the resistance of Type C increases moderately the resistance of Type B increases strongly exponentially. The initial resistance of Type B has doubled and therefore reached the end of life criterion in half of the time compared with Type C.

It is most likely that this effect is caused by the new separator and the improved drying procedure. Due to higher temperatures, more water traces in the carbon pores can be removed. Water traces in electrolyte can also lead to accelerated aging. Water can be trapped in small micropores and it is very hard to remove it [118] or water might come from parasitic reactions with oxygen-containing functional groups on the carbon surface. Cericola et al. investigated the influence on capacity fade of water traces in the electrolyte. They observed a significant impact for AN-based electrolyte and even more pronounced for PC-based electrolyte in case of a storage potential of 2.75 V. At higher voltages, other degradation processes are predominant. Cericola et al. observed higher capacitance decrease at the negative electrode and explained it by the formation of trapped gaseous hydrogen in micropores of activated carbon [68].

Regarding the differences in lifetime between Type B and C, Figure 7.14 and Figure 7.15 show the results depending on voltage and temperature. In all cases the lifetime of Type C at the same test conditions as Type B was always higher. The differences regarding resistance were even more pronounced compared with aging regarding capacitance. Hence, it can be concluded that the new separator and the improved drying procedure is even more benefi-

cial regarding resistance increase.

However, the dependency of calendric aging on temperature and voltage is comparable for both cell types the curves are nearly parallel. Only in case of the resistive aging depending on temperature of Type C there is a large spreading of results that makes it hard to see any tendency.

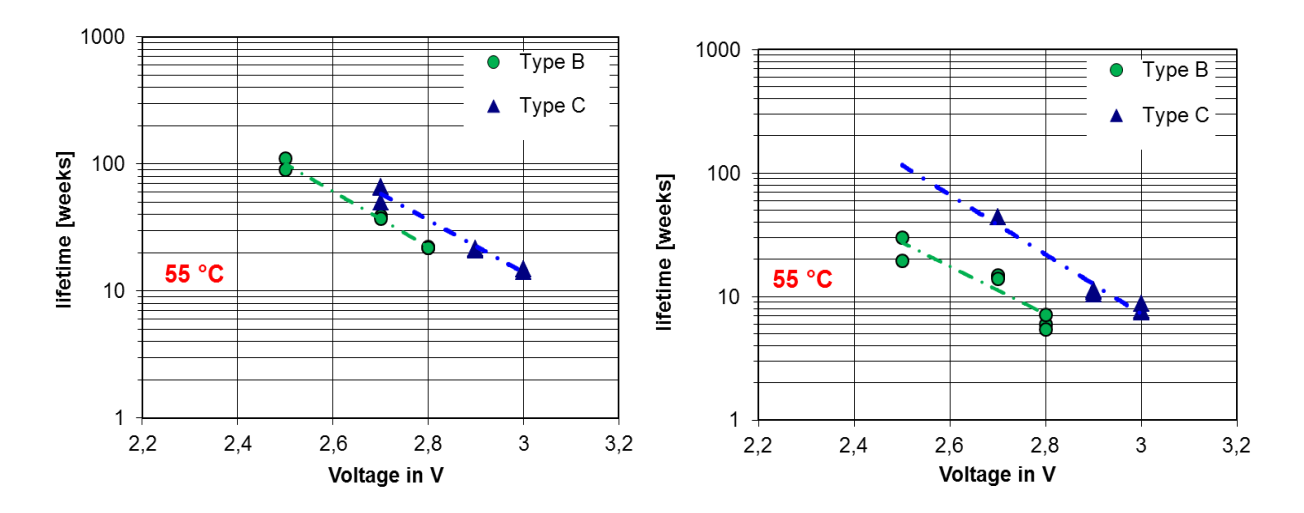


Figure 7.14: Lifetime of Type B and C depending on voltage (capacitive aging (left) and resistive aging (right))

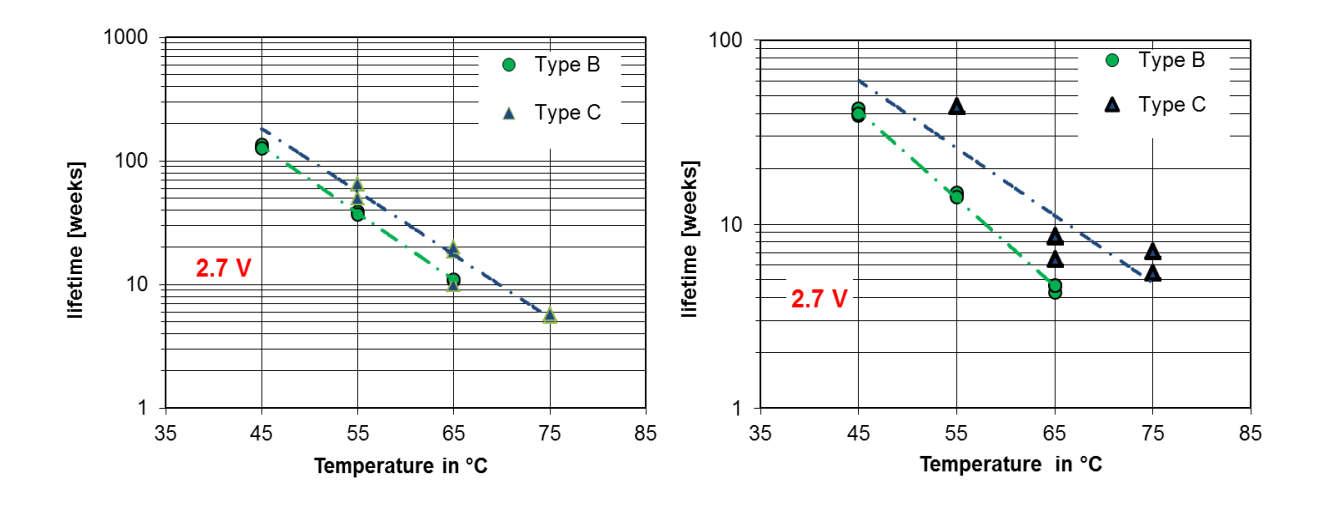


Figure 7.15: Lifetime of Type B and C depending on temperature (capacitive aging (left) and resistive aging (right))

The values for  $\Delta V$  and  $\Delta T$  for the same test conditions are compared in Table 7.6.

	Cell type	Test condition	capacitive	Resistive
ΔV	В	55 °C	138 mV	156 mV
Δν	С	55 °C	156 mV	125 mV
	В	2.7 V	5.6 K	6.3 K
ΔΤ	С	2.7 V	5.9 K	8.2 K

Table 7.6: Comparison of lifetime halving factors of Type B and C taken from results presented in Figure 7.14 and Figure 7.15

The values differ considerably, but as already observed for Type B the lifetime results for all test conditions are spreading. Since cell Type C uses the same cell case as type, it has the same leakage problems and the same spreading of calendric aging results. Therefore, it is hard to compare the aging factors but it can be generally concluded that the expected lifetime of Type C at the same cell voltage and temperature is significantly higher.

#### 7.2.1.7 Recalculating the Lifetime under Nominal Conditions

By using the determined values for the factors  $\Delta T$  and  $\Delta V$  and converting formula (7.2) as follows the achievable lifetime of this EDLC under nominal conditions (RT, RWV) can be calculated.

$$t_0 = t_{\text{lifetime}} \cdot 0.5 \left( \frac{U_{\text{RWV}} - U}{\Delta V} \right) + \left( \frac{298 \text{ K-} T}{\Delta T} \right)$$
(7.3)

As shown in Table 7.7 the calculated lifetime values for Type A differ significantly, the capacitive lifetime varies by a factor of about 2 whereas the resistive lifetime varies even by a factor larger than 5. In Figure 7.10 it could already be seen that the measured voltage dependent lifetime values<sup>10</sup> cannot be fitted to a line. Clear deviations of single measurement points from the fitted line were observed. These variations cause now the differences in calculated nominal lifetime.

Temperature	Voltage [V]	Capacitive lifetime	Resistive life- time
<b>65</b> °C	<i>U</i> <sub>N</sub> -200 mV	16.2 years	4.3 years
65 °C	U <sub>N</sub>	28.3 years	10.5 years
65 °C	<i>U</i> <sub>N</sub> +200 mV	21.2 years	9.3 years
45 °C	<i>U</i> <sub>N</sub> +200 mV	32.1 years	24.8 years

Table 7.7: Recalculated nominal lifetime of Type A for different calendric aging conditions

<sup>10</sup> The deviations can only be seen for voltage dependency because for temperature dependey there are only two measurement points due to the small test matrix.

The measured lifetime reducing factors for temperature and voltage for Type B are even more fluctuating than for cells of Type A which results in extremely varying values for the recalculated lifetime under nominal conditions as shown in Table 7.8. The values for  $\Delta T$  and  $\Delta V$  are taken from Table 7.5 for the actual voltage and temperature test conditions<sup>11</sup>.

Temperature	Voltage	Capacitive life- time	Resistive life- time
75 °C	U <sub>N</sub>	17.3 years	7.8 years
75 °c	<i>U</i> <sub>N</sub> +100 mV	75.9 years	50.8 years
65 °C	<i>U</i> <sub>N</sub> -200 mV	10.3 years	4.2 years
65 °C	<i>U</i> <sub>N</sub> -100 mV	13.8 years	4.4 years
65 °C	$U_{N}$	22.4 years	11.1 years
65 °C	<i>U</i> <sub>N</sub> +100 mV	46.7 years	21.8 years
65 °C	<i>U</i> <sub>N</sub> +200 mV	83.5 years	22.9 years
55 °C	$U_{N}$	14.8 years	3.4 years
55 °C	<i>U</i> <sub>N</sub> +200 mV	82.0 years	18.3 years
55 °C	<i>U</i> <sub>N</sub> +300 mV	69.0 years	8.4 years
45 °C	$U_{N}$	19.6 years	10.4 years
45 °C	<i>U</i> <sub>N</sub> +200 mV	95.6 years	43.6 years
45 °C	<i>U</i> <sub>N</sub> +300 mV	88.0 years	33.8 years

Table 7.8: Recalculated nominal lifetime of Type B for different calendric aging conditions

It is obvious that a recalculation of the nominal lifetime is not reasonable since the lifetime values differ by a factor of more than ten. For low voltage conditions ( $\leq$  2.5 V) the calculated values are in most cases in the range of 10-20 years fitting to the values typically given by manufacturers, but for higher voltages the lifetime values increase up to values out of reasonability. This effect was observed for all temperature conditions.

The extremely high values at high voltage conditions are very probably influenced by the leakage of the cells at these test conditions. Almost all EDLCs aged at high voltages (especially in combination with high temperatures) began to leak during testing. These effects have a strong impact on the aging characteristics but do normally not occur at nominal conditions.

From the test results of Type B for voltage depending aging at 65 °C one may conclude that at RWV and below, the voltage impact on calendric aging is neglectable since for these test conditions the measured lifetime values are nearly on a line, see Figure 7.12.

<sup>&</sup>lt;sup>11</sup>Since  $\Delta T$  and  $\Delta V$  could not be determined for 2.3 V and 2.4 V due to only one test at that voltage level, the values for 2.5 were taken instead.

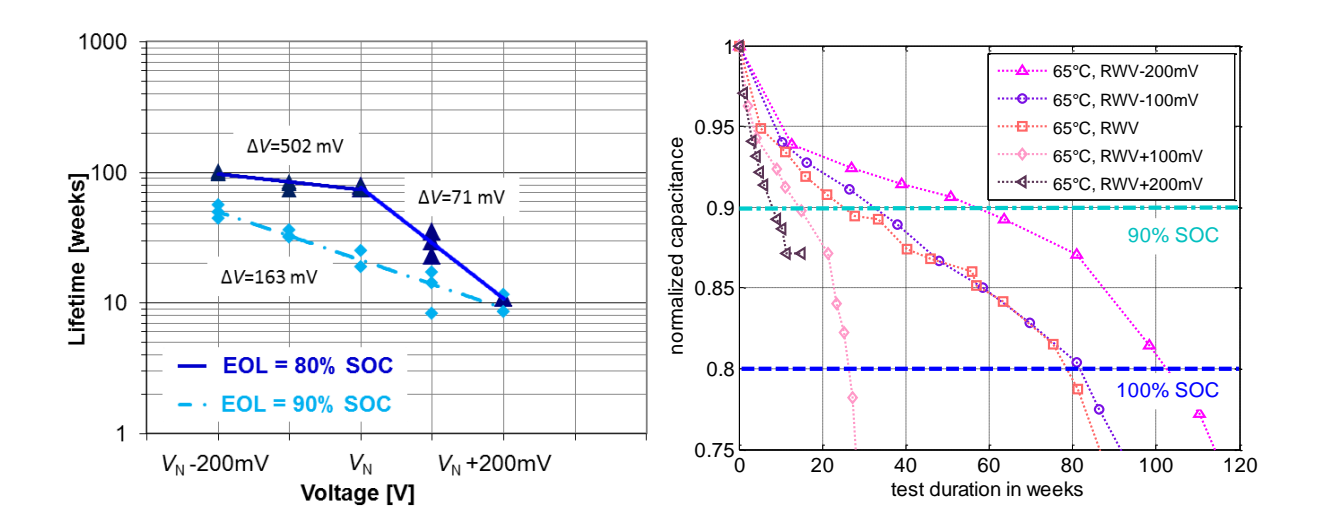


Figure 7.16: Voltage dependent aging at 65 °C, lifetime at EOL = 80% SOC compared to EOL = 90% SOC (left) and the belonging capacitance characteristics over time (right)

The determined  $\Delta T$  = 133 mV for capacitive aging (see Table 7.5) results from the fitted line through all five data points. Much smaller deviations can be obeserved if the fit is splitted to a line for RWV and lower and a second line for RWV and higher as shown in Figure 7.16. In case of EOL = 80% SOC the low voltage lifetime shows only a slight depedency on voltage whereas at high voltages the voltage dependency is very pronounced. But when these results are compared to the lifetime values for EOL = 90% SOC it can be seen that all values nearly lie on a line. As the right picture in Figure 7.16 shows, the capacitance characteristics of those cells at low voltages do almost not spread between 90% and 80% SOC but show only a nearly constant offset. The significant non-linear but accelerating voltage decrease is very pronounced for RWV-200 mV. All cells showed weight loss over lifetime including the cells at the most moderate aging condition. This gas-producing process seems to be temperature driven and independent from voltage. Such effects influences the lifetime charcteristics and makes the standard accelerated aging tests questionable.

The poor agreement in lifetime halving factors as well as in recalculated lifetime under nominal conditions makes it impossible to draw general conclusions from these tests and makes it very challenging to parameterize an aging model as later discussed in chapter 8.

#### 7.2.1.8 Purely Temperature Dependent Aging

The problem of all lifetime prediction approaches is the missing validation with real world non-accelerated tests at normal working conditions. Formula (7.2) and data as achieved from the accelerated tests and summed up e.g. in Table 7.6 suggest very long lifetimes especially at lower voltages and temperatures. Using formula (7.2) and the data for the capacitive ageing for Type C from Table 7.6 predicts a lifetime extension of more than a factor of 100,000 at 25°C and 0 Volt, hence a short-circuited cell. For Type A the lifetime of a short-

circuited cell predicted by formula (7.2) with the data of Table 7.4 is even more than 10,000,000 higher than the lifetime at standard conditions. As this is hard to believe, additional calendric aging tests of EDLCs at high temperatures without an applied potential were performed. Therefore, three cells of EDLC Type A were exposed to high ambient temperatures but not connected to a power supply as before but short-circuited. The test temperatures were 45 °C, 55 °C, and 65 °C. The respective lifetimes according to formula (7.2) should be about 10,000, 3,000, and 950 times longer than at standard conditions (2,5 V, 25 °C).

The test duration was about two years. Check-ups were carried out in the same way as in the accelerated calendric aging tests: Test devices were cooled down to room temperature and then a capacitance test and an impedance measurement were undertaken. If the extrapolation of formula (7.2) would be true, no aging beside measurement errors should occur within the test period of two years. However, Figure 7.17 shows the capacitance development during the storage process.

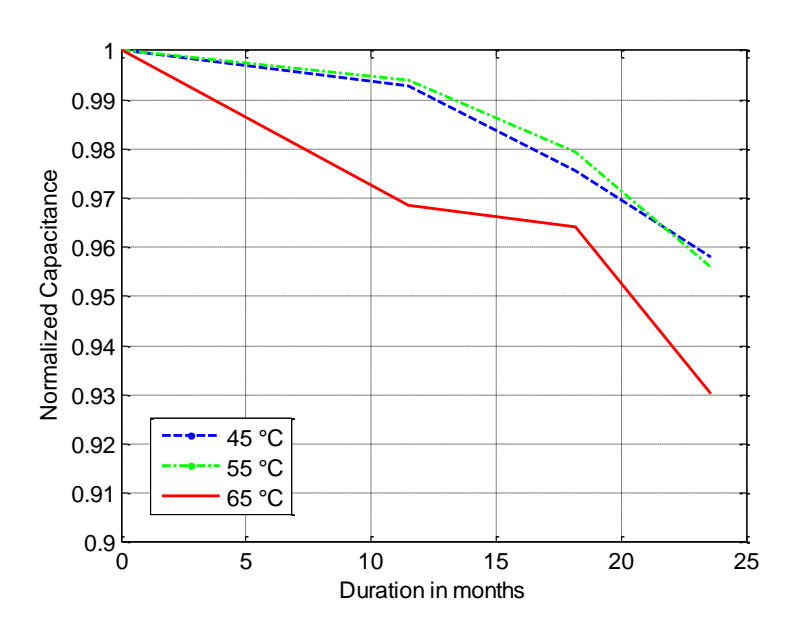


Figure 7.17: Capacitance decrease of short-circuited cells

The test devices stored at 45 °C and 55 °C showed very comparable results. The capacitance loss of both cells was about 4% over 24 months. The test device stored at 65 °C showed greater capacitance decrease, about 7% over the testing period.

A remarkable effect is moreover that the two devices stored at 55 °C and 65 °C showed after two years of testing salt deposits on the case next to the vent, compare Figure 7.18. An analysis in X-ray diffraction (XRD) of these salt deposits showed that this salt is pure tetrae-thylammonium tetrafluoroborate. Thus, internal pressure must have been occurred and pressed a small electrolyte amount through the vent. Since the solvent, acetonitrile, is very volatile the crystalline salts remained.



Figure 7.18: Salt deposition on top of the tested EDLC devices stored short-circuited at 65 °C (left) and 55 °C (right)

Since the salt deposits indicate that some electrolyte must have been escaped of the EDLC the weight of EDLC devices at the end of test was compared to the new cell's weight as shown in Table 7.9.

	New cell <sup>12</sup>	Cell stored at 45 °C	Cell stored at 55 °C	Cell stored at 65 °C
Weight <sup>13</sup>	241.5 g	241.0 g	239.6 g	233.4 g

Table 7.9: Weight of tested cells at end of test compared to a new cell

The intact cell stored at 45 °C showed as expected nearly no weight loss. But cells stored at 55 °C and 65 °C lost weight. In case 55 °C it is only in a range of 0.8% but in case of 65 °C it is about 3.4% weight loss. In both cases some solvent must be evaporated. Significant pressure evolution must be occurred and pressed electrolyte through the vent. The electrolyte salt crystalized on top of the case and the solvent evaporated which let to weight loss. This process must be temperature driven, since it was not observed at 45 °C but as a minor effect at 55 °C and then even more pronounced at 65 °C.

Hahn et al. investigated the pressure evolution in EDCLs with polypropylene-based electrolyte depending on voltage. They observed a significant pressure evolution at voltages over 2.5 V [127]. However, they did not analyze the temperature impact.

Zhu et al. investigated in [115] the aging behavior of pure carbon electrodes, without current collectors or binders, in organic acetonitrile based electrolyte at elevated temperatures. They compared the aging of different activated carbon types with and without an applied potential at a test temperature of 50 °C. While a significant aging, also depending on the carbon type, was observed for those devices with an applied potential, almost no capaci-

\_

<sup>&</sup>lt;sup>12</sup> Test cells were not weighted before storage test started. Therefore, their weights at EOT were compared to an average value of ten new cells. The weight deviation between these cells were only few milligrams.

<sup>&</sup>lt;sup>13</sup> Cells were weighted without any connectors or screws.

tance loss or changes in carbon structure was observed for those devices only stored at 50 °C without an applied potential.

From these results and the results presented in Figure 7.17 one may conclude that ambient temperatures higher than 50 °C without an applied potential lead to pressure evolution in the cell. However, at temperatures higher than 50 °C which is far below the boiling point of acetonitrile (81.6 °C), some gaseous chemical reactions independent from an applied potential must occur inside the cell but as presented in Figure 7.17 the pressure evolution and the resulting cell leakage is yet high enough at temperatures of 65 °C and higher to shorten EDLC's lifetime significantly.

These results of short-circuited Type A cells emphasize the results of Type B at voltages lower than RWV and 65 °C presented previously. Voltage independent and purely temperature driven processes led to cell leakage and performance decrease.

In any case, obviously formula (7.2) is not working for an operation at 0 Volts and this surely raises the question: For which range of temperatures and voltages is formula (7.2) with the parameters obtained at elevated temperatures and potentials valid. No definitive answer can be given within this thesis, but clearly shows the need for further investigations.

### 7.2.2 Cyclic Aging Test

Aging investigations mostly focus on calendric aging. However, it is not the case that cycling has no contribution to EDLC's aging. Due to intercalation processes it can also affect EDLC's lifetime. Therefore, this chapter presents the results of long-term cycling test of Type B.

#### 7.2.2.1 Studies on Cyclic Aging Reported in Literature

EDLCs are well known for their high cycle stability. More than 500,000 full cycles have been reported [6]. Theoretically, charge is stored in EDLCs by means of electrostatic charge separation. According to this theory charge is stored solely in an electric field and no chemical or structural changes should occur during the charging/discharging process. Therefore, unlike batteries cycle lifetime of EDLCs should be almost unlimited because no active material fatigue should take place and lead to capacity fade.

However, this theory is too simplistic, because Hahn et al. showed in a dilatometric study that insertion/intercalation processes take place during charging of EDLCs [128,129]. They investigated several carbon electrode materials in electrolytes with TEABF<sub>4</sub> in acetonitrile solvent as well as in propylene carbonate solvent. In graphitic electrode materials, the observed volume change between charged and discharged state (voltage range from 0 V to 2.5 V) was more than 10%, whereas in a commercial activated carbon electrode the observed volume change was much smaller but still about 1%. This difference can be explained by the layered structure of graphite that undergoes stronger structural changes during ion

insertion than the porous structure of activated carbon. Differences in volume change due to solvents were observed for the graphite material but not for the activated carbon material. Another interesting effect observed by Hahn et al. in [129] is the difference in volume change between positive and negative electrode. The volume change of the negative electrode was always higher. This is probably caused by the larger ion diameter of the positive ion  $TEA^+$  (0.69 nm) compared to the ion diameter of the positive ion  $BF_4^-$  (0.46 nm) [58]. Furthermore, the observed volume increase of about 1% within a voltage range from 0 V to 2.5 V for commercial activated carbon electrodes increased drastically up to higher voltages.

An important factor regarding cyclic aging is the temperature increase due to generated heat caused by the current flow [130]. Briat et al. reported that, at current pulses of 800 A, large EDLCs with 5000 F capacity heat up to a temperature of approximately 60 °C and showed a resistance increase of about 35% after 25,000 cycles [131]. This high cell temperature leads also to calendric aging and might have stronger impact on aging than pure cyclic aging. Therefore, during the cyclic aging tests presented in this thesis, all cells were cooled to minimize the calendric aging impact.

#### 7.2.2.2 Test Set-Up

Cyclic aging tests were carried out only with acetonitrile-based EDLCs using a cellulose-based paper separator. The calendric aging of this cell type, called Type B, was analyzed in chapter 7.2.1.

The main goal of these cycling tests was the analysis of the impact of charging/discharging and current rate on aging and to preferably avoid a superimposed impact of calendric aging. Therefore, since the results in chapter 7.2.1 prove that high temperatures accelerate significantly calendric aging processes, EDLC devices tested in cycling tests were continuously cooled. Thus, tests were carried out in a temperature chamber cooled in that way that the surface temperature of EDLCs during operation does not exceed 30 °C - 40 °C. Since these cooled cells aged very slowly cycling tests lasted more than three years.

Two different test profiles were carried out differing in current rate and voltage band:

- $U_{\text{max}} = 2.5 \text{ V} + I * R_{\text{i,nenn}}$ ,  $U_{\text{min}} = 1.78 \text{ V} I * R_{\text{i,nenn}}$ , I = 150 A Cyc1
- $U_{\text{max}} = 2.2 \text{ V} + I * R_{\text{i,nenn}}$ ,  $U_{\text{min}} = 1.31 \text{ V} I * R_{\text{i,nenn}}$ , I = 180 A Cyc 2
- 2 seconds pause between charge and discharge pulse<sup>14</sup>

<sup>&</sup>lt;sup>14</sup> The pause was enlarged at advanced aging state in order to avoid temperature increase due to higher internal resistance.

Tests were designed in that way that the charge conversion is comparable in both test conditions. The current and voltage characteristics of both tests are shown in Figure 7.19 for Cyc 1 and Cyc 2.

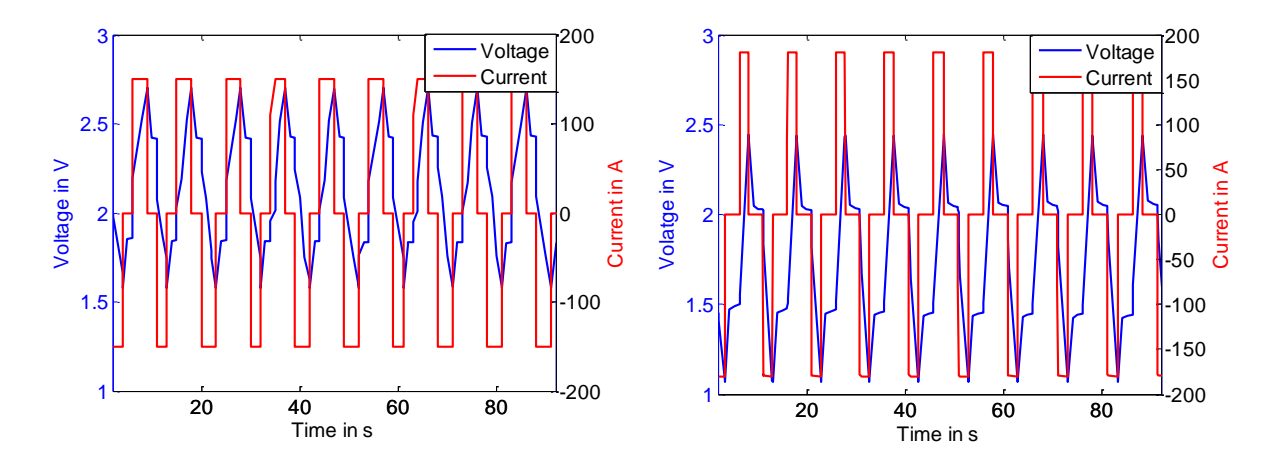


Figure 7.19: Voltage and current characteristics of Cyc 1 (left) and Cyc 2 (right)<sup>15</sup>

Four cells were initially tested under every test condition. Due to a limited availability, all four cells of one test condition were connected in series and were charged with the same test profile. However, this procedure led to some difficulties, especially at an advanced aging state, because cell voltages diverged during cycling. To minimize these problems balancing-resistors were put in parallel to every cell but, nevertheless, tests had to be frequently interrupted to balance the voltage level manually.

In a frequency of several weeks the DC-capacitance and the AC-resistance were measured as described above.

Figure 7.20 shows the capacitance and resistance development of all cells<sup>16</sup> for both test conditions. At the beginning of the tests a slight capacitance decrease can be observed. The capacitance loss of Cyc 2, which was charged and discharged at a higher current rate, is slightly higher. Afterwards, capacitance characteristics of both test conditions are nearly parallel and show almost no further decrease. Furthermore, it is obvious that the measured values for capacitance as well as for resistance vary significantly over lifetime and show no clear decrease/increase tendency.

<sup>&</sup>lt;sup>15</sup> All current pulses have the same length. Looking to Figure 7.19 might indicate different length of the pulses, but this is only a graphical effect.

<sup>&</sup>lt;sup>16</sup> One cell of Cyc 2 was damaged shortly after the begin of the testand therefore the results of only 3 cells are presented here.

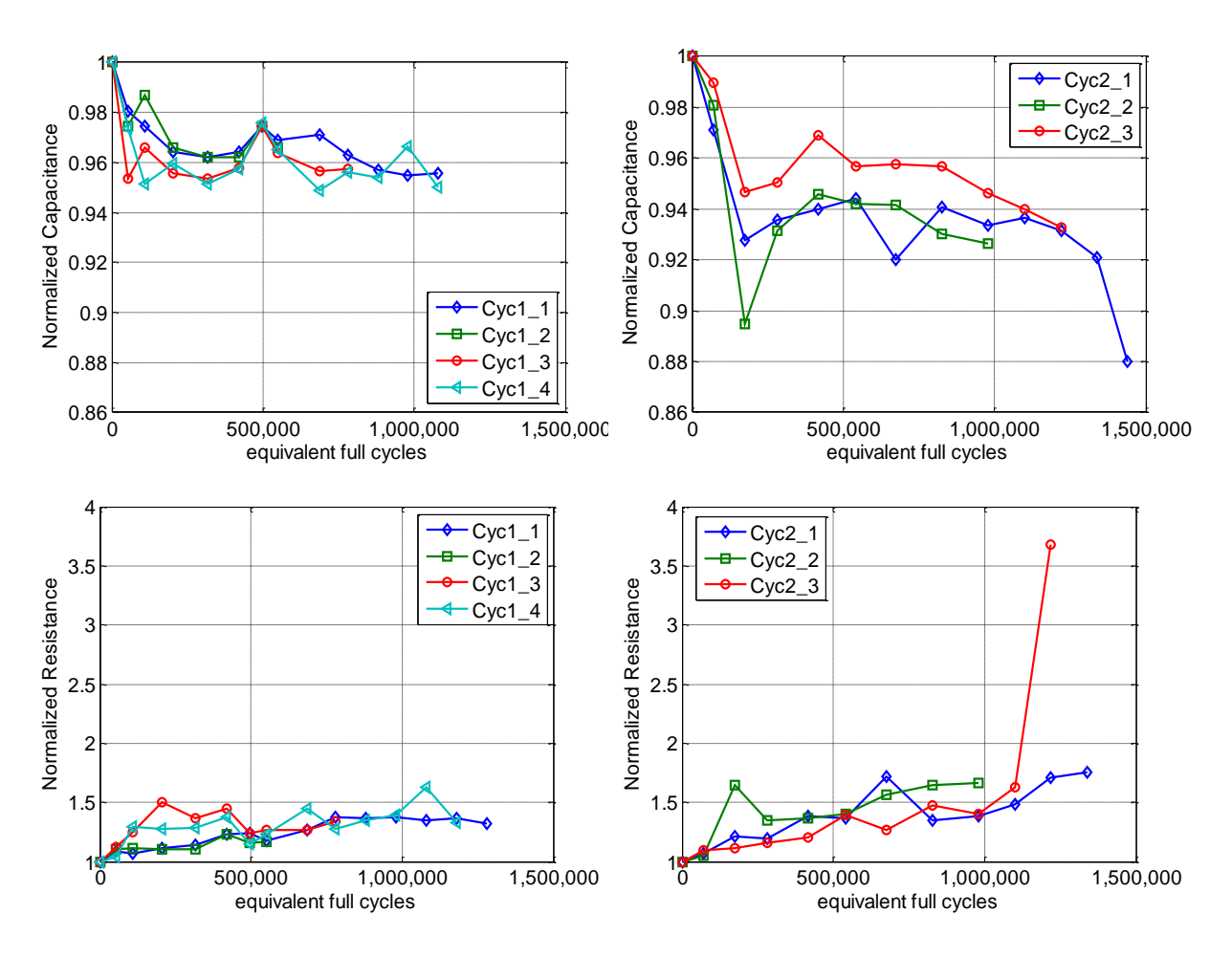


Figure 7.20: Capacitance decrease (top) and resistance increase (bottom) of both test conditions

This effect of EDLCs might be explained by regeneration phenomena which mean that the capacitance measured immediately after cycling is usually lower than the capacitance after a test interruption. Accordingly, the resistance after regeneration is lower than immediately after test. But upon continuing cycling, the measured capacitance and resistance values are comparable to those values measured before test interruption. This phenomenon was intensively studies by Chaari et al. [132,133] and Torregrossa [134]. Therefore, the time that passed between cycling test interruption and capacitance and resistance measurements for check-up were analyzed but no correlation with  $R_{\rm el}$  and C values could be found. Thus, the behavior shown in Figure 7.20 cannot be completely explained in this thesis. Another aspect is the end-of-life behavior of some cells tested in cycling tests. After more than 500,000 equivalent full cycles<sup>17</sup> by and by single cells were suddenly not chargeable any more. Probably, these cells fail due to internal short circuits. As can be seen from Figure 7.20 only cell Cyc\_2\_3 shows a sudden resistance increase during the last check-up. Other cells

-

<sup>&</sup>lt;sup>17</sup> Equivalent full cycles were calculated by deviding the summarized charge amount of one cycling test through the charge amount of one full cycle.

showed no abnormal characteristics at the last check-ups but failed suddenly during the following cycling period.

The results in Figure 7.20 show that the considered EDLCs can achieve much longer lifetime than the reported 500,000 full cycles if they are cooled. Even after significantly more than 500,000 cycles EDLC samples show only a minor capacitance loss and slight resistance increase. Over the entire testing time of more than three years none of the devices achieved the end of life criterion utilized for the calendric aging tests namely 20% capacitance loss respectively doubling of internal resistance. In contrast, cells can drop off abruptly and without warning, if they have achieved an advanced aging state.

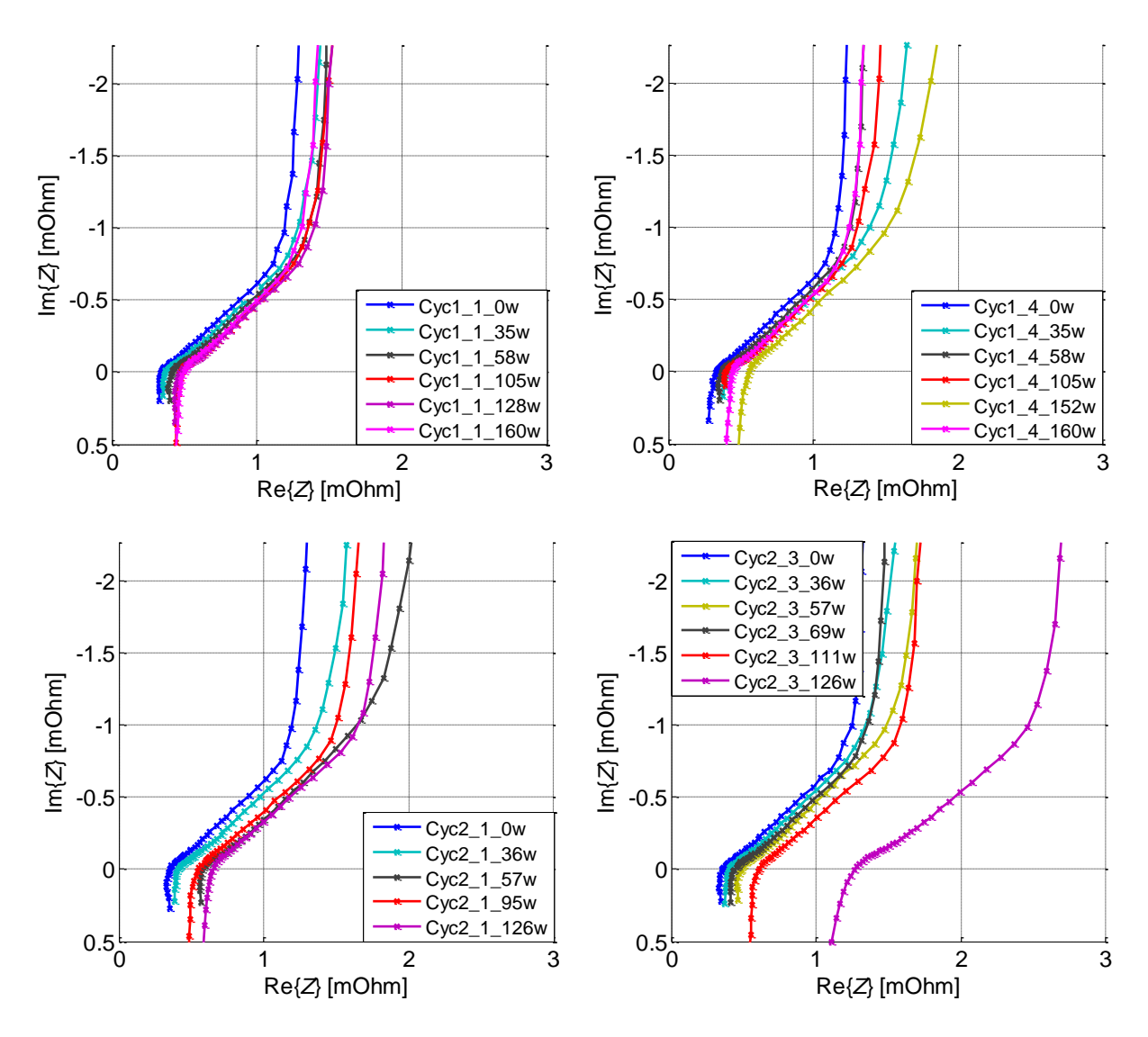


Figure 7.21: Nyquist charts of two exemplarily cells for the two cyclic aging test conditions

Figure 7.21 shows how the Nyquist plots of two exemplarily cells for each test condition changed over time. A slight increase of the internal resistance can be observed for all cells but very remarkable is the fact that the 45°-arc of most cells differs during aging. In case of cell Cyc1\_1, all Nyquist charts shows nearly the same shape and show only a slight offset off

the real part of the impedance during aging. Cell Cyc1\_4, cycled at the same conditions, shows instead different shapes in the high frequency range as well as in the low frequency domain in the Nyquist plot which means  $R_{\rm el}$  changes significantly as can also be seen from the fitted values presented in Figure 7.22. But there is no tendency that the rise of  $R_{\rm el}$  is proportional to number of cycles. The spectrum measured after 152 weeks for example shows a much higher  $R_{\rm el}$  than the spectrum measured after 160 weeks.

Similar observation can be made for cells of cycling condition 2. Here, all cells differ in their  $R_{\rm el}$  and this change is not proportional to the number of cycles, too. Figure 7.22 shows the alternating  $C_{\rm el}$  and  $R_{\rm el}$  values of all tested cells. The deviation of  $R_{\rm el}$  is up to more than 50% and no correlation between  $R_{\rm el}$  value and cycle number or current rate can be observed.  $C_{\rm el}$  values do not show such a strong alternation as  $R_{\rm el}$  values especially in case of Cyc1 where  $C_{\rm el}$  decreases almost continuously over lifetime. Only cell Cyc1\_4 shows one remarkable outlier after more than 1,000,000 cycles.  $C_{\rm el}$  values of Cyc2 alternate stronger than those of Cyc1 but further tests and therefore a larger database is needed to know if this effect is hazardous or due to the higher current rate of Cyc2.

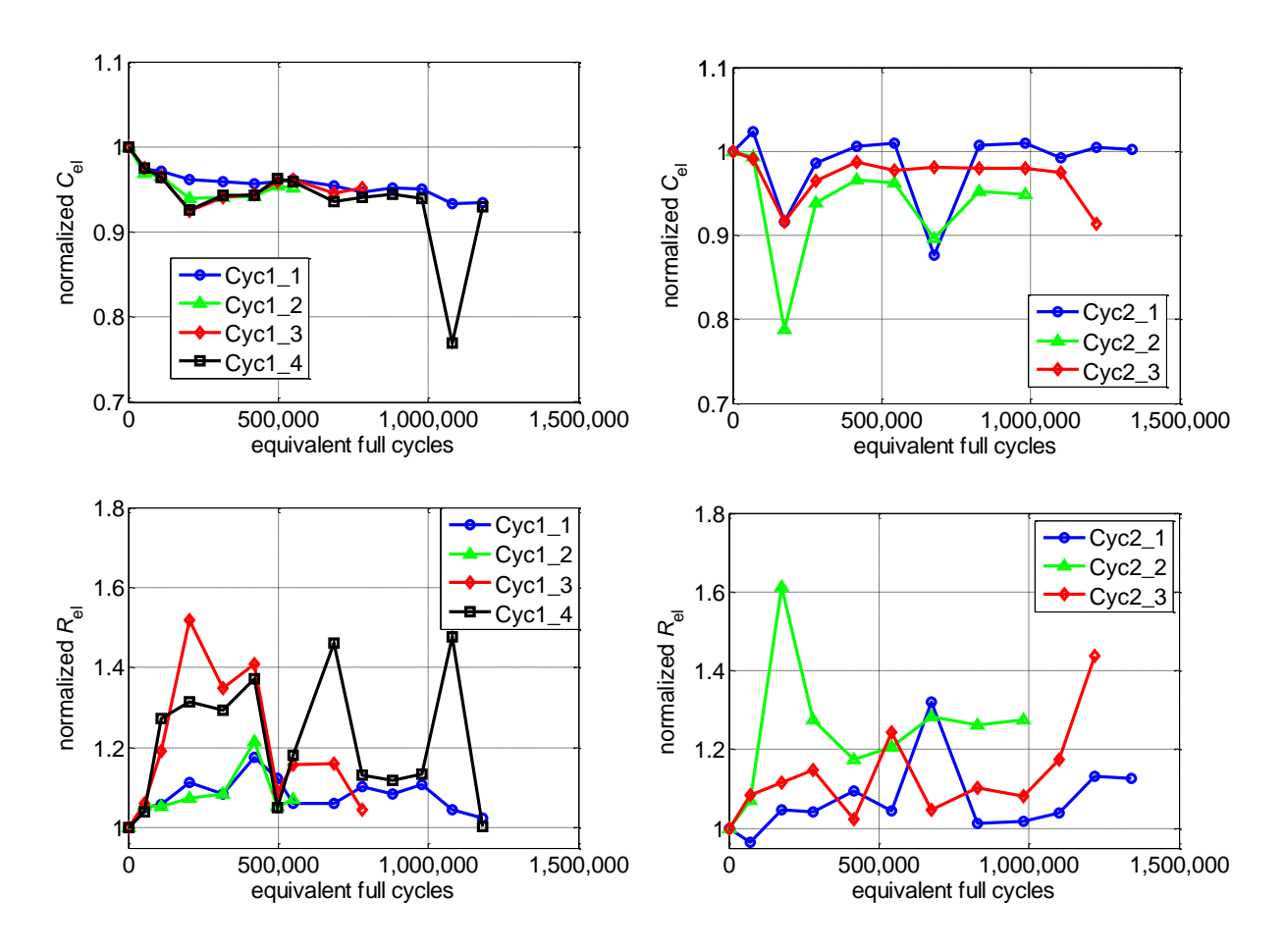


Figure 7.22: Development of  $C_{el}$  and  $R_{el}$  for both cyclic test conditions

The significant alternation of  $R_{\rm el}$  values might also be affected by regeneration effects as described above. But it must be stated again that there could not be found a clear correlation between rest time after cycling period and  $R_{\rm el}$  value.

However, this alternating behavior of  $R_{\rm el}$  seems to be correlated to the charging/discharging process during cycling because this behavior was not observed during calendric aging as can be seen from Figure 7.23. All three cells of this test condition show nearly the same behavior and almost no spreading, at least as long as they had more than 85% remaining capacitance. This capacitance value is much less than the measured capacitances at the end of cycling tests. The value of  $R_{\rm el}$  changes only in a range of about 5% and these results matches previous studies. Bohlen et al. concluded from their calendric aging tests that  $R_{\rm el}$  does not change while aging [91].

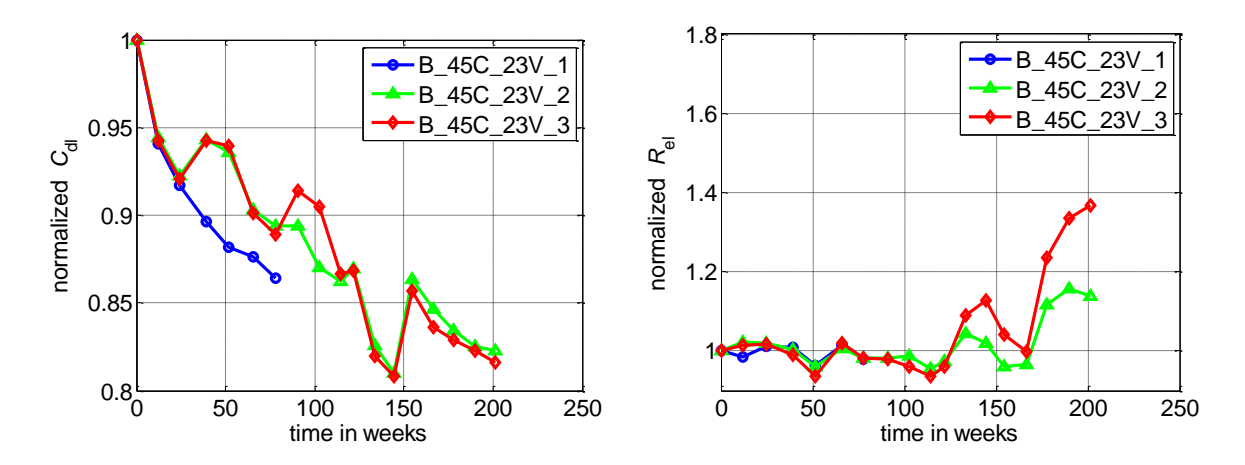


Figure 7.23: Development of  $C_d$  (left) and  $R_{el}$  (right) for a calendric aging test (45 °C, 2.3 V) of Type B.

It is known that  $R_{el}$  correlates with the diffusion processes of ions within the pores. The change of this value might be caused by changes in the pore structure due to intercalation processes. These intercalation processes were investigated in several studies [129,135–137].

#### 7.2.2.3 Determination of the Cycling Impact on Cell Aging

To determine the impact of the cyclic strain, shown in the previous chapter, the calendric share of the aging must be excluded. Therefore, the approach is to calculate the voltage-based and the temperature<sup>18</sup>-based calendric aging factors during by using the voltage and temperature dependency on calendric aging determined previously. The analysis of the calendric aging was presented in chapter 7.2.1. As shown there, the values of  $\Delta T$  and  $\Delta V$  for Type B vary extremely. Furthermore, the analysis of short-circuited cells in chapter 7.2.1.8

<sup>&</sup>lt;sup>18</sup> Calculations based on the measured temperature on cell case. The temperature of cell core might be slightly higher but since the current profile contains short pulses and pauses longer than pulses the entire cell temperature is assumed to be in a quasi steady-state.

implies that equation (7.2) is not valid for very low voltages. The cell voltage during cyclic tests is almost always lower than nominal voltage and therefore much lower than the cell voltages during the calendric aging tests presented in this thesis. Thus, the validity of equation (7.2) using the factors from calendric aging is questionable here.

Since the impact of calendric aging during cyclic aging tests cannot be precisely determined by calculations, several assumptions were made and the results are presented and discussed in the following.

From equation (7.2) the accelerated aging factors for calendric aging during cycling test were derived. Since the cell temperature is assumed to be constant over the cycling test period, the temperature dependent accelerated aging factor  $b_{T_cyc}$  is calculated in the same way as for calendric aging.

$$b_{\text{T\_cyc}} = 2^{\left(\frac{T - 298 \text{ K}}{\Delta T}\right)} \tag{7.4}$$

In contrast to temperature, cell voltage changed during charging and discharging. Since the dependency of aging on voltage is strongly non-linear the average value cannot be taken, but the voltage-based aging factor must be calculated for each time step and then integrated over time.

$$b = 2^{\left(\frac{T - 298 \text{ K}}{10 \text{ K}}\right)} \cdot \int 2^{\left(\frac{V(t) - V_{RWV}}{120 \text{ mV}}\right)} dt$$
 (7.5)

The resulting lifetime *t* is then calculated by means of the following equation:

$$t_{life} = \frac{t_0}{b_{\text{T cyc}} \cdot b_{\text{V cyc}}} \tag{7.6}$$

where  $t_0$  is the lifetime under nominal conditions (25 °C, rated working voltage).

## i) Calculation with ΔT and ΔV from calendric aging tests

As first assumption, the lifetime halving factors for temperature and voltage derived from the calendric aging are considered to be valid. Since these values vary over the test matrix (cite), the values for the lowest temperatures and voltages were taken because they come closest to the cyclic aging conditions, namely  $\Delta T = 10.2$  K (capacitive) and  $\Delta T = 10.5$  K (resistive) for 2.5 V respectively  $\Delta V = 119$  mV (capacitive) and  $\Delta V = 119$  mV (resistive) for 45 °C, according to Table 7.5. The cell temperature of Cyc 1 was 30 °C and 41 °C for Cyc 2. The voltage characteristics for both cyclic conditions are shown in Figure 7.19.

Based on this assumption the impact of calendric aging is supposed to be very low. Due to cooling and the resulting moderate temperature increase and due to the low average volt-

age, the aging acceleration factor *b* is quite low. Figure 7.24 shows that the measured capacitance and resistance characteristics lay considerably under respectively over the calculated characteristics. This result would imply that cycling has a significant impact on cell aging and additional aging effects must occur during charging and discharging.

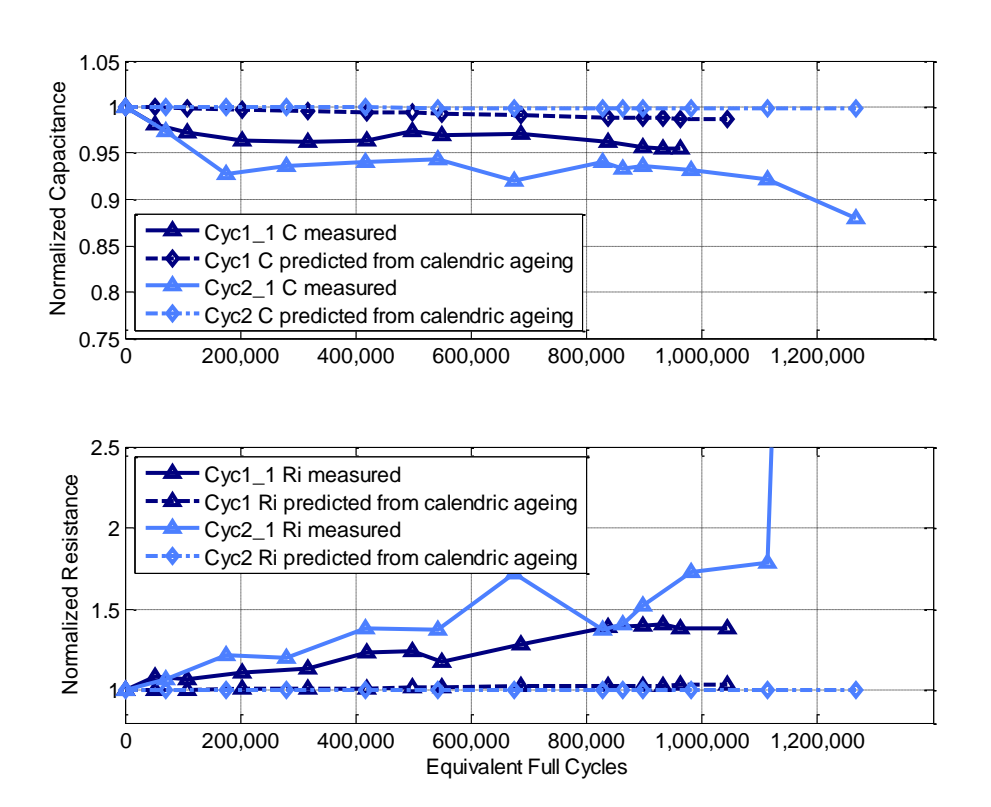


Figure 7.24: Comparison of measured cyclic aging and calculated calendric aging with aging factors from calendric aging tests.

## ii) Calculation with neglected voltage impact on calendric aging

As presented in chapter 7.2.1.8 the voltage impact determined in calendric aging test at high cell voltages do not match the aging behavior of short-circuited cells at elevated temperatures. The short-circuit does not lead to almost infinite lifetime as formula (7.2) predicts. Hence, low cell voltage cannot compensate the high temperature impact. Therefore, as a second approach, the impact of cell voltage is completely neglected which means  $b_{\rm V\_cyc}$  in formula (7.6) is set to 1.

The resulting calendric aging predictions are shown in Figure 7.25. These results are very different to the previous ones. Now the predicted resistive calendric aging matches quite well the measured resistance characteristics during cyclic tests whereas the capacitive aging is even overestimated.

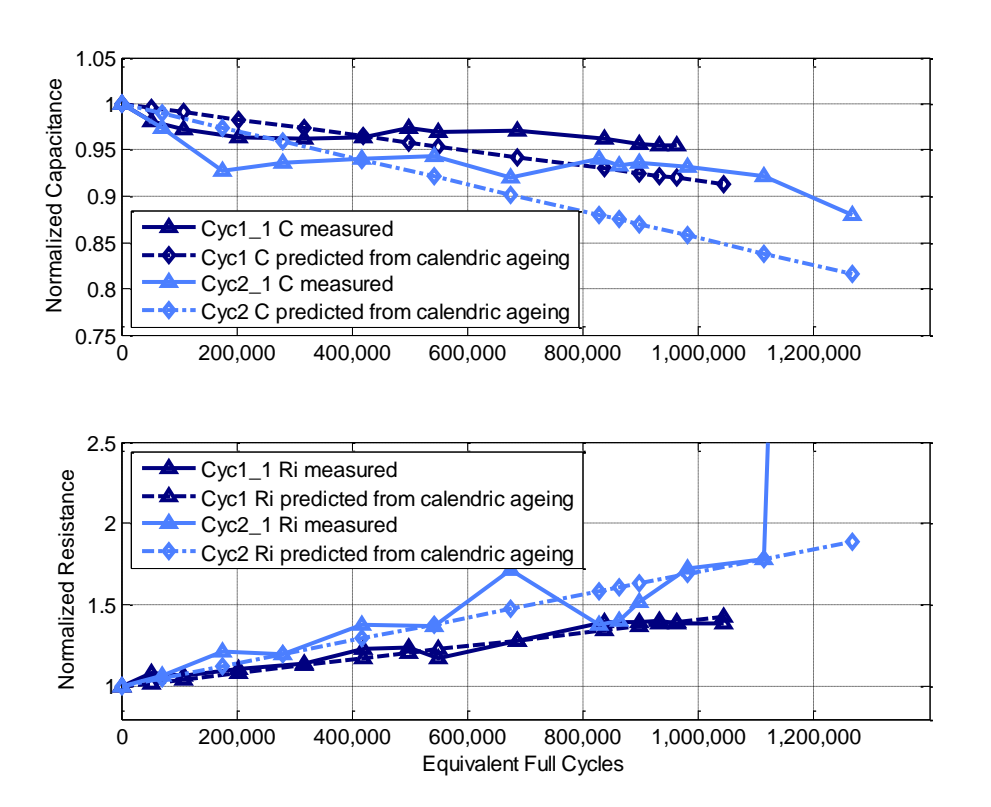


Figure 7.25: Comparison of measured cyclic aging and calculated calendric aging with  $b_{\rm V~cyc}=1.$ 

Hence, with the assumption of neglected voltage impact on calendric aging one may conclude that cyclic operation has no impact on capacitance and resistance characteristics over lifetime. Only the higher cell temperatures caused by the generated heat due to the current flow lead to accelerated aging. Stresses due to charging and discharging would not lead to a continuous capacitance decrease and resistance increase but could be the reason for sudden death at the end of cell life. This effect was observed at multiple cells aged in cyclic aging tests but at none aged in calendric aging tests. However, to analyze these phenomena in more detail further research effort is necessary.

# 7.3 Post Mortem Analysis

Selected EDLCs, aged in calendric aging tests and presented in the previous chapter, were further investigated by post mortem analysis. Therefore, cells were opened and samples from negative and positive electrodes were taken for further analysis.

This chapter presents the post mortem analysis results regarding changes in material composition and electrode's structure of both electrodes by means of microscopy, porosimetry and impedance measurements on coin cells constructed from electrode material. All results are compared to reference material received from a new EDLC of the same type.

The goal of post mortem analysis is to achieve a deeper understanding of the aging processes at each electrode and to detect potential causes for resistance increase and capacity fade that were observed in the accelerated aging tests presented in the previous chapter.

Post mortem analysis was only carried out for some devices of EDLC Type B and C.

## 7.3.1 EDLCs with Cellulose-Based Separator

Firstly, EDLCs of Type B were investigated. These devices use a standard cellulose-based separator. Since cyclic aging investigations were carried out only for this cell type the main goal was to focus exclusively on post mortem analysis of this type.

A new cell of Type B was opened and analyzed as reference. The characteristics of this cell are stated in Table 7.10.

	Rated work- ing voltage	Capacitance	Resistance
new cell Type B	2.5 V	705 F	0,34 mΩ

Table 7.10: Characteristics of new reference cell Type B

Cells are labeled in the following way:

EDLC type \_ temperature \_ voltage

Table 7.11 shows the opened cells of Type B and their properties before post mortem analysis.

	Storage temperature	Storage voltage	Remaining capacitance	Resistance increase <sup>19</sup>	Weight loss <sup>20</sup>
B_45C_2.8V	45 °C	2.8 V	84.5%	18.0%	1.7%
B_65C_2.3V	65 °C	2.3 V	60.9%	194.9%	10.9%
B_65C_2.5V	65 °C	2.5 V	14.3%	201.7%	4.5%

Table 7.11: Conditions of type B cells before post mortem analysis

\_

<sup>&</sup>lt;sup>19</sup> AC resistance measured at 1000 Hz

<sup>&</sup>lt;sup>20</sup> Cell weight without connectors before post mortem analysis compared to initial weight without connectors before aging tests

## 7.3.1.1 Cell Opening

Discharged EDLC cells were opened in a glove box under Argon atmosphere. The cap of the aluminum case was cut-off by using a pipe cutter. Since the EDLC jellyroll has a smaller diameter than the case it can be easily removed from the case.

The jellyroll was covered by a plastic foil which was removed. Afterwards electrodes and separators were wound off as far as possible.

Changes in the electrolyte composition by chromatographic measurements could not be analyzed. Even new cells had only a very small amount of electrolyte. The separator was soaked in electrolyte, and no further excess electrolyte was in the cell. This minimizes the production costs. Aged EDLCs of Type B were almost completely dried out instead and no electrolyte analysis could be undertaken.





Figure 7.26: Opened cell case with jellyroll inside (left) and wound off electrodes and separator (right) of a new cell of Type B

Carbon electrodes of a new cell have perfectly smooth surfaces, no adhesion problems, and no differences between positive and negative electrode were visible by eye. The paper separator is white on both sides and stays flexible after drying out, see Figure 7.26.

Electrodes and separator of aged cells have instead very different characteristics. Figure 7.27 shows exemplarily positive and negative electrode of cell B\_65C\_2.5V. The remaining capacitance of this sample at the end of the test was about 15% of the initial capacitance.

There is an adhesive bonding between the positive electrode and the separator, see the left picture of Figure 7.27. Especially in case of strongly aged cells, the separator could not be removed from the electrode, even not by soaking the electrode-separator compound for 24 h in acetonitrile. For some cells, the separator could at least partly be removed. The formerly white separator became brownish, especially at the side facing the positive electrode. Furthermore, it became very brittle after drying out, and the positive electrode is not flexible any more but very stiff.





Figure 7.27: Positive electrode (left) and negative electrode (right) of a severely aged EDLC with cellulose-based separator

In contrast to the positive electrode, the negative electrode could be easily separated from the paper separator, but therefore activated carbon did not adhere to the current collector any more. As can be seen from the right picture in Figure 7.27, almost no active material stayed on the current collector in worst case.

## 7.3.1.2 Laser Microscopy

As shown in the previous chapter, most cells did not deliver useable material for further analysis. Only a few probes, especially very few probes from positive electrodes, could be investigated. For further optical analysis probes of electrodes were investigated by means of a VK 9700 laser scanning microscope by Keyence. The laser microscope is a light microscope. While measuring, a focused laser beam scans the device under test.

Figure 7.28 shows laser microscope images of positive and negative electrode of cell B\_45C\_2.8V. On the positive electrode's surface, some fibers can be observed whose origin is most probably the paper separator, whereas the negative electrode shows a deep crack and no fibers. The crack might be developed during winding off.

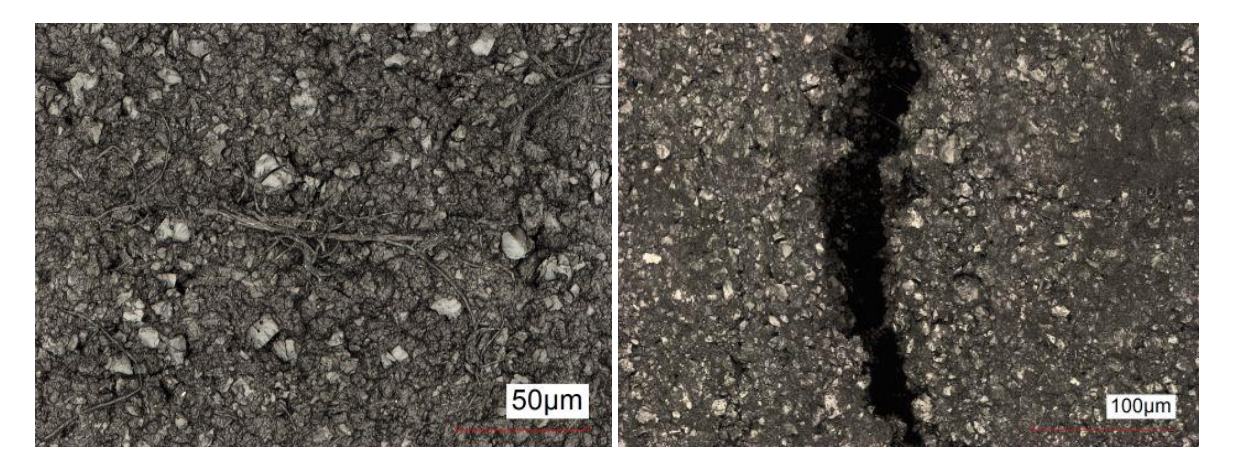


Figure 7.28: Laser microscope images of positive electrode (left) and negative electrode (right) of an aged cell (B\_45C\_2.8V)

## 7.3.2 Porosimetry

In literature researchers explain the capacitance loss of EDLCs during aging by pore blocking. This happens due to the deposition of chemical reaction products on the electrode surface [61,115]. Therefore, porosimetry should be a valuable method for aging investigations. With a mercury porosimeter it is possible to detect pores down to approximately 3 nm diameter. Since in EDLCs pore sizes in the sub-nanometer region contribute to the capacitance [87], this resolution is not high enough to detect all changes in the pore size distribution.

Smaller pores can be filled by using a gas as adsorptive medium. Three electrode samples have been analyzed with a 3Flex from Micromeritics. Their test benches use adsorption of gaseous Nitrogen. Brunauer, Emmett and Teller developed a calculation model of the specific surface of a device by means of gas adsorption measurements [138]. Commonly, gas adsorption measurements are called BET measurements related to their names. To achieve the mesoporous pore size distribution from experimental data, Barret-Joyner-Halenda (BJH) analysis can be used [139]. Therefore, all pores are initially filled with gas, typically nitrogen, and then step-wise emptied via the reduction of the pressure  $p/p_0$ . However, this method is only stable down to a mesoporous pore size range. For the analysis of smaller micropores other methods like the non-local density functional theory (NLDFT) has to be used [140]. Figure 7.29 shows the pore size distribution resulting from gas adsorption measurements.

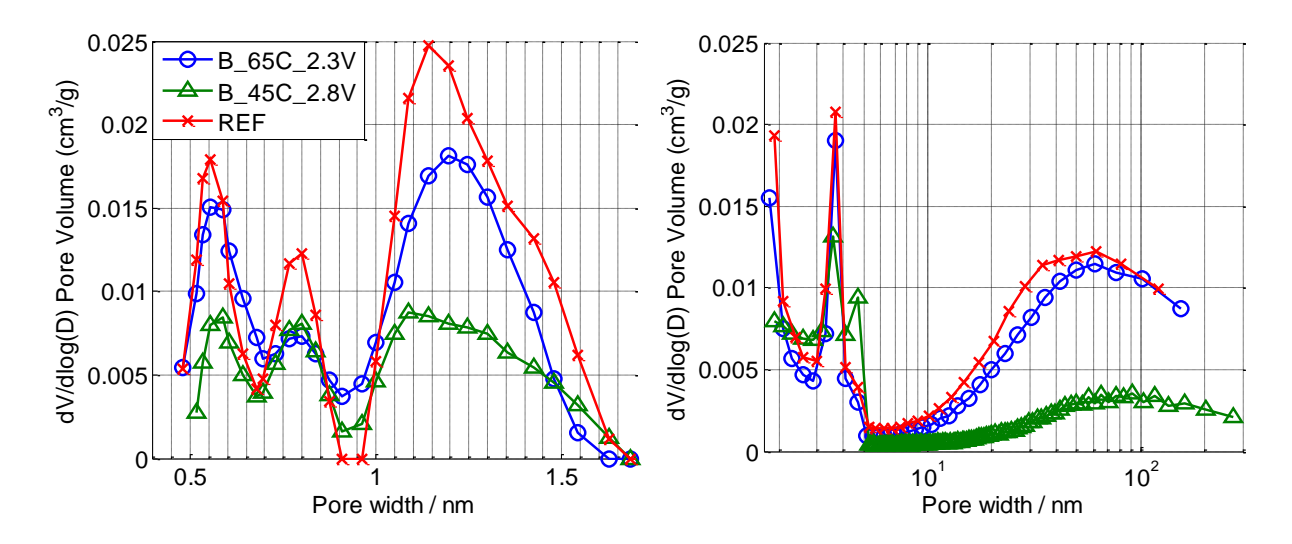


Figure 7.29: Pore size distribution of aged positive electrodes with cellulose-based separator

It can be seen from Figure 7.29 that the anode material from cell B\_65C\_2.3V did not lose pore volume in pore sizes > 1.5 nm and shows only slight pore volume decrease at smaller pore sizes compared to reference material. This result show, that 40% capacitance loss of this cell and the very high resistance increase, are not caused by structural changes in the electrode but very probably are caused by drying out. In contrast, cell B\_45C\_2.8V lost a significant amount of pore volume, in the mesopore range as well as in the micopore range.

Unlike to the observation of Bittner et al., who observed a slight decrease of pore volume with the pore size in the range of 0.5 to 0.79 nm for the negative electrode and a significantly higher pore volume decrease at the positive electrode in the pore range of 1.26 to 3.2 nm [61], no clear tendency to a pore volume loss at a certain pore size can be seen. In case of the investigated electrodes, the pore volume loss is distributed over the entire pore size distribution. Most probably pore volume decrease depends strongly on electrode material and electrolyte, respectively on decomposition products of these.

## 7.3.3 EDLCs with Polypropylene Membrane Separator

The post mortem analysis of cell type B with cellulose-based separator were not satisfying because no electrode material could be obtained for further analysis in many cases. The positive electrode material stuck to the separator and in case of negative electrodes carbon material lost adhesion to the aluminum current collector. Therefore, additional post mortem analysis of Type C cells using a propylene membrane as separator was carried out. The difference between Type B and C is, beside the separator, also the used electrolyte, compare Table 7.2. However, they are of the same size and use the same carbon electrodes.

Table 7.12 shows the storage test conditions as well as the current resistance, capacitance and weight loss of the selected type C cells before post mortem analysis.

	Storage tempera- ture	Storage voltage	Remaining capaci-tance	Resistance increase factor <sup>21</sup>	Weight loss <sup>22</sup>	Duration storage test
C_55C_3.0V	55 °C	3 V	6.72%	33.1- <sup>23</sup>	4.7%	48 weeks
C_55C_2.9V	55 °C	2.9 V	32.64%	17.5	3.1%	67 weeks
C_55C_2.7V	55 °C	2.7 V	38.04%	2.6	7.0%	67 weeks

Table 7.12: Conditions of type C cells before post mortem analysis

### 7.3.3.1 Cell Opening and Optical Inspection

According to the procedure described in chapter 7.3.1.1, Type C cells were opened with a pipe cutter under Argon atmosphere. Fortunately, even electrodes of severely aged cells

<sup>&</sup>lt;sup>21</sup> AC resistance measured at 1000 Hz

<sup>&</sup>lt;sup>22</sup> Cell weight without connectors before post mortem analysis compared to initial weight without connectors before aging tests

<sup>&</sup>lt;sup>23</sup> Resistance measurement before post mortem analysis failed because the cell resistance was too high.

could be wound off. The positive electrode stuck to the separator as well, but it could be pulled off quite easily. Comparable to the negative electrode of Type B cell, the negative electrode of Type C cell lost also some carbon material but the material loss is much less than for Type B cell.



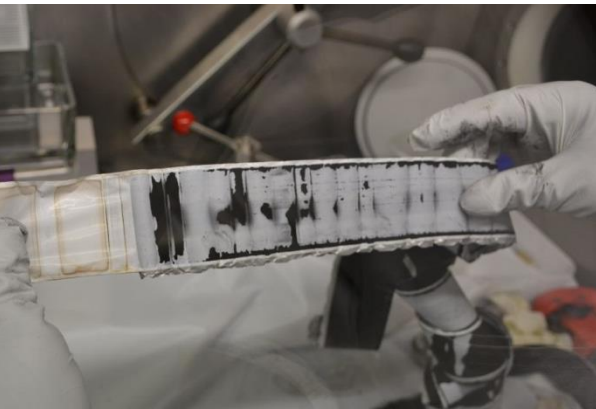


Figure 7.30: Positive electrode and the according separator side (left) and polypropylene membrane separator facing the negative electrode (right) of a severely aged EDLC

Figure 7.30 shows the jellyroll (left) with the positive electrode on top and the separator side that was facing the negative electrode (right) of cell C\_55C\_3V. The separator side that was in contact with the positive electrode shows light to dark brownish discoloration whereas the contact side with the negative electrode is still white. However, as can be seen from the right picture, due to adhesion loss some carbon material stayed on the separator when the negative electrode was pulled off.

The new reference cell contained some access electrolyte, but a very small amount of electrolyte remained in aged cells and evaporated immediately. Thus, no electrolyte analysis could have been undertaken. Therefore, post mortem analysis focused on the electrodes.

While new positive and negative electrodes showed no difference in optical inspection, electrodes of aged cells showed in contrast a significant difference in positive and negative electrode. The negative electrode showed severe adhesion loss of the active carbon material. It is evident that residues formed on the positive electrode which was on the one hand visible by eye and on the other hand the handling of the cell implied the occurrence of surface tensions.

## 7.3.3.2 Weight Analysis of all Cell Parts

For the detection of possible weight changes, all cell parts were weighted immediately after cell opening. Table 7.13 shows the results of three aged Type C cells compared to a new ref-

erence cell<sup>24</sup>. Deviations between the measured entire cell mass and the sum of case and jellyroll mass can be explained by evaporation of electrolyte. Although the cell parts were weighted immediately after cell opening, some electrolyte evaporation could not be avoided since acetonitrile is very volatile. After the entire jellyroll was weighted, it was wound off and afterwards the single electrodes were weighted. During the winding off process the electrolyte in the electrodes evaporated. Therefore, the presented mass data are masses of dried electrodes. Differences in jellyroll mass and the summarized mass of both electrodes are not only due to electrolyte and separator but also due to the winding spindle. The winding spindle has a mass of about 10 g.

Furthermore, the presented mass values for negative and positive electrode refer to the aluminum current collector coated on both sides with activated carbon. Due to the jellyroll structure both electrodes are not exactly of the same length. The inner laying positive electrode is with *I*=232.5 cm slightly shorter than the negative electrode (*I*=237.5 cm).

	Weight cell	Weight case	Weight jellyroll	Weight neg. electrode	Weight pos. elec- trode
New cell	163.8 g	66.4 g	90.7 g	32.3 g	32.1 g
C_55C_3.0V	159.7 g	67.8 g	91.6 g	32.3 g	39.4 g
C_55C_2.9V	161.6 g	66.4 g	92.4 g	29.7 g	41.9 g
C_55C_2.7V	155.2 g	67.5 g	87.5 g	31.5 g	36.2 g <sup>25</sup>

Table 7.13: Mass values of cell parts

Weight measurements in Table 7.13 show that the weight of the positive electrode increases significantly during aging. Aged positive electrodes were up to 30% heavier than a new positive electrode. Furthermore, even by optical inspection differences in the aged positive electrode surface could be observed. The electrode is stiffer and seems to be thicker as it would have a deposit layer on the surface.

The weight loss of some aged negative electrodes, especially of cell C\_55C\_2.9V, compared to the new electrode can probably be explained by adhesion problems of the activated car-

<sup>&</sup>lt;sup>24</sup> The reference cell underwent only one charge/discharge cycle for capacitance determination and one impedance measurement after receiving it from manufacturer. Afterwards these tests the reference cell was opened immediately.

<sup>&</sup>lt;sup>25</sup> Since the electrode was broken during post mortem analysis the electrode mass value was extrapolated.

bon material. During the winding off procedure some carbon material got lost and therefore the electrode became lighter.

#### 7.3.3.3 Laser Microscopy

For further optical analysis of EDLC, electrodes were investigated by a laser microscope. The used test set up was a Keyence laser microscope at the ISEA lab. By means of laser microscopic pictures the electrodes' surface with a resolution in  $\mu$ m-range could be investigated. Thus, it is not possible to see the detailed pore structure, but the possible layer on the positive electrode that was observed after cell opening can be analyzed.

Although, the connection between the aged positive electrode and the polypropylene membrane separator is not as strong as the connection between electrode and paper separator, electrode and separators stuck together in case of Type C, too. In most cases the separator can be pulled off quite easily, but sometime some carbon material stays on the separator surface as shown in Figure 7.33.

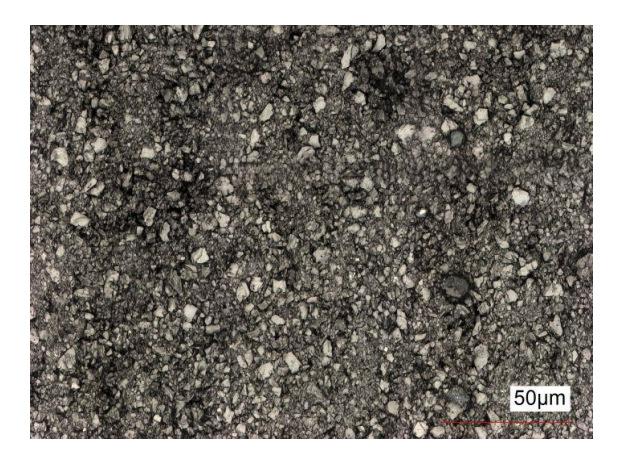
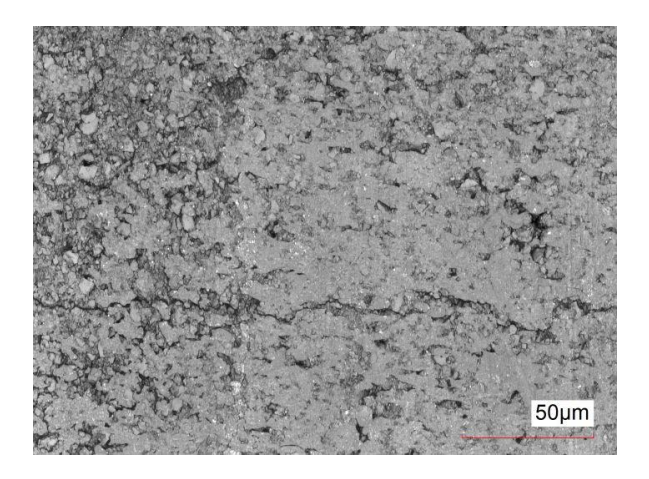




Figure 7.31: Laser microscope pictures of new positive electrode (left) and new negative electrode (right)



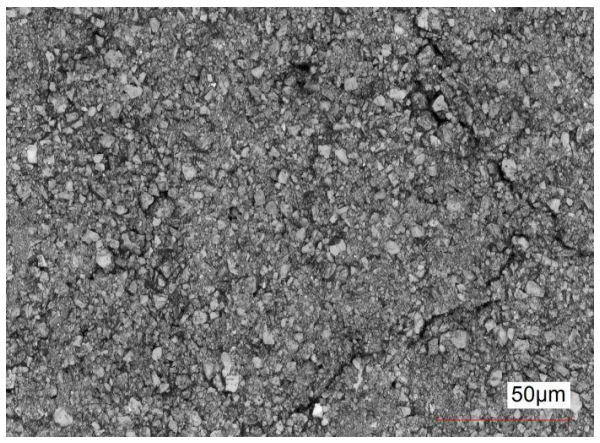
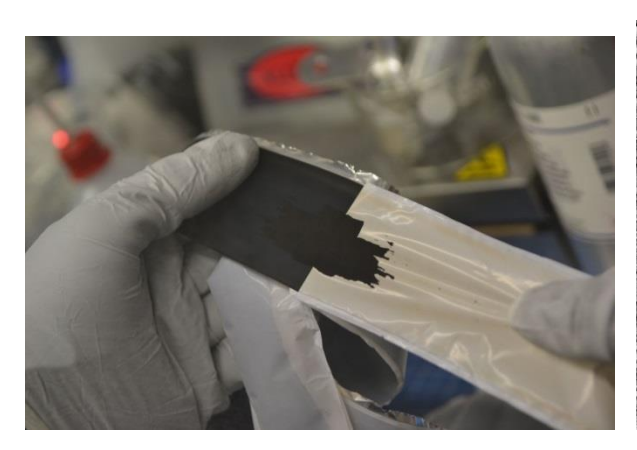


Figure 7.32: Laser microscope pictures of aged positive electrode (left) and aged negative electrode (right) (exemplarily of cell C\_55C\_2.7V)

From Figure 7.32 it becomes clear, that the aged positive electrode has a less porous surface compared to new activated carbon electrodes, and it seems to be covered by a layer, whereas the negative electrode contains large cracks but shows no obvious changes in pore structure.



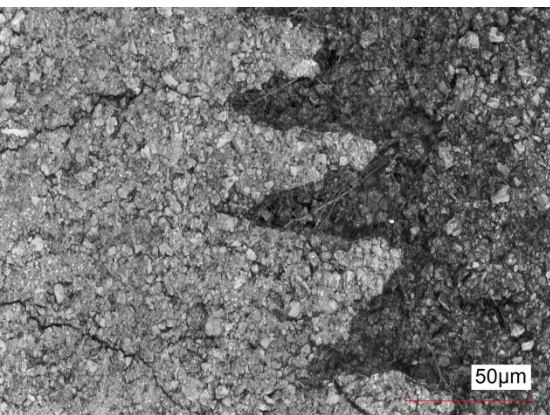


Figure 7.33: Some carbon material from positive electrode stays on separator during pulling off

As already mentioned, some carbon material was torn away by separating the positive electrode and the PP-membrane. This transition is shown in Figure 7.33 and suggests a superficial residue formation.

#### 7.3.3.4 Scanning Electron Microscopy (SEM)

Scanning electron microscopy (SEM) was undertaken for one negative and one positive electrode of a new cell as well as for both electrodes of an aged cell for comparison. Measurements were carried out at Gemeinschaftslabor für Elektronenmikroskopie, GFE; RWTH Aachen University.

The working principle of a SEM is as follows: SEM images of a sample are produced by scanning it with a focused beam of electrons. The electrons interact with the atoms in the sample and produce signals that can be detected. These signals contain information about the sample's surface topology and composition. The achievable resolution of SEM is better than 1 nm.

SEM pictures were taken from cross sections of the EDLC samples. Additionally, energy dispersive X-ray spectroscopy (EDX) for qualitative elemental analysis of the electrodes was carried out.

Height	neg. electrode new	pos. electrode new	neg. electrode aged	pos. electrode aged
Overall	225 μm	220 μm	174 μm	278 μm
Al current collector	28 μm	30 μm	25 μm	30.53 μm
C top <sup>26</sup>	92 μm	71 μm	38.63 μm	117 μm
C bottom <sup>27</sup>	104 μm	117 μm	109.75 μm	131.3 μm

Table 7.14: Thicknesses of different electrode layers (derived from SEM pictures)

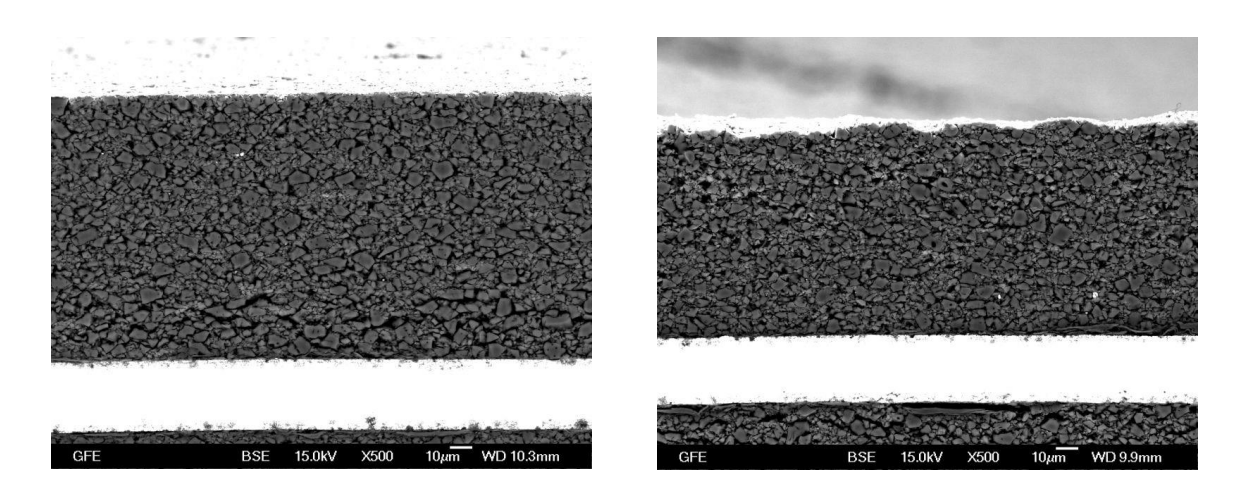


Figure 7.34: SEM pictures of cross sections through new electrodes (left: positive electrode, right: negative electrode<sup>28</sup>)

Figure 7.34 shows cross section SEM pictures of new positive and negative reference electrode. Both electrodes offer a similar pore structure with carbon particles of varied sizes. No obvious cracks, neither on electrode surface nor through the cross section, can be observed. Furthermore, the pore structure is homogeneous through the entire cross section.

Surprisingly, carbon coatings of both sides of the aluminum current collector do not have the same thickness. The reason why the coatings on both sides of the current collector have different thickness is not clear, maybe it is due to the manufacturing process. Differences in changing the coating thicknesses between negative and positive electrode are reported in literature. Since negative and positive ions are of different sizes, different advantages in

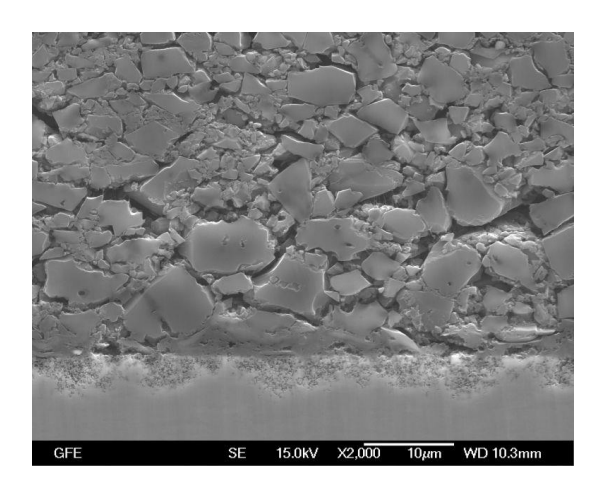
<sup>&</sup>lt;sup>26</sup> Thickness of active material on top side of Al current collector

<sup>&</sup>lt;sup>27</sup> Thickness of active material on bottom side of Al current collector

<sup>&</sup>lt;sup>28</sup> The smaller height of the activated carbon layer on top of the aluminum current collector of the negative electrode compared to the positive electrode can be explained by the differences in thickness of both carbon layers.

coating thicknesses are reported in literature [141,142]. In discharged state both electrodes are at the same potential but during charging only the overall potential is controlled and is limited by the degradation potentials of the single electrodes. If the degradation potential of one electrode is reached, the other electrodes might be far away from its degradation potential. By different electrode masses the whole potential window can be used. Cericola et al. investigated differences in mass ratio and found out that a mass ratio of 0.65 (positive electrode mass / total electrode mass) is optimal regarding aging for an EDLC using acetonitile based electrolyte [143]. But this cannot be the reason here because there are practically no differences in thickness between both electrodes.

Within carbon particles thin fibers can be seen on both electrodes. These fibers should be the binder of the activated carbon electrode, probably PTFE. Furthermore, the carbon-aluminum interface of both electrodes shows that the aluminum surface is slightly affected and has therefore a very rough surface. In some exceptional cases the contact between carbon and aluminum of the negative electrode is even interrupted over a distance of some  $\mu$ m, see Figure 7.35.



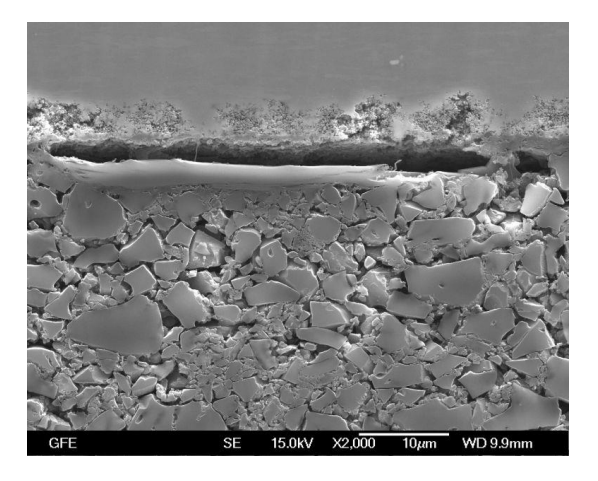
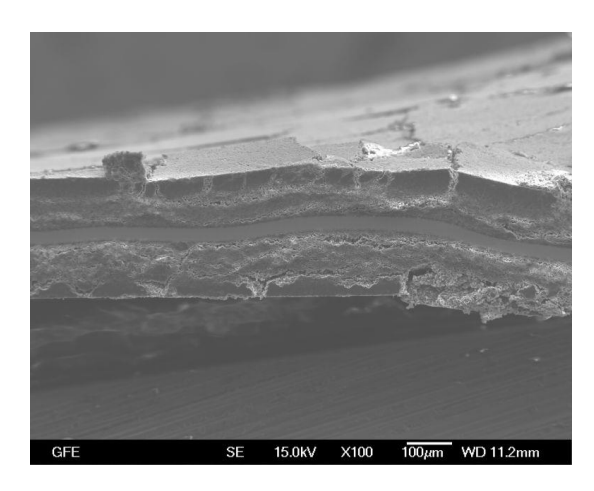


Figure 7.35: Carbon-aluminum interface (left: positive electrode top and aluminum down, right: aluminum top and negative electrode down)

As expected, new electrodes show no significant differences in carbon structure. But that is not the case for aged electrodes. Laser microscopic analysis has already shown differences in aged negative and positive electrodes. SEM pictures in Figure 7.36 show remarkable differences between both electrodes. The negative electrode has still a quite smooth surface but suffers from adhesion loss between active material and current collector. This results in exfoliation of activated carbon and in decreased electrode thickness when the electrode was wound off. Whereas the height of the positive electrode increased significantly, compare Table 7.14, which matches the measured mass increase of the positive electrode after cell opening. Furthermore, the positive electrode surface is crisscrossed by cracks, some even down to the current collector. Certainly, some cracks might also originate from the cell

opening and winding off but the major origin must be the aging process, which explains the bad electrical performance of the considered cell. However, no obvious surface layer on top of the positive electrode can be observed. The structural changed go through the entire cross section.



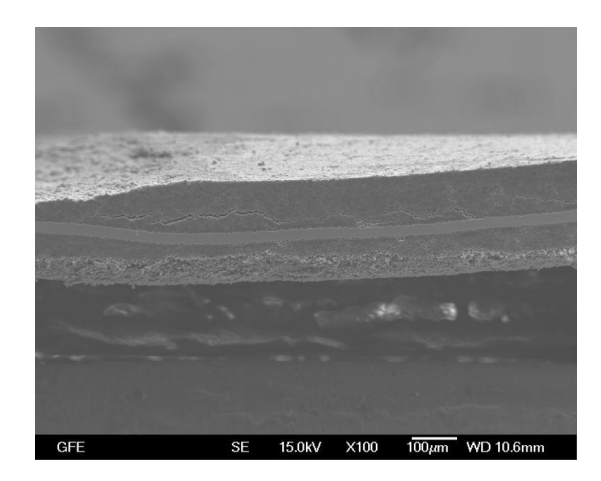
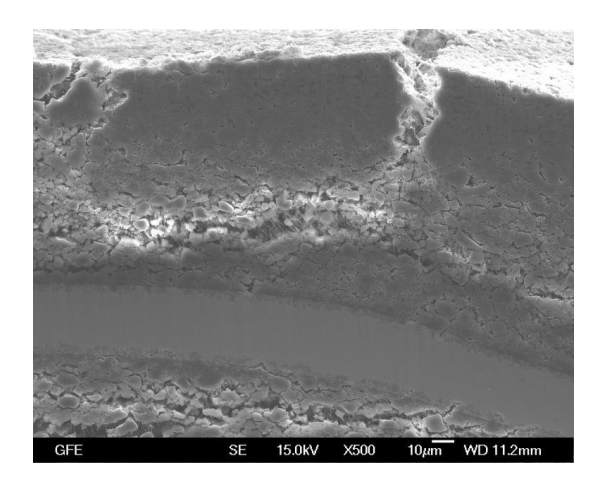


Figure 7.36: SEM pictures of cross sections through aged electrodes (left: positive electrode, right: negative electrode)

Figure 7.37 gives a closer look on the crack in the positive electrode. Within the crack numerous fibers are visible. Such fibers have already been observed between carbon particles of new electrodes, but the number of fibers seems to be much higher in case of the aged positive electrode. Since the positive electrode accelerated in mass and thickness during aging, these additional fibers could be due to reaction products resulting from chemical reactions during aging. Furthermore, the porosity of activated carbon seems to decrease in direction to the electrode surface, which fits to the theory of pore blocking at the electrodes surface.

In contrast to activated carbon the aluminum current collector does not undergo significant changes during aging. The slight affecting of aluminum surface was observed at the new electrode as well, see Figure 7.35.

As shown before, cracks in the positive electrode proceed vertically as well as horizontally and are furthermore connected by fibers. These cracks insulate the carbon material from the current collector and lead to capacity fade.



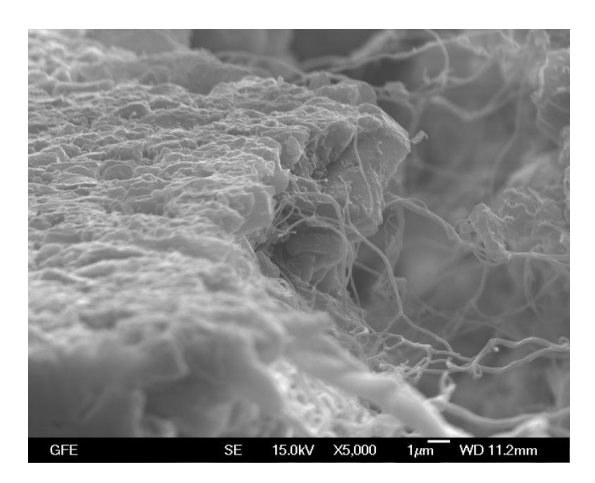
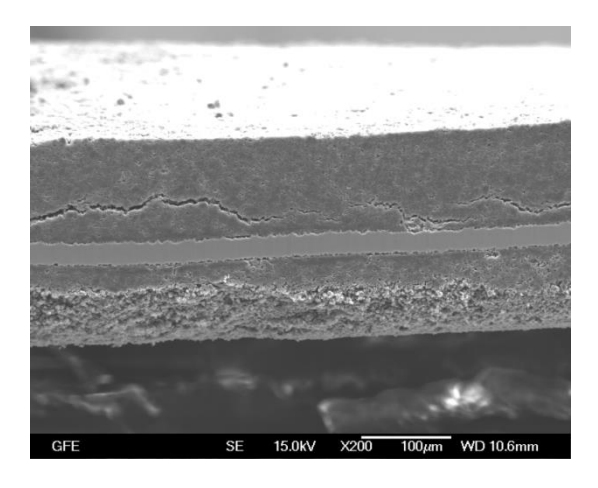


Figure 7.37: Cracks in activated carbon of aged positive electrodes filled with fibers (left) and a zoom in one of these cracks (right)

Cracks can be observed in negative electrodes as well, but in contrast to positive electrodes, these cracks are all more or less horizontal. Furthermore, as shown in Figure 7.38 (right), these cracks are not connected by fibers. Since the observed fibers in the new electrodes were assigned to the binder, a probable reason for exfoliation can be the loss of binder. Furthermore, the aluminum surface of the current collector is much more affected compared to new electrodes. Due to the high roughness, contact between carbon and aluminum is not provided over the whole electrode length. This contact loss, the cracks in the material and possible exfoliation lead also to insulation of the active material and therefore capacitance loss. Remarkable is further that the thickness of the aluminum layer decreases by approximately  $5~\mu m$  during aging, compare Table 7.14.



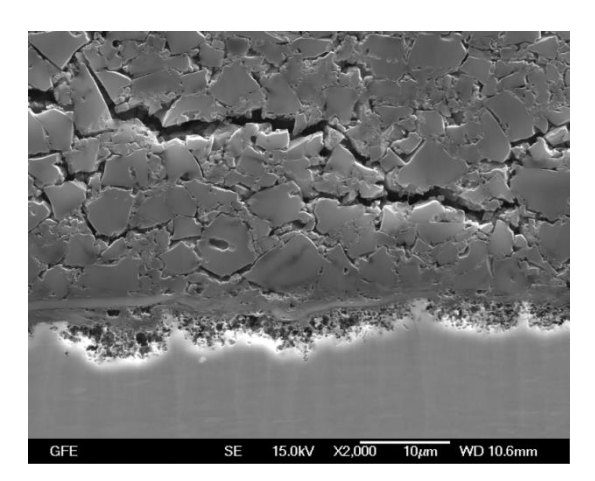


Figure 7.38: Aged negative electrode with cracks in the carbon and affected current collector

EDX measurements show a quite pure composition of the single electrode layers in case of both the new and the aged negative electrode. Most notably, the fluorine amount of the aged positive electrode is by a factor of 10 higher than the fluorine amount of the aged neg-

ative electrode. Possible sources of fluorine are the electrolyte salt and the binder of the negative electrode. Since the negative electrode obviously lost binder during the aging process it seems to be likely that fluorine diffused in direction to the positive electrode and reacted there.

Within cracks in the aged positive electrodes carbon also Flour and aluminum were detected beside carbon by EDX. Thus, aluminum seems to diffuse as well.

#### 7.3.4 Coin Cells

To analyze the differences in the aging behavior of positive and negative electrodes on the EDLC's impedance, coin cells were prepared from the electrode probes received from cell opening. The target was the analysis of different capacitance decrease of both electrodes and the different contributions to the impedance behavior.

#### 7.3.4.1 Coin Cell Construction

Coin cells of size CR2025 were built by using electrode probes of aged cells. A coin cell case kit from MTI was taken for cell construction. Electrode samples were used untreated. Thus, they were not washed or dried before cell construction to avoid removing of any aging products.

Therefore, electrode discs with a diameter of 16 mm and separator discs with 20 mm diameter were cut out. Separator material of a new reference Type C cell was used as well as new Type C electrolyte. Electrolyte could be taken from new Type C cells because this cell type was a prototype and possess a significant amount of excess electrolyte<sup>29</sup>. Hence, the observed changes in impedance behavior are only due to aging of the electrodes.

During the entire construction process all materials and cell parts were kept under argon atmosphere to avoid any air contact.

Several types of cells were built. Cells with only one aged electrode, positive or negative, were compared to a reference cell with new material for both electrodes and to a cell with two aged electrodes. Additionally, symmetrical cells with two positive electrodes or two negative electrodes were built. Therefore, the influence of aged negative respectively positive electrode on the behavior of the entire aged cell was analyzed.

#### 7.3.4.2 Cells with Both-Sided Coated Electrode

The first coin cells were constructed with both-sided coated electrodes as they are used in commercial cells. For the dynamic behavior analysis of the different coin cells impedance

\_

<sup>&</sup>lt;sup>29</sup> Unfortunately, there was no excess electrolyte any more in case of aged cell of type C.

spectroscopy measurements has been carried out by using a Zahner Zennium. All measurements were done in the potentiostatic mode with excitation amplitude of 5 mV in a frequency range of 3 MHz to 10 mHz.

Figure 7.39 shows the results of four coin cells constructed from the same material in the same way. Electrode discs from a new reference cell of Type C were utilized. Every cell consists of a positive electrode disc and a negative electrode disc. To simplify the cell labelling, the following scheme is used: e.g. Ref\_AC1 stands for new reference material (Ref) with one positive electrode disc (A) and one negative electrode disc (C) and cell number 1 of this type. For simplification A for positive electrode is taken from anode and C for negative electrode from cathode respectively.

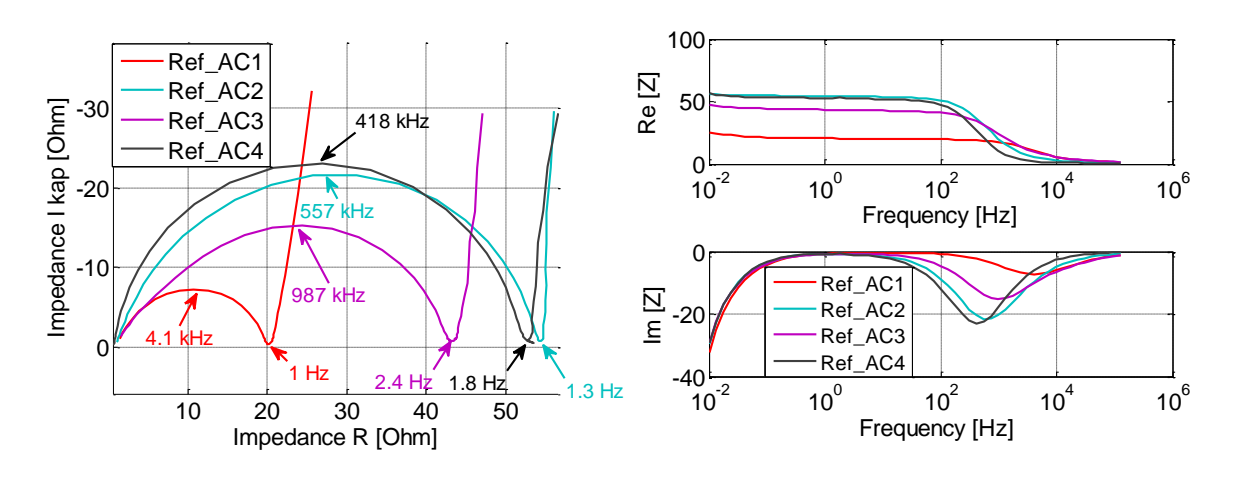


Figure 7.39: Nyquist plot (left) and real and imaginary part of impedance over frequency (right) of coin cells with double sided electrodes

The results of all impedance measurements show a significant semi-circle in the Nyquist plot (Figure 7.39, left picture). Besides having a comparable ohmic resistance, the diameter of the semi-circle differs significantly although the same material is used. However, at lower frequencies all Nyquist plots show the typical EDLC behavior, a 45° arc and a more or less vertical line. These similarities are even more obvious in a plot of real and imaginary part of the impedance over frequency (Figure 7.39, right picture). At lower frequencies, real part behavior differs only by an offset and the imaginary parts matches very well. Thus, the regarded coin cells do not differ in capacitive behavior, but in the behavior at lower frequencies which results in the semi-circle of the Nyquist chart.

Many researchers have observed such semi-circles in Nyquist charts of EDLC lab cells. Yoo et al. assign this semi-circle to an interfacial impedance [144]. Pell et al. explain this impedance by ion transport processes caused by sub-optimal electrolyte concentrations [145]. Portet et al. showed that the contact resistance between the aluminum current collector and the porous carbon influences strongly the semi-circle [146]. Other approaches analyze the influence of the type of electrolyte [144], the influence of surface oxides [147] and the influence of different types of current collectors [148].

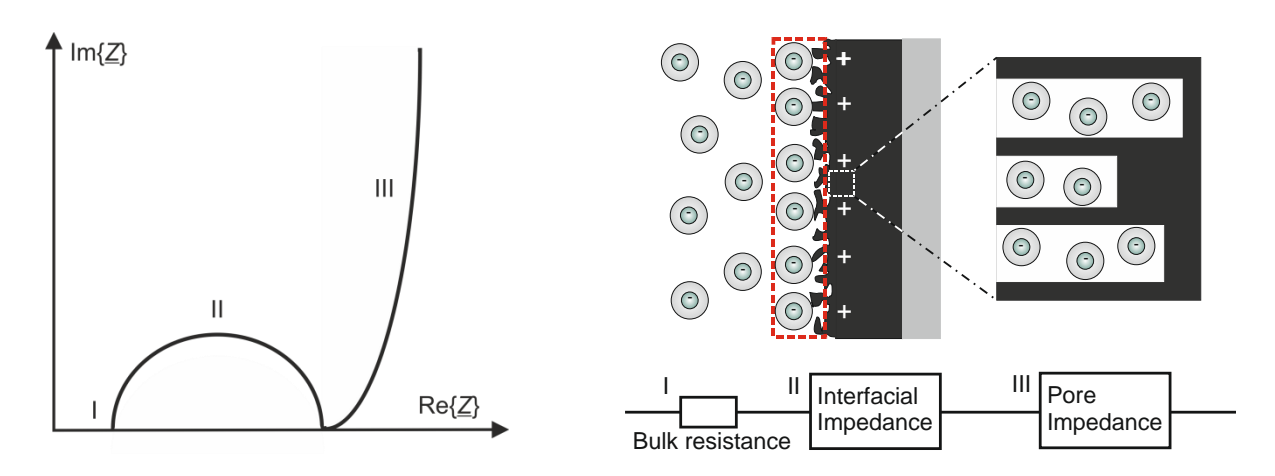


Figure 7.40: Impedance spectra of a porous carbon electrode based on [144]

However, Yoo et al. divided the EDLC Nyquist plot into three sections as shown in Figure 7.40. Section I is the intersection with the x-axis and corresponds to the bulk electrolyte resistance, section II is the semi-circle and corresponds to the interfacial impedance depending on the electrolyte-electrode interface, and section III corresponds to the pore impedance and shows the significant 45° arc up to an almost vertical line at low frequencies.

The experimental results in Figure 7.39 show that the variation in the impedance spectra of all coin cells is in the semi-circle of section II. The internal resistance and the low frequency part of the pore impedance are very similar for all cells. This result shows that the different shapes of Nyquist charts are not due to bad cell manufacturing, but due to differences in interfacial impedance. That means the contact resistance varies from cell to cell.

Figure 7.41 shows a schematic of the carbon electrode/coin cell interface. Since the electrode discs made from the commercial EDLC material are still coated on both sides with activated carbon material, the aluminum coin cell case has no direct contact with the current collector but with the porous carbon electrode. Additionally, not only the separator is soaked in electrolyte, but there is also some amount of access electrolyte in the cell. Therefore, also carbon pores on the electrode contact side with the coin cell case are probably filled with electrolyte. Thus, due to the porous structure of the electrode the coin cell case can have direct contact to carbon. But in case of a pore filled with electrolyte, charged ions will also accumulate at the case face, if a potential is applied, and lead to an electrochemical double layer. According to Figure 7.41 this effect results in a parallel connection of the carbon/case contact resistance and the double layer capacitance. Such a parallel connection of one resistor and one capacitor results in a semi-circle in the Nyquist plot.

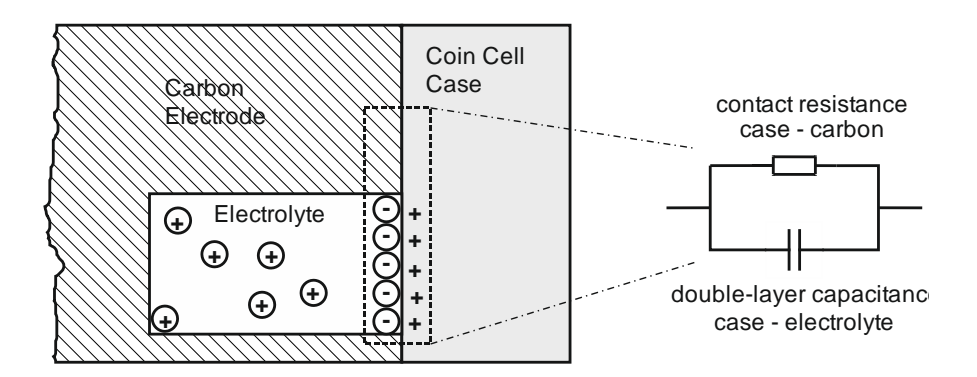


Figure 7.41: Explanation of the semi-circle in the Nyquist charts of coin cells with both-sided electrodes

To avoid these undesired semi-circles, electrode samples were prepared in a different way. Therefore, one side of the carbon layer of the electrodes was removed before disc cutting. This was done by using N-Methyl-2-pyrrolidon (NMP) from Merck Millipore since the binder, probably PTFE, was not water-soluble. For this procedure, some NMP was put on the upper electrode side and then the carbon layer was removed carefully by scraping the carbon layer off with a knife and wiping with a tissue. Attention had to be paid that no NMP was in contact with the other carbon side and that this carbon side was not damaged during the scraping procedure.

### 7.3.4.3 Nyquist Plots of Single-Sided Cells

New coin cells were constructed by using the electrode material with one removed carbon side. To analyze the single electrode's impact on the aging, again symmetrical cells with the same electrodes on both sides as well as full cells with negative and positive electrodes, also new against aged electrode, were constructed. The results were compared to a reference cell with new electrode material on both sides. Electrolyte and separator were again taken from a new cell. Hence, only the influence of aged carbon electrode is analyzed. The testing procedure was as follows: Coin cells were short-circuited for 30 min and then EISmeasurements were performed by using a Zahner Zennium in a frequency range of 3 MHz to 10 mHz.

Figure 7.42 shows a zoom of the measured Nyquist plots of coin cells made of electrode material from cell C\_55C\_2.9V. This cell had about 30% remaining capacitance and a 17.5 times higher resistance as can be seen from Table 7.12. The differences in Nyquist plot shapes between cells made from negative electrodes and positive electrodes are remarkable. The negative electrode cell CC shows a slightly higher semi-circle and the capacitive angle has decreased. In contrast, the positive electrode cell AA shows a significantly higher internal resistance and a large semi-circle. This impedance behavior is far away from the typical porous electrode. The previous porous structure must be more or less destroyed. This semi-circle indicates pore shapes with blocked pore opening according to Keiser [75] and/or

charge transfer reactions [149]. Furthermore, it can be concluded that the positive electrode dominates the impedance behavior of the entire cell.

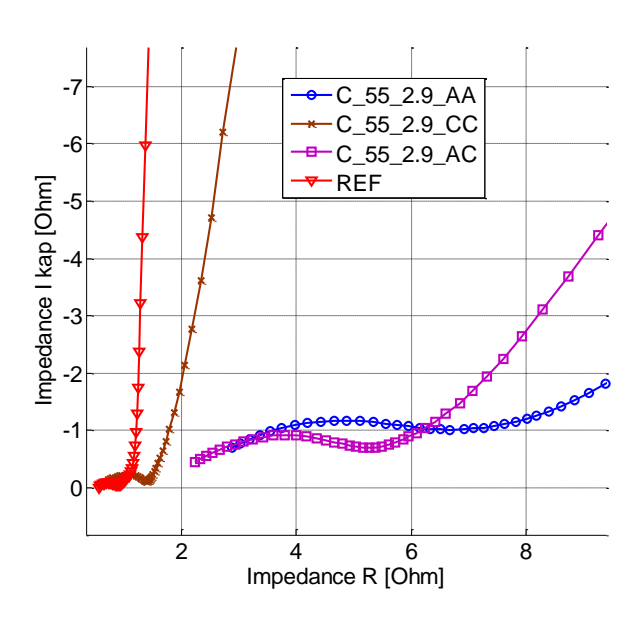


Figure 7.42: Nyquist plots of coin cells made from material of cell C 55C 2.9V

A similar behavior can be observed from the Nyquist plots of cell C\_55C\_3.0V, see Figure 7.43. This cell had only about 6% capacitance left and had such a high resistance that made it impossible to conduct an EIS measurement of the whole cell. The EIS measurements of the coin cells show in principle a comparable behavior. The resistances and the semi-circle diameter are larger, but again the negative electrode shows a higher internal resistance and a lager diffusion arc (right picture), whereas the positive electrode shows an extreme semi-circle (left picture).

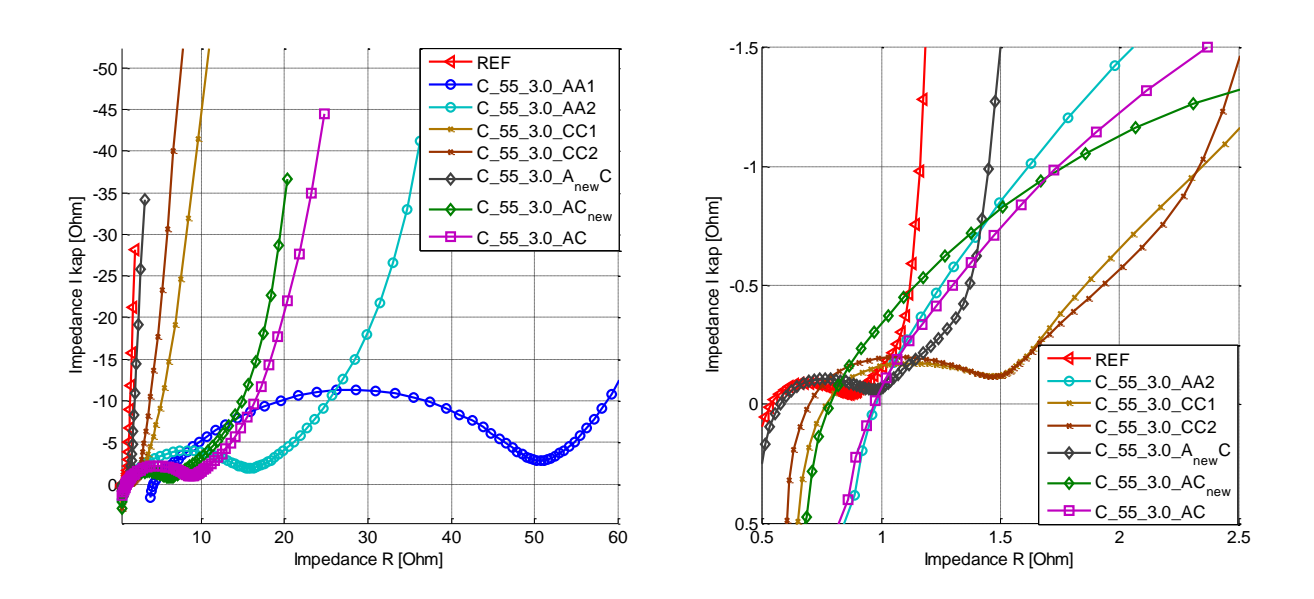


Figure 7.43: Nyquist plots of coin cells from cell C\_55C\_3.0V (left) and zoomed in (right)

The aged positive electrode dominated not only the whole-cell-behavior, but also the cell with one aged and one new electrode showed very different behavior if an aged positive electrode was used. The aged negative electrode in combination with the new electrode showed only a larger diffusion arc whereas the cell with aged positive electrode showed a large semi-circle.

## 7.3.4.4 Imaginary Capacitance

Additionally, beside the Nyquist plots also the imaginary capacitance according to chapter 3.1.2.2 was analyzed. Since the diffusion processes in the damaged aged electrode are probably very slow, the electrochemical impedance was measured in a frequency range from 3 MHz down to  $100 \, \mu$ Hz.

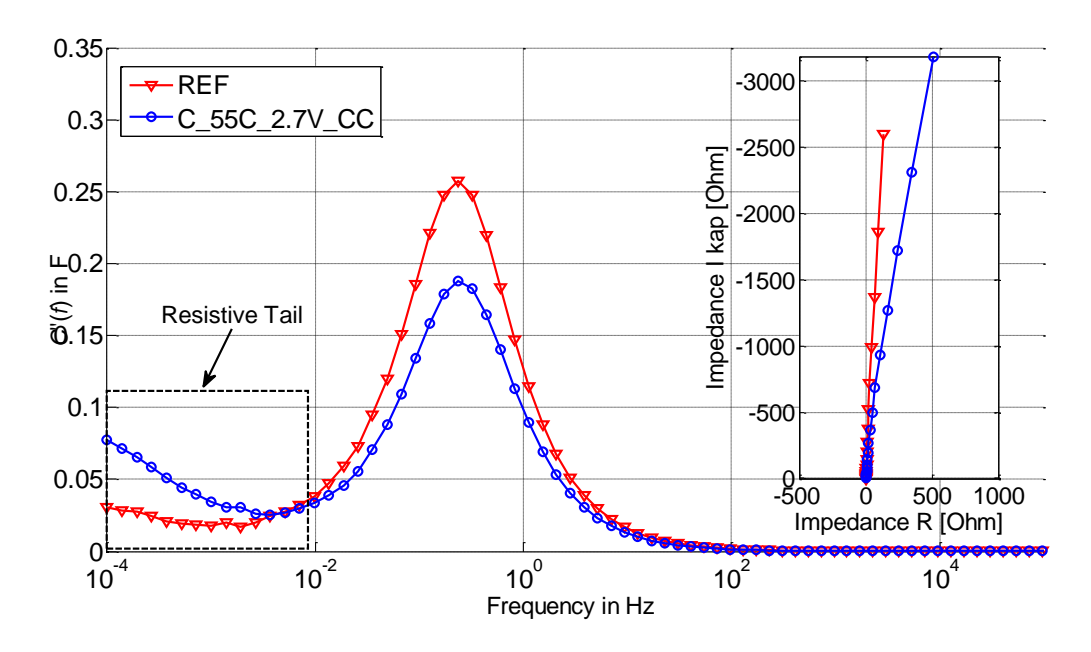


Figure 7.44: Imaginary Capacitances of a reference electrode and an aged negative electrode with a remarkable resistive tail and the belonging Nyquist plots (small figure)

Figure 7.44 shows the imaginary capacitance vs. the frequency in logarithmic scale of a new cell and an aged cell. The capacitance can be calculated from the imaginary capacitance according to equation (3.13) and the time constant according to equation (3.14) respectively.

Beside the capacitance peak another peak with smaller amplitude at low frequency can be observed, especially in case of the aged cell. This peak is called "resistive tail" in literature [79]. This behavior corresponds with the angle of the low-frequency part of the Nyquist plot. In case of an ideally polarized electrode the low-frequency region of the Nyquist plot is a vertical line. In reality, a deviation from the ideal 90° angle can be observed even for new electrodes as can be seen for the reference cell in Figure 7.44. This vertical line becomes inclined with an increased leakage current. Therefore, the extent of leakage current can be estimated from the degree of inclination.

However, not only the leakage current leads to a non-vertical line in the low-frequency part in the Nyquist plot of an EDLC. An inclination can also be observed for ideally polarized electrodes if they have non-uniform pore geometry. To distinguish between leakage current and non-uniform pore geometry as causes for the inclination of the low-frequency part, an impedance measurement should be made up to extremely low frequencies. The pore geometry would lead to a vertical line in the Nyquist plot whereas the leakage current results in a semi-circle [79].

In the measurement shown in Figure 7.44 the minimum frequency is 100  $\mu$ Hz and no conclusion can be given if the impedance spectrum ends in a vertical line or a semi-circle. However, a difference in pore size distribution would lead to a broader or smaller capacitance peak [79]. This cannot be observed in the measurements, and therefore an increase in leakage current extent is the most probable explanation for the inclination increase. Thus, it can be concluded that the aged negative electrode has a smaller capacitance than the reference cell, no change in time constant but a higher leakage current.

The capacitance C from the low frequency part of the impedance, when the EDLCs show capacitive behavior, can be calculated according to equation (7.7).

$$C = \frac{1}{2\pi f \cdot |Im\{Z\}|} \tag{7.7}$$

However, since the EDLC shows no ideal behavior, which means no vertical line but an angle less than 90° as observed in the Nyquist plot, the capacitance is not independent from frequency. Another method of capacitance calculation is the calculation by means of the imaginary capacitance as described in chapter 3.1.2.2. By means of this method the capacitance is calculated over the whole frequency range. Exemplarily, the capacitance values of a coin cell made from new reference electrodes calculated at different frequencies by means of equation (7.7) are shown in Table 7.15.

REF	10 mHz	1 mHz	100μHz	С
Capacitance	0.54 F	0.60 F	0.61 F	0.55 F

Table 7.15: Capacitance derived from imaginary part of the impedance at different frequencies according to equation (7.7) compared to the capacitance C calculated from the imaginary capacitance plot by means of equation (3.13)

Since the non-ideal behavior of an EDLC increases with aging, the capacitance of the investigated coin cells was determined by means of the imaginary capacitance

Figure 7.45 shows the peaks of the imaginary capacitance of coin cells made from material of cell C\_55C\_2.9V compared to the reference cell. Symmetrical cells with two aged positive respectively two aged negative electrodes were tested as well as one cell with two aged electrodes and one cell with aged positive electrode and new negative electrode. The peaks of the coin cells containing aged negative electrode material on one or even both sides are very small. This is caused by the loss of carbon material during the winding off procedure of the negative electrode. Especially cell C\_55C\_2.9V showed severe adhesion problems. Since significantly less material stayed on the current collector, the capacitance values of these coin cells were very small.

Nevertheless, significant differences in peaks shapes and positions can be observed. The peak of cell C\_55C\_2.9V\_AA is much broader and has a much lower peak frequency compared to reference. This effect is caused by a broader pore size distribution as described by Taberna et al. in [25]. Furthermore, the peak shift indicates a considerably higher time constant of aged positive electrodes. The Nyquist plot shows in addition an angle much less than 90° in the low frequency part which indicates higher leakage currents.

Beside small capacitance values, cell C\_55C\_2.9V\_CC and cell C\_55C\_2.9V\_A<sub>new</sub>C shows at least higher peak frequencies than the reference. This is probably caused by the lower electrode's thickness caused by the material loss. The aged full cell shows a small capacitance resulting from the negative electrode but a low peak frequency resulting from the positive electrode.

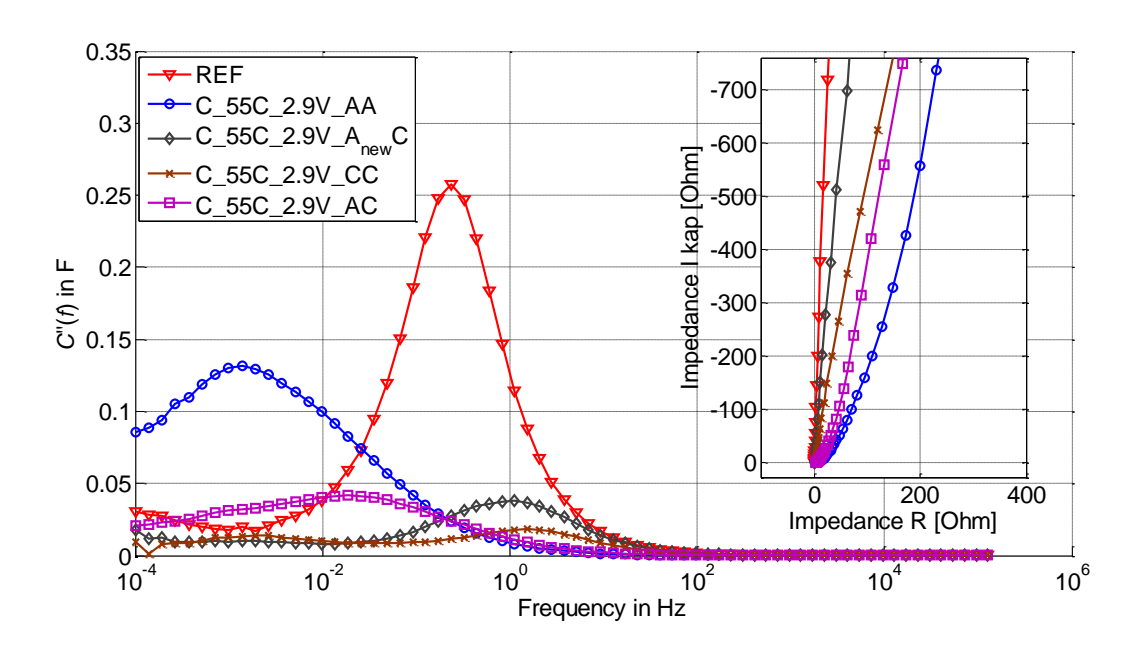


Figure 7.45: Imaginary Capacitances of coin cells made from cell C\_55C\_2.9V<sup>30</sup> and corresponding Nyquist plots

<sup>&</sup>lt;sup>30</sup> A coin cell with new positive electrode and aged negative electrode was constructed as well but failed in measurement. Hence, no results can be presented here.

According to equation (3.13) and to equation (3.14) the capacitance and the time constant of every measured coin cell was calculated, see Table 7.16.

cell	capacitance	time constant
REF	0.55 F	1.71 s
C_55C_2.9V_AA	0.58 F	292.14 s
C_55C_2.9V_A <sub>new</sub> C	0.09 F	0.36 s
C_55C_2.9V_CC	0.05 F	0.14 s
C_55C_2.9V_AC	0.17 F	21.73 s

Table 7.16: Capacitance and time constant values of cell C\_55C\_2.9V derived from the imaginary capacitance shown in Figure 7.45

The capacitance of cell C\_55C\_2.9V\_AA is even slightly higher than the reference cell's capacitance. This can be due to deviations in electrode disk cutting for coin cell preparation. However, the positive electrode's capacitance did not decrease but the time constant increases drastically. The cells using aged negative electrode material show indeed very low time constants.

However, the results contradict the assumption, that the capacitance of symmetrical cell can be halved to get the single electrode capacitance and calculate from these results the capacitances of full cells with different electrodes. The series connection of the single electrode capacitance values does not match e.g. the full cell made of aged electrodes.

Coin cells made from cell C\_55C\_3.0V show a similar behavior compared to cell C\_55C\_2.9V, as can be seen from Figure 7.46. The peak of cell C\_55C\_3.0V\_CC shows only a very slight shift to lower frequencies whereas the peak of cell C\_55C\_3.0V\_AA is shifted to much higher time constants.

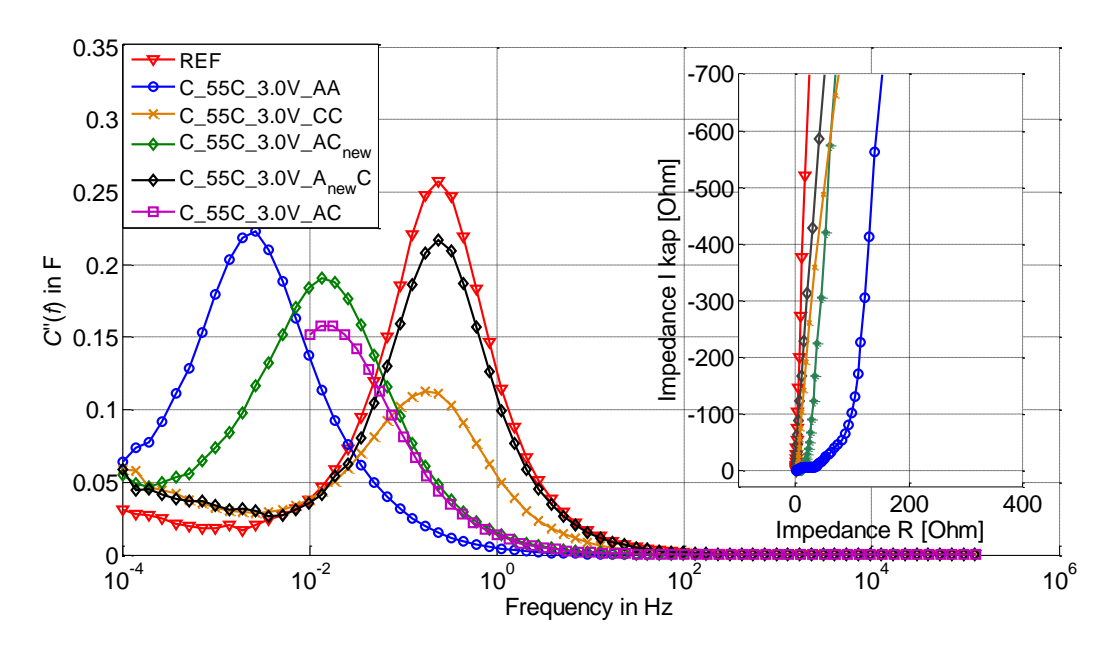


Figure 7.46: Imaginary Capacitance of cell C\_55C\_3.0V31

From the values for capacitance and time constant shown in Table 7.17, it can be seen again that only the aged negative electrode shows significant capacitance loss, whereas the aged positive electrode did not lose capacitance but its time constant increased. Moreover, the aged positive electrode dominates the time constant behavior in non-symmetrical cells.

cell	capacitance	time constant
REF	0.55 F	1.71 s
C_55C_3.0V_AA	0.56 F	151.99 s
C_55C_3.0V_CC	0.29 F	2.33 s
C_55C_3.0V_A <sub>new</sub> C	0.48 F	1.71 s
C_55C_3.0V_AC <sub>new</sub>	0.54 F	29.99 s
C_55C_3.0V_AC	0.40 F	22.72 s

Table 7.17: Capacitance and time constant values of cell C\_55C\_3.0V derived from the imaginary capacitance shown in Figure 7.46

The tendency that the time constant of the positive electrode is shifted to larger values and that the negative electrode shows almost no time constant shift but its capacitance decreases can be observed from cell C\_55C\_2.7V as well, compare Figure 7.47. But in contrast to the material of the previously presented cells the time constant shift is much less, although the remaining capacitance of cell C\_55C\_2.7V with about 38% is comparable to the remaining

<sup>&</sup>lt;sup>31</sup> The full cell with aged negative and positive electrode could only be measured till 10 mHz.

capacitance of 32% of cell C\_55C\_2.9V. The differences between both cells lay in the resistance increase. It is much higher in case of cell C\_55C\_2.9V.

From the calculated capacitances and time constants shown in Table 7.18 it can be concluded that the differences in time constants are much less than observed for previous cells, but a significant capacitance loss can be observed as well. In case of the presented cell there is not such a significant difference in capacitance loss between aged positive and negative electrode.

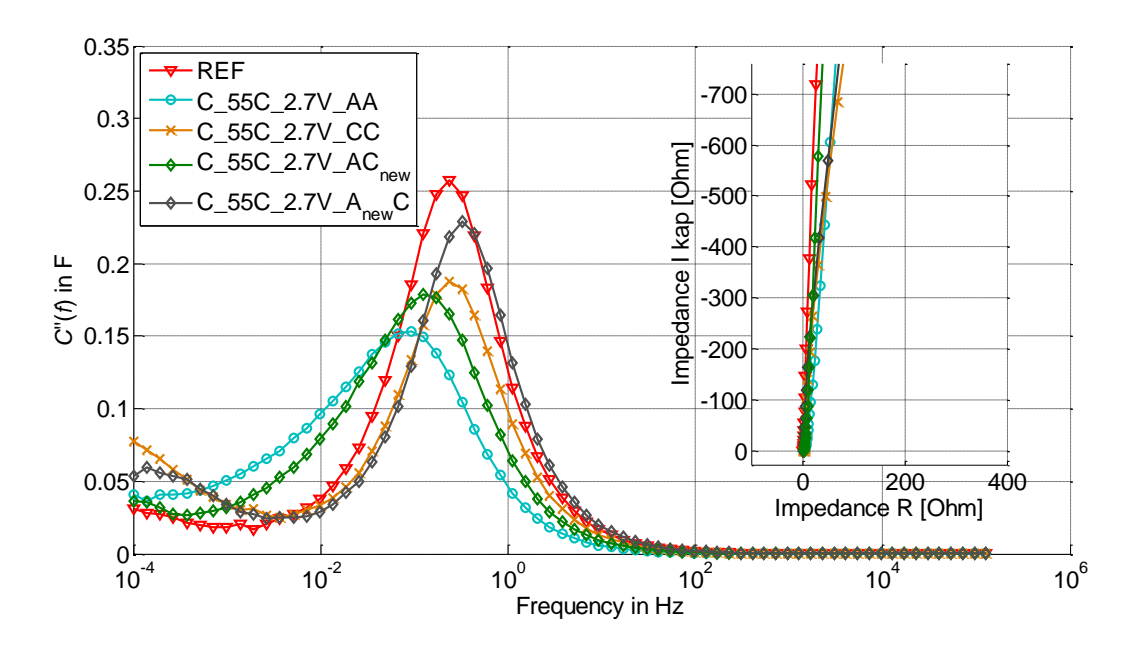


Figure 7.47: Imaginary Capacitance of cell C 55C 2.7V

cell	capacitance	time constant
REF	0.55 F	1.71 s
C_55C_2.7V_AA	0.38 F	4.39 s
C_55C_2.7V_CC	0.55 F	1.70 s
C_55C_2.7V_A <sub>new</sub> C	0.45 F	3.03 s
C_55C_2.7V_AC <sub>new</sub>	0.42 F	1.71 s

Table 7.18: Capacitance and time constant values of cell C\_55C\_2.7V derived from the imaginary capacitance shown in Figure 7.46

Assuming the fiber materials are responsible for the deceleration of the diffusion processes in the positive electrode there seems to be fewer fibers and therefore lower cell resistance if cells were stored at lower voltages. Thus, the reaction that results in the fibers as reaction product is voltage dependent. Furthermore, the adhesion loss of the negative electrode and therefore its capacitance decrease is much lower than in case of higher voltages.

The effect that the characteristics of cell C\_55C\_3.0V are not worse than the results of cell C\_55C\_2.9V, in some cases they are even better, although it was stored at a higher voltage level can be explained by the fact that C\_55C\_3.0V was stored for a shorter period of time. With the same storage time the results of C\_55C\_3.0V should be worse and give evidence to the voltage dependent processes that lead very high time constants at the positive electrode.

#### 7.3.5 Conclusions from Post Mortem Analysis

A detailed post mortem analysis of opened Type B cells was not possible because on the one hand the paper separator built a compound with the positive electrode, and on the other hand the carbon material of the negative electrode had in worst case no adhesion to the current collector any more. The electrodes respectively the electrode-separator-compound show that the use of the paper separator led to chemical reactions that strongly affects the electrodes and reduced the cell's lifetime. Thus, since Type B electrodes were not suitable for further analysis, the electrode analysis had to focus on cell Type C for which a polypropylene separator was used.

By means of visual inspection and laser microscope investigations a layer on top of the negative electrode and adhesion problems at the negative electrode were observed. REM pictures of the electrodes of cell C\_55C\_3.0V show cracks in both electrodes. In case of the negative electrode binder material seems to be missing and this effect leads probably to adhesion loss. In case of the negative electrode, there is no surface layer, although the porosity seems to decrease in direction of the surface. But fiber materials keep the cracked carbon material together. However, in both cases there is no electrical contact to the current collector due to the cracks which leads to capacity loss.

The capacity loss was measured at coin cells made from the electrode material to analyze differences in aging and the resulting electrical behavior of both electrodes. Capacitance decrease could be observed for both electrodes. The capacity fade was even bigger in case of the negative electrode, but this is very probably caused by material loss during the coin cell construction process due to the poor adhesion of the aged negative active mass. The high time constants at the positive electrode of cells stored at high voltages indicate that the film formation at this electrode occurs predominately at voltages higher than RWV.

Significant differences were observed for the shape of Nyquist plots and the time constants from the imaginary capacitance. The negative electrode shows, beside an internal resistance increase, only minor changes in Nyquist plot shape and time constant, whereas in the Nyquist plots of the positive electrode a large semi-circle evolves. This semi-circle can be probably assigned to charge transfer processes. The positive electrode's Nyquist plot shape dominates the Nyquist plot and the time constant of the whole cell.

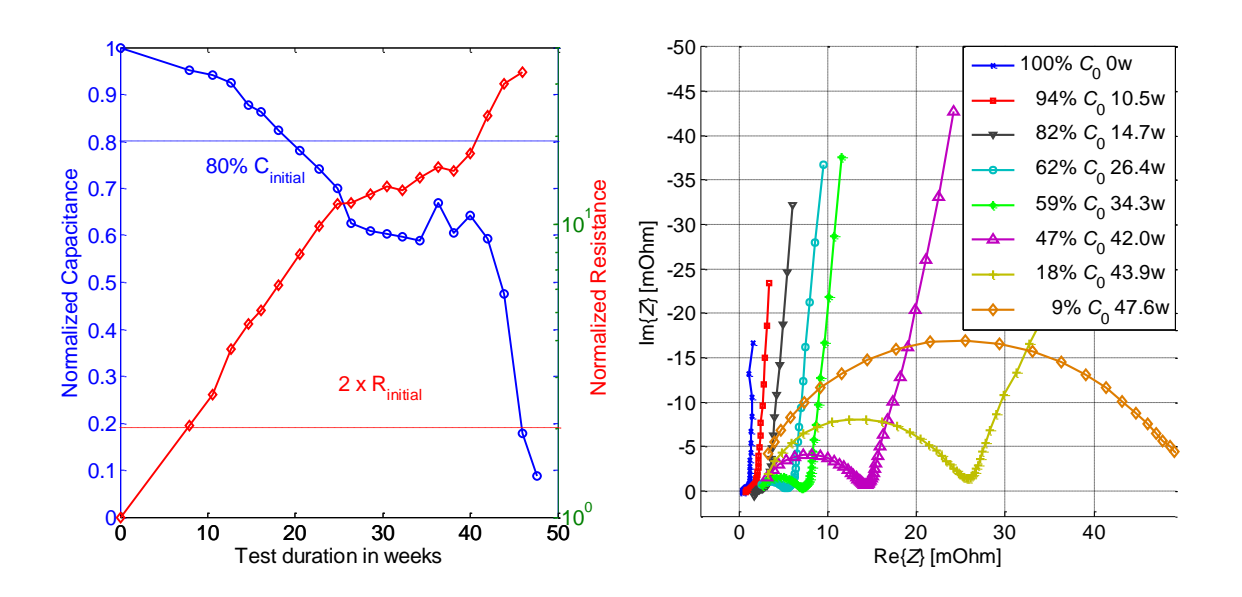


Figure 7.48: Resistance and capacitance characteristics (left) and Nyquist plots (right) during calendric aging test of cell C\_55C\_3.0V

As shown in Figure 7.48 (left), the capacitance of cell C\_55C\_3.0V decreases nearly linearly till about 60% of the initial capacitance, then it stayed almost unchanged for almost 20 weeks and finally it breaks down dramatically. In Figure 7.48 (right) the corresponding Nyquist plots are shown. To achieve better clarity, not all spectra measured during the accelerated aging test are presented. From the first five spectra, belonging to the nearly linear capacitance decrease, one can observe that the capacitance decreases whereas the resistance increases and a small semi-circle arises. However, the general Nyquist plot shape does not change remarkably. In contrast, the last three spectra, belonging to the large capacitance drop and resistance increase, differ significantly. A large semi-circle arises and the capacitive part is far away from 90°. One can conclude that there must be a charge-transfer with high resistance and significant leakage currents.

The sudden capacitance drop and resistance increase at the end of the test can be explained by cracks in the electrodes. Many cracks were observed in SEM images. Probably the cracks are formed continuously during aging. Each crack impedes the direct way of the electrons though the carbon material to the current collector. Therefore, the electrons must pass a longer way around the crack which results in a higher resistance. This phase lasts approximately till 60% remaining capacitance. This can be described as a perculation process. Then there is suddenly no viable way anymore for the electrons to the current collector because cracks completely insulate many parts of the active material from the current collector.

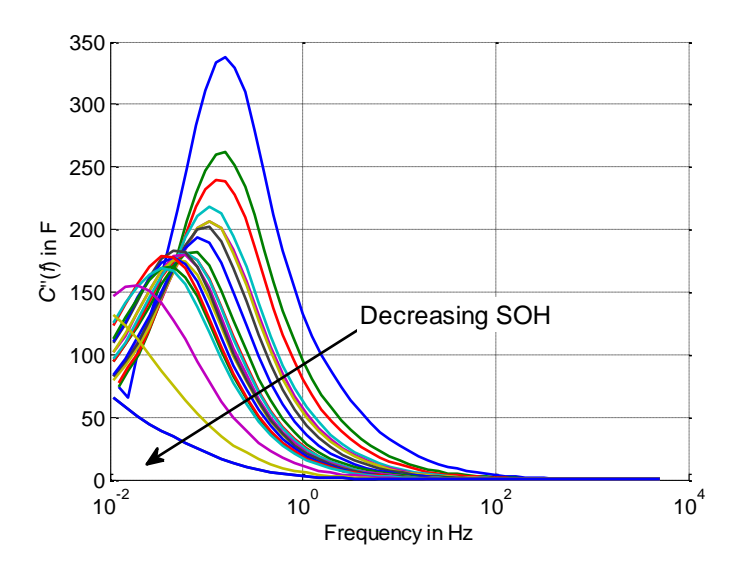


Figure 7.49: Development of imaginary capacitance peaks of cell C\_55C\_3.0V

Additionally, Figure 7.49 shows the development of the imaginary capacitance peaks and therefore the time constants of the material. Initially, the peak height decreases but the peak frequency does not change significantly. With ongoing aging, the peaks shift slowly to lower frequencies, but only the last three peaks, corresponding to strong capacity fade, show a large peak frequency shift.

Summarizing the post mortem results, one can conclude that significantly different aging processes occur at negative and positive electrode. Both electrodes show cracks leading to capacitance loss and resistance increase, but the positive electrode is responsible for the deceleration of diffusion and/or charge transfer processes.

However, the post mortem analysis results presented in this thesis can only be first indications on the processes in single electrodes since only few cells could be analyzed at a condition far beyond EOL criterion. Further research is necessary to achieve a detailed understanding which chemical processes occur and which chemical products are formed.

# 7.4 Conclusions from Experimental Aging Investigations

Typically, aging tests of EDLCs, both calendric and cyclic aging, are performed at very high temperatures, up to more than 60 °C as well as at potentials up to more than 3 V [120,121,124,125]. These tests lead to fast results but the deductions to normal use conditions is questionable. Various calendric aging tests in this thesis, performed with two different commercial EDLCs, both with AN-based electrolyte and carbon-based electrodes, showed that the derived aging factors for temperature and voltage impact differ remarkably between moderate and highly accelerated aging conditions for all investigated cell types. These results are contradictory to the work of Kötz et al. who measured in [123] 10 K and 100 mV as lifetime halving factors at various test conditions. In a previous work Kötz et al.

measured an acceleration factor of 1.5-2 for an voltage increase by 0.1 V and an acceleration factor of 1.7 to 2.5 V for a temperature increase by 10 K [82]. But for these tests they analyzed the leakage current at various temperature and voltage conditions using only one single EDLC for all test conditions. They did not store the cells over a longer period at accelerated aging conditions. Long-term calendric aging tests for more than 3 years are not reported in literature.

It is not possible to deduce any general aging factors from the calendric aging results in this thesis because the results differ significantly. Additional effects at high temperatures or high voltages might accelerate the aging during storage tests. Kötz et al. aged their cells at conditions up to 85 °C and 3.5 V [82,123] which is far beyond the test conditions in this thesis but they did so by means of leakage current analysis. Other effects occurring during storage tests in this thesis, like drying of EDLCs' electrodes during storage time due to leaky cells, certainly affect the results. However, a variation of aging factors was observed for leaky cells as well as for tight cells in this thesis. Both cell types showed different capacitance and voltage characteristics but had in common a strong variation of the deduced impact factors.

Another aspect is the difference between capacitive and resistive calendric aging which is usually not regarded in other studies. The results in this thesis imply that there can be a significant difference in achievable lifetime as well as in voltage and temperature dependency. However, in case of all investigated cell types a shorter resistive lifetime was observed. This contradicts the study of Kötz et al. where the capacitive lifetime was shorter [123]. This emphasizes that it hard to deduce general conclusion for ELDCs by testing just one special cell type. Even the cells of Type A and B aged in this thesis showed quite different aging characteristics.

Additional processes like gas evolution at high temperatures and/or high voltages and the possibly resulting leakage influence the results. Thus, drawing conclusions from these results to the behavior under nominal life conditions is nearly impossible. Post mortem analysis of selected cells aged in calendric test gave first indications on the different processes at positive and negative electrodes. Especially in case of highly accelerated aging at high voltages the negative electrode showed very poor adhesion whereas a film rose at the positive electrode's surface. This film depends on cell voltage during storage and leads to very slow diffusion processes. Further work is needed to understand these processes in more detail and its consequences for the definition of reasonable test matrices for aging tests.

Considering equation (7.2) the lifetime of an EDLC should be nearly infinite for a short-circuited cell because any high temperature should be compensated. Experimental results clearly indicate that EDLCs age at high temperatures even if they are at 0 V. Hence, equation (7.2) is not valid for such low voltages and can also not be used for highly accelerated aging conditions since there are no constant aging factors in this case as shown previously. Thus, the question if there is a validity range for this formula for rough lifetime estimations at all must be clarified in further studies.

The question of the calendric aging impact on cyclic aging could not be answered in this thesis. Impedance spectra showed alternating effects at check-ups during cyclic tests. But these effects seem to be reversible and do not results in capacity fade or resistance increase.

By neglecting the voltage impact on calendric aging the results indicate that only the generated heat during cycling and not charging and discharging affects the aging. Weingarth et al. showed that the capacitance characteristics of a storage test fits well to those characteristics of a cycling test at the same temperature and a maximum cell voltage of  $V=V_{\text{storage}}+0.3 \text{ V}$  [125]. However, for these experiments they do not cool the cycled cells. Their reference temperature is the ambient temperature and not the cell temperature as in this thesis. Hahn et al. showed in their dilatometric study that a significant volume change occurs during cycling [128]. Sudden death of cycled cells near EOL as observed in this thesis might be caused by intercalation processes but their impact on the long-time characteristics of capacitance and voltage must be investigated in further research.

Summing up the accelerated aging tests in this thesis showed:

- The general assumption that 10 K temperature increase or 100 mV voltage increase halves lifetime is not valid over the whole temperature and voltage range.
- As long as the real impact of calendric aging during cyclic test is not clear, the cyclic aging effects cannot be deduced properly.
- Short-circuit and low voltage tests at elevated temperatures (65 °C) showed voltage independent but temperature driven aging processes. Thus, low voltages could not compensate high temperature.
- Sudden death of cycling test cells near EOL might be caused by intercalation processes which must be shown in further studies.
- Many different processes like adhesion loss at the negative electrode or film formation at the positive electrode lead to EDLC aging. High cell voltage seems to be one of the mayor impact factors. Further research is necessary for a better understanding of aging processes, their impact factors and a proper aging test definition.

Aging Model 137

## 8. Aging Model

Although not all aging processes, such as the chemical reactions and decomposition products, are not understood in detail yet, a first approach was undertaken to develop an aging model. The goal of this model is not to represent single chemical processes. But the goal is to develop a tool that enables the user to simulate voltage and temperature impact on capacitive and resistive aging of single cells or of an entire module. Moreover, by means of the model, lifetime prediction for the calendric aging should be achieved. However, model parameterization is challenging since the aging processes are not fully understood yet. But the approach for calendric aging model is presented here. A full lifetime prediction model for cyclic operation is not possible now. Experimental results shown beforehand showed in many cases that aging processes during cycling are obviously different from those occurring at calendric aging. Nevertheless, in chapter 8.3 a first approach is presented for an improved model for cyclic lifetime prediction. This is still a heuristic model and even though it is not perfect it is a first important step into the direction of a cyclic aging model for EDLCs.

Hence, the electro-thermal model developed in chapter 6 was enlarged to an aging model. Again, this model is modular now consisting of three blocks: electrical, thermal, and aging model depending on each other as shown in Figure 8.1.

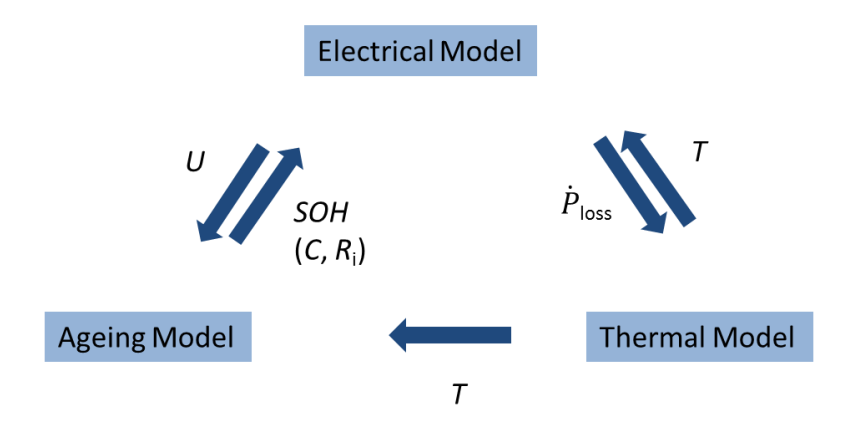


Figure 8.1: Schematics of the aging model

Basis for the model are the results of the accelerated aging tests presented in chapter 7.2. From these results, the dependency of aging on temperature and voltage can be concluded. With the knowledge of this dependency the model parameters can be adapted.

The new model is now able to represent the capacity loss and the resistance increase due to aging. Therefore,  $R_i$  and C parameters of the equivalent circuit, on which the electrical model is based, must be adapted to the aging condition of the simulated cells. Initially, only calendric aging is considered since it is the major contribution to EDLC aging.

The influence factors of voltage and temperature determined in chapter 7.2.1.5 serve as basis for the calendric aging calculations of the model. During simulation, the factors are

calculated based on simulated temperature and cell voltage, are adapted in each time step to the present aging condition, and then integrated. The resistance values affect then the thermal model and lead to higher temperatures which lead to faster aging processes.

## 8.1 Calendric Aging Model

The aging model developed by Bohlen in [109] assumed the capacitance decrease during calendric aging to be linear. But the results of accelerated aging test presented in chapter 7.2.1 indicates clearly that initially the capacitance decreases strongly non-linear followed by a slower quasi-linear capacitance decrease.

Schmalstieg et al. developed an aging model for Li-ion batteries which shows also non-linear characteristics in capacitance decrease [150]. They assumed the capacitance to be proportional to  $t^{0.75}$ . But for the capacitance development during the calendric aging tests of EDLCs presented in this thesis, a proportionality of the capacitance to  $t^{0.5}$  showed best results.

The capacitance C(t) is then calculated by means of the following equation:

$$C(t) = C_{initial} \cdot \left(1 - 0.2 \cdot \sqrt{a \cdot t} / \sqrt{t_0}\right) \tag{8.1}$$

where  $C_{\text{initial}}$  is the cell capacitance at 100% SOH,  $t_0$  the cell lifetime under nominal conditions (25 °C, rated voltage) and a the accelerated aging factor which is calculated by:

$$a = 2^{\left(\frac{U - U_{\text{RWV}}}{\Delta V}\right) + \left(\frac{T - 298 \text{ K}}{\Delta T}\right)}$$
(8.2)

where U is the cell potential,  $U_{RWV}$  the rated voltage, T the storage temperature, and  $\Delta V$  and  $\Delta T$  the lifetime halving aging factors that were introduced in chapter 7.2.1.5.

In case of  $t = t_0/a$  the capacitance results to 80% of the initial capacitance which is defined as end of life criterion (SOH=0%).

In contrast to the non-linear capacitance characteristics, the resistance increase observed in the calendric aging tests was initially nearly linear. Since only the resistance characteristics before reaching the end of life criterion are considered in this aging model, the resistance increase in the presented aging model is assumed to be linear. Hence, the resistance R(t) is calculated by means of the following equation:

$$R(t) = R_{initial} \cdot (1 + a \cdot t/t_0)$$
(8.3)

Aging Model 139

where  $R_{\text{initial}}$  is the cell resistance at 100% SOH,  $t_0$  the lifetime under normal conditions, and the aging factor a is calculated according to equation (8.2).

In case of  $t = t_0/a$  the resistance results to 200% of the initial resistance which is defined as end of life criterion (SOH=0%).

The model still is not able to show the sudden decrease in capacity or increase in internal resistance that has been observed in several experiments. Therefore, the validity range of the model is somehow limited at maximum to the standard lifespan which includes an increase of the resistance by a factor of two and a loss of capacitance of 20%.

## 8.2 Validation of Calendric Aging Model

For the validation of the calendric aging model, the capacitance decrease and resistance increase of Type B cells were simulated for several test conditions. Since this model cannot be easily parameterized due to the large spread in aging factors deduced from the calendric aging tests, see chapter 7.2.1.5, just a first approach can be given here to show the general applicability of the calendric aging model. Since the most reasonable aging factors as well as lifetime values under nominal conditions were deduced from the lowest aging acceleration, these values were taken here. The model parameters are shown in Table 8.1.

	U <sub>RWV</sub>	$t_0^{32}$	ΔV	ΔΤ
Capacitive	2.5 V	20 years	79 mV	10.2 K
Resistive	2.5 V	10 years	118 mV	10.5 K

Table 8.1: Aging model parameters

As can be observed from the left plot in Figure 8.2, the capacitive aging behavior is represented quite well by the model. The simulated curves for 65 °C and 2.3 V as well as for 65 °C and 2.7 V match the measurement very well, only in case of the curve for 65 °C and 2.5 V there is a slight deviation. However, the model does not represent the capacitance break down, as it was observed in the measurements for C < 80%  $C_{\text{initial}}$ . The aging processes leading to this strong capacitance decrease are not considered in this model. Nevertheless, the model should be able to represent the aging behavior before reaching the end of life criterion.

 $<sup>^{32}</sup>$   $t_0$  was determined by using equation (7.2) is the average value that was calculated from the measured lifetime at different test conditions and the accelerated aging factors.

The initial resistance characteristics of calendric aging tests at 65 °C and 2.3 V as well as at 65 °C and 2.7 V are quite well represented by the model, see right plot in Figure 8.2. Only the measured resistance increase for 65 °C and 2.5 V is slightly lower than the calculated curve.

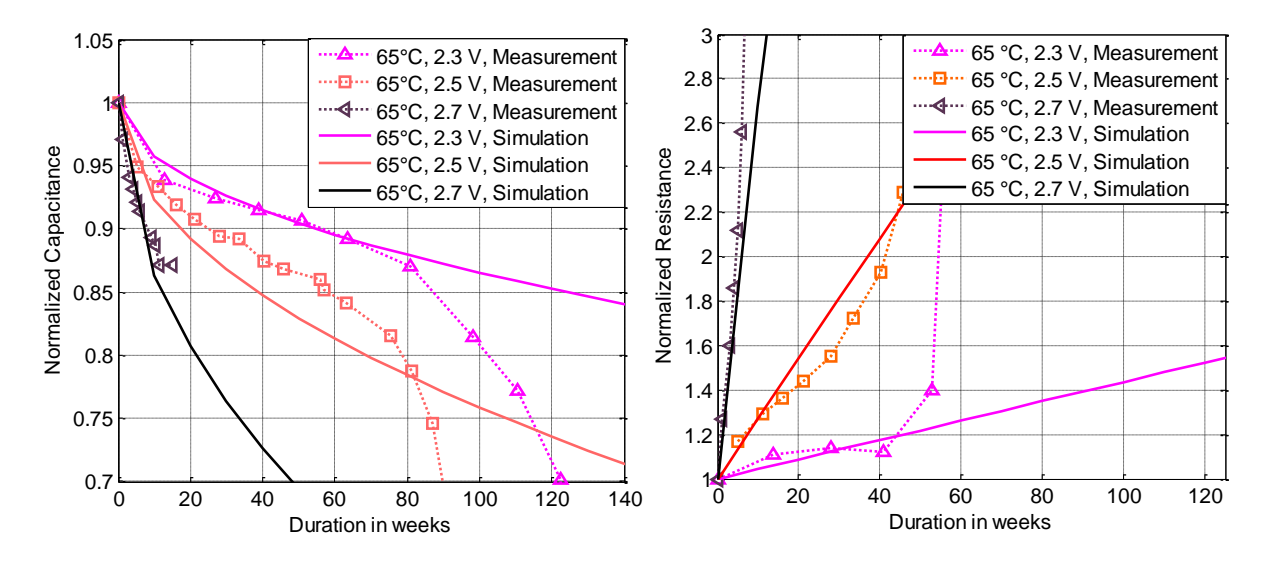


Figure 8.2: Comparison of measured and simulated normalized capacitance (left) and resistance characteristics (right) depending on voltage

Since the previous simulations differ only in voltage, additional simulations for calendric aging tests at 2.5 V but different temperatures were carried out. Figure 8.3 shows the normalized capacitance development of four different temperatures. In case of 55 °C and 75 °C the simulation results correlate well with the measured data. But in case of other temperatures some deviations can be observed. The measured capacitance decrease is lower than simulated in these cases.

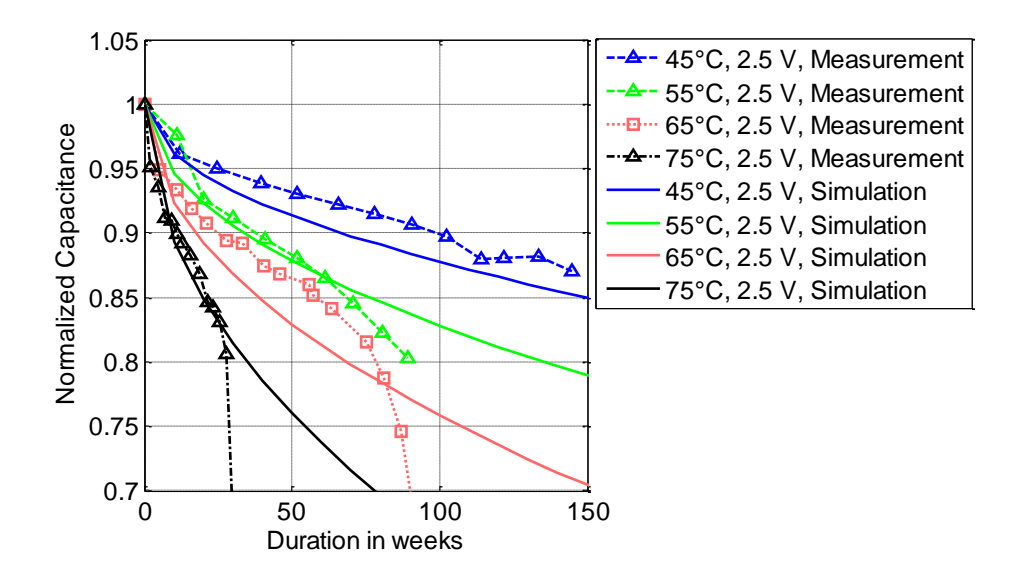


Figure 8.3: Comparison of measured and simulated normalized capacitance characteristics depending on temperature

Aging Model 141

The correlation between simulated and measured resistance is not very good, as can be seen from Figure 8.4. The simulated curve of 75 °C matches the measured data quite well at the beginning, almost till reaching the end of life criterion (2 x  $R_{\text{initial}}$ ). At the other test conditions clear deviations between measured and simulated curves can be observed, especially at 45 °C.

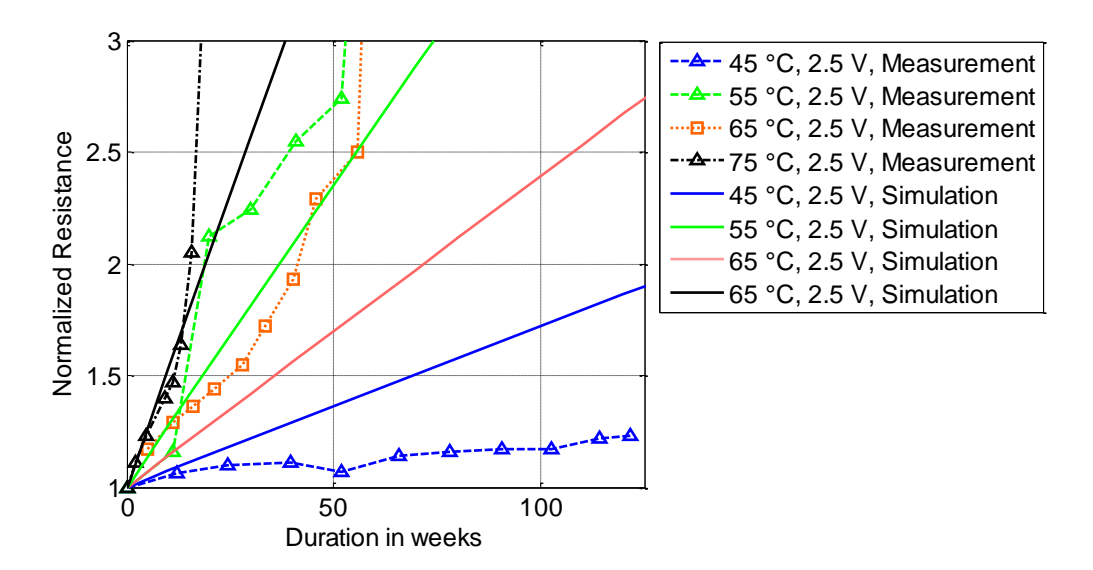


Figure 8.4: Comparison of measured and simulated normalized resistance characteristics depending on temperature

Certainly, the presented differences between some measurements and their simulations result from the fact that no model parameters valid for all tests conditions could be found. The assumed model parameters were taken from the lowest aging acceleration condition and the most reasonable re-calculated lifetime values under nominal conditions. Other parameters for voltage and temperature dependency as well as for the nominal lifetime lead to different results. Figure 8.5 shows the simulated resistance characteristics exemplarily with a stronger temperature dependency of  $\Delta T = 7.1$  K instead of 10.5 K, once again for  $t_0 = 10$  years (left) but additionally also with  $t_0 = 20$  years.

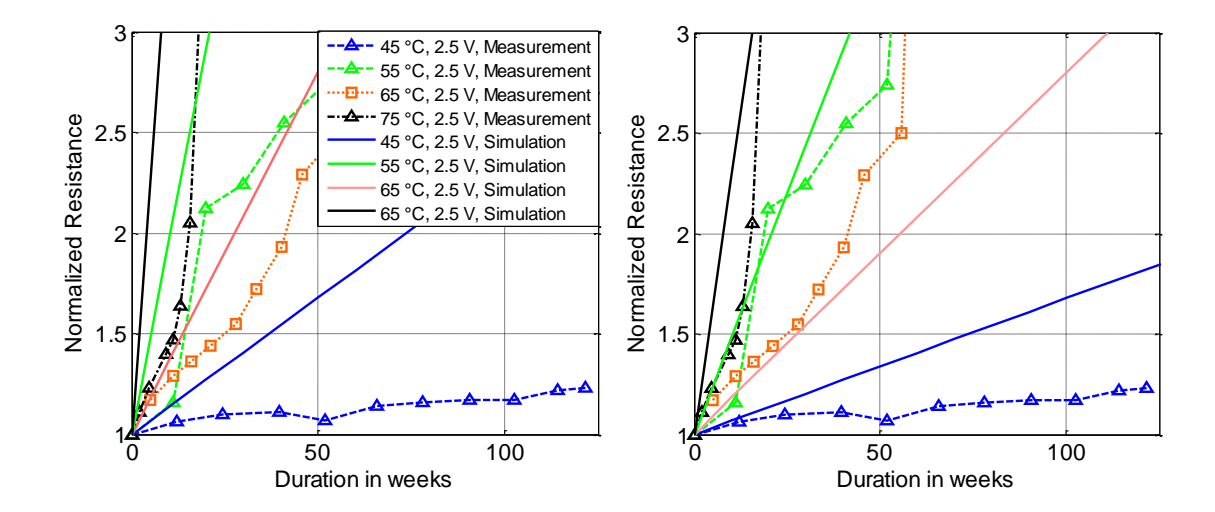


Figure 8.5: Measured and simulated normalized resistance characteristics depending on temperature with  $\Delta T = 7.1 \, \text{K}$  and  $t_0 = 10 \, \text{years}$  (left) and  $\Delta T = 7.1 \, \text{K}$  and  $t_0 = 20 \, \text{years}$  (right)

In the left case, the results are worse than for  $\Delta T = 10.5$  K and t0 = 10 years. Whereas in the right case, the simulated curve for 45 °C and 55 °C fits better to the measurement but for 65 °C and 75 °C the correlation got worse. Thus, it can be concluded that an excellent congruence between measured and simulated data cannot be achieved with one and the same parameter set.

Thus, the parameterization of the calendric aging model is a big challenge. The approach of one parameter set is most likely too simple. Further research has to be undertaken to analyze in which temperature and voltage range with which parameter set the model is applicable. Nevertheless, with a good parameterization the model can be very helpful for calendric aging prediction. It was shown that with appropriate parameters calendric aging behavior within the range of 100% SOH till the capacitance break down at about 85% SOC can be represented by the developed aging model. The capacitance characteristics are thereby proportional to  $\sqrt{t}$ , whereas the resistance increase, at least within the considered aging range, depends linearly on time.

#### 8.3 Modeling of Cyclic Aging

Even in operation, EDLC's aging is dominated by calendric aging due to the temperature increase during cycling, unless cells are not cooled as done during the tests presented in chapter 7.2.2. But nevertheless, also cycling contributes to the aging processes but it is not clear in which measure, continuous aging contribution or only leading to a sudden death, because the influence of calendric aging could not be clearly identified. Because of this and since there are only results from two cycle life tests at different conditions, it is now not possible to parameterize a model representing the cyclic aging. However, a general approach for an

Aging Model 143

aging model was undertaken to represent cyclic aging by the developed ageing model, too. This model could be parameterized if there were additional results of further cycle life tests indicating that there is a continuous aging contribution of cycling.

The results presented in chapter 7.2.2 indicate that the current rate has a strong impact on cyclic aging. Cells cycled at 180 A aged faster than cells cycled at 150 A, although the voltage band was higher in the second case. Hence, the accelerated aging factor in equation (8.2) must be enlarged by an additional current dependent cyclic aging factor b(I), see equation (8.4).

$$a = b(I) \cdot 2^{\left(\frac{U - U_{\text{RWV}}}{\Delta V}\right) + \left(\frac{T - 298 \text{ K}}{\Delta T}\right)}$$
(8.4)

The results cyclic aging tests presented in this thesis clearly indicate that the dependency of the aging factor cyclic aging factor b on current rate is not linear but follows the following equation:

$$b(I) = k \cdot I^{x} \tag{8.5}$$

where *k* is the proportionality constant, and *x* the power of *l* that has to be determined.

To parameterize the cyclic aging model in an adequate way multiple additional aging tests must be undertaken, since in the two present results current rate and voltage band was varied. By means of the additional results, the dependency on current rate can be determined to parameterize the model. Moreover, the impact of other factors like cycle depth can be investigated and used for model parameterization.

Until now it is totally unclear if the depth of cycles also has an impact on the cycle lifetime as well. This would need further experimental investigations as well. Unfortunately, this requires very time-consuming tests, because at this point in time acceleration of these tests makes no sense as long as the aging processes have not been understood.

#### 8.4 Application of Aging Models on EDLC Modules

Although, the impact of temperature, voltage and cycling conditions on EDLCs' aging could not be generally identified in this thesis, chapter 8.2 showed that the calendric aging of a single cell can be represented quite well by the developed calendric aging model if using an appropriate parameter set for the simulated test conditions. With a deeper understanding of the aging processes and improved model parameterization this model can be a very helpful tool.

For the use of the presented aging model for lifetime prediction of different pack configurations it was implemented in the module model developed in chapter 6. To show the possibilities of this module aging model an example configuration is simulated in the following.

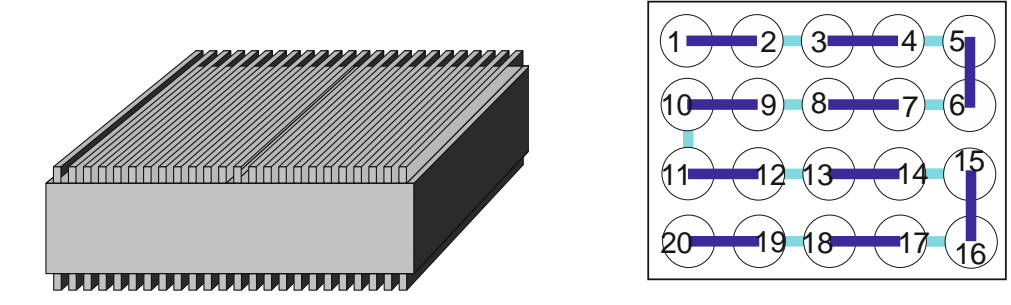


Figure 8.6: Example configuration with 20 cells (3000 F) in a closed aluminum housing with cooling fins at two sides

As shown in Figure 8.6 this configuration consists of 20 cylindrical cells connected in series with 3000 F capacitance each. The cell connection is put into a completely closed aluminum casing with cooling fins on top as well as on bottom side of the module. The temperature distribution of the module cells is calculated for a continuous cycling condition with a constant current rate of 180 A with 2 seconds pause between each charge and discharge step and a voltage band between 37 V and 54 V. The applied current profile is shown in Figure 8.7. The ambient temperature as well as the initial cell temperature was 23 °C.

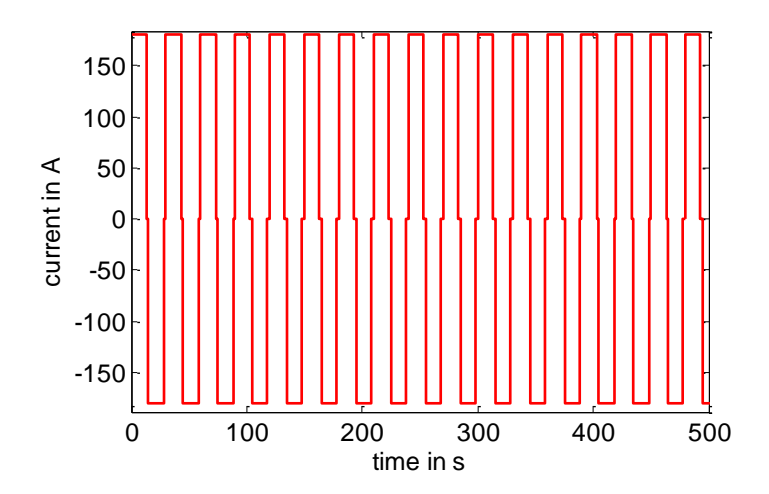


Figure 8.7: Simulated current profile

Two different cooling conditions were simulated for this module configuration. For the first simulation, no forced air cooling was assumed. Hence, the module was only cooled by free convection with 23 °C ambient air temperature. Figure 8.8 shows the resulting temperature distribution, in this case the cells' core temperature of the simulated cell configuration as well as the temperature characteristics of selected cells.

Aging Model 145

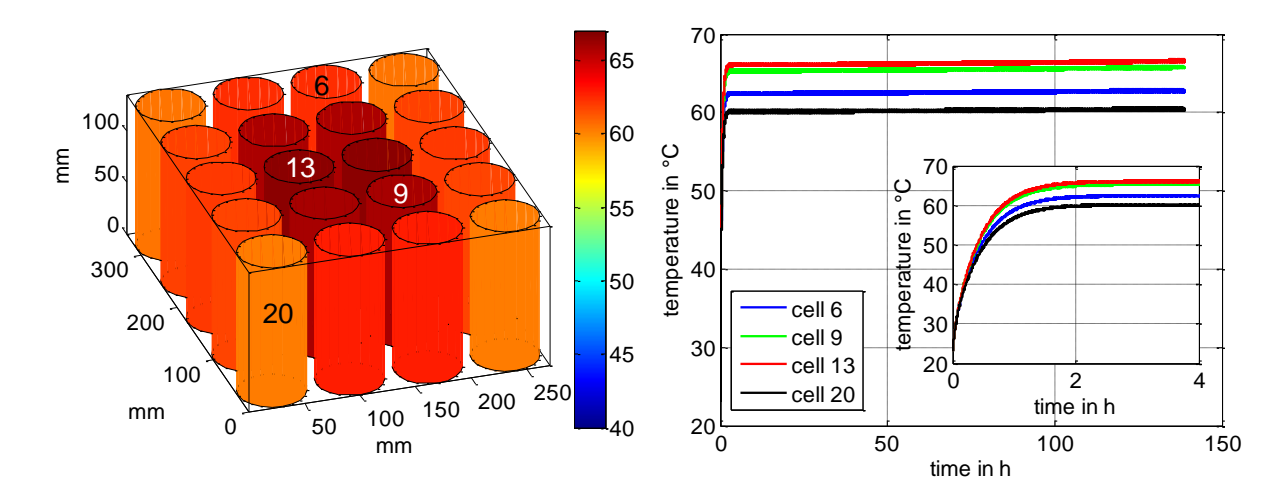


Figure 8.8: Temperature distribution after 140 h<sup>33</sup> and temperature characteristics of selected module cells in case of no forced air cooling

All cells heat up significantly due to the challenging current profile and the closed module casing. Additionally, a temperature spread, >7 °C, between e.g. cell 13 in the module middle and cell 20 at one modules edge can be observed.

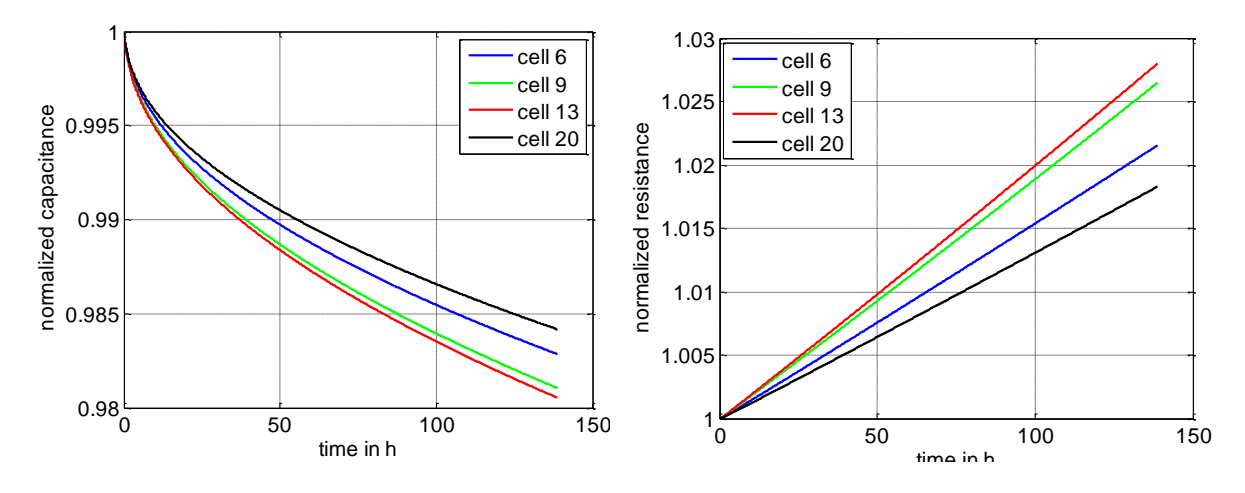


Figure 8.9: Capacitance and resistance spread of module cells in case of no forced air cooling

By means of the implemented aging model it is possible to analyze the capacitance and resistance characteristics of all module cells over time. Figure 8.9 presents the characteristics for the above selected cells. The temperature spread leads to a significant difference in capacitance and resistance. The spread becomes larger with ongoing cycling which is reasonable because a higher internal resistance causes higher generated heat values and therefore higher temperatures which again lead to higher resistance.

To increase the cells lifetime cooling strategies are necessary. The developed model is able to represent module cooling like forced air cooling on bottom and top of the module via the

-

<sup>&</sup>lt;sup>33</sup> 140 h correlates to 16,000 cycles.

cooling fins. Figure 8.10 shows the simulation results of the presented module configuration with applied forced air cooing, the air speed was 5 m/s and the air inlet temperature 23 °C.

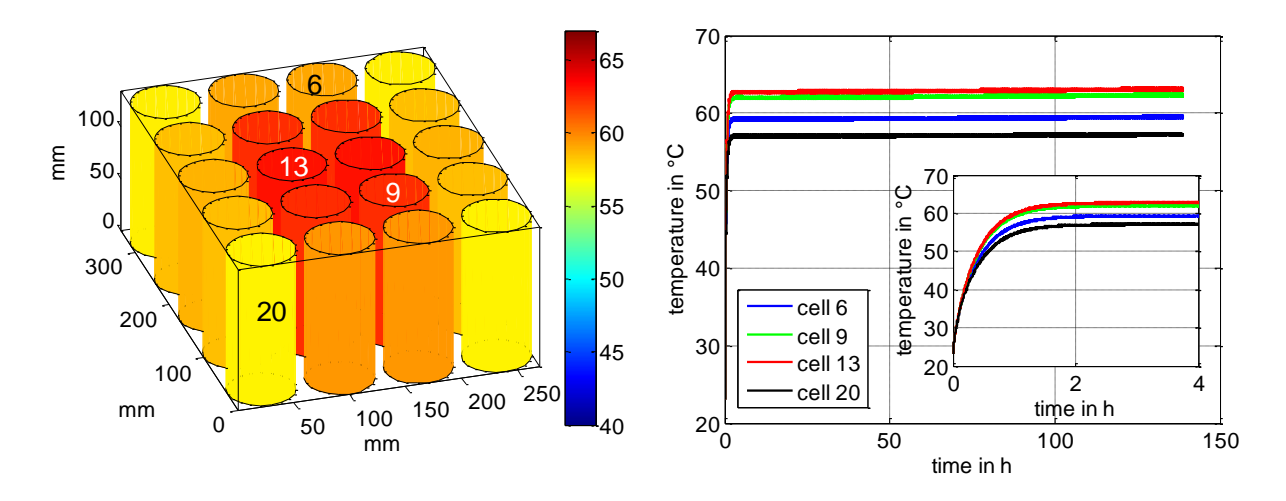


Figure 8.10 Temperature distribution after 140 h and temperature characteristics of selected module cells in case of 5 m/s air cooling

The air cooling decreases the cell core temperature; however, the core cells are still several degrees warmer than the outer cells. The resulting capacitance and resistance characteristics can be seen from Figure 8.11.

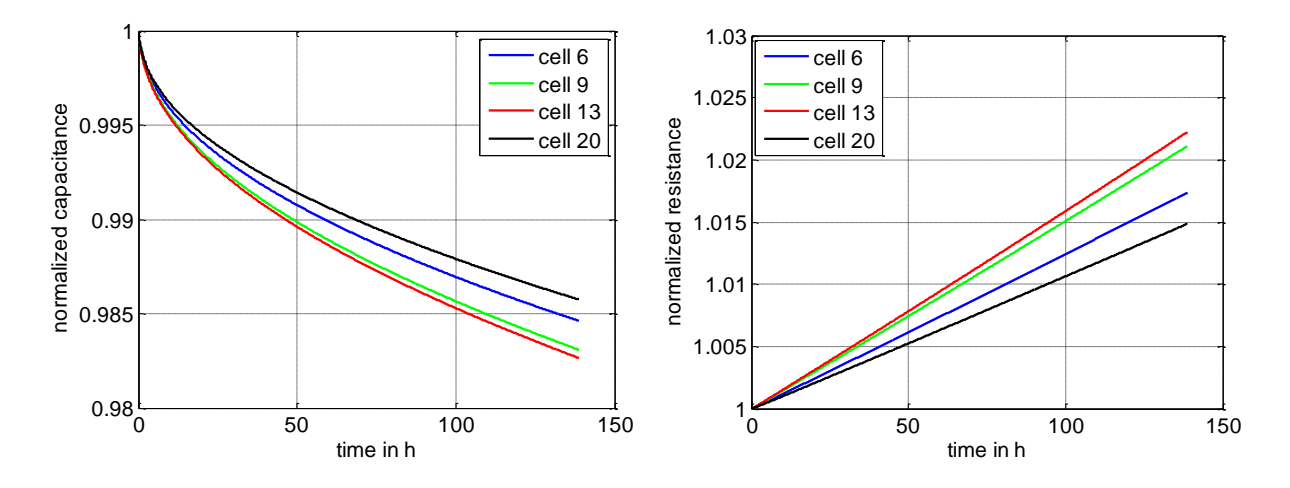


Figure 8.11: Capacitance and resistance spread of module cells in case of air cooling (5 m/s)

The capacitance decreases after 140 h respectively 16,000 cycles is lower and the spread is slightly lower. But the difference in resistance increase compared to no cooling are even more pronounced. Resistance increase of cell 13 is significantly lower and the difference to cell 20 is lower.

It depends on the system application and therefore the current profile and desired lifetime, whether a forced air cooling is sufficient or other cooling strategies like water cooling are needed. By means of the developed aging model the impact on module's lifetime of air

Aging Model 147

speed and air inlet temperature as well as ambient temperature can be simulated. It is further possible to simulate cooling just on one module side and the module can be enlarged to represent water cooling as well. Hence, for system design such a model is able to predict the module's lifetime for the applied current profile and ambient conditions and helps to find the optimum operating and cooling strategy in a very time-consuming way.

The aging model developed in this thesis builds the basis for future lifetime prediction models for EDLCs modules and packs. The general applicability of the model was presented in this chapter. If further work leads to a better understanding of the aging processes as well as the best practice in performing accelerated aging tests this model can be adopted and can significantly contribute to system design. Highly accelerated calendric aging tests produce unexpected side reactions and the resulting temperature and voltage dependency cannot be easily transformed to nominal conditions. Thus, a simple linear dependency over the whole temperature and voltage range is not valid. However, the aging model can be adopted in a fast and easy way.

#### 9. Conclusion and Outlook

#### 9.1 Conclusion

Electrochemical Double Layer Capacitors (EDLCs) are widely used in many different applications, due to their high-power capability and high cycle life. Many different materials can be utilized for EDLCs, but they differ in their characteristics such as resistance, deep temperature performance and safety. Experimental results show, that acetonitrile-based EDLCs outperform propylene-carbonate-based EDLCs regarding resistance and performance especially at deep temperatures. Hybrid capacitors do have a significantly higher cell voltage and therefore higher energy density than EDLCs, but they suffer from deep ambient temperatures.

Hence, acetonitrile-based EDLCs are the most common commercial type. To investigate their suitability for certain applications and predict their dynamic electrical behavior, impedancebased models with equivalent circuit diagrams representing the EDLC are a very helpful tool. However, the highly porous structure of the EDLC's carbon electrode leads to certain effects that cannot be represented by a simple equivalent circuit diagram consisting of a capacitor and a resistance. A transmission line model consisting of numerous RC-branches is more suitable to represent voltage relaxation caused by ion diffusion processes. However, this kind of model matches only highly dynamic processes and is not able to represent longer lasting diffusion processes properly, as they occur after current cut-off due to ion redistribution processes. Moreover, the basic transmission line model considers only homogeneous pore size distribution of an ideally cylindrical pore. Narrow micropores are not considered. Therefore, these slow diffusion processes, which occur during ion redistribution processes, cannot be represented. There are other model approaches considering different pore sizes, dividing them into macro, meso and micropores, which are able to represent self-discharge measurements very well. Indeed, these models fail in simulating very dynamic EDLC behavior. Therefore, an electrical model was developed in this thesis that combines the parameterization approaches of the transmission line model for dynamic processes and the selfdischarge model. It consists of five RC-branches three of them representing the dynamic part and two more branches representing processes with large time constants like ion redistribution. This model was parameterized by impedance spectroscopy and ion-redistribution and self-discharge measurements and is able to represent impedance spectroscopy as well as ion-redistribution and self-discharge measurements.

Another important aspect regarding modeling is the thermal behavior. Hot spots within the module can lead to accelerated aging of the concerned cell and should be avoided. Therefore, a modular electro-thermal model of a single cell was initially developed in this thesis. The electrical model calculates the current and therefore the generated Joule heat, whereas the thermal model calculates the heat transfer through the cell and to the environment. Ba-

sis of the thermal model is the finite differences method (FDM) which allows simulating a spatially resolved temperature distribution by dividing the cell into multiple volume elements. The electro-thermal model was further enlarged to a module model, considering the heat transfer between neighbored cells and from module case to ambiance. The module model allows further investigating of different cooling strategies like forced air cooling or water cooling.

Although, energy is stored purely electrostatically in theory, undesirable parasitic chemical reactions occur in EDLCs and can lead to aging processes such as decomposition of the electrolyte. These aging processes lead to resistance increase and capacity fade and depend strongly on temperature and voltage. To understand which factors influence these processes, accelerated aging tests are a fast way to investigate the aging behavior of EDLCs. Generally, it can be distinguished between calendric aging tests and cyclic aging tests. Nevertheless, even accelerated tests last between few month and years. This limits also the number of available aging data and findings from a series of aging tests could be hardly transferred into a new set-up for aging tests within the limited time of such a thesis. As described below, post-mortem analysis was added as an additional tool to achieve a more detailed insight into the aging processes. During calendric aging tests cells are stored at constant voltage and constant temperature, whereas during cyclic aging tests cells are continuously charged and discharged. It is often proposed in literature that a temperature increase by 10 K or a voltage increase by 100 mV halves the capacitor's lifetime. But calendric aging tests on different commercial EDLCs in this thesis have clearly shown that these factors do not match the aging behavior of any of the investigated cells. The voltage impact factor is in a range of 50 mV to 130 mV and the temperature impact factor is in a range from 5.6 K to 10.5 K and therefore much higher in many cases than expected. The calendric aging results show that all cell types showed differences in their aging behavior. Separator materials, drying processes and others influence significantly the aging behavior. Thus, for a good lifetime prediction model, it is not possible to transfer the aging test results from one cell type to another.

Another aspect is cyclic aging. EDLCs offer very long cycle life and theoretically there should be no limit since the storage process is purely electrostatic. But in reality, even in EDLCs, some kind of intercalation process in the carbon material occur which is comparable to batteries and lead to aging processes. However, the predominant aging influence is still calendric aging and it is quite difficult to distinguish clearly between the calendric and cyclic aging impact, especially because EDLCs heat up significantly while cycling at high current rates. Therefore, EDLCs which were exposed to cyclic test in this thesis were continuously cooled to approximately room temperature or slightly above. Due to this measure, cells have reached more than 1,000,000 equivalent full cycles over a testing period of more than three years. There are hardly any other results published in literature showing experimental results for more than one million full equivalent cycles. Surprisingly the cells which failed did not fail after a continuous aging process with increasing resistance and decreasing capacitance but they failed quite suddenly and unexpected. This is quite different from the failure

picture known from the calendric aging tests. It is not clear now if cycling only leads to a sudden death or if it leads to a continuous aging as well.

Since the accelerated aging tests show only the aging impact on the electrical performance but do not indicate what happens inside the cells, further analysis is necessary. Therefore, selected cells, which were exposed to calendric aging tests, were opened afterwards and a post mortem analysis was undertaken. EDLCs with paper separator showed thereby no electrode material that could be further analyzed anymore. The negative electrode has no adhesion to the current collector anymore, and the positive electrode built a stick compound with the separator. In contrast, EDLCs with polypropylene membrane showed also some adhesion problems at the negative electrode, but the material was still usable. The positive electrode stuck a little bit to the separator as well, but it could be pulled-off easily. Furthermore, aged positive electrodes are much stiffer than new electrodes and show significant weight increase. Laser microscope images indicate that a certain layer developed on the positive electrodes' surface. By means of SEM images, it can be observed that there is no real layer on top of the electrode but many fibers can be seen, connecting the multiply cracks in the carbon material. EDX measurements indicated that these fibers contain a high fluorine amount. Negative electrodes show many cracks as well, but in contrast to positive electrodes, there is no connecting material which explains the adhesion loss.

An electrode that has lost almost its entire capacitance shows countless cracks. Due to these cracks, a high ratio of activated carbon material is cut-off from the current collector. First cracks result in longer ways for electrons through the carbon material, because they must find a way around this crack, but at a certain point there is no path available anymore and the capacitance breaks down and the resistance increases exponentially.

Furthermore, the diffusion rate of the positive electrode is strongly affected by the fiber material that was built. Coin cells were made from the aged electrode materials. From impedance measurements of symmetrical cells (positive or negative electrodes on both sides), it could be observed that, beside resistance increase and capacity loss, negative electrodes do not change significantly in dynamic behavior and time constant. In contrast, positive electrodes show a large semi-circle in the Nyquist plot which means there must be some kind of charge transfer and the time constant of the positive electrode increases significantly. Moreover, the results show that the whole cell dynamic behavior is dominated by the positive electrode.

This thesis was started to gain a more detailed insight into EDLC aging and to show how life-time in cyclic real-world applications could be derived from the typically performed calendric life tests. However, the results presented in this thesis show that aging processes during cycling and calendar life tests cannot be clearly divided. Different processes which results in alternating impedance spectra were experimentally shown but it is not clear if these processes are completely reversible. However, the good news is that all tested EDLC devices achieved more than 500,000 full equivalent cycles under test conditions which assured sufficient cooling. But on the other hand, it is obvious that the aging processes occurring during

cycling are not yet well understood. If the low cell voltage has no beneficial impact, continuous cyclic aging would be dominated by calendric aging due to generated heat. But this should be clarified in further research. The very time-consuming cycle tests and the "sudden death" characteristics, which make extrapolations worthless, will make this a challenging task.

These difficulties make also the parameterization of an aging model to a big challenge. For module design, operating and cooling strategies such a model is extremely helpful but an appropriate parameterization is needed. By performing highly accelerated aging test results can be received very soon but taking these parameters for simulation of less pronounced aging conditions failed. The range where these parameters are valid covers not the whole temperature and voltage range. Additional processes occur at temperatures and voltages above the operational limit. Thus, highly accelerated aging tests are not appropriate for conclusions to real life conditions.

#### 9.2 Outlook

This thesis pointed out that the definition of appropriate accelerated aging tests is a big challenge. Future work is needed to analyze the dependency on temperature and voltage over the whole operation range. Additional calendric aging tests with a large matrix of test conditions is needed to analyze if there is no voltage dependency at low voltages as indicated in this thesis and which test conditions are appropriate and which not. These investigations could help by answering the question which size of aging matrix is sufficient. For the analysis of cyclic aging additional cycle tests must be performed and at the same time calendric aging tests at the same temperature and voltage conditions. By means of these tests it should be clarified if EDLCs age during cyclic tests only due to the generated heat and intercalation processes can lead to sudden death or if there are additional processes during cycling that lead to continuous aging.

First results of the post mortem analyses indicated, that there are different aging processes, leading on the one hand probably to loss of binder material at the negative electrode, and on the other hand to fiber materials that fill the cracks in the positive electrode. Further research is necessary to investigate the origin of these processes and the detailed composition of the resulting reaction products. Further analysis of additional aged EDLCs, also by using other characterization methods such as Raman, XRD and others could give more information. BET measurements would be very useful for the analysis of pore size distribution and could answer the question in which way especially micropores are affected by chemical reactions due to aging processes.

However, all aged cells that were analyzed in this thesis were in an aging state far beyond the typical end of life criterion of 20% capacitance loss or doubling of internal resistance. Therefore, reactions might have been occurred that would not have been occurred in a minor aging state. To investigate how aging processes affect the cell during the entire aging

process, new aging tests must be carried out. Multiple cells should be aged at the same aging condition, and in defined time intervals one after another can be taken out, and opened for post-mortem analysis. Thus, the development of the electrodes' structure and the decomposition products during the aging process could be investigated.

Another important aspect is the impact of cyclic aging. The cells of Type B exposed to calendric aging tests, were not useable for post-mortem-analysis. Moreover, they were in a much worse condition regarding capacitance and resistance than the cyclic aged cells of the same type. Therefore, no comparison in post mortem analysis of cells could be undertaken. New tests that allow comparing the calendric and the cyclic aging of the same cell type could give information about the additional contribution to EDLC aging due to cycling, and how it is influenced by current rate and voltage.

With the knowledge of the electrochemical processes caused by calendric and cyclic aging, a physical-based model can be developed that allows the detailed representation of storage processes as well as the aging processes at every single electrode.

#### 10. References

[1] C. Ashtiani, R. Wright, G. Hunt, Ultracapacitors for automotive applications, Journal of Power Sources 154 (2006) 561–566.

- [2] A. Burke, Ultracapacitor technologies and application in hybrid and electric vehicles, Int. J. Energy Res. 34 (2010) 133–151.
- [3] B.E. Conway, Electrochemical supercapacitors: Scientific fundamentals and technological applications, Plenum Press, New York, 1999.
- [4] A. Burke, Ultracapacitors: why, how, and where is the technology, Journal of Power Sources 91 (2000) 37–50.
- [5] P. Kurzweil, CAPACITORS | Electrochemical Double-Layer Capacitors, in: J. Garche (Ed.), Encyclopedia of Electrochemical Power Sources, Elsevier, 2009, pp. 607–633.
- [6] R. Kötz, M. Carlen, Principles and applications of electrochemical capacitors, Electrochimica Acta 45 (2000) 2483–2498.
- [7] P. Sharma, T.S. Bhatti, A review on electrochemical double-layer capacitors, Energy Conversion and Management 51 (2010) 2901–2912.
- [8] H. Budde-Meiwes, J. Drillkens, B. Lunz, J. Muennix, S. Rothgang, J. Kowal, D.U. Sauer, A review of current automotive battery technology and future prospects, Proceedings of the Institution of Mechanical Engineers, Part D: Journal of Automobile Engineering 227 (2013) 761–776.
- [9] D. Cericola, R. Kötz, Hybridization of rechargeable batteries and electrochemical capacitors: Principles and limits, Electrochimica Acta 72 (2012) 1–17.
- [10] P. Kurzweil, CAPACITORS | Electrochemical Hybrid Capacitors, in: J. Garche (Ed.), Encyclopedia of Electrochemical Power Sources, Elsevier, 2009, pp. 658–664.
- [11] D. Cericola, P.W. Ruch, R. Kötz, P. Novák, A. Wokaun, Simulation of a supercapacitor/Liion battery hybrid for pulsed applications, Journal of Power Sources 195 (2010) 2731–2736.
- [12] D. Cericola, P.W. Ruch, R. Kötz, P. Novák, A. Wokaun, Characterization of bi-material electrodes for electrochemical hybrid energy storage devices, Electrochemistry Communications 12 (2010) 812–815.
- [13] A.W. Golubkov, D. Fuchs, J. Wagner, H. Wiltsche, C. Stangl, G. Fauler, G. Voitic, A. Thaler, V. Hacker, Thermal-runaway experiments on consumer Li-ion batteries with metaloxide and olivin-type cathodes, RSC Adv 4 (2014) 3633–3642.
- [14] P.H. Smith, T.N. Tran, T.L. Jiang, J. Chung, Lithium-ion capacitors: Electrochemical performance and thermal behavior, Journal of Power Sources 243 (2013) 982–992.
- [15] V. Ruiz, S. Roldán, I. Villar, C. Blanco, R. Santamaría, Voltage dependence of carbon-based supercapacitors for pseudocapacitance quantification, Electrochimica Acta 95 (2013) 225–229.
- [16] J.P. Zheng, Ruthenium Oxide-Carbon Composite Electrodes for Electrochemical Capacitors, Electrochem. Solid-State Lett. 2 (1999) 359.
- [17] M. Mastragostino, C. Arbizzani, F. Soavi, Conducting polymers as electrode materials in supercapacitors, Solid State Ionics 148 (2002) 493–498.
- [18] B.E. Conway, V. Birss, J. Wojtowicz, The role and utilization of pseudocapacitance for energy storage by supercapacitors, Journal of Power Sources 66 (1997).
- [19] B.E. Conway, Transition from "Supercapacitor" to "Battery" Behavior in Electrochemical Energy Storage, Journal of The Electrochemical Society 138 (1991) 1539–1548.

- [20] E. Frackowiak, F. Béguin, Carbon materials for the electrochemical storage of energy in capacitors, Carbon 39 937–950.
- [21] P. Simon, Y. Gogotsi, Materials for electrochemical capacitors, Nat Mater 7 (2008) 845–854.
- [22] H. Helmholtz, Studien über electrische Grenzschichten, Ann. Phys. Chem. 243 (1879) 337–382.
- [23] D.L. Chapman, LI. A contribution to the theory of electrocapillarity, Philosophical Magazine Series 6 25 (1913) 475–481.
- [24] M. Gouy, Sur la constitution de la charge électrique à la surface d'un électrolyte, J. Phys. Theor. Appl. 9 (1910) 457–468.
- [25] O. Stern, Zur Theorie der elektrolytischen Doppelschicht, Zeitschrift für Elektrochemie und angewandte physikalische Chemie 30 (1924) 508–560.
- [26] C.H. Hamann, W. Vielstich, Elektrochemie, 4th ed., Wiley-VCH, Weinheim, 2005.
- [27] R.P. Richner, Entwicklung neuartig gebundener Kohlenstoffmaterialien für elektrische Doppelschichtkondensatorelektroden. Dissertation, 2001.
- [28] E. Pollak, G. Salitra, D. Aurbach, Can conductivity measurements serve as a tool for assessing pseudocapacitance processes occurring on carbon electrodes?, Journal of Electroanalytical Chemistry 602 (2007) 195–202.
- [29] V. Ruiz, C. Blanco, E. Raymundo-Piñero, V. Khomenko, F. Béguin, R. Santamaría, Effects of thermal treatment of activated carbon on the electrochemical behaviour in supercapacitors, Electrochimica Acta 52 (2007) 4969–4973.
- [30] B.E. Conway, W.G. Pell, Double-layer and pseudocapacitance types of electrochemical capacitors and their applications to the development of hybrid devices, Journal of Solid State Electrochemistry 7 (2003) 637–644.
- [31] W. Schmickler, E. Santos, Interfacial electrochemistry, 2nd ed., Springer, Berlin, London, 2010.
- [32] W. Schmickler, M. Lingner, Grundlagen der Elektrochemie, Vieweg, Braunschweig/Wiesbaden, 1996.
- [33] T. Morimoto, K. Hiratsuka, Y. Sanada, K. Kurihara, Electric double-layer capacitor using organic electrolyte, Journal of Power Sources 60 (1996) 239–247.
- [34] L. Wei, G. Yushin, Nanostructured activated carbons from natural precursors for electrical double layer capacitors, Nano Energy 1 (2012) 552–565.
- [35] C. Hu, W. Qu, R. Rajagopalan, C. Randall, Factors influencing high voltage performance of coconut char derived carbon based electrical double layer capacitor made using acetonitrile and propylene carbonate based electrolytes, Journal of Power Sources 272 (2014) 90–99.
- [36] D. Bhattacharjya, J.-S. Yu, Activated carbon made from cow dung as electrode material for electrochemical double layer capacitor, Journal of Power Sources 262 (2014) 224– 231.
- [37] D. Qu, Studies of the activated carbons used in double-layer supercapacitors, Journal of Power Sources 109 (2002) 403–411.
- [38] J.R. Dahn, W. Xing, Y. Gao, The "falling cards model" for the structure of microporous carbons, Carbon 35 (1997) 825–830.
- [39] A.G. Pandolfo, A.F. Hollenkamp, Carbon properties and their role in supercapacitors, Journal of Power Sources 157 (2006) 11–27.
- [40] A. Burke, R&D considerations for the performance and application of electrochemical capacitors, Electrochimica Acta 53 (2007) 1083–1091.

[41] F. Béguin, E. Frackowiak, Supercapacitors: Materials, systems, and applications, Wiley-VCH, Weinheim, op. 2013.

- [42] O. Barbieri, M. Hahn, A. Herzog, R. Kötz, Capacitance limits of high surface area activated carbons for double layer capacitors, Carbon 43 (2005) 1303–1310.
- [43] Du, C., Pan, N., Supercapacitors using carbon nanotubes films by electrophoretic deposition, Journal of Power Sources 160 (2006) 1487–1494.
- [44] C. Portet, P.L. Taberna, P. Simon, E. Flahaut, Influence of carbon nanotubes addition on carbon–carbon supercapacitor performances in organic electrolyte, Journal of Power Sources 139 (2005) 371–378.
- [45] E. Frackowiak, K. Metenier, V. Bertagna, F. Beguin, Supercapacitor electrodes from multiwalled carbon nanotubes, Appl. Phys. Lett. 77 (2000) 2421.
- [46] R. Signorelli, D.C. Ku, J.G. Kassakian, J.E. Schindall, Electrochemical Double-Layer Capacitors Using Carbon Nanotube Electrode Structures, Proc. IEEE 97 (2009) 1837–1847.
- [47] B. Fang, L. Binder, A modified activated carbon aerogel for high-energy storage in electric double layer capacitors, Journal of Power Sources 163 (2006) 616–622.
- [48] S.-W. Hwang, S.-H. Hyun, Synthesis and characterization of tin oxide/carbon aerogel composite electrodes for electrochemical supercapacitors, Journal of Power Sources.
- [49] D.-W. Wang, F. Li, M. Liu, G.Q. Lu, H.-M. Cheng, 3D Aperiodic Hierarchical Porous Graphitic Carbon Material for High-Rate Electrochemical Capacitive Energy Storage, Angew. Chem. Int. Ed. 47 (2008) 373–376.
- [50] X. Lu, H. Dou, B. Gao, C. Yuan, S. Yang, L. Hao, L. Shen, X. Zhang, A flexible graphene/multiwalled carbon nanotube film as a high performance electrode material for supercapacitors, Electrochimica Acta 56 (2001) 5115–5121.
- [51] D. Weingarth, D. Cericola, F. Mornaghini, T. Hucke, R. Kötz, Carbon additives for electrical double layer capacitor electrodes, Journal of Power Sources 266 (2014) 475–480.
- [52] J.P. Zheng, Resistance distribution in electrochemical capacitors with a bipolar structure, Journal of Power Sources 137 (2004) 158–162.
- [53] L.L. Zhang, X.S. Zhao, Carbon-based materials as supercapacitor electrodes, Chemical Society reviews 38 (2009) 2520–2531.
- [54] Gregory Salitra, Abraham Soffer, Linoam Eliad, Yair Cohen, and Doron Aurbach, Carbon Electrodes for Double-Layer Capacitors I. Relations Between Ion and Pore Dimensions, Journal of The Electrochemical Society 147 (2000) 2486–2493.
- [55] J. Kang, S.H. Jayaram, J. Rawlins, J. Wen, Characterization of thermal behaviors of electrochemical double layer capacitors (EDLCs) with aqueous and organic electrolytes, Electrochimica Acta 144 (2010) 200–210.
- [56] M. Arulepp, L. Permann, J. Leis, A. Perkson, K. Rumma, A. Jänes, E. Lust, Influence of the solvent properties on the characteristics of a double layer capacitor, Journal of Power Sources 133 (2004) 320–328.
- [57] T.-H. Wu, C.-T. Hsu, C.-C. Hu, L.J. Hardwick, Important parameters affecting the cell voltage of aqueous electrical double-layer capacitors, Journal of Power Sources 242 (2013) 289–298.
- [58] M. Ue, K. Ida, S. Mori, Electrochemical Properties of Organic Liquid Electrolytes Based on Quaternary Onium Salts for Electrical Double-Layer Capacitors, J. Electrochem. Soc. 141 (1994) 2989–2996.
- [59] J. Chmiola, C. Largeot, P.-L. Taberna, P. Simon, Y. Gogotsi, Desolvation of Ions in Subnanometer Pores and Its Effect on Capacitance and Double-Layer Theory, Angew. Chem. 120 (2008) 3440–3443.

- [60] A. Brandt, A. Balducci, Theoretical and practical energy limitations of organic and ionic liquid-based electrolytes for high voltage electrochemical double layer capacitors, Journal of Power Sources 250 (2014) 343–351.
- [61] A.M. Bittner, M. Zhu, Y. Yang, H.F. Waibel, M. Konuma, U. Starke, C.J. Weber, Ageing of electrochemical double layer capacitors, Journal of Power Sources 203 (2012) 262–273.
- [62] R. Lin, P.L. Taberna, J. Chmiola, D. Guay, Y. Gogotsi, P. Simon, Microelectrode Study of Pore Size, Ion Size, and Solvent Effects on the Charge/Discharge Behavior of Microporous Carbons for Electrical Double-Layer Capacitors, J. Electrochem. Soc. 156 (2009) A7.
- [63] S.I. Fletcher, F.B. Sillars, R.C. Carter, A.J. Cruden, M. Mirzaeian, N.E. Hudson, J.A. Parkinson, P.J. Hall, The effects of temperature on the performance of electrochemical double layer capacitors, Journal of Power Sources 195 (2010) 7484–7488.
- [64] A. Balducci, R. Dugas, P.L. Taberna, P. Simon, D. Plée, M. Mastragostino, S. Passerini, High temperature carbon–carbon supercapacitor using ionic liquid as electrolyte, Journal of Power Sources 165 (2007) 922–927.
- [65] M. Galinski, A. Lewandowski, I. Stepniak, Ionic liquids as electrolytes, Electrochimica Acta 151 (2006) 5567–5580.
- [66] A. Lewandowski, A. Olejniczak, M. Galinski, I. Stepniak, Performance of carbon–carbon supercapacitors based on organic, aqueous and ionic liquid electrolytes, Journal of Power Sources 195 (2010) 5814–5819.
- [67] T. Sato, G. Masuda, K. Takagi, Electrochemical properties of novel ionic liquids for electric double layer capacitor applications, Electrochimica Acta 49 (2004) 3603–3611.
- [68] D. Cericola, P.W. Ruch, A. Foelske-Schmitz, D. Weingarth, R. Kötz, Effect of Water on the Aging of Activated Carbon Based Electrochemical Double Layer Capacitors During Constant Voltage Load Tests, International Journal of Elctrochemical Science 6 (2011) 988– 996.
- [69] K. Tonurist, T. Thomberg, A. Jänes, T. Romann, V. Sammelselg, E. Lust, Influence of separator properties on electrochemical performance of electrical double-layer capacitors, Journal of Electroanalytical Chemistry 689 (2013) 8–20.
- [70] IEC (2006) 62391-1, Fixed electric double-layer capacitors for use in electronic equipment –Part 1: Generic specification, 1st ed., 2006.
- [71] A. Chu, Comparison of commercial supercapacitors and high-power lithium-ion batteries for power-assist applications in hybrid electric vehicles I. Initial characterization, Journal of Power Sources 112 (2002) 236–246.
- [72] J. Kowal, E. Avaroglu, F. Chamekh, A. Šenfelds, T. Thien, D. Wijaya, D.U. Sauer, Detailed analysis of the self-discharge of supercapacitors, Journal of Power Sources 196 (2011) 573–579.
- [73] E. Barsoukov, J.R. Macdonald, Impedance spectroscopy: Theory, experiment, and applications, 2nd ed., John Wiley & sons, New York, 2005.
- [74] A. Burke, M. Miller, Testing of electrochemical capacitors: Capacitance, resistance, energy density, and power capability, Electrochimica Acta 55 (2010) 7538–7548.
- [75] H. Keiser, K.D. Beccu, M.A. Gutjahr, Abschätzung der Porenstruktur poröser Elektroden aus Impedanzmessungen, Electrochimica Acta 21 (1976) 539–543.
- [76] P.L. Taberna, P. Simon, Fauvarque, Electrochemical Characteristics and Impedance Spectroscopy Studies of Carbon-Carbon Supercapacitors, Journal of The Electrochemical Society 150 (2003) A292-A300.
- [77] J. Chmiola, G. Yushin, R. Dash, Y. Gogotsi, Effect of pore size and surface area of carbide derived carbons on specific capacitance, Journal of Power Sources 158 (2006) 765–772.

[78] H.D. Yoo, J.H. Jang, B.H. Ka, C.K. Rhee, S.M. Oh, Impedance analysis for hydrogen adsorption pseudocapacitance and electrochemically active surface area of Pt electrode, Langmuir the ACS journal of surfaces and colloids 25 (2009) 11947–11954.

- [79] J.H. Jang, S. Yoon, B.H. Ka, Y.-H. Jung, S.M. Oh, Complex Capacitance Analysis on Leakage Current Appearing in Electric Double-layer Capacitor Carbon Electrode, J. Electrochem. Soc. 152 (2005) A1418.
- [80] H. Blanke, O. Bohlen, S. Buller, R.W. de Doncker, B. Fricke, A. Hammouche, D. Linzen, M. Thele, D.U. Sauer, Impedance measurements on lead—acid batteries for state-of-charge, state-of-health and cranking capability prognosis in electric and hybrid electric vehicles, Journal of Power Sources 144 (2005) 418–425.
- [81] S. Yoon, C.W. Lee, S.M. Oh, Characterization of equivalent series resistance of electric double-layer capacitor electrodes using transient analysis, Journal of Power Sources 195 (2010) 4391–4399.
- [82] R. Kötz, M. Hahn, R. Gallay, Temperature behavior and impedance fundamentals of supercapacitors, Journal of Power Sources 154 (2006) 550–555.
- [83] R. de Levie, On porous electrodes in electrolyte solutions: I. Capacitance effects, Electrochimica Acta 8 (1963) 751–780.
- [84] R. de Levie, On porous electrodes in electrolyte solutions—IV, Electrochimica Acta 9 (1964) 1231–1245.
- [85] R. de Levie, Fractals and rough electrodes, Journal of Electroanalytical Chemistry and Interfacial Electrochemistry 281 (1990) 1–21.
- [86] D. Qu, H. Shi, Studies of activated carbons used in double-layer capacitors, Journal of Power Sources 74 (1998) 99–107.
- [87] H. Shi, Activated carbons and double layer capacitance, Electrochimica Acta 41 (1996) 1633–1639.
- [88] B.W. Ricketts, C. Ton-That, Self-discharge of carbon-based supercapacitors with organic electrolytes, Journal of Power Sources 89 (2000) 64–69.
- [89] J. Niu, B.E. Conway, W.G. Pell, Comparative studies of self-discharge by potential decay and float-current measurements at C double-layer capacitor and battery electrodes, Journal of Power Sources 135 (2004) 332–343.
- [90] M. Kaus, J. Kowal, D.U. Sauer, Modelling the effects of charge redistribution during self-discharge of supercapacitors, Electrochimica Acta 55 (2010) 7516–7523.
- [91] O. Bohlen, J. Kowal, D.U. Sauer, Ageing behaviour of electrochemical double layer capacitors, Journal of Power Sources 172 (2007) 468–475.
- [92] S. Buller, Impedance based simulation models for energy storage devices in advanced automotive power systems. Dissertation, Shaker, Aachen.
- [93] S. Buller, M. Thele, R. DeDoncker, E. Karden, Impedance-Based Simulation Models of Supercapacitors and Li-Ion Batteries for Power Electronic Applications, IEEE Trans. on Ind. Applicat. 41 (2005) 742–747.
- [94] L. Zubieta, R. Bonert, Characterization of double-layer capacitors for power electronics applications, IEEE Trans. on Ind. Applicat. 36 (2000) 199–205.
- [95] J. Kang, J. Wen, S.H. Jayaram, A. Yu, X. Wang, Development of an equivalent circuit model for electrochemical double layer capacitors (EDLCs) with distinct electrolytes, Electrochimica Acta 115 (2014) 587–598.
- [96] F. Belhachemi, S. Rael, B. Davat, A physical based model of power electric double-layer supercapacitors, in: World Congress on Industrial Applications of Electrical Energy and 35th IEEE-IAS Annual Meeting, Rome, Italy, 8-12 Oct. 2000, pp. 3069–3076.

- [97] N. Devillers, S. Jemei, M.-C. Péra, D. Bienaimé, F. Gustin, Review of characterization methods for supercapacitor modelling, Journal of Power Sources 246 (2014) 596–608.
- [98] P. Guillemet, C. Pascot, Y. Scudeller, Compact thermal modeling of Electric Double-Layer-Capacitors, in: 2008 14th International Workshop on Thermal Inveatigation of ICs and Systems (THERMINIC), Rome, Italy, pp. 118–122.
- [99] P. Guillemet, C. Pascot, Y. Scudeller, Electro-thermal analysis of Electric Double-Layer-Capacitors, in: 2008 14th International Workshop on Thermal Inveatigation of ICs and Systems (THERMINIC), Rome, Italy, pp. 224–228.
- [100] A. d'Entremont, L. Pilon, First-principles thermal modeling of electric double layer capacitors under constant-current cycling, Journal of Power Sources 246 (2014) 887–898.
- [101] H. Gualous, H. Louahlia, R. Gallay, Supercapacitor Characterization and Thermal Modelling With Reversible and Irreversible Heat Effect, IEEE Trans. Power Electron. 26 (2011) 3402–3409.
- [102] J. Schiffer, D. Linzen, D.U. Sauer, Heat generation in double layer capacitors, Journal of Power Sources 160 (2006) 765–772.
- [103] Y. Dandeville, P. Guillemet, Y. Scudeller, O. Croisnier, L. Athouel, T. Brousse, Measuring time-dependent heat profiles of aqueous electrochemical capacitors under cycling, Thermochimica Acta 526 (2011) 1–8.
- [104] Verein Deutscher Ingenieure, VDI-Wärmeatlas: Berechnungsblätter für den Wärmeübergang, 6th ed., VDI-Verl., Düsseldorf, 1991.
- [105] W. Wagner, Wärmeübertragung, 7th ed., Vogel Business Media, Würzburg, 2011.
- [106] Y.A. Çengel, Heat and mass transfer: A practical approach, 3rd ed., McGraw-Hill, Boston, ©2007.
- [107] P.W. Ruch, D. Cericola, A. Foelske, R. Kötz, A. Wokaun, A comparison of the aging of electrochemical double layer capacitors with acetonitrile and propylene carbonate-based electrolytes at elevated voltages, Electrochimica Acta 55 (2010) 2352–2357.
- [108] P.W. Ruch, D. Cericola, A. Foelske-Schmitz, R. Kötz, A. Wokaun, Aging of electrochemical double layer capacitors with acetonitrile-based electrolyte at elevated voltages, Electrochimica Acta 55 (2010) 4412–4420.
- [109] O. Bohlen, J. Kowal, Dirk Uwe Sauer, Ageing behaviour of electrochemical double layer capacitors, Journal of Power Sources 173 (2007) 626–632.
- [110] P. Kurzweil, M. Chwistek, Electrochemical stability of organic electrolytes in supercapacitors: Spectroscopy and gas analysis of decomposition products, Journal of Power Sources 176 (2008) 555–567.
- [111] S. Ishimoto, Y. Asakawa, M. Shinya, K. Naoi, Degradation Responses of Activated-Carbon-Based EDLCs for Higher Voltage Operation and Their Factors, J. Electrochem. Soc. 156 (2009) A563.
- [112] M. Hahn, R. Kötz, R. Gallay, A. Siggel, Pressure evolution in propylene carbonate based electrochemical double layer capacitors, Electrochimica Acta 52 (2006) 1709– 1712.
- [113] R. Kötz, M. Hahn, P. Ruch, R. Gallay, Comparison of pressure evolution in supercapacitor devices using different aprotic solvents, Electrochemistry Communications 10 (2008) 359–362.
- [114] P. Azaïs, L. Duclaux, P. Florian, D. Massiot, M.-A. Lillo-Rodenas, A. Linares-Solano, J.-P. Peres, C. Jehoulet, F. Béguin, Causes of supercapacitors ageing in organic electrolyte, Journal of Power Sources 171 (2007) 1046–1053.

[115] M. Zhu, C.J. Weber, Y. Yang, M. Konuma, U. Starke, K. Kern, A.M. Bittner, Chemical and electrochemical ageing of carbon materials used in supercapacitor electrodes, Carbon 46 (2008) 1829–1840.

- [116] P. Kurzweil, M. Chwistek, R. Gallay (Eds.), Capacitance Determination and Abusive Aging Studies of Supercapacitors Based on Acetonitrile and Ionic Liquids, 2006.
- [117] K. Chiba, T. Ueda, Y. Yamaguchi, Y. Oki, F. Shimodate, K. Naoi, Electrolyte Systems for High Withstand Voltage and Durability: I. Linear Sulfones for Electric Double-Layer Capacitors, J. Electrochem. Soc. 158 (2011) A872-A882.
- [118] H. Ye, N. Naguib, Y. Gogotsi, TEM Study of Water in Carbon Nanotubes, Jeol News 39 (2004) 2–7.
- [119] M. Ayadi, O. Briat, A. Eddahech, R. German, G. Coquery, J.M. Vinassa, Thermal cycling impacts on supercapacitor performances during calendar ageing, Microelectronics Reliability 53 (2013) 1628–1631.
- [120] H. Gualous, R. Gallay, G. Alcicek, B. Tala-Ighil, A. Oukaour, B. Boudart, P. Makany, Supercapacitor ageing at constant temperature and constant voltage and thermal shock, Microelectronics Reliability 50 (2010) 1783–1788.
- [121] H. Gualous, R. Gallay, M. Al Sakka, A. Oukaour, B. Tala-Ighil, B. Boudart, Calendar and cycling ageing of activated carbon supercapacitor for automotive application, Microelectronics Reliability 52 (2012) 2477–2481.
- [122] D.-H. Hwang, J.-W. Park, J.-H. Jung, A study on the lifetime comparison for Electric Double Layer Capacitors using Accelerated Degradation Test, in: 2011 International Conference on Quality, Reliability, Risk, Maintenance, and Safety Engineering (ICQR2MSE), Xi'an, China, pp. 302–307.
- [123] R. Kötz, P.W. Ruch, D. Cericola, Aging and failure mode of electrochemical double layer capacitors during accelerated constant load tests, Journal of Power Sources 195 (2010) 923–928.
- [124] A. Oukaour, B. Tala-Ighil, M. AlSakka, H. Gualous, R. Gallay, B. Boudart, Calendar ageing and health diagnosis of supercapacitor, Electric Power Systems Research 95 (2013) 330–338.
- [125] D. Weingarth, A. Foelske-Schmitz, R. Kötz, Cycle versus voltage hold Which is the better stability test for electrochemical double layer capacitors?, Journal of Power Sources 225 (2013) 84–88.
- [126] O. Bohlen, Impedance-based battery monitoring. Dissertation, Shaker, Aachen.
- [127] M. Hahn, A. Würsig, R. Gallay, P. Novák, R. Kötz, Gas evolution in activated carbon/propylene carbonate based double-layer capacitors, Electrochemistry Communications 7 (2005) 925–930.
- [128] M. Hahn, O. Barbieri, R. Gallay, R. Kötz, A dilatometric study of the voltage limitation of carbonaceous electrodes in aprotic EDLC type electrolytes by charge-induced strain, Carbon 44 (2006) 2523–2533.
- [129] M. Hahn, O. Barbieri, F.P. Campana, R. Kötz, R. Gallay, Carbon based double layer capacitors with aprotic electrolyte solutions: the possible role of intercalation/insertion processes, Appl. Phys. A 82 (2006) 633–638.
- [130] C. Pascot, Y. Dandeville, Y. Scudeller, P. Guillemet, T. Brousse, Calorimetric measurement of the heat generated by a Double-Layer Capacitor cell under cycling, Thermochimica Acta 510 (2010) 53–60.
- [131] O. Briat, W. Lajnef, J.M. Vinassa, E. Woirgard, Power cycling tests for accelerated ageing of ultracapacitors, Microelectronics Reliability 46 (2006) 1445–1450.

- [132] R. Chaari, O. Briat, J.Y. Delétage, J.M. Vinassa, Power Electronics and Applications (EPE 2011), proceedings of the 2011-14th European Conference on: Aug. 30 2011-Sept. 1 2011. Performances regeneration of supercapacitors during accelerated ageing tests in power cycling, IEEE, Piscataway, NJ, 2011.
- [133] R. Chaari, O. Briat, J.Y. Delétage, R. Lallemand, J. Kauv, G. Coquery, J.M. Vinassa (Eds.), Ageing Quantification of Supercapacitors During Power Cycling Using Online and Periodic Characterization Tests, 2011.
- [134] D. Torregrossa, K.E. Toghill, H.H. Girault, M. Paolone, Understanding the ageing process, recovering phase and fault diagnosis of electrochemical double layer capacitors, in: 2014 IEEE Conference on Technologies for Sustainability (SusTech), Portland, OR, USA, pp. 239–244.
- [135] P.W. Ruch, M. Hahn, F. Rosciano, M. Holzapfel, H. Kaiser, W. Scheifele, B. Schmitt, P. Novák, R. Kötz, A. Wokaun, In situ X-ray diffraction of the intercalation of (C2H5)4N+ and BF4– into graphite from acetonitrile and propylene carbonate based supercapacitor electrolytes, Electrochimica Acta 53 (2007) 1074–1082.
- [136] L.J. Hardwick, M. Hahn, P. Ruch, M. Holzapfel, W. Scheifele, H. Buqa, F. Krumeich, P. Novák, R. Kötz, An in situ Raman study of the intercalation of supercapacitor-type electrolyte into microcrystalline graphite, Electrochimica Acta 52 (2006) 675–680.
- [137] L.J. Hardwick, P.W. Ruch, M. Hahn, W. Scheifele, R. Kötz, P. Novák, In situ Raman spectroscopy of insertion electrodes for lithium-ion batteries and supercapacitors: First cycle effects, Journal of Physics and Chemistry of Solids 69 (2008) 1232–1237.
- [138] S. Brunauer, P.H. Emmett, E. Teller, Adsorption of Gases in Multimolecular Layers, J. Am. Chem. Soc. 60 (1938) 309–319.
- [139] J. Rouquerol, D. Avnir, C.W. Fairbridge, D.H. Everett, J.M. Haynes, N. Pernicone, Ramsay, J. D. F., Sing, K. S. W., K.K. Unger, Recommendations for the characterization of porous solids (Technical Report), Pure and Applied Chemistry 66 (1994).
- [140] M. Luisa Ojeda, J. Marcos Esparza, A. Campero, S. Cordero, I. Kornhauser, F. Rojas, On comparing BJH and NLDFT pore-size distributions determined from N2 sorption on SBA-15 substrata, Phys. Chem. Chem. Phys. 5 (2003) 1859.
- [141] C. Arbizzani, M. Biso, D. Cericola, M. Lazzari, F. Soavi, M. Mastragostino, Safe, high-energy supercapacitors based on solvent-free ionic liquid electrolytes, Journal of Power Sources 185 (2008) 1575–1579.
- [142] Y. Wen, J. Cheng, G. Cao, Y. Yang, Matching ratio between positive and negative electrodes for double-layer capacitors, J Appl Electrochem 37 (2007) 543–548.
- [143] D. Cericola, R. Kötz, A. Wokaun, Effect of electrode mass ratio on aging of activated carbon based supercapacitors utilizing organic electrolytes, Journal of Power Sources 196 (2011) 3114–3118.
- [144] H.D. Yoo, J.H. Jang, J.H. Ryu, Y. Park, S.M. Oh, Impedance analysis of porous carbon electrodes to predict rate capability of electric double-layer capacitors, Journal of Power Sources 267 (2014) 411–420.
- [145] W.G. Pell, B.E. Conway, N. Marincic, Analysis of non-uniform charge/discharge and rate effects in porous carbon capacitors containing sub-optimal electrolyte concentrations, Journal of Electroanalytical Chemistry 491 (2000) 9–21.
- [146] C. Portet, P.L. Taberna, P. Simon, C. Laberty-Robert, Modification of Al current collector surface by sol-gel deposit for carbon-carbon supercapacitor applications, Electrochimica Acta 49 (2004) 905–912.

[147] Y.-R. Nian, H. Teng, Influence of surface oxides on the impedance behavior of carbon-based electrochemical capacitors, Journal of Electroanalytical Chemistry 540 (2003) 119–127.

- [148] J.H. Jang, S.M. Oh, Complex Capacitance Analysis of Porous Carbon Electrodes for Electric Double-Layer Capacitors, J. Electrochem. Soc. 151 (2004) A571-A577.
- [149] J. Kowal, Spatially-resolved impedance of nonlinear inhomogeneous devices: [using the example of lead-acid batteries]. Dissertation, Shaker, Aachen, 2010.
- [150] J. Schmalstieg, M. Ecker, S. Käbitz, D.U. Sauer, A holistic aging model for Li(NiMnCo)O2 based 18650 lithium-ion batteries, Journal of Power Sources 257 (2014) 325–334.

#### A. Appendix

#### A.1 Constants

F	Faraday's constant, 96,485 As/mol
R	Gas constant, 8.314 J/(mol K)
k	Boltzmann's constant, $k=R/N_A$ , 1.38·10 <sup>-23</sup> J/K
$arepsilon_0$	Electric field constant, 8.854·10 <sup>-12</sup> F/m
е	Elementary charge, 1.602·10 <sup>-19</sup> C
N <sub>A</sub>	Avogadro's constant, 6.022·10 <sup>23</sup> mol <sup>-1</sup>
σ	Stefan-Boltzmann's constant, 5.67·10 <sup>-8</sup> W/(m <sup>2</sup> K <sup>4</sup> )

#### A.2 Glossary

End of Life (EOL) means the criteria that are commonly used to define the end of EDLCs lifetime (20% capacitance loss or doubling of the internal resistance) (see chapter 7.2).

End of Test (EOT) means the criteria that define e.g. the capacitance loss or resistance increase that have to be reached until the calendric or cyclic aging test is stopped (see chapter 7.2).

*Impedance* means the complex electrical impedance obtained by impedance spectroscopy (see chapter 3.1.2.1).

State of charge (SOC) is defined as the actual capacity of a battery (or EDLC) minus the ready discharged capacity divided by the nominal capacity. The actual capacity can vary with temperature and discharge current.

State of health (SOH) is defined as the available capacity of a battery (or EDLC) (at 100% SOC, nominal temperature and nominal discharge current) divided by the nominal capacity. This value is typically given in % and decreases with aging. For a new battery (or EDLC), this value can be larger than 100%.

#### A.3 Abbreviations

AC	alternating current
AN	Acetonitrile
BET	Brunauer–Emmett–Teller theory (used for determining the internal surface area of electrode materials)
ВЈН	Barret-Joyner-Halenda analysis
СРЕ	constant-phase-element
DC	direct current
EDLC	electrochemical double layer capacitor
EDX	X-ray spectroscopy
EIS	electrochemical impedance spectroscopy
EOL	end of life
EOT	end of test
ESR	equivalent series resistance
FDM	finite difference method
HF	hydrofluoric acid
IL	ionic liquid
ISEA	Institute for Power Electronics and Electrical Drives
КОН	potassium hydroxide
LIB	Lithium ion battery
LIC	Lithium ion capacitor
NLDFT	non-local density functional theory
NMP	N-Methyl-2-pyrrolidon

PC	propylene carbonate
PP	Polypropylene
PTFE	Polytetrafluoroethylene
RWV	rated working voltage
SEI	solid electrolyte interface
SEM	scanning electron microscopy
SOC	state of charge
SOH	state of health
TBF <sup>-</sup>	Tetrafluroroborate
TEA <sup>+</sup>	tetraethyl ammonium
TEABF	tetraethyl ammonium tetrafluroroborate
UPS	uninterruptable power supply
XRD	X-ray diffraction

#### A.4 Derivation of equation (3.12) for the complex capacitance analysis

If an electrochemical system satisfies causality, linearity, stability, and convergence, the real and imaginary parts of a complex function  $F(\omega) = F'(\omega) + jF''(\omega)$  are correlated according to Kramers-Kronig relation:

$$F'(W) - F'(\infty) = -\left(\frac{2}{\pi}\right) \int_0^\infty \frac{[XF''(X) - WF''(W)] dX}{X^2 - W^2}$$

Here,  $W \equiv \omega \tau_0$ ,  $X \equiv x/x_0$  and the values of  $\tau_0 = 1/(2\pi f_0)$  and  $x_0$  are arbitrary. The real and imaginary parts of complex capacitance are further correlated as follows:

$$C'(0) - C'(\infty) = -\left(\frac{2}{\pi}\right) \int_0^\infty \frac{[XC''(X)]dX}{X^2}$$
$$= -\left(\frac{2}{\pi}\right) \int_{-\infty}^\infty C''(X)d[\ln X]$$

With x=f Hz and  $x_0=1$  Hz, then

$$C'(0) = C'(\infty) - \left(\frac{2}{\pi}\right) \int_{-\infty}^{\infty} C''(f) d[\ln f]$$

$$=C'(\infty)-2.303\left(\frac{2}{\pi}\right)\int_{-\infty}^{\infty}C''(f)d[\log f]$$

For a finite value of  $Z(\infty)=R_{\rm ESR}$ ,  $C'(0)=C_{\rm tot}$  and  $C'(\infty)=C''(\infty)=0$  are valid. Thus, the total capacitance is expressed as

$$C_{\text{tot}} = -1.466 \int_{-\infty}^{\infty} C''(f) d[\log f]$$

Therefore, the area of capacitive peak on the imaginary capacitance plots (vs  $\log f$ ) has a linear relationship with the total capacitance of the electrochemical system.

#### A.5 Publications

#### Journals with peer-review

Grzegorz Pilatowicz, Andrea Marongiu, Julia Drillkens, Philipp Sinhuber, *A critical overview of definitions and determination techniques of the internal resistance using lithium-ion, lead-acid, nickel metal-hydride batteries and electrochemical double layer capacitors as examples,* Journal of Power Sources, Vol. 296, No. 1, pp. 365-376, 2015

Heide Budde-Meiwes, Julia Drillkens, Benedikt Lunz, Jens Münnix, Susanne Rothgang, Julia Kowal, Dirk Uwe Sauer, *A Review of Current Automotive Battery Technology and Future Prospects*, Institution of Mechanical Engineers, Part D: Journal of Automobile Engineering, Vol. 227, No. 5, pp. 761-776, 2013

Dominik Schulte, Julia Drillkens, Bjoern Schulte, Dirk Uwe Sauer, *Nafion Hybrid Membranes* for Use in Redox Flow Batteries, Journal of the Electrochemical Society, Vol. 157, No. 9, pp. A989-A992, 2010

#### Journals without peer-review

Julia Kowal, Julia Drillkens, Dirk Uwe Sauer, *Superkondensatoren – Elektrochemische Doppelschichtkondensatoren*, MTZ Motortechnische Zeitschrift, Vol. 74, Jahrgang, No 02, pp. 158-163, 2013

#### **Books**

Julia Kowal, Julia Drillkens, Dirk Uwe, Sauer, *Die Elektrifizierung des Antriebsstrangs*, pp. 68-76, ISBN: 9783658046446,

#### Conference publications

Julia Drillkens, Florian Krause, Julia Kowal, Dirk Uwe Sauer, *Prediction of Self-Discharge Behavior of Supercapacitors Using Impedance Spectroscopy*, ISEECAP 2013, June 2013, Taormina, Italy

Julia Drillkens, Tjark Thien, Danielle Hangue, Julia Kowal, Dirk Uwe Sauer, *Impedance-Based Electro-Thermal Model for Supercapacitor Modules for Optimum System Design*, AABC, February 2013, Pasadena, CA, USA

Julia Drillkens, Yusuf Yurdagel, Jiahua Zhang, Julia Kowal, Dirk Uwe Sauer, *Investigation of Cyclic Ageing of Electrochemical Double Layer Capacitors*, Power our Future, Vitoria-Gasteiz, March 2012, Spain

Julia Drillkens, Yusuf Yurdagel, Julia Kowal, Dirk Uwe Sauer, *Maximizing the lifetime of electrochemical double layer capacitors at given temperature conditions by optimized operating strategies*, 4th European Symposium on Super Capacitors & Applications, ESSCAP 2010, October 2010, Bordeaux, France

Julia Drillkens, Florian Krause, Julia Kowal, Dirk Uwe Sauer, *Investigation of the Relationship between Model Parameterization of Supercapacitors by Using Self-discharge and Impedance Measurements*, Kraftwerk Batterie, February 2013, Aachen, Germany

Julia Drillkens, Yusuf Yurdagel, Julia Kowal, Dirk Uwe Sauer, *Ageing Behavior and Operating Strategies for Lifetime Maximization of Electrochemical Double Layer Capacitors*, Kraftwerk Batterie, March 2011, Aachen, Germany

Julia Drillkens, Yusuf Yurdagel, Julia Kowal, Dirk Uwe Sauer, *Electrochemical Double Layer Capacitors: Electrical Behavior, Applications and Lifetime*, International Renewable Energy Storage Conference, IRES, November 2010, Berlin, Germany

Julia Drillkens, Dominik Schulte, Dirk Uwe Sauer, Long-Term Stability of Nafion Hybrid Membranes for Use in Vanadium Redox-Flow Batteries, ECS Transactions, April 2010, Vancouver, Canada

#### **Patents**

Florian Neumann, Thomas Gerhard Grieß, Julia Drillkens, Karolina Caban-Kucharczyk, Dirk Uwe Sauer, Energiespeichervorrichtung mit mindestens einer Speicherzelle und Verfahren zur Volumenkompensation von Elektrodenmaterialien einer derartigen Speicherzelle, DE 102012101265 A1, 22.08.2013

#### B. Deutsche Zusammenfassung

#### B.1 Einleitung

Elektrochemische Doppelschicht Kondensatoren werden aufgrund ihrer hohen Leistungsdichte und Zyklenlebensdauer in vielen Bereichen eingesetzt. Doch obwohl das Energiespeicherprinzip rein elektrostatisch ist, führen parasitäre elektrochemische Reaktionen zur Alterung der Zelle. Mit der Kenntnis der Einflussfaktoren dieser Alterungsprozesse ist eine Lebensdauerprognose möglich. Dazu wird ein elektrisch-thermisches Alterungsmodell benötigt wie es in dieser Dissertation entwickelt wird. Es muss das durch die komplexe Porenstruktur von EDLCs bedingte elektrische Verhalten abbilden können wie auch die durch den Strom generierte Wärme sowie den Wärme-Transfer. Durch die zusätzliche Abbildung der Alterung, kann mittels eines solchen Modells der Alterungszustand der einzelnen Zellen im Modul, bedingt durch die Betriebs- und Umweltbedingungen, bestimmt und eine Lebensdauerprognose abgegeben werden. Zur Parametrierung eines solchen Alterungsmodells müssen allerdings die Einflussfaktoren der Alterung bekannt sein. Typischerweise werden sie mithilfe von stark beschleunigten Alterungstests bestimmt um in möglichst kurzer Zeit Ergebnisse zu produzieren. In dieser Arbeit soll durch lang andauernde und umfangreiche Alterungstests untersucht werden wie valide solche Testergebnisse zur Modellparametrierung verwendet werden können.

Zunächst wird in Kapitel 2 auf die Grundlagen von EDLCs, deren Funktionsprinzip wie auch die möglichen Zellmaterialien und deren Eigenschaften eingegangen. Anschließend werden in Kapitel 3 verschiedenen Charakterisierungsmethoden vorgestellt und die elektrischen Eigenschaften verschiedener Zelltypen verglichen. In Kapitel 4 wird dann auf die komplexe Porenstruktur von EDLCs eingegangen und die Ionen-Umverteilungsprozesse anhand von Selbstentlade-Messreihen erklärt. Weiterhin werden in Kapitel 5 verschiedene Ansätze zur elektrischen Modellierung diskutiert. Insbesondere werden Modellansätze zur Abbildung der Spannungsrelaxationsprozesse durch die Ionen-Umverteilungsprozesse in den Poren untersucht und ein Modellansatz entwickelt, der es erlaubt sowohl hoch dynamische Prozess wie auch über Wochen dauernde Selbstentlademessungen abzubilden. Aufbauend auf den elektrischen Modellansätzen wird dann in Kapitel 6 ein elektro-thermisches Modell entwickelt, das flexibel auf verschiedene Modulanordnungen angepasst werden kann. Abschließend wird dann in Kapitel 7 das Alterungsverhalten mithilfe von umfassenden kalendarischen und zyklischen Alterungstests sowie einer Post-Mortem-Analyse ausgewählter Zellen untersucht. Die Ergebnisse der beschleunigten Alterungstests fließen dann in ein modulares elektro-thermisches Alterungsmodell ein.

#### B.2 Grundlagen

In dieser Dissertation werden in erster Linie elektrochemische Doppelschichtkondensatoren betrachtet, die Energie durch die Ausrichtung von Ionen im Elektrolyten elektrostatisch speichern. Beim Laden bildet sich an der Elektrode/Elektrolyt-Grenzschicht eine sogenannte Helmholtz-Schicht aus. Unter der Berücksichtigung einer diffusen Elektrolytschicht (Gouy-Chapman) und einer Solvationshülle (Stern) kann der Potentialverlauf entlang der Elektrode ermittelt werden.

EDLCs sind kommerziell auch oft unter dem Namen Supercaps oder Superkondensatoren in verschiedenen Geometrien, zylindrisch oder prismatisch, erhältlich. Der Begriff Superkondensatoren wird hier allerdings als Überbegriff für die Kondensatoren-Gruppe, zu der neben EDLCs auch Hybrid-Kondensatoren wie auch Pseudokondensatoren gehören, benutzt. Hybrid-Kondensatoren kombinieren eine Kondensator-Elektrode mit einer Batterie-Elektrode. Die häufigste Variante ist der sogenannte Lithium-Ionen-Kondensator (LIC), der aus EDLC-Kohlenstoffelektrode und einer Graphit-Interkalations-Elektrode besteht. Dazu werden Lithium enthaltende Elektrolyte verwendet. LICs können zu weitaus höheren Spannungen geladen werden als EDLCs (> 4 V zu < 3 V) und besitzen daher eine deutlich höhere Energiedichte. Allerdings zeigen sie ein schlechtes Tieftemperaturverhalten.

Eine weitere Gruppe sind Pseudokondensatoren. Dabei wird die Energie nicht elektrostatisch, sondern durch Adsorptionsprozesse oder Redoxreaktionen gespeichert. Kommerziell werde sie jedoch kaum verwendet, da die Elektrodenmaterialien, Metalloxide wie Rutheniumoxid, sehr teuer sind.

In kommerziellen EDLCs wird heutzutage in erster Linie aktivierter Kohlenstoff als Elektrodenmaterial kombiniert mit Bindermaterial und Leitfähigkeitszusätzen eingesetzt. Durch thermische oder chemische Aktivierungsprozesse wird die Oberfläche des Materials stark erhöht. Jedoch ist darauf zu achten, dass die entstehende Porenstruktur auch zu den Ionengrößen des Elektrolyten passt. Als Separator wird oft ein Zellulose-basierter Papier-Separator eingesetzt. Wegen der höheren Beständigkeit wird er mittlerweile allerdings häufig durch einen Kunststoff-Separator ersetzt. Der am häufigsten eingesetzte Elektrolyt ist TEABF gelöst in organischem Lösungsmittel wie Acetonitril oder Propylencarbonat. Er zeichnet sich durch eine gute Leitfähigkeit auch bei tiefen Temperaturen aus. Wässriger Elektrolyt wird wegen seiner geringen Spannungsfestigkeit (ca. 1,4 V im Vergleich zu 2,8 V bei organischem Elektrolyt) kommerziell praktisch nicht eingesetzt. Neuerdings wird auch viel im Bereich Ionischer Flüssigkeiten (IL) als EDLC-Elektrolyt geforscht. Mithilfe von ILs sind deutlich höhere Zellspannungen und damit auch höhere Energiedichten möglich. Allerdings gibt es Probleme mit der elektrischen Performance bei niedrigen Temperaturen aufgrund der hohen Viskosität in diesem Temperaturbereich.

#### B.3 Elektrische Charakterisierung

Bei den Charakterisierungsmethoden zur Bestimmung z.B. von Kapazität und Widerstand eines EDLCs kann generell zwischen DC und AC-Methoden unterschieden werden. Bei der DC-Methode wird die Kapazität anhand eines Steigungsdreiecks des Spannungsverlaufs bei der Entladung oder anhand des Integrals über den Entladestrom bestimmt, der Widerstand dagegen über den ohmschen Spannungsabfall zu Beginn der Entladung. Durch das Einprägen eines Wechselstromsignals bei einer bestimmten Frequenz, typischerweise 100 HZ oder 1000 Hz, kann der AC-Widerstand bestimmt werden. Dieser Wert ist in der Regel geringer als der DC-Widerstand. Allgemein zeigen experimentelle Ergebnisse, dass der gemessene Wert von Kapazität und Widerstand stark von der Messmethodik und den Messbedingungen abhängt.

Darüber hinaus ist die elektrochemische Impedanzspektroskopie (EIS) ein hilfreiches Mittel um das dynamische Verhalten von EDCLs zu charakterisieren. Hierbei wird ein sinusförmiges Wechselstrom- oder Wechselspannungssignal über einen weiten Frequenzbereich auf den Prüfling eingeprägt und über die Antwort des Systems die komplexe Impedanz des Prüflings bestimmt. Ein EDLC zeigt nur bei sehr hohen Frequenzen leicht induktives Verhalten in erster Linie bedingt durch Kabel und Anschlüsse, zeigt dann bei mittleren Frequenzen einen 45°-Ast im Nyquist-Plot der durch Diffusionsprozesse in den Poren verursacht wird, um sich dann bei tiefen Frequenzen nahezu rein kapazitiv zu verhalten.

Kommerzielle EDCLs mit unterschiedlichen Lösungsmitteln im Elektrolyten zeigen bei EIS Untersuchungen deutliche Unterschiede. EDCLs, die Acetonitril (AN) verwenden, besitzen aufgrund der höheren Leitfähigkeit einen geringeren Innenwiderstand und schnellere Diffusionsprozesse im Vergleich zu EDLCs mit Propylencarbonat (PC) als Lösungsmittel. Auch das Tieftemperaturverhalten von AN-basierten EDLCs ist erheblich besser.

Gerade beim Tieftemperaturverhalten gibt es auch deutliche Unterschiede zwischen EDCLs und Lithium-Ionen Kondensatoren (LIC). Während ein LIC bei Raumtemperatur und darüber ein zum EDLC vergleichbares Impedanzspektrum zeigt, nähert sich dieses bei tiefen Temperaturen dem einer Lithium-Ionen-Batterie an. LIC besitzen zwar aufgrund der höheren Zellspannung im Vergleich zu EDCLs eine höhere Energiedichte aber ein deutlich schwächeres Tieftemperaturverhalten.

#### B.4 Die Porenstruktur aktivierten Kohlenstoffs

Die Porenstruktur von aktiviertem Kohlenstoff, wie er als Elektrodenmaterial in EDLCs verwendet wird, ist äußerst komplex. Durch verschiedene Aktivierungsprozesse kann erreicht werden, dass sich eine komplexe Porengrößenverteilung ergibt. Man unterscheidet generell zwischen Makroporen ( $\emptyset > 500\,$  Å), Mesoporen (20 Å <  $\emptyset < 500\,$  Å) und Mikroporen ( $\emptyset < 20\,$ Å). Da mit einem stark mikroporösen Material höhere Oberflächen und somit auch höhe-

re Kapazitäten erreicht werden können wird diese vorwiegend in EDCLs eingesetzt. Da diese kleinen Poren aber nur über lange Diffusionswege erreicht werden können, führt dies zu großen Zeitkonstanten, die sich auf das elektrische Verhalten des EDLCs auswirken.

Ein wichtiger Aspekt ist außerdem, dass die Porenstruktur des Elektrodenmaterials zu den lonen des Elektrolyten passen muss. Zu kleine Poren können von den größeren Ionen nicht erreicht werden und tragen so nicht zur Kapazität bei. Allerdings hat sich in Experimenten gezeigt, dass die Ionen des Elektrolytsalzes, die normalerweise von einer Hülle aus Lösungsmittelmolekülen umgeben sind, diese Solvationshülle teilweise oder ganz abstreifen können, um auch sehr kleine Mikroporen noch zu erreichen. So können auch kleine Mikroporen, die einen geringen Durchmesser als das Ion mit Solvationshhülle besitzen, zur Kapazität beitragen und diese deutlich erhöhen.

Ferner führt die Porenstruktur auch zu Umverteilungsprozessen in den Poren nachdem der EDCL geladen oder entladen wurde. Beim Laden sammeln sich die Ionen zunächst an der Porenöffnung und führen so zu einer hohen Zellspannung. Nach Abschalten des Stroms werden dann einige Ionen tiefer in die Pore rein diffundieren um eine gleichmäßige Ionenverteilung in der Pore zu erreichen. Dies führt dazu, dass die Spannung wieder sinkt. Ein entgegengesetztes Verhalten zeigt sich beim Entladen, dann ist zu beobachten, dass die Spannung wieder steigt. Man kann sich diesen Prozess, der durch die langsamen Diffusionsprozesse in tieferen Porenschichten begründet ist, als ein Netzwerk aus mehreren parallel geschalteten Kondensatoren vorstellen, bei dem zuerst der erste geladen wird und der sich dann über die nächsten Kondensatoren entlädt bis sich ein Gleichgewicht einstellt. Dieser Prozess ist stark von der Zellspannung, der Temperatur und der Ladevorgeschichte abhängig.

In Selbstentladeexperimenten ist zu beobachten, dass die Spannung zunächst stark exponentiell, dann schwächer exponentiell und später nahezu linear abfällt. Der exponentielle Abfall ist auf die Ionen-Umverteilungsprozesse in den Poren zurückzuführen und nur der lineare Spannungsabfall wird durch irreversible Reaktionen hervorgerufen, die zur Selbstentladung führen.

#### B.5 Modellierung poröser Kohlenstoff-Elektroden

Da aufgrund der komplexen Porenstruktur Umverteilungsprozesse in den Poren stattfinden, die das Spannungsverhalten eines EDLCs stark beeinflussen, kann ein EDLC nicht hinreichend durch ein einfaches Ersatzschaltbild bestehend aus einer Kapazität und einem Widerstand beschrieben werden. De Levie veröffentlichte in den 1960er Jahren den Ansatz poröse Elektroden durch ein Kettenleiternetzwerk bestehend aus RC-Gliedern zu beschreiben. Mit solch einem Ersatzschaltbild können dynamische Prozesse gut abgebildet werden, allerdings setzt De Levie ideale zylindrische Poren voraus und trägt auch den verschiedenen Porengrößen nicht Rechnung. Daher ist es mit diesem Ansatz nicht möglich langandauernde Umverteilungsprozesse in den Poren, wie sie bei Selbstentlademessungen auftreten, abzubilden. Da-

raufhin wurden reine Selbstentlade-Modelle entwickelt, die die Selbstentlademessungen, auf die sie parametriert wurden, gut repräsentieren aber nicht in der Lage sind ein dynamisches Stromprofil abzubilden.

Ein in dieser Arbeit entwickelter Ansatz für ein elektrisches Ersatzschaltbild, das aus insgesamt fünf RC-Gliedern besteht, von denen die ersten drei durch Impedanzspektroskopie parametriert werden, die das dynamische Verhalten mit kleinen Zeitkonstanten repräsentieren, und zwei weitere RC-Glieder, die durch Selbstentlademessungen parametriert werden und das Langzeitverhalten abbilden, zeigt eine gute Übereinstimmung sowohl bei einem Impedanzspektrum als auch bei einer Selbstentlademessung an derselben Zelle.

#### B.6 Elektro-thermisches Modell

Für die Auslegung eines EDLC-Moduls ist die Kenntnis des thermischen Verhaltens der Zellen und der Temperaturverteilung im Modul essentiell. Die Temperaturentwicklung einer Zelle ist dabei sowohl von der durch Stromfluss generierten Wärme wie auch der Wärmeübertragung zu den benachbarten Zellen und der Umgebung abhängig.

In dieser Arbeit wurde daher zunächst ein modulares elektro-thermisches Einzelzell-Modell entwickelt, bei dem sich das elektrische und das thermische Modell gegenseitig bedingen. Das elektrische Modell berechnet die generierte Wärme, während das thermische Modell den Wärmeübergang unter Berücksichtigung von Wärmeleitung, Wärmestrahlung und Konvektion berechnet. Darüber hinaus wird auch die reversible Wärme, die durch Entropieänderungen entsteht, berechnet. Um die Temperaturverteilung ortaufgelöst darstellen zu können wird die Finite-Differenzen-Methode (FDM) angewandt. Dazu wird die Zelle abhängig von deren Geometrie in mehrere Volumen-Elemente unterteilt. Während der thermischen Simulation wird dann für jedes Volumenelement eine Energiebilanz aus generierter und abgeführter Wärme erstellt und daraus die Temperatur dieses Volumenelements berechnet. Bei Validierungsmessungen zeigen Simulation und Messung sowohl elektrisch als auch thermisch gute Übereinstimmungen.

Dieses Einzelzell-Model wurde dann zu einem Modulmodell erweitert. Das elektrische Modell wurde derart angepasst, dass alle Modell-Parameter wie Strom, Spannung, Temperatur ect. als Vektor in einer Größe entsprechend der Anzahl der Zellelemente hinterlegt sind. Dies verringert die Rechenzeit und erlaubt auch die Modul-Konfiguration flexibel im Hinblick auf Anzahl und Verschaltung der Zellen zu ändern. Außerdem gibt es das Modell in zwei Varianten, einmal für prismatische und einmal für zylindrische Zellen. Darüber hinaus berücksichtigt das Modulmodell auch die Wärmeentwicklung über die Zellverbinder wie auch den Wärmeübergang über das Modulgehäuse. Durch Variation des Wärmeübergangs am Gehäuse können z.B. forcierte Luftkühlung oder auch Wasserkühlung simuliert und so Kühlstrategien für das entsprechende Modul entwickelt werden.

#### B.7 Alterungsverhalten

Auch wenn Energie bei EDCLs theoretisch rein elektrostatisch gespeichert wird, so gibt es auch bei EDLCs parasitäre chemische Reaktionen die zur Alterung der Zelle, z.B. durch Zersetzung des Elektrolyten, führen. Diese Prozesse sind stark von Spannung und Temperatur abhängig. Typischerweise wird die Lebensdauer mit folgenden Faktoren abgeschätzt: 100 mV Spannungserhöhung bzw. 10 K Temperaturerhöhung halbieren die Lebensdauer. Dies sind aber nur Richtwerte, die überprüft werden müssen.

Zur Untersuchung des Alterungsverhaltens von Batterien oder EDLCs werden beschleunigte Alterungstests eingesetzt. Man unterscheidet dabei generell zwischen kalendarischen Alterungstest, bei denen die Zellen bei konstanter Temperatur und Spannung gelagert werden, und zyklischen Alterungstests, bei denen die Zellen mit konstantem Strom in einem bestimmten Spannungsband zyklisiert werden.

In dieser Arbeit wurden kalendarische Alterungstests an kommerziellen EDCLs von zwei verschiedenen Herstellern, hier Typ A und Typ B genannt, durchgeführt. Die Zellen zeigen ein unterschiedliches Alterungsverhalten und beide zeigen bei unterschiedlichen Testbedingungen eine unterschiedliche Spannungs- und Temperaturabhängigkeit der Alterung die im Bereich von 50 mV bis 140 mV bzw.5 K bis 10.5 K liegen kann. Die Zellen von Typ B besitzen einen Papierseparator, der sich vermutlich negativ auf das Alterungsverhalten der Zellen auswirkt. Daher wurden zusätzlich noch Zellen vom Typ C gealtert, die eine Polypropylen Membran verwenden. Diese Zellen besitzen eine deutlich längere Lebensdauer und altern über einen längeren Bereich nahezu linear. Durch die Kunststoff-Membran konnten die Zellen bei der Fertigung bei einer deutlich höheren Temperatur getrocknet werden und so deutlich mehr Wasser aus der Kohlenstoff-Elektrode entfernt werden. Die Testergebnisse zeigen deutlich, dass der höhere Wasseranteil des Papierseparators sich negativ auf die Lebensdauer der Zelle auswirkt.

Zusätzlich zu den kalendarischen Alterungstests wurde auch zyklische Alterungstests an Zellen des Typs B durchgeführt. Dabei wurden zwei verschiedene Varianten durchgeführt, einmal mit höherem Strom und niedrigeren Spannungsband und einmal mit niedrigerem Strom und höheren Spannungsband. Da es generell schwierig ist den rein zyklischen Alterungseinfluss bei EDLCs zu bestimmen, da die kalendarische Alterung dominiert, wurden die Zellen während des Tests stets gekühlt. So sollte verhindert werden, dass die Zellen aufgrund der durch den Stromfluss generierten Wärme zu stark kalendarisch altern. Über einen Test-Zeitraum von mehr als drei Jahren konnten mehr als eine Million äquivalente Vollzyklen erreicht werden, bei einer Kapazitätsabnahme von lediglich wenigen Prozent und einer Widerstandserhöhung um einen Faktor von 1,3 bis 1,5. Allerdings fielen einige der Zellen ohne Vorwarnung aus, vermutlich durch interne Kurzschlüsse. Der Vergleich der zyklischen Alterung und der kalendarischen Alterung bei der gegebenen Temperatur und Spannung ist extrem schwierig, da die kalendarische Alterung nicht klar bestimmt werden kann. Die Impedanzspektren während der zyklischen Alterung zeigen deutliche Unterschiede im Vergleich zur kalendarischen Alterung, nimmt man allerdings an, dass die Spannung der Zelle die Alte-

rung in diesem Bereich nicht beeinflusst, könnte die kontinuierliche Alterung während der Zyklisierung auch allein durch den Temperaturanstieg bedingt sein. Der plötzliche Ausfall der Zellen dagegen tritt bei rein kalendarischer Alterung nicht auf.

Da während der beschleunigten Alterungstests nur die Auswirkungen auf die elektrische Performance festgestellt werden können, wurden die Zellen nach Beendigung der Tests auch geöffnet und eine Post-Mortem-Analyse durchgeführt um Erkenntnisse über chemische Prozesse in der Zelle zu erlangen. Zunächst wurden Zellen vom Typ B geöffnet, deren Elektroden waren allerdings nicht mehr für weitere Analysen verwendbar. Der Kohlenstoff der negativen Elektrode blätterte nahezu komplett ab, während die positive Elektrode einen festen Verbund mit dem Separator einging. Daher wurden auch Zellen vom Typ C geöffnet. Auch hier blätterte teilweise etwas Kohlenstoff von der negativen Elektrode ab, allerdings ließ sich die positive Elektrode relativ gut vom Separator abziehen. Letztere hat im Vergleich zur Referenzelektrode eines neuen EDLCs deutlich an Gewicht gewonnen. Lasermikroskop -Aufnahmen lassen vermuten, dass sich eine Deckschicht auf der positiven Elektrode gebildet hat. In REM-Aufnahmen zeigt sich dann, dass es keine geschossene Deckschicht gibt, sondern sich in den zahlreich entstandenen Rissen Fasern gebildet haben, die diese Risse zusammenhalten. Auch der negativen Elektrode zeigen sich zahlreiche Risse, allerdings ist kein verbindendes Faser-Material zu erkennen. Diese Risse in beiden Elektroden führen zunächst dazu, dass Elektronen einen längeren Weg zu den Ableitern zurücklegen müssen. Ab einem gewissen Punkt sind dann aber Teile des Aktivmaterials von dem Ableiter elektrisch abgeschnitten, was zu dem starken Kapazitätsabfall und Widerstandsanstieg gegen Ende der Alterung führt. Impedanzmessungen an symmetrischen Knopfzellen (pos. Gegen pos. Elektrode und neg. gegen neg. Elektrode), die aus dem Elektrodenmaterial der gealterten Zellen gefertigt wurden, zeigen, dass sich das dynamische Verhalten der negativen Elektrode kaum ändert, wohingegen bei der positiven Elektrode im Nyquist-Plot ein deutlicher Halbkreis entsteht, der auch Ladungstransferprozesse schießen lässt. Das Impedanzverhalten der gesamten Zelle wird von der positiven Elektrode dominiert. Außerdem ist auch zu beobachten, dass sich die Zeitkonstante der positiven Elektrode deutlich zu größeren Werten verschiebt, während es bei der negativen Elektrode nur geringe Änderungen gab.

#### B.8 Alterungsmodell

In dieser Arbeit wurde zunächst das in Kapitel 6 entwickelte Modell um ein modulares Alterungsmodell erweitert. Abhängig von Temperatur und Spannung wird die kalendarische Alterung berechnet und anhand der Ergebnisse die Werte für Kapazität und Widerstand der Zelle in jedem Zeitschritt entsprechend der Alterung angepasst. Es besteht die Option dieses Modell um die Abbildung der zyklischen Alterung zu erweitern. Dieses Modell wurde anschließend zu einem Modulmodell erweitert, das auch in der Lage ist verschiedene Modul-Konfigurationen wie auch Kühlstrategien zu simulieren, so dass eine Lebensdauerprognose abgegeben werden kann anhand der das System optimiert werden kann. Die Herausforde-

rung ist allerdings dieses Modell optimal zu parametrieren, da die Alterungstests in dieser Arbeit gezeigt haben, dass die Alterungsprozesse zu komplex sind um sie in simplen Abhängigkeitsfaktoren für Temperatur und Spannung auszudrücken. Das entwickelte Modell soll die Basis bilden, um eine zuverlässige Lebensdauerprognose für ein optimales System-Design abgeben zu können nachdem durch weitere Untersuchungen ein tieferes Verständnis der Alterung geschaffen wurde.

#### B.9 Zusammenfassung und Ausblick

Elektrochemische Doppelschichtkondensatoren (EDLC) finden aufgrund ihrer hohen Leistungsdichte und Zyklenfestigkeit ein breites Anwendungsspektrum. Die Abbildung des elektrischen Verhaltens eines EDLCs in einem Modell ist allerdings komplex, da aufgrund der Porenstruktur Ionen-Umverteilungsprozesse in der Zelle stattfinden, die zu einer Relaxation der Zellspannung führen. Bei bisher publizierten Modellen handelt es sich meist um Modelle, die entweder hoch-dynamische Profile abbilden können dafür aber Schwächen im Langzeitverhalten haben oder umgekehrt. In dieser Arbeit wurde daher ein elektrisches Modell entwickelt, das in der Lage ist sowohl hoch-dynamische Prozesse wie auch Selbstentlademessungen abzubilden.

Das elektrische Modell wurde anschließend zu einem modularen elektrisch-thermischen Modell erweitert, das es erlaubt ortsaufgelöst die Temperatur-Entwicklung der Zelle bei gegebenem Stromprofil zu simulieren. Durch die Erweiterung zu einem Modulmodell kann auch die Temperaturentwicklung im Modul abgebildet und so mögliche Hotspots erkannt werden. Außerdem können verschiedene Kühlstrategien analysiert werden.

Trotz rein elektrostatischer Energiespeicherung können auch bei EDLCs Nebenreaktionen ablaufen, die stark von Temperatur und Spannung abhängig sind und zur Alterung der Zelle führen. In kalendarischen Alterungstest an verschiedenen kommerziellen EDLCs zeigte sich, dass die allgemein angenommenen Abschätzungs-Faktoren, die zu einer Halbierung der Lebensdauer führen (10 K Temperaturerhöhung und 100 mV Spannungserhöhung) nicht zutreffen. Die Alterungsfaktoren variierten bei beiden untersuchten Zelltypen stark. Außerdem zeigte sich, dass die Alterung bei Zellen verschiedener Hersteller durch den Einsatz unterschiedlicher Zellmaterialien sehr unterschiedlich ablaufen kann. Bei Zyklentests zeigte sich außerdem, dass zusätzliche Effekte im Vergleich zur kalendarischen Alterung auftreten. Allerdings konnte nicht abschließend geklärt werden inwieweit diese reversibel sind. Außerdem konnte der genaue Einfluss der kalendarischen Alterung nicht exakt bestimmt werden.

Durch die Post-Mortem-Analyse einiger kalendarisch gealterter Zellen konnte gezeigt werden, dass unterschiedliche Prozesse dazu führen, dass aufgrund von Rissen Aktivmaterial von der negativen Elektrode abblättert, während die Risse an der positiven Elektrode durch ein Faser-haltiges Material zusammengehalten werden. Dieses Material führt zu einem stark veränderten dynamischen Verhalten der Elektrode und zu einer stark erhöhten Zeitkonstante. Das elektrische Verhalten der gesamten Zelle wird durch die positive Elektrode dominiert.

Aus der Post-Mortem-Analyse konnten erste Hinweise auf Alterungsmechanismen gewonnen werden, die allerdings noch nicht ausreichen, um die Alterung in einem physikalischen Modell abzubilden. Anhand der Ergebnisse der beschleunigten Alterungstests konnte jedoch das Modulmodell um ein Alterungsmodell erweitert werden, das die Entwicklung von Kapazität und Widerstand über die Alterung prognostiziert.

Da mithilfe der in dieser Arbeit durchgeführten kalendarischen und zyklischen Alterungstests nicht abschließend geklärt werden konnte, welche Faktoren die Alterung in welchen Bereich wie beeinflussen, sind weitere Alterungstests nötig. Neben der Frage der optimalen Auslegung von beschleunigten Alterungstests ist insbesondere auch die Frage des Einflusses der kalendarischen Alterung bei Zyklentests zu klären.

Aufbauend auf den Ergebnissen dieser Arbeit kann durch weitere Analysen insbesondere auch die der Porenstruktur durch BET-Messungen ein tieferes Verständnis der Alterungsprozesse in EDLCs erlangt werden. Mithilfe weiterer Tests, bei denen Zellen, die bei gleichen Testbedingungen gealtert werden, in verschiedenen Alterungszuständen untersucht werden, kann sie Veränderung der Porenstruktur über den Alterungsprozess untersucht werden. Außerdem kann der Einfluss der zyklischen Alterung durch neue Testreihen weiter analysiert werden.

Mit der Kenntnis der wesentlichen Alterungsprozesse bedingt durch Temperatur, Spannung und Stromrate kann dann ein physikalisch-basiertes Modell entwickelt werden, das sowohl in der Lage ist den Energiespeicherprozess als auch die Alterungsmechanismen und deren Auswirkungen auf die Zelleparameter wie Kapazität und Widerstand abzubilden.

#### **ABISEA Band 1**

Eßer, A.

Berührungslose, kombinierte Energie- und Informationsübertragung für bewegliche Systeme

1. Auflage 1992, 130 Seiten ISBN 3-86073-046-0

## ABISEA Band 2 Vogel, U.

Entwurf und Beurteilung von Verfahren zur Hochausnutzung des Rad-Schiene-Kraftschlusses durch Triebfahrzeuge 1. Auflage 1992, 130 Seiten ISBN 3-86073-060-6

## ABISEA Band 3 Redehorn, Th.

Stromeinprägendes Antriebssystem mit fremderregter Synchronmaschine 1. Auflage 1992, 130 Seiten ISBN 3-86073-061-4

#### ABISEA Band 4 Ackva, A.

Spannungseinprägendes Antriebssystem mit Synchron-maschine und direkter Stromregelung 1. Auflage 1992, 135 Seiten ISBN 3-86073-062-2

#### ABISEA Band 5 Mertens, A.

Analyse des
Oberschwingungsverhaltens
von taktsynchronen Delta Modulationsverfahren zur
Steuerung von
Pulsstromrichtern bei hoher
Taktzahl
1. Auflage 1992, 170 Seiten
ISBN 3-86073-069-X

## ABISEA Band 6 Geuer, W.

Untersuchungen über das Alterungsverhalten von Bleiakkumulatoren 1. Auflage 1993, 100 Seiten ISBN 3-86073-097-5

# ABISEA Band 7 Langheim, J.

Einzelradantrieb für Elektrostraßenfahrzeuge 1. Auflage 1993, 215 Seiten ISBN 3-86073-123-8 (vergriffen)

#### ABISEA Band 8 Fetz, J.

Fehlertolerante Regelung eines Asynchron-Doppelantriebes für ein Elektrospeicherfahrzeug 1. Auflage 1993, 136 Seiten ISBN 3-86073-124-6 (vergriffen)

# ABISEA Band 9 Schülting, L.

Optimierte Auslegung induktiver Bauelemente für den Mittelfrequenzbereich 1. Auflage 1993, 136 Seiten ISBN 3-86073-174-2 (vergriffen)

## ABISEA Band 10 Skudelny, H.-Ch.

Stromrichtertechnik 4. Auflage 1997, 259 Seiten ISBN 3-86073-189-0

# ABISEA Band 11 Skudelny, Ch.

Elektrische Antriebe 3. Auflage 1997, 124 Seiten ISBN 3-86073-231-5

# ABISEA Band 12 Schöpe, F.

Batterie-Management für Nickel-Cadmium Akkumulatoren 1. Auflage 1994, 156 Seiten ISBN 3-86073-232-3 (vergriffen)

## ABISEA Band 13 v. d. Weem, J.

Schmalbandige aktive Filter für Schienentriebfahrzeuge am Gleichspannungs-fahrdraht 1. Auflage 1995, 125 Seiten ISBN 3-86073-233-1

## ABISEA Band 14 Backhaus, K.

Spannungseinprägendes Direktantriebssystem mit schnelllaufender geschalteter Reluktanzmaschine 1. Auflage 1995, 156 Seiten ISBN 3-86073-234-X (vergriffen)

#### ABISEA Band 15 Reinold, H.

Optimierung dreiphasiger Pulsdauermodulationsverfahren 1. Auflage 1996, 116 Seiten ISBN 3-86073-235-8

#### ABISEA Band 16 Köpken, H.-G.

Regelverfahren für Parallelschwingkreisumrichter 1. Auflage 1996, 125 Seiten ISBN 3-86073-236-6

## ABISEA Band 17 Mauracher, P.

Modellbildung und Verbundoptimierung bei Elektrostraßenfahrzeugen 1. Auflage 1996, 192 Seiten ISBN 3-86073-237-4

# ABISEA Band 18 Protiwa, F.-F.

Vergleich dreiphasiger Resonanz-Wechselrichter in Simulation und Messung 1. Auflage 1997, 178 Seiten ISBN 3-86073-238-2

# ABISEA Band 19 Brockmeyer, A.

Dimensionierungswerkzeug für magnetische Bauelemente in Stromrichteranwendungen 1. Auflage 1997, 182 Seiten ISBN 3-86073-239-0

## ABISEA Band 20 Apeldoorn, 0.

Simulationsgestützte Bewertung von Steuerverfahren für netzgeführte Stromrichter mit verringerter Netzrück-wirkung 1. Auflage 1997, 132 Seiten ISBN 3-86073-680-9

## ABISEA Band 21 Lohner, A.

Batteriemanagement für verschlossene Blei-Batterien am Beispiel von Unterbrechungsfreien Stromversorgungen 1. Auflage 1998, 144 Seiten ISBN 3-86073-681-7

# ABISEA Band 22 Reinert, J.

Optimierung der Betriebseigenschaften von Antrieben mit geschalteter Reluktanzmaschine

1. Auflage 1998, 168 Seiten ISBN 3-86073-682-5

### ABISEA Band 23 Nagel, A.

Leitungsgebundene Störungen in der Leistungselektronik: Entstehung, Ausbreitung und Filterung 1. Auflage 1999, 160 Seiten ISBN 3-86073-683-3

## ABISEA Band 24 Menne, M.

Drehschwingungen im Antriebsstrang von Elektrostraßenfahrzeugen -Analyse und aktive Dämpfung 1. Auflage 2001, 192 Seiten ISBN 3-86073-684-1

#### ABISEA Band 25 von Bloh, J.

Multilevel-Umrichter zum Einsatz in Mittelspannungs-Gleichspannungs-Übertragungen 1. Auflage 2001, 152 Seiten ISBN 3-86073-685-X

# ABISEA Band 26 Karden, E.

ISBN 3-8265-9766-4

Using low-frequency impedance spectroscopy for characterization, monitoring, and modeling of industrial batteries

1. Auflage 2002, 154 Seiten

# ABISEA Band 27 Karipidis, C.-U.

A Versatile DSP/ FPGA Structure optimized for Rapid Prototyping and Digital Real-Time Simulation of Power Electronic and Electrical Drive Systems 1. Auflage 2001, 164 Seiten ISBN 3-8265-9738-9

# ABISEA Band 28 Kahlen, K.

Regelungsstrategien für permanentmagnetische Direktantriebe mit mehreren Freiheitsgraden 1. Auflage 2003, 158 Seiten ISBN 3-8322-1222-1

# ABISEA Band 29 Inderka, R.

Direkte Drehmomentregelung Geschalteter Reluktanzantriebe 1. Auflage 2003, 190 Seiten ISBN 3-8322-1175-6

# ABISEA Band 30 Schröder, S.

Circuit-Simulation Models of High-Power Devices Based on Semiconductor Physics 1. Auflage 2003, 124 Seiten ISBN 3-8322-1250-7

# ABISEA Band 31 Buller, S.

Impedance-Based Simulation Models for Energy Storage Devices in Advanced Automotive Power Systems 1. Auflage 2003, 136 Seiten ISBN 3-8322-1225-6

### ABISEA Band 32 Schönknecht, A.

Topologien und Regelungsstrategien für das induktive Erwärmen mit hohen Frequenz-Leistungsprodukten 1. Auflage 2004, 1 70 Seiten ISBN 3-8322-2408-4

## ABISEA Band 33 Tolle, T.

Konvertertopologien für ein aufwandsarmes, zweistufiges Schaltnetzteil zum Laden von Batterien aus dem Netz 1. Auflage 2004, 150 Seiten

# ABISEA Band 34 Götting, G.

ISBN 3-8322-2676-1

Dynamische Antriebsregelung von Elektrostraßenfahrzeugen unter Berücksichtigung eines schwingungsfähigen Antriebsstrangs
1. Auflage 2004, 166 Seiten ISBN 3-8322-2804-7

#### ABISEA Band 35 Dieckerhoff, S.

Transformatorlose Stromrichterschaltungen für Bahnfahrzeuge am 16 2/3Hz Netz 1. Auflage 2004, 158 Seiten ISBN 3-8322-3094-7

## ABISEA Band 36 Hu, J.

Bewertung von DC-DC-Topologien und Optimierung eines DC-DC-Leistungsmoduls für das 42-V-Kfz-Bordnetz

1. Auflage 2004, 156 Seiten ISBN 3-8322-3201-X

# ABISEA Band 37 Detjen, D.-0.

Characterization and Modeling of Si-Si Bonded Hydrophobie Interfaces for Novel High-Power BIMOS Devices

1. Auflage 2004, 146 Seiten ISBN 3-8322-2963-9

#### ABISEA Band 38 Walter, J.

Simulationsbasierte Zuverlässigkeitsanalyse in der modernen Leistungselektronik

1. Auflage 2004, 134 Seiten ISBN 3-8322-3481-0

# ABISEA Band 39 Schwarzer, U.

IGBT versus GCT in der Mittelspannungsanwendung - ein experimenteller und simulativer Vergleich 1. Auflage 2005, 184 Seiten ISBN 3-8322-4489-1

## ABISEA Band 40 Bartram, M.

IGBT-Umrichtersysteme für Windkraftanlagen: Analyse der Zyklenbelastung, Modellbildung, Optimierung und Lebensdauervorhersage
1. Auflage 2006, 195 Seiten ISBN 3-8322-5039-5

## ABISEA Band 41 Ponnaluri, S.

Generalized Design, Analysis and Control of Grid side converters with integrated UPS or Islanding functionality 1. Auflage 2006, 163 Seiten ISBN 3-8322-5281-9

## ABISEA Band 42 Jacobs, J.

Multi-Phase Series Resonant DC-to-DC Converters 1. Auflage 2006, 185 Seiten ISBN 3-8322-5532-X

#### ABISEA Band 43 Linzen, D.

Impedance-Based Loss Calculation and Thermal Modeling of Electrochemical Energy Storage Devices for Design Considerations of Automotive Power Systems 1. Auflage 2006, 150 Seiten ISBN 3-8322-5706-3

# ABISEA Band 44 Fiedler, J.

Design of Low-Noise Switched Reluctance Drives 1. Auflage 2007, 183 Seiten ISBN 978-3-8322-5864-I

# ABISEA Band 45 Fuengwarodsakul, N.

Predictive PWM-based Direct Instantaneous Torque Control for Switched Reluctance Machines 1. Auflage 2007, 150 Seiten ISBN 978-3-8322-6210-5

## ABISEA Band 46 Meyer, C.

Key Components for Future Offshore DC Grids 1. Auflage 2007, 196 Seiten ISBN 978-3-8322-6571-7

# ABISEA Band 47 Fujii, K.

Characterization and Optimization of Soft-Switched Multi-Level Converters for STATCOMs 1. Auflage 2008, 206 Seiten ISBN 978-3-8322-6981-4

# ABISEA Band 48 Carstensen, C.

Eddy Currents in Windings of Switched Reluctance Machines 1. Auflage 2008, 190 Seiten ISBN 978-3-8322-7118-3

## ABISEA Band 49 Bohlen, 0.

Impedance-based battery monitoring 1. Auflage 2008, 200 Seiten ISBN 978-3-8322-7606-5

# ABISEA Band 50 Thele. M.

A contribution to the modelling of the charge acceptance of lead-acid batteries - using frequency and time domain based concepts
1. Auflage 2008, 168 Seiten ISBN 978-3-8322-7659-1

#### ABISEA Band 51 König, A.

High Temperature DC-to-DC Converters for Downhole Applications 1. Auflage 2009, 160 Seiten ISBN 978-3-8322-8489-3

## ABISEA Band 52 Dick, C. P.

Multi-Resonant Converters as Photovoltaic Module-Integrated Maximum Power Point Tracker 1. Auflage 2010, 192 Seiten ISBN 978-3-8322-9199-0

## ABISEA Band 53 Kowal, J.

Spatially-resolved impedance of nonlinear inhomogeneous devices - using the example of lead-acid batteries -

1. Auflage 2010, 214 Seiten ISBN 978-3-8322-9483-0

#### ABISEA Band 54 Roscher, M.

Zustandserkennung von LiFeP04-Batterien für Hybrid- und Elektrofahrzeuge 1. Auflage 2011, 194 Seiten ISBN 978-3-8322-9738-I

## ABISEA Band 55 Hirschmann, D.

Highly Dynamic Piezoelectric Positioning 1. Auflage 2011, 156 Seiten ISBN 978-3-8322-9746-6

## ABISEA Band 56 Rigbers, K.

Highly Efficient Inverter Architectures for Three-Phase Grid Connection of Photovoltaic Generators 1. Auflage 2011, 254 Seiten ISBN 978-3-8322-9816-9

## ABISEA Band 57 Kasper, K.

Analysis and Control of the Acoustic Behavior of Switched Reluctance Drives 1. Auflage 2011, 214 Seiten ISBN 978-3-8322-9869-2

#### ABISEA Band 58 Köllensperger, P.

The Internally Commutated Thyristor - Concept, Design and Application 1. Auflage 201 J, 212 Seiten ISBN 978-3-8322-9909-5

## ABISEA Band 59 Schoenen, T.

Einsatz eines DC/DC-Wandlers zur Spannungsanpassung zwischen Antrieb und Energiespeicher in Elektro-und Hybridfahrzeugen 1. Auflage 2011, 138 Seiten ISBN 978-3-8440-0622-3

#### ABISEA Band 60 Hennen, M.

Switched Reluctance Direct Drive with Integrated Distributed Inverter 1. Auflage 2012, 150 Seiten ISBN 978-3-8440-0731-2

## ABISEA Band 61 van Treek, D.

Position Sensorless Torque Control of Switched Reluctance Machines 1. Auflage 2012, 144 Seiten ISBN 978-3-8440-IO 14-5

# ABISEA Band 62 Bragard, M.

Tue Integrated Emitter Turn-Off Thyristor. An Innovative MOS-Gated High-Power Device

1. Auflage 2012, 172 Seiten ISBN 978-3-8440-1152-4

#### ABISEA Band 63 Gerschler, J. B.

Ortsaufgelöste Modellbildung von Lithium-Ionen-Systemen unter spezieller Berücksichtigung der Batteriealterung 1. Auflage 2012, 350 Seiten ISBN 978-3-8440-1307-8

#### ABISEA Band 64 Neuhaus, C.

Schaltstrategien für Geschaltete Reluktanzantriebe mit kleinem Zwischenkreis 1. Auflage 2012, 144 Seiten ISBN 978-3-8440-1487-7

# ABISEA Band 65 Butschen, T.

Dual-ICT- A Clever Way to Unite Conduction and Switching Optimized Properties in a Single Wafer 1. Auflage 2012, 178 Seiten ISBN 978-3-8440-1771-7

### ABISEA Band 66 Plum. T.

Design and Realization of High-Power MOS Turn-Off Thyristors 1. Auflage 2013, 130 Seiten ISBN 978-3-8440-1884-4

# ABISEA Band 67 Kiel, M.

Impedanzspektroskopie an Batterien unter besonderer Berücksichtigung von Batteriesensoren für den Feldeinsatz 1. Auflage 2013, 232 Seiten ISBN 978-3-8440-1973-5

#### ABISEA Band 68 Brauer, H.

Schnelldrehender Geschalteter Reluktanzantrieb mit extremem Längendurchmesserverhältnis

1. Auflage 2013, 202 Seiten ISBN 978-3-8440-2345-9

#### ABISEA Band 69 Thomas, S.

A Medium-Voltage Multi-Level DC/DC Converter with High Voltage Transformation Ratio

1. Auflage 2014, 236 Seiten ISBN 978-3-8440-2605-4

# ABISEA Band 70 Richter, S.

Digitale Regelung von PWM Wechselrichtern mit niedrigen Trägerfrequenzen 1. Auflage 2014, 134 Seiten ISBN 978-3-8440-2641-2

## ABISEA Band 71 Bösing, M.

Acoustic Modeling of Electrical Drives - Noise and Vibration Synthesis based on Force Response Superposition 1. Auflage 2014, 208 Seiten ISBN 978-3-8440-2752-5

#### ABISEA Band 72 Waag, W.

Adaptive algorithms for monitoring of lithium-ion batteries in electric vehicles 1. Auflage 2014, 242 Seiten ISBN 978-3-8440-2976-5

#### ABISEA Band 73 Sanders, T.

Spatially Resolved Electrical In-Situ Measurement Techniques for Fuel Cells 1. Auflage 2014, 138 Seiten ISBN 978-3-8440-3121-8

# ABISEA Band 74 Baumhöfer, T.

Statistische Betrachtung experimenteller Alterungsuntersuchungen an Lithiumlonen Batterien 1. Auflage 2015, 174 Seiten ISBN 978-3-8440-3423-3

#### ABISEA Band 75 Andre, D.

Systematic Characterization of Ageing Factors for High-Energy Lithium-Ion Cells and Approaches for Lifetime Modelling Regarding an Optimized Operating Strategy in Automotive Applications
1. Auflage 2015, 210 Seiten ISBN 978-3-8440-3587-2

# ABISEA Band 76 Merei, G.

Optimization of off-grid hybrid PV-wind-diesel power supplies with multitechnology battery systems taking into account battery aging

1. Auflage 2015, 194 Seiten ISBN 978-3-8440-4148-4

#### ABISEA Band 77 Schulte. D.

Modellierung und experimentelle Validierung der Alterung von Blei-Säure Batterien durch inhomogene Stromverteilung und Säureschichtung
1. Auflage 2016, 168 Seiten ISBN 978-3-8440-4216-0

#### ABISEA Band 78 Schenk, M.

Simulative Untersuchung der Wicklungsverluste in Geschalteten Reluktanzmaschinen 1. Auflage 2016, 142 Seiten

Auflage 2016, 142 Seiter
 ISBN 978-3-8440-4282-5

# ABISEA Band 79 Wang, Y.

Development of Dynamic Models with Spatial Resolution for Electrochemical Energy Converters as Basis for Control and Management Strategies 1. Auflage 2016, 198 Seiten ISBN 978-3-8440-4303-7

#### ABISEA Band 80 Ecker. M.

Lithium Plating in Lithiumlon Batteries: An Experimental and Simulation Approach 1. Auflage 2016, 170 Seiten ISBN 978-3-8440-4525-3

# ABISEA Band 81 Zhou, W.

Modellbasierte Auslegungsmethode von Temperierungssystemen für Hochvolt-Batterien in Personenkraftfahrzeugen 1. Auflage 2016, 192 Seiten ISBN 978-3-8440-4589-5

#### ABISEA Band 82 Lunz. B.

Deutschlands Stromversorgung im Jahr 2050 Ein szenariobasiertes Verfahren zur vergleichenden Bewertung von Systemvarianten und Flexibilitätsoptionen 1. Auflage 2016, 196 Seiten ISBN 978-3-8440-4627-4

#### ABISEA Band 83 Hofmann. A.

Direct Instantaneous Force Control Key to Low-Noise Switched Reluctance Traction Drives 1. Auflage 2016, 244 Seiten ISBN 978-3-8440-4715-8

## ABISEA Band 84 Budde-Meiwes, H.

Dynamic Charge Acceptance of Lead-Acid Batteries for Micro-Hybrid Automotive Applications 1. Auflage 2016, 168 Seiten ISBN 978-3-8440-4733-2

### ABISEA Band 85 Engel, S. P.

Thyristor-Based High-Power On-Load Tap Changers Control under Harsh Load Conditions 1. Auflage 2016, 170 Seiten

ISBN 978-3-8440-4986-2

#### ABISEA Band 86 VanHoek, H.

Design and Operation Considerations of Three-Phase Dual Active Bridge Converters for Low-Power Applications with Wide Voltage Ranges 1. Auflage 2017, 242 Seiten ISBN 978-3-8440-5011-0

# ABISEA Band 87 Diekhans, T.

Wireless Charging of Electric Vehicles - a Pareto-Based Comparison of Power Electronic Topologies 1. Auflage 2017, 156 Seiten ISBN 978-3-8440-5048-6

## ABISEA Band 88 Lehner, S.

Reliability Assessment of Lithium-Ion Battery Systems with Special Emphasis on Cell Performance Distribution 1. Auflage 2017, 202 Seiten ISBN 978-3-8440-5090-5

#### ABISEA Band 89 Käbitz. S.

Untersuchung der Alterung von Lithium-Ionen-Batterien mittels Elektroanalytik und elektrochemischer Impedanzspektroskopie 1. Auflage 2017, 257 Seiten urn:nbn:de:hbz:82-rwth-2016-120944

# ABISEA Band 90 Witzenhausen, H.

Elektrische
Batteriespeichermodelle:
Modellbildung,
Parameteridentifikation und
Modellreduktion
1. Auflage 2017, 286 Seiten
urn:nbn:de:hbz:82-rwth2017-034373

# ABISEA Band 91 Münnix, J.

Einfluss von Stromstärke und Zyklentiefe auf graphtitische Anoden 1. Auflage 2017, 178 Seiten DOI: 10.18154/RWTH-2017-01915

#### ABISEA Band 92 Pilatowicz, G.

Failure Detection and Battery Management Systems of Lead-Acid Batteries for Micro-Hybrid Vehicles Electrochemical double layer capacitors (EDLC), also known under the brand names supercapacitors or ultracapacitors, are energy storage devices that offer high power density, very high cycling capability and mechanical robustness. Although the energy storage principle is purely physical parasitic chemical reactions might occur during the storage process of EDLCs and lead to accelerated aging.

This thesis investigates the ageing processes of EDLCs and their impact factors such as elevated temperatures and cell voltages. Extensive test matrices of cyclic and calendric aging tests were performed with test periods up to more than three years. Post-mortem analysis of selected cells was performed to achieve a deeper understanding of the different aging processes at single electrodes.

Finally, a model was developed to simulate the electrical and thermal behavior of single cells as well as different module configurations. Additionally, an approach to represent the aging behavior as well was developed. This model is a useful tool for optimization of system design and operating strategies.